AN EXPERIMENTAL INVESTIGATION OF LEADING EDGE VORTICAL FLOW ABOUT A DELTA WING DURING WING ROCK

A Thesis
by

MICHAEL DENIS NELSON

Submitted to the Office of Graduate Studies of
Texas A&M University
in partial fulfillment of the requirements
for the degree of

MASTER OF SCIENCE

December 1991

Major Subject: Aerospace Engineering

REPORT DOCUMENTATION PAGE

Form Approved
OMB No 0704-0188

1. AGENCY USE ONLY (Leave blank)	2. REPORT DATE	3. REPORT TYPE AND DATES COVERED
	December 1991	THESIS/~~DISSERTATION~~

4. TITLE AND SUBTITLE
An Experimental Investigation of Leading Edge Vortical Flow About a Delta Wing During Wing Rock

5. FUNDING NUMBERS

6. AUTHOR(S)
Michael Denis Nelson, Captain

7. PERFORMING ORGANIZATION NAME(S) AND ADDRESS(ES)
AFIT Student Attending: Texas A & M University

8. PERFORMING ORGANIZATION REPORT NUMBER
AFIT/CI/CIA- 91-066

9. SPONSORING / MONITORING AGENCY NAME(S) AND ADDRESS(ES)
AFIT/CI
Wright-Patterson AFB OH 45433-6583

10. SPONSORING / MONITORING AGENCY REPORT NUMBER

11. SUPPLEMENTARY NOTES

12a. DISTRIBUTION / AVAILABILITY STATEMENT
Approved for Public Release IAW 190-1
Distributed Unlimited
ERNEST A. HAYGOOD, Captain, USAF
Executive Officer

12b. DISTRIBUTION CODE

13. ABSTRACT (Maximum 200 words)

14. SUBJECT TERMS

15. NUMBER OF PAGES
184

16. PRICE CODE

17. SECURITY CLASSIFICATION OF REPORT	18. SECURITY CLASSIFICATION OF THIS PAGE	19. SECURITY CLASSIFICATION OF ABSTRACT	20. LIMITATION OF ABSTRACT

AN EXPERIMENTAL INVESTIGATION OF LEADING EDGE VORTICAL FLOW ABOUT A DELTA WING DURING WING ROCK

A Thesis
by

MICHAEL DENIS NELSON

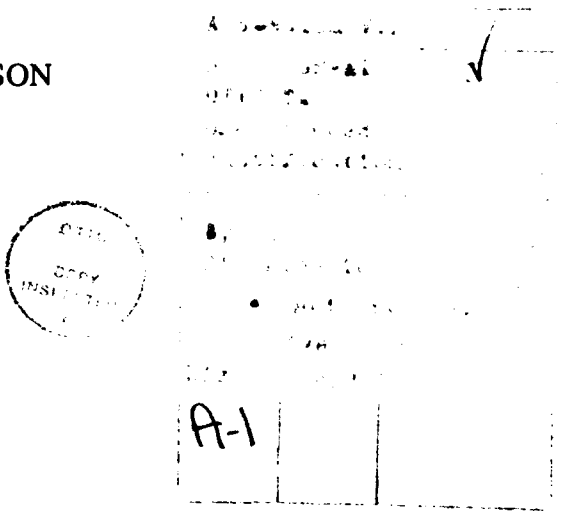

Approved as to style and content by:

Donald T. Ward
(Chair of Committee)

Leland A. Carlson
(Member)

Ricardo L. Diaz
(Member)

Walter E. Haisler
(Department Head)

December 1991

ABSTRACT

An Experimental Investigation of Leading Edge Vortical Flow
About A Delta Wing During Wing Rock

(December 1991)

Michael Denis Nelson, B.S. University of Kansas

Chair of Advisory Committee: Dr. Donald T. Ward

The primary objective of this research was to further investigate the dynamic motion of an 80° delta wing during wing rock in both a water and wind tunnel. Both vortical flow data and wing motion data were recorded using a video-based motion analysis system. This system provided adequate means to nonintrusively measure dynamic data. The data revealed hysteresis differences between the wind tunnel and water tunnel tests. The hysteresis in the C_ℓ versus ϕ, during water tunnel testing, traveled in the opposite direction of the wind tunnel results. Visualization of the water tunnel vortical flowfields provided quantified right and left vortex locations at specific roll angles during wing rock. The contribution to the rolling moment based on these vortex positions was analyzed. The results show a decrease in rolling moment before reaching the maximum roll amplitude and an increase in rolling moment after passing through the maximum roll angle.

In addition, added mass experiments were conducted in the wind tunnel. The wind tunnel rolling moment was 15 times larger than water tunnel results, due to the difference in densities of the mediums. Although dynamic similitude was not achieved between the two fluids, a foundation for further investigation has been laid.

DEDICATION

This thesis is dedicated to my wife, Nivia, who's love and patience has sustained me, and our son, Benjamin, who's love and wonderment has encouraged me. It is also dedicated to those who fought and to those who died in Operation Desert Storm. May God bless and keep them.

ACKNOWLEDGEMENTS

I would like thank all those folks who contributed to the success of this effort. I would like to first mention Dr. Donald Ward, my graduate advisor. His guidance and support have greatly assisted me in the completion of this study. I would also like to thank those on my committee, Dr. Leland Carlson and Dr. Ricardo Diaz, for their support of this project. I want to thank Mike Birdsell and Paul Petty for their guidance and machine work on the lathe and milling machines. Thanks to all the personnel at the Texas A&M Low Speed Wind Tunnel for all the effort put forth during wind tunnel testing. I also want to thank Dr. Anwar Ahmed and Javed Khan for their support in during water tunnel testing. A special thanks to James Myatt, who helped during water tunnel tests and the rest of the graduate students who contributed along the way. A generous thanks to the United States Air Force Academy's Aerospace Engineering Department for their sponsorship of the masters program.

Thanks especially go to my wife, Nivia, and son Benjamin, and to the Lord, Jesus Christ, who is my Helper.

TABLE OF CONTENTS

LIST OF TABLES

PAGE

LIST OF FIGURES

LIST OF SYMBOLS

Symbols

b	wing span, ft
$\bar{c}$	wing root chord, ft
C_l	rolling moment coefficient
C_{l_0}	rolling moment coefficient at zero sideslip
C_{l_p}	roll damping coefficient based on body-fixed axes
$C_{l_{p_0}}$	roll damping coefficient at zero sideslip
$C_{l_{\bar{p}}}$	dimensionless variation of roll damping derivative with roll rate, $\partial C_l / \partial \bar{p}$
C_{l_β}	dimensionless variation of roll damping derivative with sideslip, $\partial C_l / \partial \beta$
C_{l_β}	variation of rolling moment coefficient with sideslip
f	oscillation frequency, Hz
I_{xx}	moment of inertia about body x-axis, slug-ft^2
k	dimensionless reduced frequency, $\Omega b/2V_\infty$
L	rolling moment, ft-lb
P	period of limit cycle roll oscillations, sec
p	roll rate about x-axis, rad/sec or deg/sec
$\bar{p}$	dimensionless reduced roll rate, $pb/2V_\infty$
$\bar{q}$	dynamic pressure, lb/ft^2
Re	Reynolds number
s	wing semi-span, b/2
S	planform area, ft^2
t	time variable, sec
T	period of roll oscillations, sec
V	flow velocity, ft/sec or ips
V_∞	wind or water tunnel freestream velocity, ft/sec or ips
x	x-body axis location, inches

y	y-body axis location, inches
z	z-body axis location, inches
α	angle of attack, deg
α_o	angle of attack at zero roll angle, deg
α_s	sting angle of attack, deg
β	sideslip angle, deg or rad
ΔE	net energy, ft-lbs
Θ	wing sweep half angle, deg
Θ_A	apex half angle, deg
$\bar{\Theta}_A$	effective apex half angle, deg
Λ	wing leading-edge sweep angle, deg
ρ	fluid density, slug/ft^3
ϕ	roll or bank angle, deg or rad
$\dot{\phi}$	roll rate. deg/sec or rad/sec
$\ddot{\phi}$	roll acceleration, deg/sec^2 or rad/sec^2
ω	frequency of roll oscillations, rad/sec
Ω	frequency of limit cycle roll oscillation, rad/sec
μ	damping coefficient due to bearing friction

CHAPTER I
INTRODUCTION

Problem Statement

Wing rock is a dynamic mode of motion typically encountered on aircraft with slender bodies and highly swept wings flying at high angles of attack. This oscillatory motion has been observed to occur on an aircraft at angles of attack of 19°.[1] The lift generated at these high angles of attack occurs in the nonlinear region of the lift curve slope and is dependent on the vortical flow about the aircraft. The vortices that emanate from the forebody of the aircraft can become asymmetric with respect to the aircraft, and when this asymmetry occurs, the aircraft begins to oscillate. The oscillation or wing rock is primarily about the roll axis, however, specific wing rock motion for each aircraft will be different depending on the aircraft's configuration and flight condition. The buildup of wing rock will continue until a stable limit cycle is established. This type of motion has been observed on various aircraft such as the HP-115[1], F-5, F-14, and the F-18[2].

Numerous studies have investigated the wing rock motion of delta wings at high angles of attack. These studies include wind and water tunnel tests, mathematical modeling, computational fluid dynamic simulations, and full scale flight investigations. The studies reviewed below concentrate primarily on a single degree-of-freedom model about the roll axis, which is the same approach taken for the current research. Investigations continue into the mechanisms of wing rock and the devices necessary to control this phenomenon.

Wing Rock Literature Review

Wing rock is primarily a roll oscillation, and much of the current research considers a single degree of freedom model about the roll axis. Morris[3] conducted experiments both in a water tunnel and a wind tunnel using an 80° swept delta wing model(the same used in this current research). During water tunnel free-to-roll tests, he was able to track the locations of the leading edge vortices at the quarter, half, and three-quarters root chord of the model by utilizing a video based motion analysis system. The roll rate, $\dot{\phi}$, and roll acceleration, $\ddot{\phi}$, were computed using the video extracted bank angle of the model and a central difference routine. The rolling moment coefficient, C_ℓ, was then computed using the acceleration data and plotted versus roll angle. The C_ℓ versus ϕ curve in the water tunnel gave a hysteresis loop that was in the opposite in direction to the wind tunnel measurements (Fig. 1), both Morris' and others[4-8] (Fig. 2). However, though Morris conducted several tests in the water tunnel, the wing rock hysteresis loops remained the same.

Also, because water is over 800 times as dense as air, added mass effects had to be taken into account to relate the extrapolated moments. Morris estimated the added mass based on the assumed volume of water displaced by the delta wing during a wing rock cycle. Then with the estimated added mass, the rolling moment coefficient of the wing was computed from the acceleration data. Without the added mass effect included, the rolling moment was a factor of 15 less than that of the wind tunnel results (Fig. 3). Morris also observed that the vortices in the water tunnel had more curvature above the wing than did their wind tunnel counterparts. However, the leading edge vortices were not quantified during the wind tunnel tests, only relative motion data were gathered.

Arena[4], Nelson, and Schiff[5] completed wind tunnel testing on an 80° delta wing to study wing rock motion and vortex positions. The vortex locations were

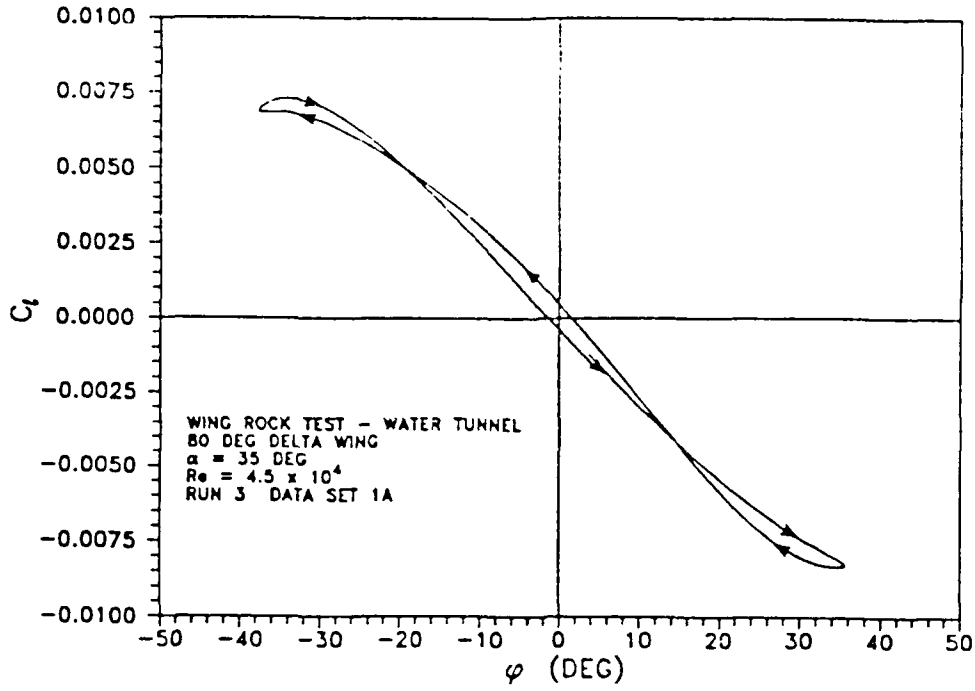

Fig. 1 Water tunnel rolling moment coefficient curve.[3]

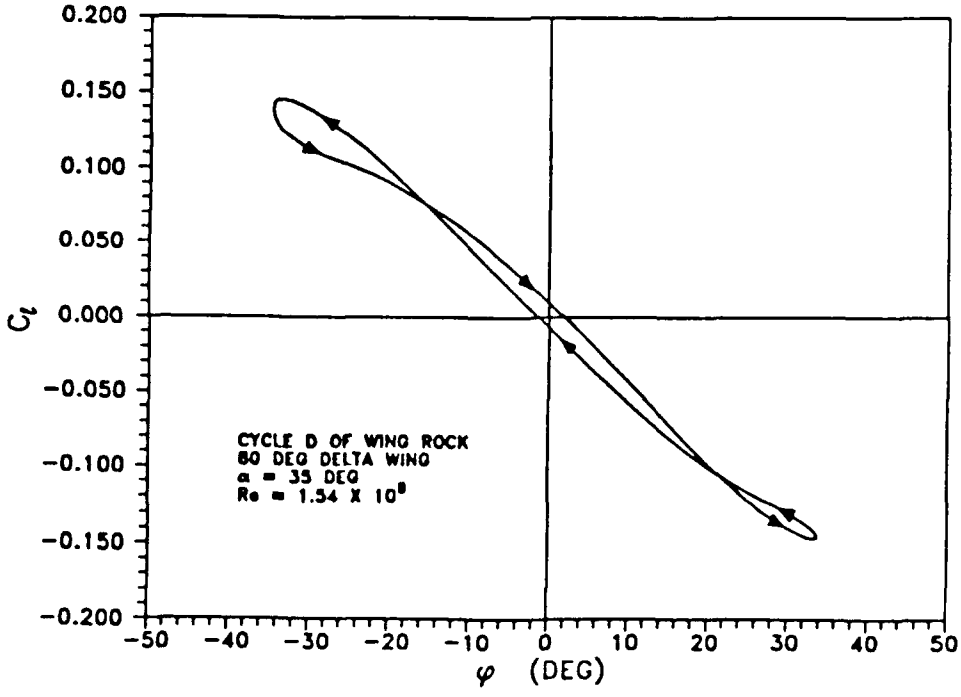

Fig. 2 Wind tunnel rolling moment coefficient curve.[3]

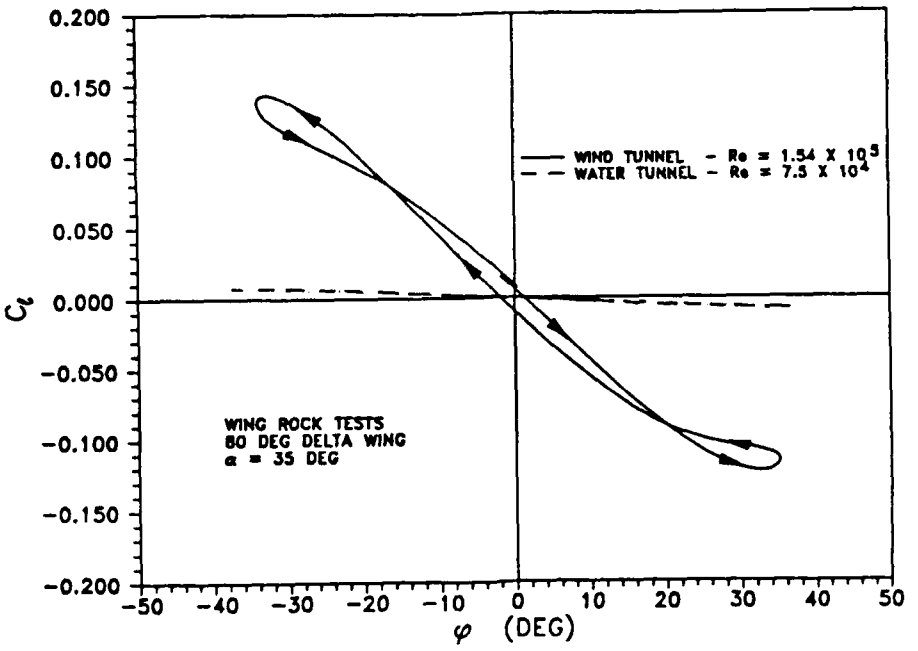

Fig. 3 Comparison of rolling moment coefficient in water and wind tunnel.[3]

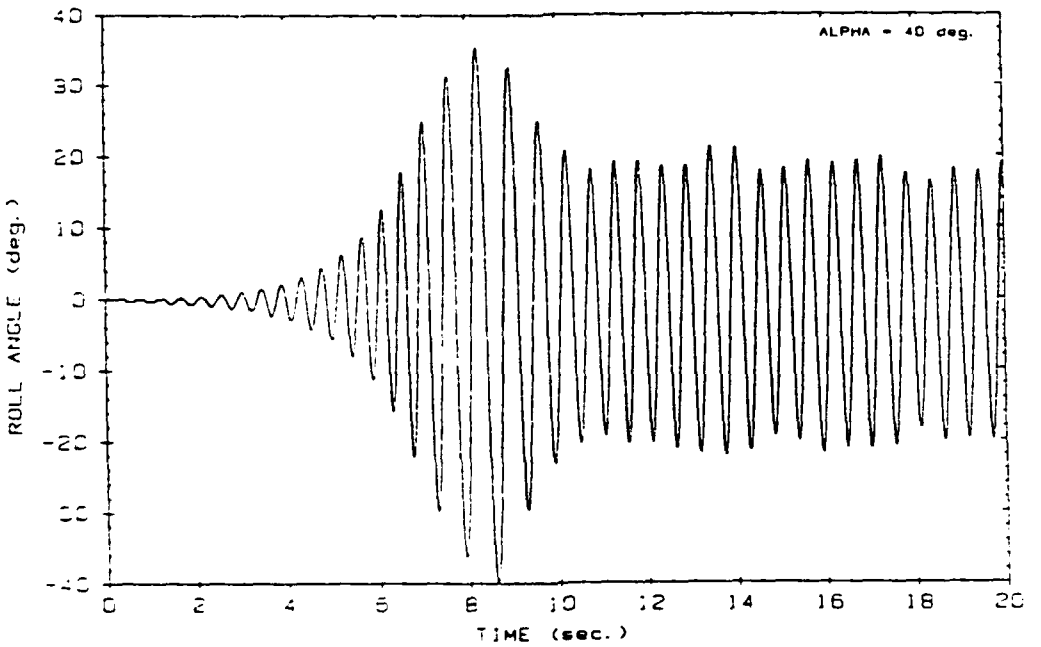

Fig. 4 Wing rock time history for α=40° (No initial breakdown).[5]

quantified with respect to roll angle at the 95% chord station of the model. Their model was mounted on a free-to-roll air bearing spindle which virtually eliminated any frictional forces. The tests were conducted at angles of attack of α=30° and α=40°, and at the Reynolds number, Re = 3.48 x 10^5. At α=30° a stable limit cycle was established for the model. This α was chosen for study because vortex breakdown did not occur over the wing; yet the amplitude of motion here was the largest of a variety of angles of attack[6]. At α=40° an interesting bi-stable condition was discovered for the initial conditions of ϕ, $\dot{\phi}$, and $\ddot{\phi}$ = 0. During the first condition, there was no vortex breakdown over the wing as the limit cycle built up. Then suddenly a vortex burst occurred which caused a damping of the motion until a limit cycle was established at a smaller amplitude (Fig. 4). The second condition, which initially had asymmetric breakdown on the wing, would not overshoot the stable limit cycle as the first condition had. Flow visualization tests were also conducted.

Titanium Tetra-Chloride ($TiCl_4$) was used as the flow visualization seed and ported through a thin probe to the front of the apex of the wing. By placing a laser light sheet at the desired chord location, a cross section of the leading edge vortices was illuminated. A 60 Hz video camera with a high speed shutter (1/1000 sec) was used to film the data which was then digitized and reduced using a frame grabber computer board on a Macintosh II computer. An example of the normal versus spanwise position of the vortices during a wing rock cycle is shown in Fig. 5.

Arena found hysteresis in the normal direction of the vortex location during the wing rock motion, but no hysteresis in the spanwise direction. It was further concluded that a time lag in the normal direction of the upward moving vortex was the cause of this hysteresis. A set of vortex position parameters were also constructed to describe the motion of the wing by using the vortex locations at x/c = 0.95. Arena's results will be further discussed in the analysis section.

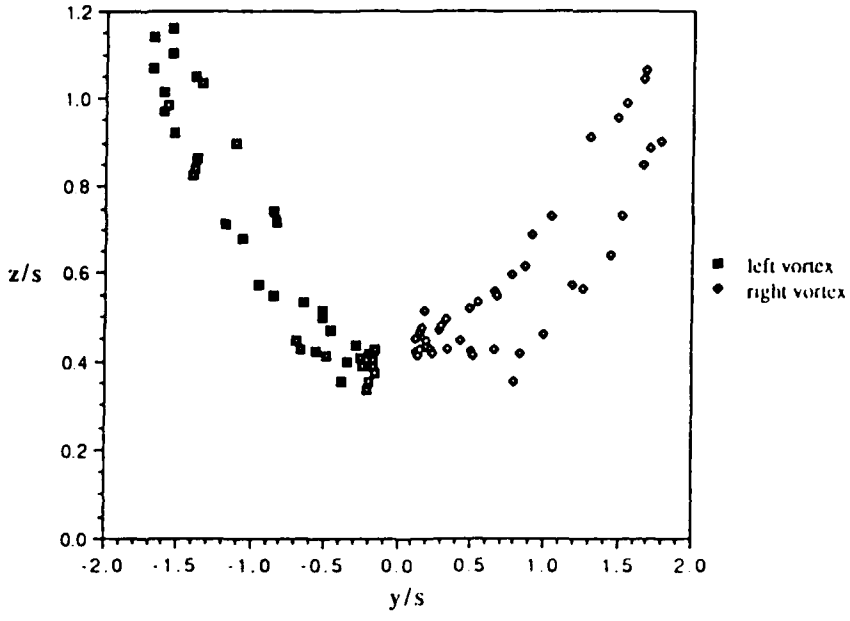

Fig. 5 Spanwise and normal vortex positions at x/c = 0.95 (α=30°).[4]

Many other studies have been conducted on the phenomenon of wing rock, including general observations, mathematical models, and a variety of explanations of its mechanics. Nguyen, Yip, and Chambers[7] conducted wing rock tests on an 80° delta wing model at the NASA Langley Research Center 10' x 12' wind tunnel. The model was mounted two inches above a free-to-roll apparatus as shown in Fig. 6. The wing rock roll angles were measured with a potentiometer that was attached to the free-to-roll apparatus. By taking first and second derivatives of the smoothed roll angle data, roll velocity and roll acceleration were computed. The roll acceleration was then used to compute the aerodynamic rolling moment of the delta wing (Fig. 7). During the experiment, roll oscillations reached maximum amplitudes of $\phi = \pm 40°$ for $\alpha = 32°$ and $\alpha = 37°$. Their analysis suggested that at small roll angles, the aerodynamic roll damping was unstable ($C_{l_p} > 0$), while at the large roll angles, the damping was stable ($C_{l_p} < 0$). These data also agreed well with forced oscillation tests which predicted unstable roll damping at angles of attack above $\alpha = 20°$. The

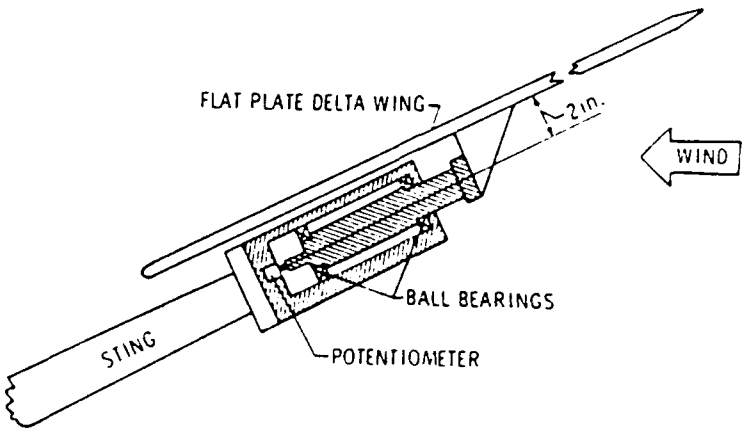

Fig. 6 Free-to-roll test apparatus.[7]

free-to-roll wing rock did not occur until $\alpha = 27°$. They believed that the aerodynamic forces could not overcome the friction forces in the bearings until an angle of attack of $\alpha = 27°$ was reached.

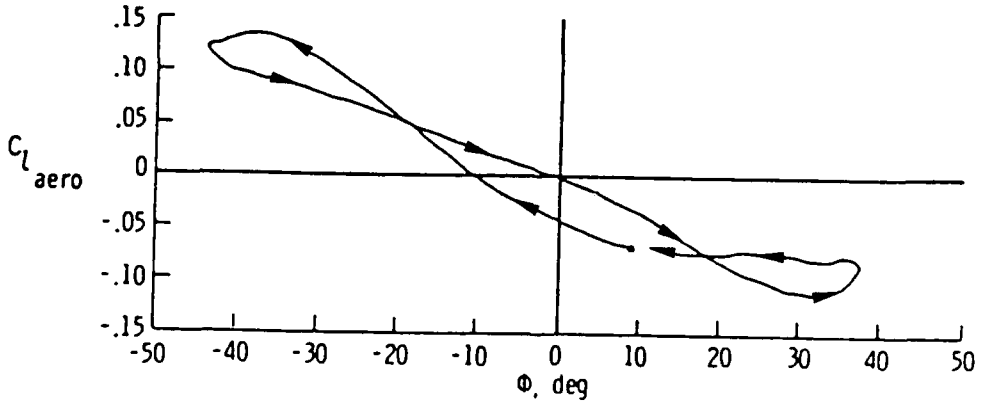

Fig. 7 C_ℓ versus ϕ, $\alpha = 32°$.[7]

The experiments also involved some flow visualization with helium bubbles. The leeward vortex on the upward moving wing varied in the normal position above the wing while the windward vortex moved close to the wing. It was concluded that the leeward vortex on the upward moving wing was the primary mechanism driving the wing rock motion.

Levin and Katz[8] conducted experiments with two sharp-edged delta wings with leading edge sweeps of $\Lambda = 76°$ and $\Lambda = 80°$ (Fig. 8). As seen in this figure, the models required a large housing along the centerline of the models for the potentiometer and sting-balance mounts. The 1m x 1m wind tunnel was operated at 32 m/sec (Re = 5 x 10^5 based on the 80° wing). Wing rock would not initiate with the $\Lambda = 76°$ delta wing or even be sustained with initial roll angles up to $\phi_o = 40°$.

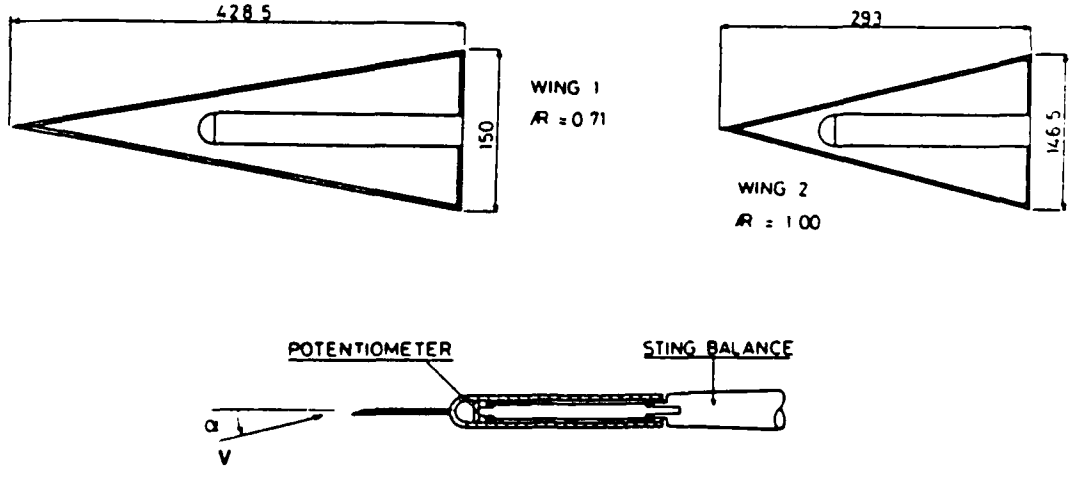

Fig. 8 Free-to-roll models.[8]

They concluded that wing rock would not occur on wings with aspect ratios greater than or equal to one, with the same flow conditions and bearing friction. They reasoned that roll damping was diminished on wings with smaller aspect ratios and were more likely to encounter wing rock.

The 80° delta wing went through both static and dynamic tests, in which the static results revealed larger normal and side forces than the dynamic experiments. This result was believed to be due in part to vortex bursting over the wing. A range of angles of attack were investigated as well. Wing rock would self-initiate between $\alpha = 25°$ and $\alpha = 51°$, where the oscillations ceased. During wing rock if the angle of attack was decreased below $\alpha = 25°$, the wing rock motion continued until the angle of attack reached $\alpha = 19.5°$. Levin and Katz also summarized that by

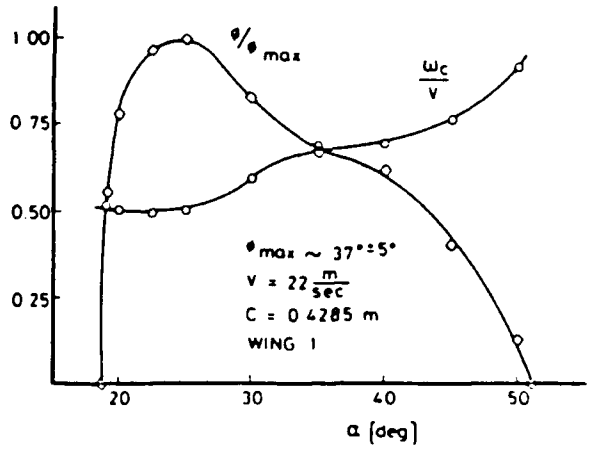

Fig. 9 Wing rock amplitudes and reduced frequency.[8]

increasing the tunnel speed, the amplitudes of the roll angles increased while the reduced frequency, k, remained the same. Also, increasing the angle of attack moderately increased the reduced frequency (Fig. 9).

Jun and Nelson[9] conducted flow visualization experiments on an 80° delta wing during static and dynamic tests. The low-speed wind tunnel was operated at a Reynolds number of 3.15×10^5, based on the centerline chord of the model. The model was mounted on a free-to-roll apparatus that allowed variation in angle of attack between $\alpha = 20°$ and $\alpha = 40°$ at 5° increments. A laser light sheet and smoke were used to quantify vortex core locations at the ¼, ½, and ¾ chord of the model. Data acquisition was accomplished using both still and high-speed motion pictures of the vortex cores.

Both static and dynamic data were presented for the ¾ chord only. Static measurements were made at $\alpha = 30°$, 35°, and 40° and for roll angles of $\phi = 0°$, ±15°, ±30° and ±45°. Results showed that there was no hysteresis present in vortex positions. Dynamic measurements were made for $\alpha = 40°$. The dynamic data that

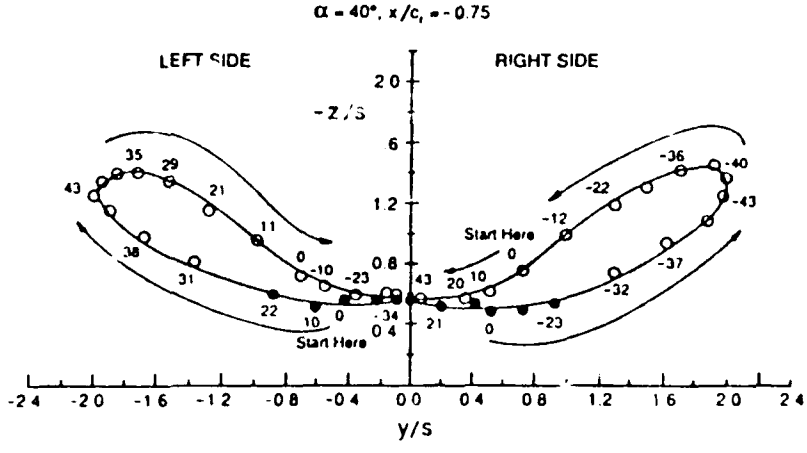

Fig. 10 Dynamic vortex core position data. Solid symbols indicate vortex breakdown has occurred.[9]

quantified vortex positions revealed an asymmetry between vortices which caused the wing to rock. From Fig. 10, the hysteresis in the vortex cores is evident. It was also noted that the vortex breakdown occurred further aft on the dynamic model as compared with the static model.

Ericsson[10] used previous wing rock experiments with delta wings[7-8] and a study of a blunt cylinder in a pitching motion to show that wing rock is caused by asymmetric leading edge vortices. He also concluded that the vortex burst over the wing was the flow mechanism which limits the amplitude of the wing rock motion. Ericsson's analysis included results from Polhamus' work[11] with delta wings (Fig. 11) in which the vortex asymmetry and vortex breakdown were related to the angle of attack, α.

To explain the effect of the leading edge vortices on the motion of the wing, Ericsson established an effective apex half-angle, $\bar{\Theta}_A$, for the left and right wing semi-spans. For small angles, ($\Theta_A \leq 15$ deg, $\beta \leq 15$ deg), the following equations were derived.

$$\bar{\Theta}_A = \Theta_A + \Delta\Theta_A \tag{1}$$

$$(\Delta\Theta_A)_{R,L} = \pm \tan\alpha_0 \sin\phi \tag{2}$$

$$(\Delta\Theta_A)_{R,L} = \pm \beta/\cos\alpha_0 \tag{3}$$

where the right wing semi-span equations have the plus signs and the left have the minus signs.

Ericsson explained that at an α - Θ_A combination where vortex asymmetry occurred (Fig. 12), the semi-span with the lifted-off vortex lost lift, dipped down, and

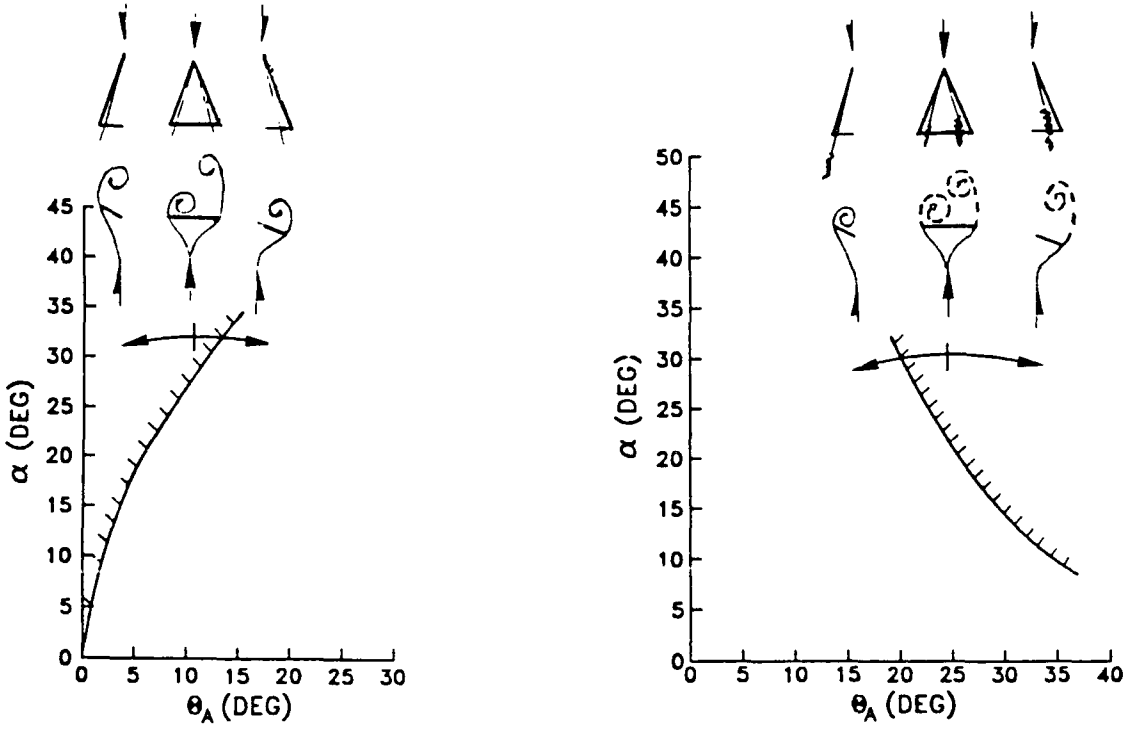

a) Vortex asymmetries. b) Vortex burst.

Fig. 11 Boundaries for vortex asymmetry and vortex burst.[11]

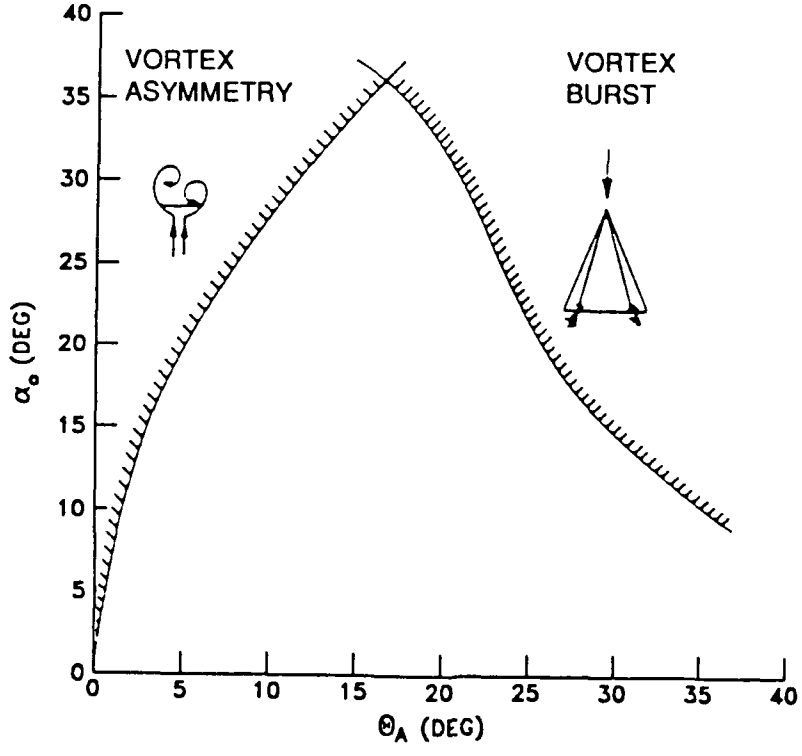

Fig. 12 Wing rock caused by asymmetric vortices.[10]

rotated about the roll axis. As the roll angle increased, the effective apex angle, Θ_A, also increased (see eqs. (1) and (2)) which resulted in the reattachment of the vortex. The wing motion, with the reattached vortex providing a restoring rolling moment, was reversed. Because of the convective time lag of the flow field, the wing remained dynamically unstable in roll until the limit cycle amplitude was reached.

Ericsson also analyzed the vortex burst over a wing. He reasoned that vortex breakdown, which also has time lag effects, was dynamically stabilizing and damping to the wing rock motion. He also notes, that vortex breakdown, by itself, would have led to a roll divergence because of asymmetric burst locations over the wing. He concluded that vortex breakdown had a damping effect on the roll oscillations and could not be the cause of wing rock.

There also have been analytical and computational studies of slender wing rock. Hsu and Lan[12] presented a new nonlinear aerodynamic mathematical model for calculating limit cycle amplitude and frequency of a slender delta wing in wing rock. They derived both a single degree of freedom(DOF) model and a three DOF model. The 1 DOF was modeled as;

$$(I_{xx}/\bar{q}Sb)\dot{p}=C_\ell(t) \tag{4}$$

where I_{xx} was the rolling moment of inertia, $\bar{q}$ the dynamic pressure, S the reference wing area, b the wing span, $\dot{p}$ the roll angular acceleration, and $C_\ell(t)$ the total aerodynamic rolling moment coefficient.

Using aerodynamic data from previous test results of an 80° delta wing, the total aerodynamic rolling moment was written as;

$$C_\ell(t)=C_{\ell_0}+C_{\ell_\beta}\beta+C_{\ell_{\bar{p}}}\bar{p} \tag{5}$$

where

$$C_{l_x} = C_{l_{p0}} + C_{l_{p\beta}} |\beta| + C_{l_{pp}} |\bar{p}| \tag{6}$$

and where $\bar{p}$ was the non-dimensional reduced roll rate, pb/2V.

Hsu then reformulated the above equation into dimensional form and solved the equation utilizing the Beecham-Titchener method[13]. The following equations give the frequency and amplitude of a wing rock motion.

$$\Omega = [-(\bar{q}Sb/I_{xx}) \sin\alpha_s C_{l_\beta}]^{1/2} \tag{7}$$

where $P = 2\pi/\Omega$,

and

$$A = -(3\pi/4) C_{l_{p0}} / [\sin\alpha_s C_{l_{p\beta}} + (\Omega b/V) C_{l_{pp}}] \tag{8}$$

Hsu and Lan used wing rock data from experiments of Nguyen, Yip and Chambers[7], and Levin and Katz[8] to compare predictions with their model (Fig. 13 and Fig. 14). Their code worked well up to α = 38°, after which a converged solution was difficult to obtain. They also noted that vortex breakdown for this wing would not occur before α = 33° as seen in Fig. 13.

The total aerodynamic rolling moment coefficient versus bank angle is shown in Fig. 15. The rolling moment coefficient history is for one cycle of wing rock at α = 32° without C_{l_0} in Eq. (5). While Hsu and Lan's model predicted the hysteresis relatively well, there were some asymmetries in the test data. They reasoned that these were likely due to vortex asymmetries at high angles of attack and zero sideslip. Hsu and Lan concluded that to correctly predict the frequency and amplitude of wing

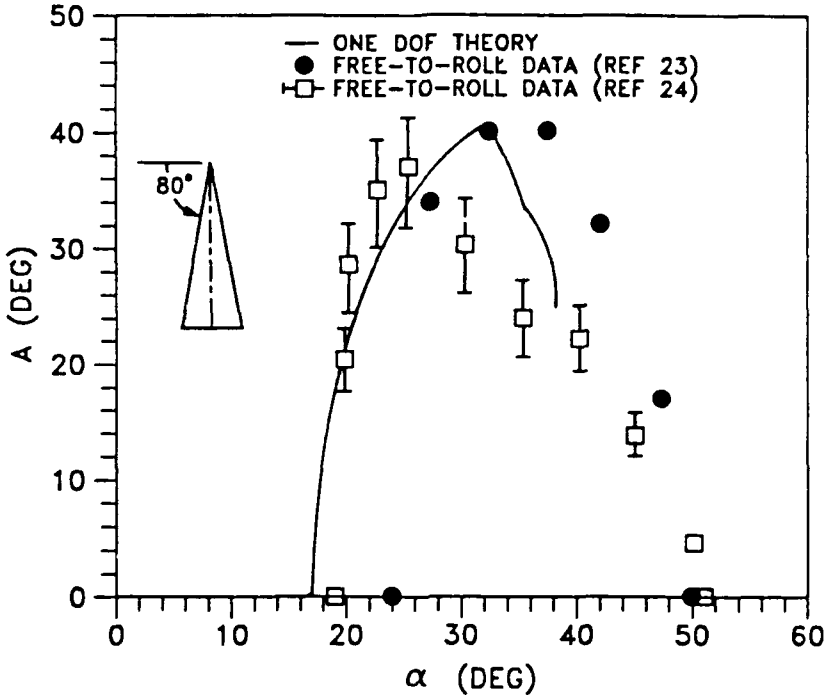

Fig. 13 Steady-state amplitude of wing rock for an 80° delta wing.[12]

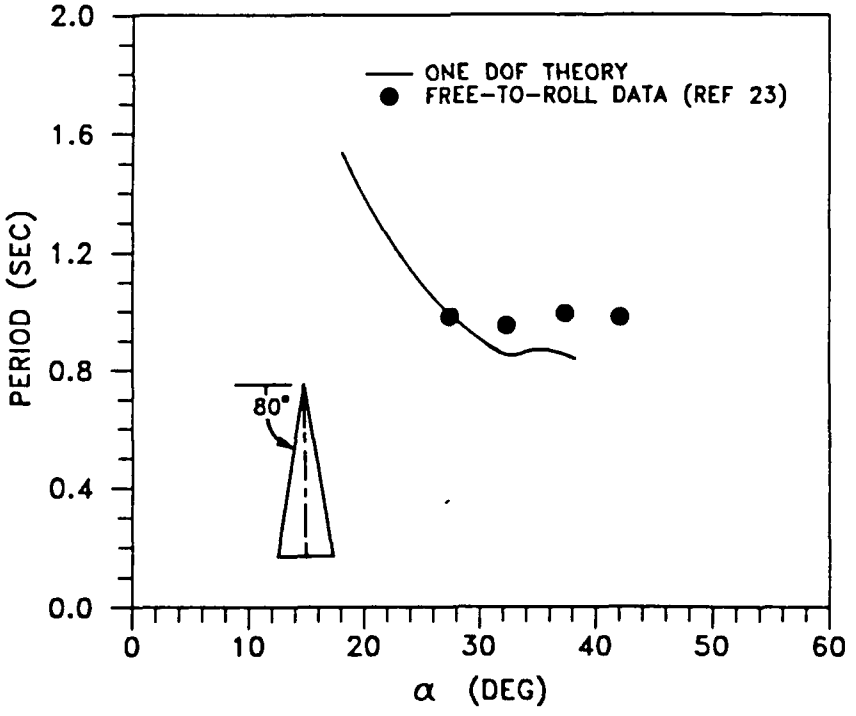

Fig. 14 Steady-state periods of wing rock far an 80° delta wing.[12]

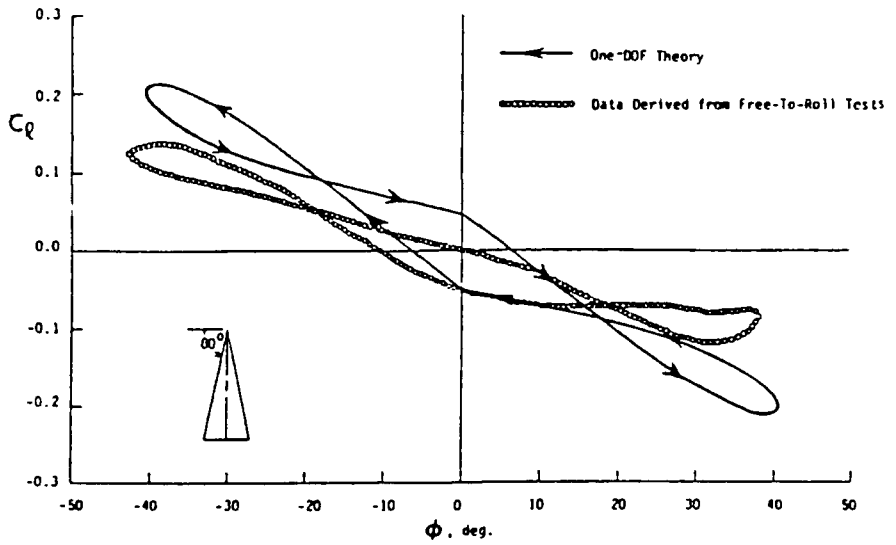

Fig. 15 History of the total aerodynamic rolling moment coefficient vs bank angle of wing rock at $\alpha = 32°$.[12]

rock motion, the aerodynamic derivatives must be accurately extrapolated from test data. They used a steady-flow aerodynamics computer code at some average dynamic conditions to iteratively solve for the aerodynamic derivatives. They theorized that to sustain wing rock, the total aerodynamic roll damping must be negative at small bank angles and positive at large bank angles.

Konstadinopoulos, Mook, and Nayfeh[14] also studied wing rock utilizing a numerical simulation. An Unsteady Vortex Lattice Method (UVLM) was used and results were compared with the data from two previous experiments of Nguyen, Yip, and Chambers[7] and Levin and Katz[8]. The UVLM computed the aerodynamic loads while a predictor-corrector scheme integrated the equations of motion. The results of the simulation included a history of the wing rock motion as well as the flowfield during the motion.

The study investigated two models; one that was configured the same as the Nguyen et al. setup (centerline of model two inches above roll axis) and one like the Levin and Katz setup (roll axis along centerline of model). The equation of motion for the simulation included a bearing friction term which had to be estimated. Computationally, several values of friction were investigated until the results compared well with the experiments. For an appropriate value of damping, the simulation's predicted amplitude and period were in close agreement with the experimental data. However, the UVLM code did not contain provision for vortex breakdown and subsequently, above a critical α, the simulation results were different from experimental findings. In fact, if the initial conditions were set for a large decay to the steady state amplitude, the simulation actually entered a roll divergence.

The authors were able to described the flowfield during the wing rock motion, utilizing the UVLM code. They concluded that the vortex system on the upward moving wing was the primary mechanism for wing rock. This vortex was closer to the wing as the wing rolled from its maximum roll angle. As the wing rotated through $\phi = 0°$, the vortex moved outboard and the opposite vortex moved closer to the wing. This motion resulted in slowing, stopping, and ultimately reversal of the motion of the wing.

CHAPTER II

EXPERIMENTAL EQUIPMENT AND TEST PROCEDURES

Rationale for Experimental Approach

These experiments were conducted to further quantify the dynamics and flowfield properties of an 80° delta wing during wing rock. Morris'[3] results revealed an opposite hysteresis loop in the C_l versus ϕ curve. Also due to apparent mass terms, the moments between water and wind tunnel data were a factor of over 15 times different. An investigation in both a water tunnel and wind tunnel was conducted to subsequently study the above issues.

Overview of Experiments

Experiments were conducted on an 80° delta wing (almost identical to that used by Morris[3]) in both a water tunnel and a wind tunnel. The model was allowed to roll freely about its longitudinal axis at a fixed angle of attack of 35°. Tests were run to quantifying steady motion, buildup motion, and decay motion of wing rock in both tunnels using a video-based motion analysis system. An added mass investigation was also undertaken in which inertia was added incrementally to the model in the wind tunnel. Additionally, flow visualization experiments were conducted in both tunnels to quantify the leading edge vortex flowfield during wing rock.

Model and Test Facilities

Delta Wing Model and Added Mass Attachment

The delta wing model (Fig. 16) was constructed of ⅛" aluminum plate. It had a leading edge sweep of $\Lambda = 80°$ and a 10" root chord. The delta wing had a sharp leading edge with a 20° bevel cut on the upper surface of the model. The apex had been slightly damaged and was reshaped prior to testing. The root chord measured 9.8" and the leading edge sweep was slightly less than 80° at the apex. This change likely contributed to some differences in the data. The model was mounted to a support rod to which the free-to-roll bearings and fixture were attached. The support rod consisted of a ⅜" brass tube which was attached along the centerline of the model, reaching the 80% chord. The brass tube contained a steel drill rod for added stiffness.

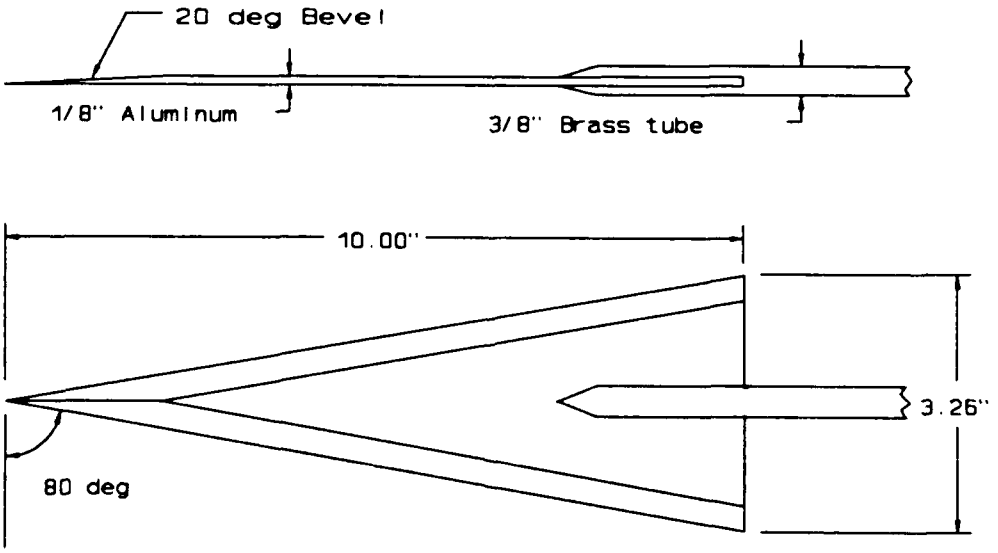

Fig. 16 Delta wing model.

The free-to-roll component was the same that Morris used, but the outside casing had been machined down to accommodate an added mass attachment. For both tunnel tests, the model was painted flat black, enhancing the contrast of the tracking points on the model and the flow visualization seed. Three white tracking points were placed on the model to accurately track the rolling motion. Points one and two were along the centerline of the model, with the first at the trailing edge and the second at the 60% root chord. The third tracking point was a white spherical pinhead located at one wingtip of the model. To counter balance the model, a second black pinhead was attached to the other wingtip. These three targets were tracked with the video-based motion analysis system with little difficulty (an updated version of the system used by Morris).

Added mass experiments were also conducted in the wind tunnel during testing, by incrementally adding inertia disks to the model between runs. The mass had to be added without disturbing or changing the flowfield around the model. For this reason, the ⅜" brass support rod was lengthened and an added mass attachment was designed and constructed (Fig. 17). This attachment fit over the free-to-roll components and rotated without interference. The attachment consisted of 3 major elements; a 3.5" diameter plastic propeller spinner, an attachment fixture with a collar, and ten steel disks. The spinner was painted flat black along with the support rod. It was connected to the attachment fixture by two screws. The attachment fixture was constructed with a 1.25" OD aluminum tube and an aluminum plug. This plug was machined to contour the forward inside section of the spinner. This fixture was connected to the support rod by two set screws. An aluminum collar was also machined to restrain the disks from rotating or translating along the tube. The disks were machined from ¼" steel plate and contoured to the inside of the

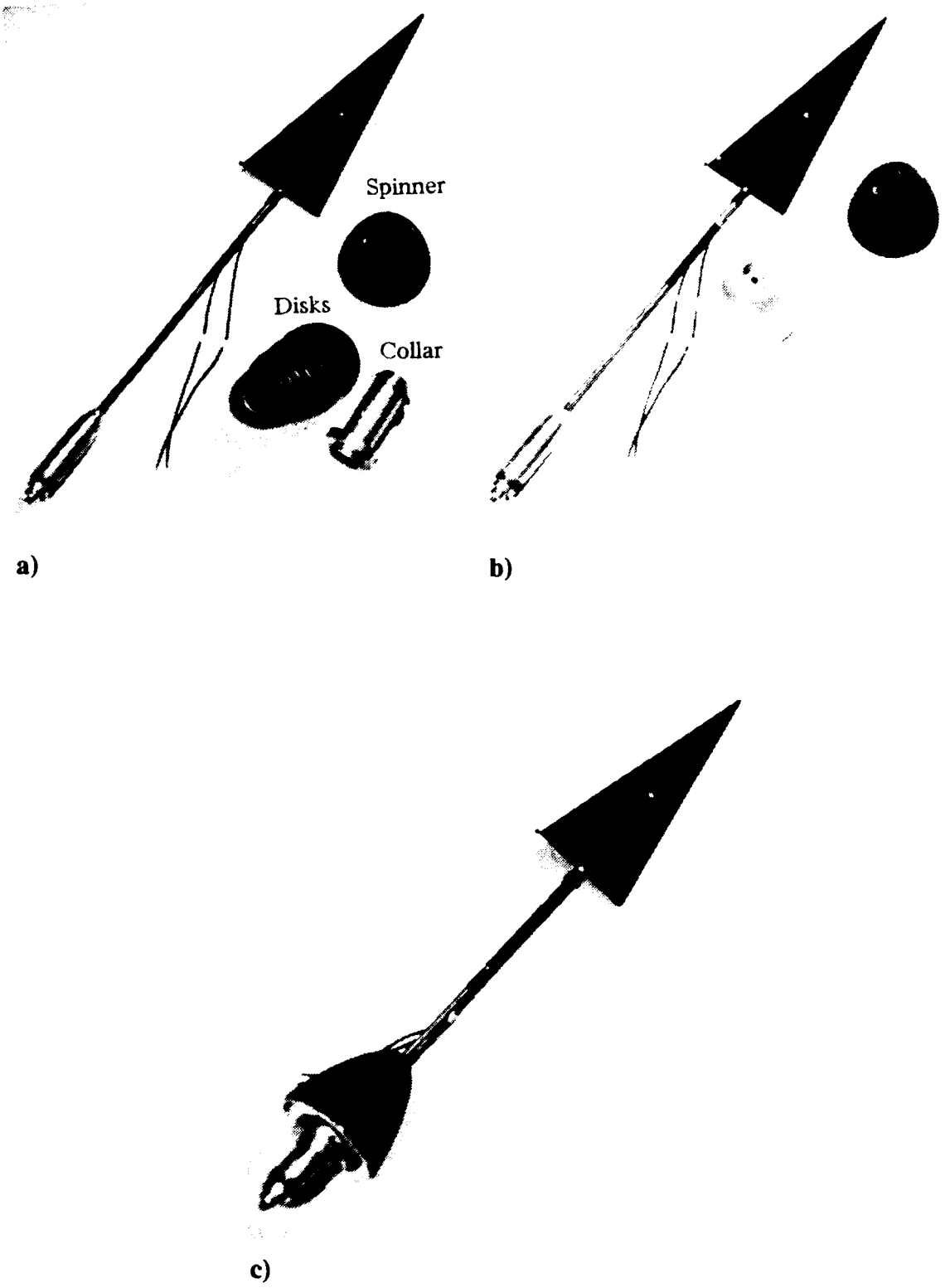

Fig. 17 Delta wing model with added mass components.

spinner. They were bored through their centers to provide a close fit over the attachment fixture's tube.

As mentioned above, the support rod was lengthened to reduce flowfield interference between the model and the added mass attachment. The rod was lengthened originally to give a distance between the model and added mass attachment of four spinner diameters[15], which is an experimental rule of thumb to reduce the upstream interference effect on the model's flowfield. Unfortunately, during wind tunnel testing the model had vibrational problems, evidently due to lack of stiffness in the support rod, which led to an unsteady wing rock limit cycle. The roll amplitudes regularly increased and decreased in magnitude, giving a low frequency beating type signal. The rod was incrementally shortened until this beat frequency was not noticeable. The resultant rod length was 14.75" long from the model's trailing edge, which placed the spinner 2.5 diameters behind the model, 1.5 diameters less than originally planned. Since the sting was at $\alpha = 35°$, the leading edge vortices were high above the spinner and the flow interference at the model was expected to be minimal. Further discussion of the spinner interference will be discussed in the results section.

Water Tunnel Facility

Water tunnel tests were conducted in the Texas A&M water tunnel. The horizontal continuous flow tunnel had a 2' wide x 3' high x 6' long test section. The tunnel flow rate capacity was 24 inches per second (ips) and honeycomb filters were located upstream to smooth the flow. The tunnel test section was constructed of tempered glass to allow flow visualization on three sides of the test section. A window was located downstream in the collecting area, giving a view upstream. Fig. 18 is a picture of the model with the added mass attachment from this view.

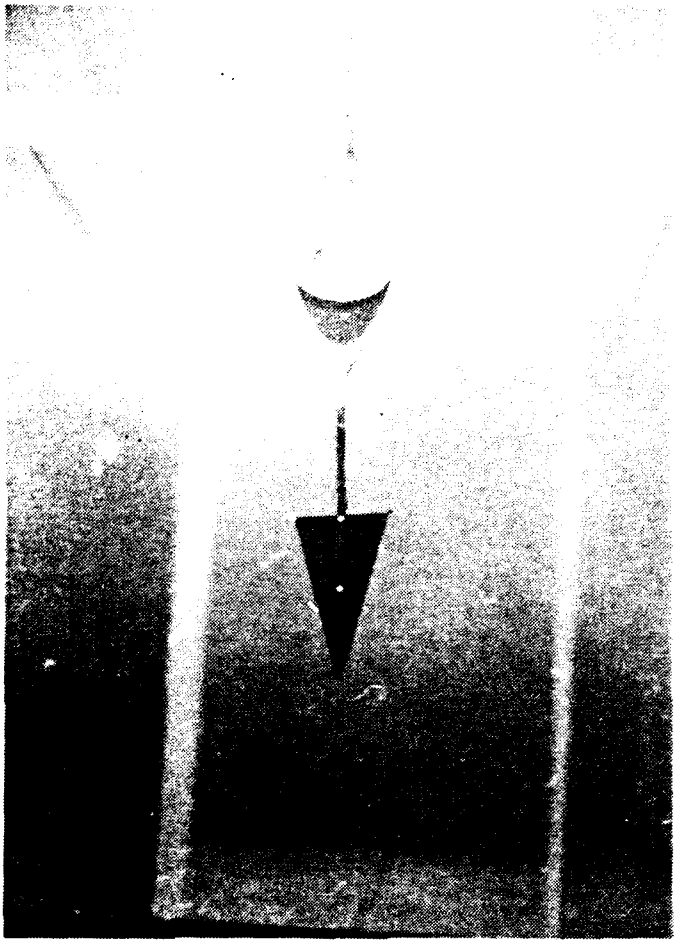

Fig. 18 Delta wing model and added mass attachment inverted in water tunnel.

The model was inverted in the tunnel and mounted on a sting at a fixed angle of attack of 35°, and a sideslip angle of 0°. Above the test section, there was an electrically driven traverse mechanism that controlled the sting. Once the proper angles were aligned, this mechanism was turned off and the model then remained fixed in the test section, except for its rolling motion about the longitudinal axis.

Wind Tunnel Facility

Wind tunnel tests were conducted at the Texas A&M Low Speed Wind Tunnel. The closed circuit tunnel had a test section 7' wid by 10' high by 12' long which contained plexiglass and glass viewing windows on the side and above. The tunnel operated at dynamic pressures up to 100 pounds per square foot (psf) which corresponded to freestream velocities up to 290 feet per second (fps). The High Angle of attack Robotic Sting[16] (HARS), a computer controlled robotic sting capable of α sweeps from 0° to 90°, was installed in the tunnel. The sting was fixed at α = 35° and β = 0° for all tests.

Fig. 19 Baseline model in wind tunnel.

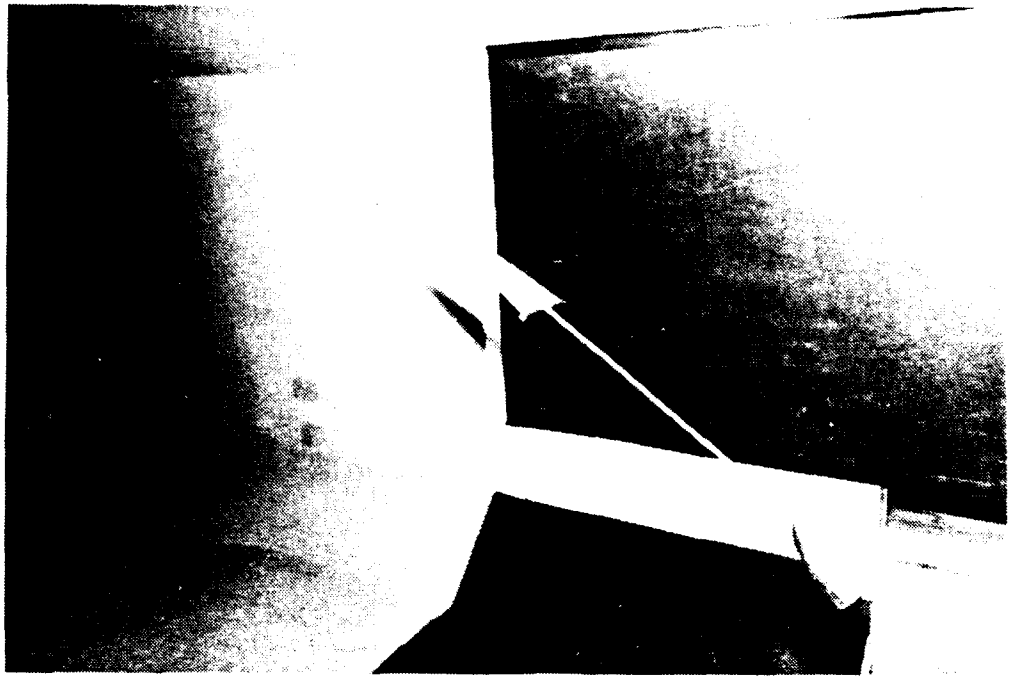

Fig. 20 Model with spinner in wind tunnel.

Data Acquisition and Reduction System

The primary tool for data acquisition and analysis was the ExpertVision[17-18] (EV) 3D system, developed by the Motion Analysis Corporation (MAC). The system was comprised of three multi-speed video cameras, a VP-320 video processor, and EV3D software. The EV software was run on a Sun color SparcStation 1+, a product of Sun Microsystems, Inc.. Two NAC 200 Hz video recorders and a 60 Hz Panasonic AG-6300 video recorder were also used. In addition, two Sony 60 Hz video recorders were borrowed to simultaneously collect 60 frames/sec data with the Panasonic recorder.

In addition to the MAC equipment, a C based code (Appendix A) was designed and written to transform the reduced video data into a model fixed axis system.

Video Cameras and Recorders

The three MAC multi-speed video cameras operated at 60 Hz, 180 Hz or 200 Hz and were remotely controlled by the VP-320 video processor. When the camera speed was increased, the contrast between objects decreased. Therefore, appropriate setup and lighting was required to adequately acquire data, especially at higher data rates. Each camera had an external power supply that also interfaced video signal cables between the camera and video processor. The cameras had the standard lens c-type mount which allowed a variety of lenses to be used. During testing, telephoto lenses were used on all three cameras to narrow the field of view on the delta wing. The high speed NAC video recorders were used during wind tunnel testing, while the 60 Hz recorders were used both in the wind tunnel and water tunnel. Both sets of recorders used standard VHS video tapes. The video recorder was also used to playback the VHS tapes. This recorder had frame by frame edit controls and audio meters to monitor signals.

Video Processor

The VP-320 video processor was the hardware interface between the video data streams and the computer. The VP-320 had a three camera capability, with an additional expansion slot for a fourth. It transformed raw video into numerical data which were later reduced using the EV software. The VP-320 had the capability of processing real-time data or processing video tape data during playback. In the playback mode, one camera view was processed at a time. These data were stored in binary format on the computer's hard disk. Data were acquired by maximizing the contrast between tracking targets and the background during testing. The video processor threshold was adjusted until the outlines of the targets were illuminated on the video monitor. With the processor in the video off mode, the actual pixel

locations of the targets were observed. This information from each frame was stored on the computer and processed with the EV software.

The VP-320 not only commanded camera rates and data acquisition rates but also included features such as background filters, editing windows and masking capabilities. The features were independently controlled for each camera input, increasing the flexibility and versatility of the system. During testing, the video processor was operated by a triggering device that simultaneously sent an audio signal to all video tape recorders. This signal synchronized the video data for all three cameras as well as the real-time data that was processed. During the playback mode of a video tape, the VP-320 began processing data when the audio signal was detected, ensuring synchronization of the data for all three cameras.

ExpertVision Software

Two window driven software packages were part of the EV system. The Video Analog Collection (VAC) program[19] was used explicitly for data acquisition and it interfaced with the VP-320 video processor. VAC commanded the number of frames or the amount of time in seconds that the VP-320 would process and store data on the computer. It also managed the data files written to the computer and subsequently incremented test numbers (part of the data filename) after each run.

The second program, called EV, was designed with a number of data reduction and analysis modules. Data reduction routines included modules such as CALI, TRAC, and TRED. The CALI module was used with video data from a calibration fixture. Two of the calibration stands used are shown in Fig. 21 and Fig. 22. An attractive feature of the system was that the camera locations did not have to be measured; only the calibration point locations relative to the stand had to be known. At least six non-coplanar points were required by the system to perform a calibration.

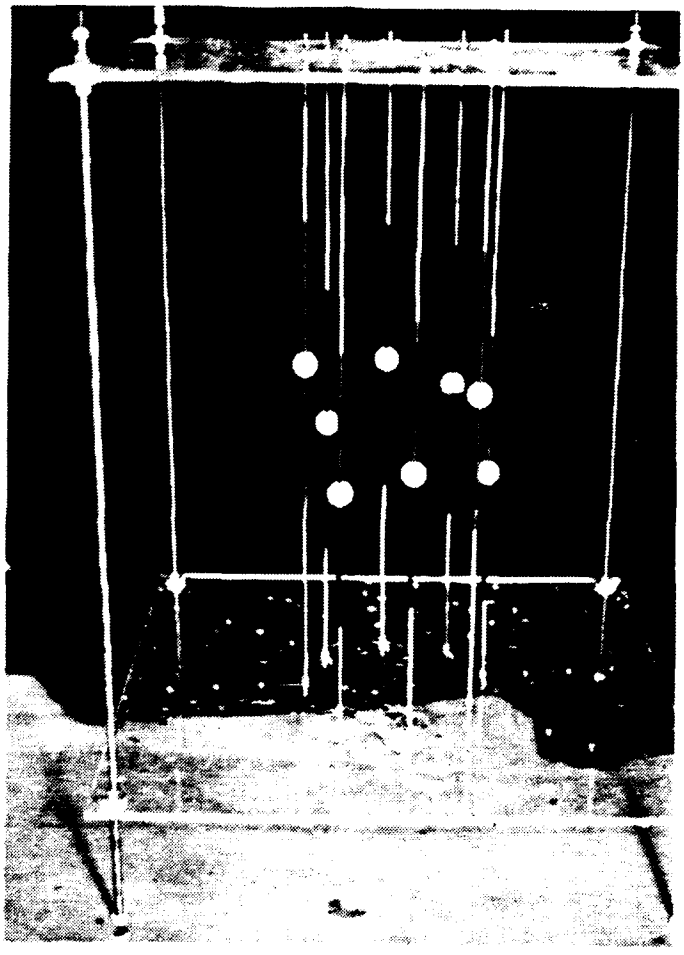

Fig. 21 Cylindrical 8-point calibration stand.

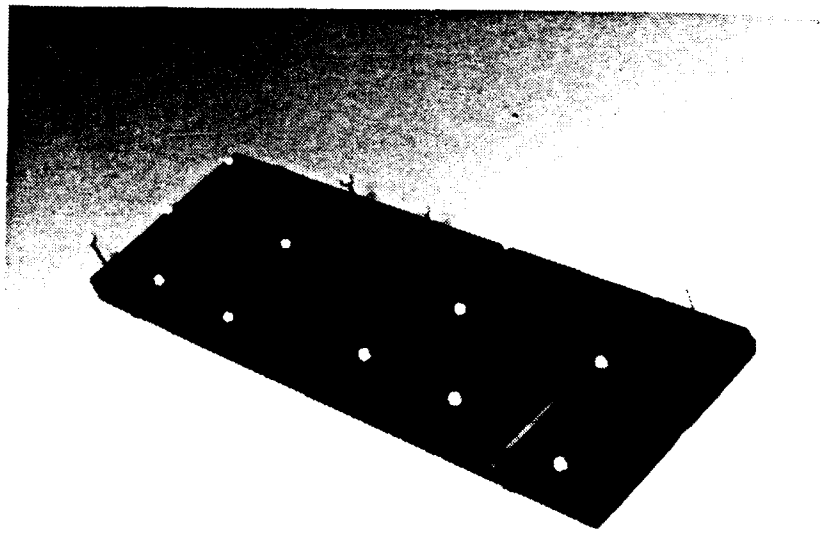

Fig. 22 Delta wing piggyback 15-point calibration stand.

The CALI routine prompted for calibration point locations relative to a user chosen calibration stand reference frame. Then each camera view was displayed and the routine prompted for each point's identity. After the calibration points in each camera view were identified by the operator, the module calculated two pieces of information: the physical locations of the cameras relative to the calibration stand reference frame and the residual errors of the calibration algorithms. This information was used to determine if the calibration was satisfactory or not. If not, the cameras were re-positioned and another calibration video was taken. The cameras were not required to be orthogonal to each other, but nearly orthogonal locations produced lower residuals. The CALI routine output an environment file that was used to quantify the paths of targets tracked during testing. If any of the cameras were moved or bumped while testing, another calibration of the system was required. To insure reducible data, calibrations were taken prior to and after each tunnel run.

The TRAC module computed the centroid of each target in every frame and then tracked the centroid frame by frame, resulting in a time series path for each target. If information was not continuous or points disappeared during TRAC, they were assigned as an unnamed target. Using the track editor (TRED) module, path information was corrected and discontinuities joined. For example, if the wingtip of the delta wing was hidden by the flow visualization seed for an instant, it was reassigned as an unnamed target for the rest of the TRAC reduction. The TRED module recognized the unnamed path as the moving wingtip. This information was then reassigned to the wingtip target and spliced together using the JOIN command.

The analyzing modules included functions such as SMOO, SPLI, and DIF, as well as many more statistical routines. The SMOO module was a Tukey window smoothing algorithm which was used to smooth the roll angle data. A window of points, specified by the user, was used to smooth the data. For example, if a window

of 25 points was entered, 12 points prior and 12 points aft of the central point to be smoothed would be weighted according to their relative position to the central point based on a normal distribution. After being weighted the points were then smoothed. The larger the window the more the data were smoothed. For these tests, a window of between 21 and 55 points was used for most data sets. The SPLI module was used to split the paths into X, Y and Z components, giving three individual paths in these X, Y, and Z directions. Velocities and accelerations of these data were computed using the DIF operator, a central differencing routine. A convenient feature of the EV software was the user created programs that called these modules. For example, a simple program called DATA1.EV was written to automatically smooth a track file, split this smoothed file into three path files in their respective X, Y, and Z coordinate directions, and then twice perform a central differencing. The resulting output were nine data files; 3 path files, 3 velocity files and 3 acceleration files, one for each coordinate direction. The flexible and user friendly routines of EV made reduction of large quantities of data fairly routine.

User written codes

After reducing the video data into numerical data, the information was transformed to a body fixed axis system, via a C based program called DYNAMIC (see Appendix A). This user written code had a menu driven screen and was comprised of two major modules. The first module used a data file containing the three static points of the delta wing model, fixed at a zero roll angle. Taking into account nonorthogonal points, the subroutine established a reference frame from which roll angles were calculated. The second module was the more intensive dynamic data transformation subroutine. It took the nine binary dynamic data files[20] previously discussed, and computed a 3-2-1 Euler transformation on the information to the body

fixed axis system. The data were arranged such that the three tracking points were the first points in the dynamic data files. The flow visualization data points followed these data. By using all three tracking points, comparisons were made with the static wing tracking points to determine the relative angles of rotation between the two reference frames. The roll angle was also calculated using the dot product between the static and dynamic wingtip vectors. Using this information and the velocity and acceleration data, roll rates and roll accelerations were computed. Having numerically computed the roll inertia of the model and knowing the test conditions, the rolling moment coefficient was also computed.

The second part of the module was designed to reduce the flow visualization data files. These data included right and left vortex core locations which were

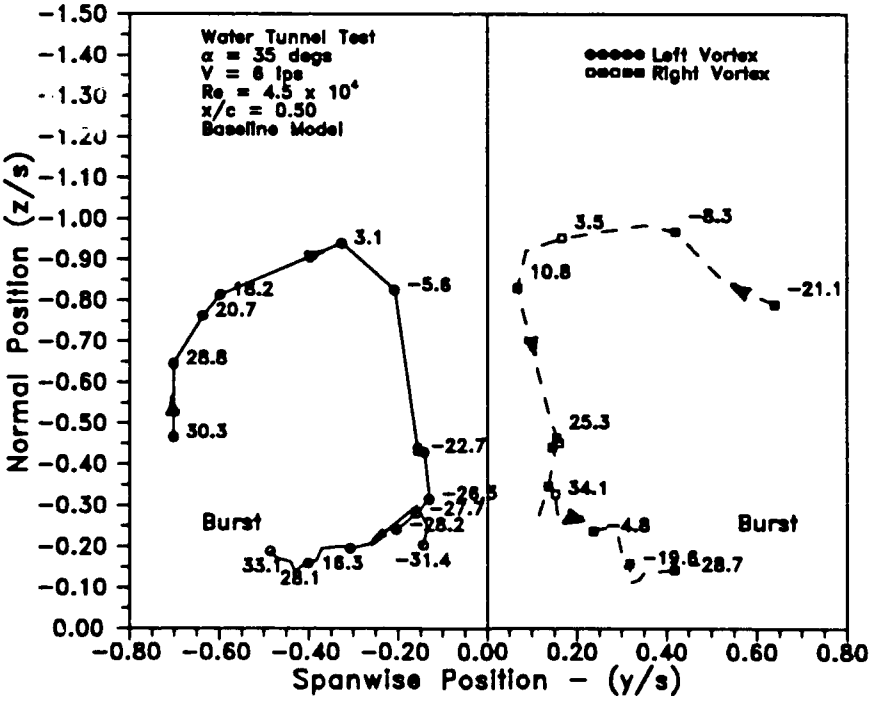

Fig. 23 Example of flowfield at a chordwise station.

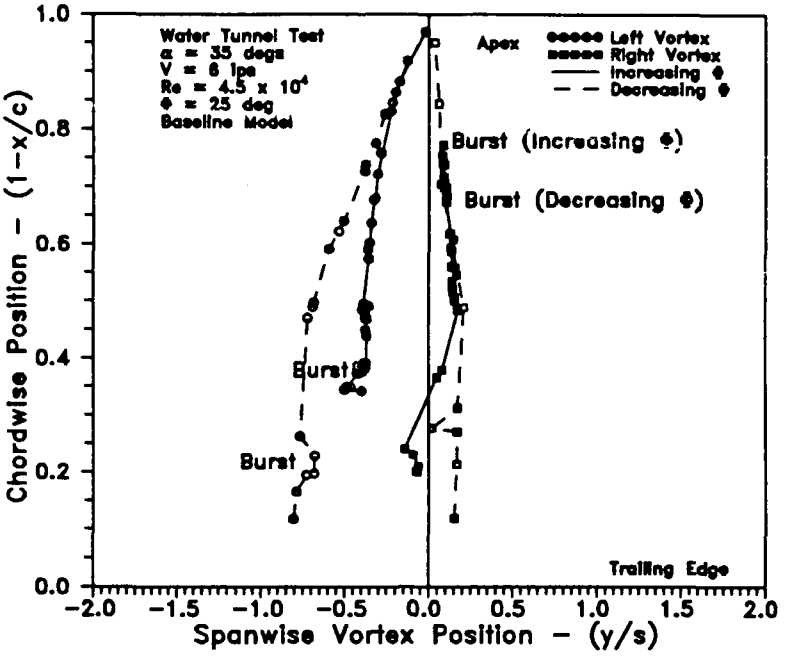

Fig. 24 Spanwise position of vortex paths.

reduced to the body fixed axis system. With water tunnel data, the code extracted vortex core locations at wing chord locations of $0.25\bar{c}$, $0.50\bar{c}$, $0.65\bar{c}$, $0.75\bar{c}$, $0.85\bar{c}$, and $0.95\bar{c}$ (Fig. 23). Included in this information was the direction of travel for vortex core movements and the respective roll amplitude at each extracted location. Right and left vortex data were also extracted for bank angles of $\phi = \pm5°$, $\pm15°$, $\pm25°$, and $\pm30°$ in the spanwise and normal directions over the length of the wing. Due to hysteresis of the vortices during wing rock, these data were further segregated depending on the wing's direction of travel; that is, whether increasing or decreasing through a specified bank angle (Fig. 24 and Fig. 25).

During wind tunnel flow visualization tests, only the wingtip could be consistently tracked. The DYNAMIC program was modified to a REDUCE program which used only the wingtip as the reference. Similar data were output as seen in Fig. 23.

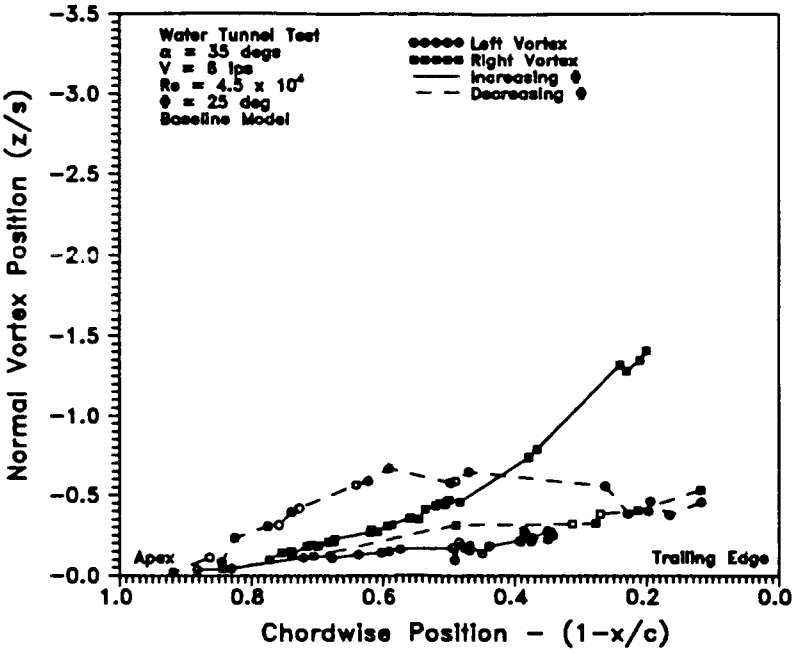

Fig. 25 Normal positions of vortex paths.

Data Acquisition and Analysis Procedure

Water Tunnel Data Acquisition and Analysis

During the water tunnel tests, the tunnel was operated at V_∞ = 6, 10, 12, and 15 ips. These freestream velocities corresponded to Reynolds numbers of Re = 4.5 x 10^4, 7.5 x 10^4, 9.0 x 10^4, and 1.125 x 10^5, respectively, based on the chord length of the model. The model was fitted on the bottom surface with two 0.05" OD hypodermic tubing. The tubing ran along the centerline of the model from just past the trailing edge to the apex of the delta wing. The tubing ends at the apex were tapered to reduce interference with the leading edge vortices. The purpose of the tubing was to port dye, which acted as a flow visualization medium, to the apex of

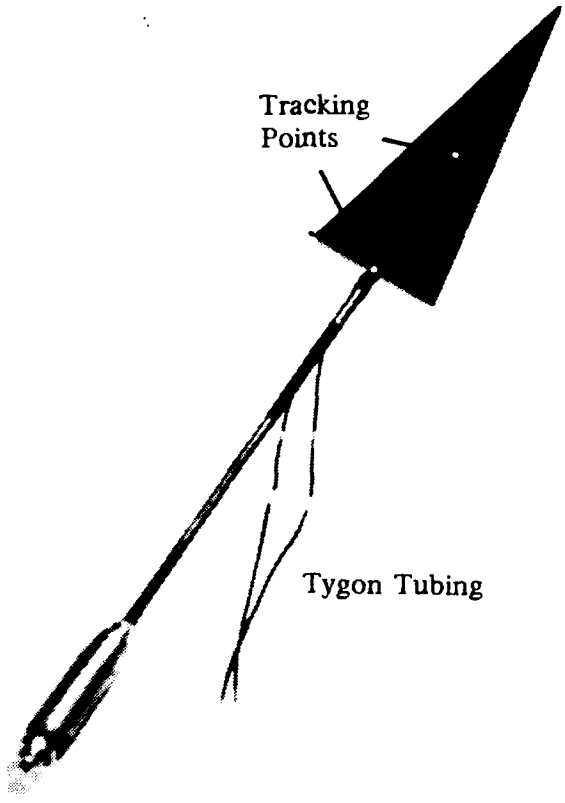

Fig. 26 Baseline Model.

the model. The dye was then entrained into the leading edge vortices, providing a visual mark of the dynamic vortex location. Tygon tubing connected the hypodermic tubing to a syringe that was used to pulse the dye. Fig. 26 shows the baseline model with the tubing.

Three video cameras operating at 60 Hz were used to track the wing and vortices. Camera one was underneath the test section looking up at the model. Camera two was at the aft section of the tunnel looking upstream toward the model.

Camera three had a side view of the model. To reduce external video noise, the background of the test section was shrouded with a black drop cloth which covered any reflecting objects. Whole milk was used in the dye system and it provided good contrast with the black model. The milk was pulsed such that discrete individual packets of milk were entrained in the vortex cores. The video analysis system then tracked each of the packets as they moved along the wing. A two person team was required to conduct these tests. One was responsible for operating the equipment while the other pulsed the dye or initialized the model during buildup or decay tests.

Data reduction was highly automated due to the EV software and the user code described previously. Unlike Morris[3], no frame by frame editing of the video data was completed. The contrast levels between the packets of dye and the model were adequate to capture the vortex paths. During flow visualization testing, five sequential runs were made at each tunnel speed. Hindsight showed that more runs would have contributed to a fuller, more complete data package. The chordwise data sets were acquired in similar fashion as a Poincaré Section[21] is constructed. As targets flowed through an established plane, their locations were recorded. Therefore, all five data sets were used to form a single chordwise data set. Once the proper lighting and color scheme for maximum contrast were established, water tunnel testing was conducted with little difficulty.

Wind Tunnel Data Acquisition and Analysis

Wind tunnel tests were conducted at a dynamic pressure of $\bar{q}$ = 1 psf, which corresponded to a freestream velocity of 29.0 fps and a Reynolds number of 1.54 x 10^5. Investigations in the wind tunnel included steady, buildup, and decaying wing rock motion, added mass experiments, and flow visualization tests. During wing

rock, a yard stick was used to initialize the model to either a small roll angle near zero, or a very large roll angle greater than the steady wing rock amplitude. The yard stick was then removed and the subsequent motion tracked. Added mass experiments were conducted in the same manner for each inertia configuration. Because the sting had a hollow mount for the model, the spinner of the model could be moved forward shortening the support rod. Tests were conducted and data were gathered for spinner locations of 2.0 spinner diameters aft and 2.5 spinner diameters aft. Since the water tunnel sting could not accommodate this capability, only data for the latter spinner configuration were reduced.

Added mass experiments began by tracking the baseline model configuration. After the test, the model was removed from the tunnel and the added mass attachment was connected to the support rod. The model was then tested again and data collected. The model was again removed from the tunnel and the first disk was added. With the model installed, another run was made. This process continued until all ten disks were added. By increasing the inertia, the effect of the apparent mass in the water tunnel was simulated. Balance of the model was critical to achieve accurate wing rock data. The model was installed on the sting and a quick balance check was made. Fine tuning of the model with the added mass attachment was accomplished by adjusting the spinner's two mounting screws. With this completed, the model was again ready for testing.

Wind tunnel flow visualization experiments involved a 5 watt laser, a glass rod, and a smoke wand. The laser was installed on top of the tunnel pointing in the upstream direction (Fig. 27). The beam was directed through a 1" diameter glass rod which was placed at roughly the same angle as the delta wing. This setup diffused the beam into a plane of light or laser light sheet. The light sheet "cut" the model in the spanwise sense at a desired chord location. Adjustments were made to place

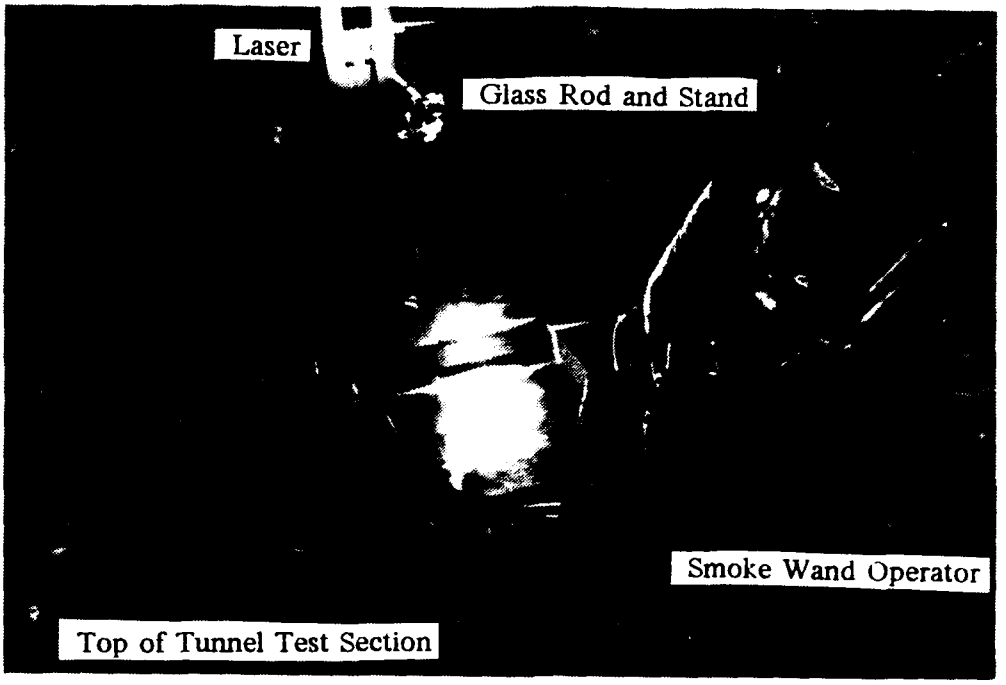

Fig. 27 Laser and glass rod arrangement.

the light sheet at the previously discussed chordwise locations. These adjustments were made by moving the glass rod forward or backward while the tunnel was running. Care was necessary to make sure the light sheet w.. directed at the model and not to one side or the other. All specified chord locations were surveyed for each model configuration without shutting down the tunnel, greatly expediting data gathering. In Fig. 28, pictures were taken during a flow visualization run while looking down on the model.

Flow visualization data reduction became a frame by frame editing chore because of contrast variations during each wing rock cycle. A number of reasons for these variations included smoke engulfing the model, light sheet not positioned correctly, smoke wand position not fixed. The smoke was a heated light grade oil which vaporized as it passed through the wand. Control of the volume of smoke was uncertain; it was basically an all or nothing si uation. In addition, as the light sheet was moved, the intensity of the sheet shifted to the right or left of the wing. If it

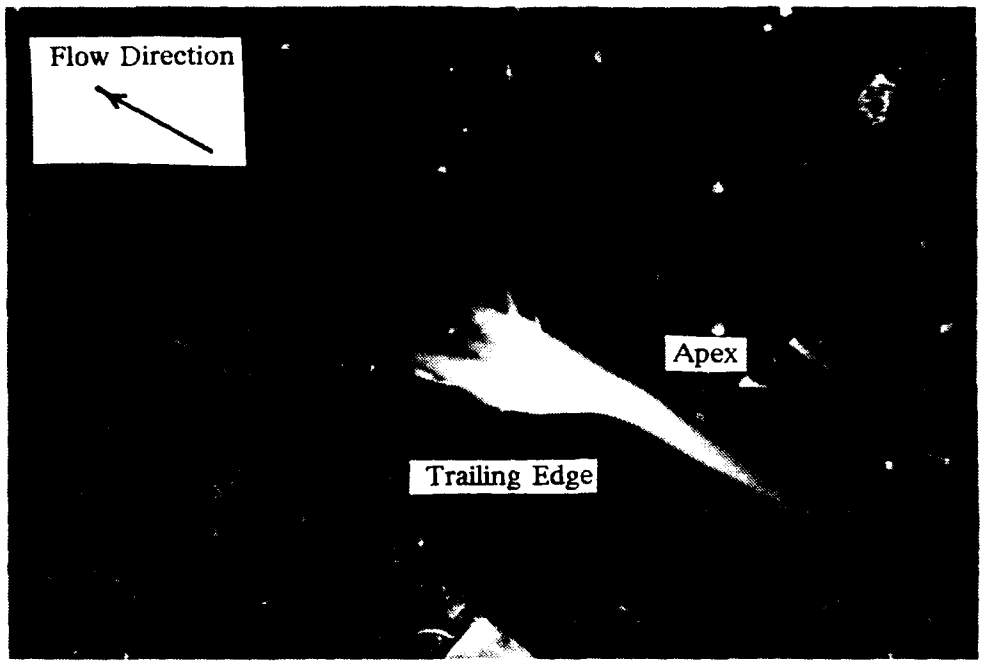

a)

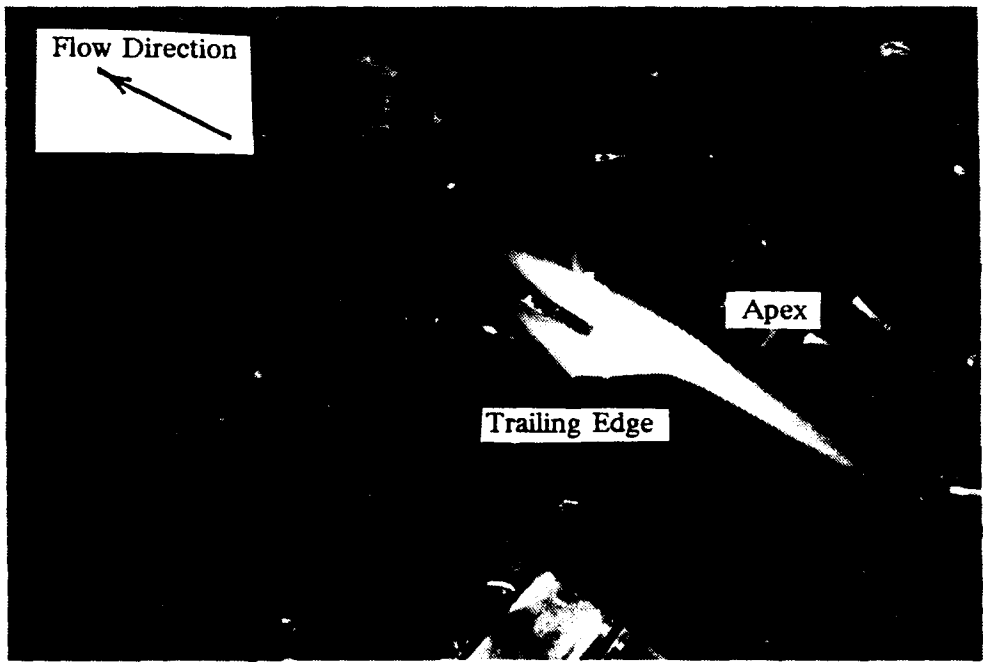

b)

Fig. 28 Flow visualization of delta wing at x/c = 0.75.

remained unadjusted, the data were not reducible. Finally, the smoke wand was hand held in the test section from the ceiling above. Sometimes inconsistent placement of the smoke wand led to low quality data.

The reduction process included playing back video data tapes with different threshold settings and then editing the data files until a track of each vortex could be made. This process required approximately a full day to reduce one chord location. Fig. 29 are pictures of the leading edge vortices at the x/c = 0.95 station as recorded from camera one. These pictures were actually taken of the video monitor during the playback mode.

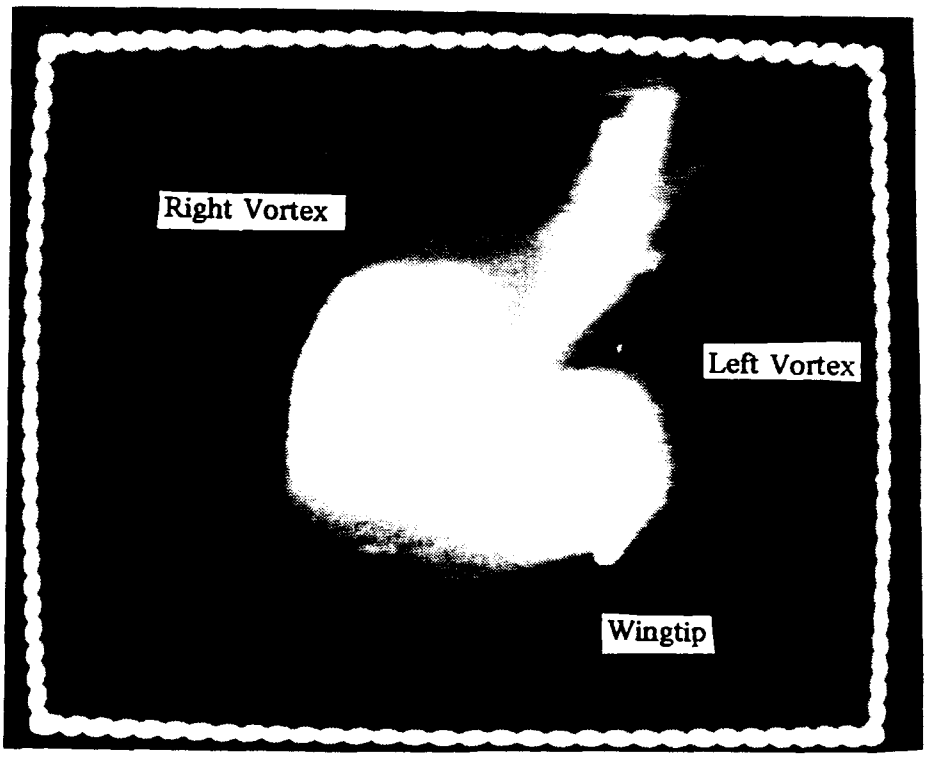

a)

Fig. 29 Leading edge vortices at x/c = 0.95.

b)

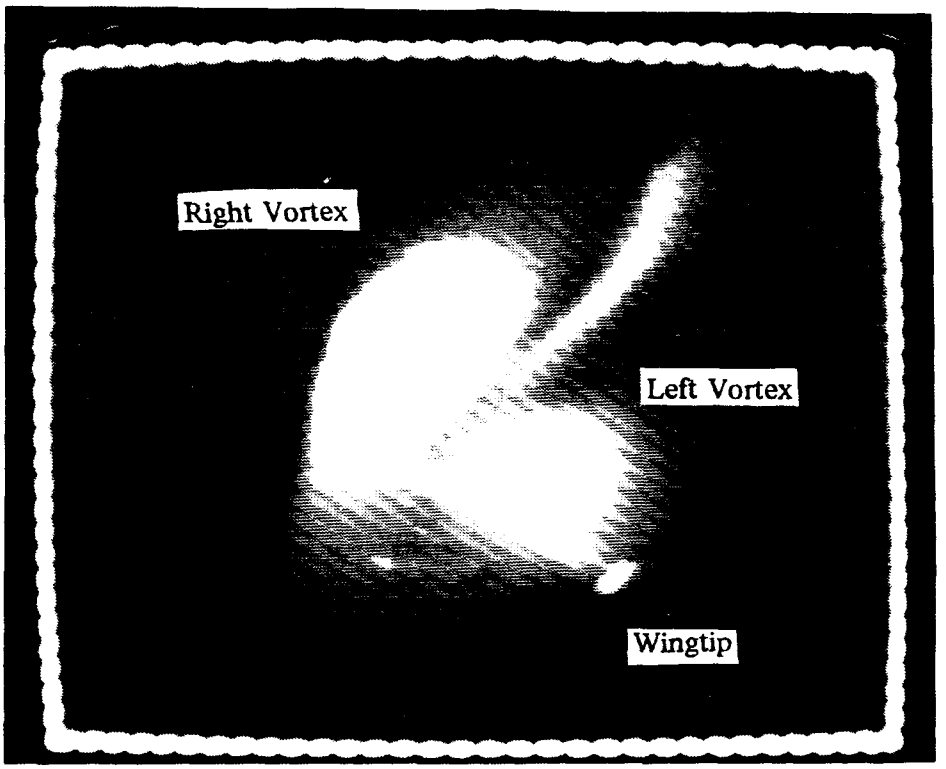

c)

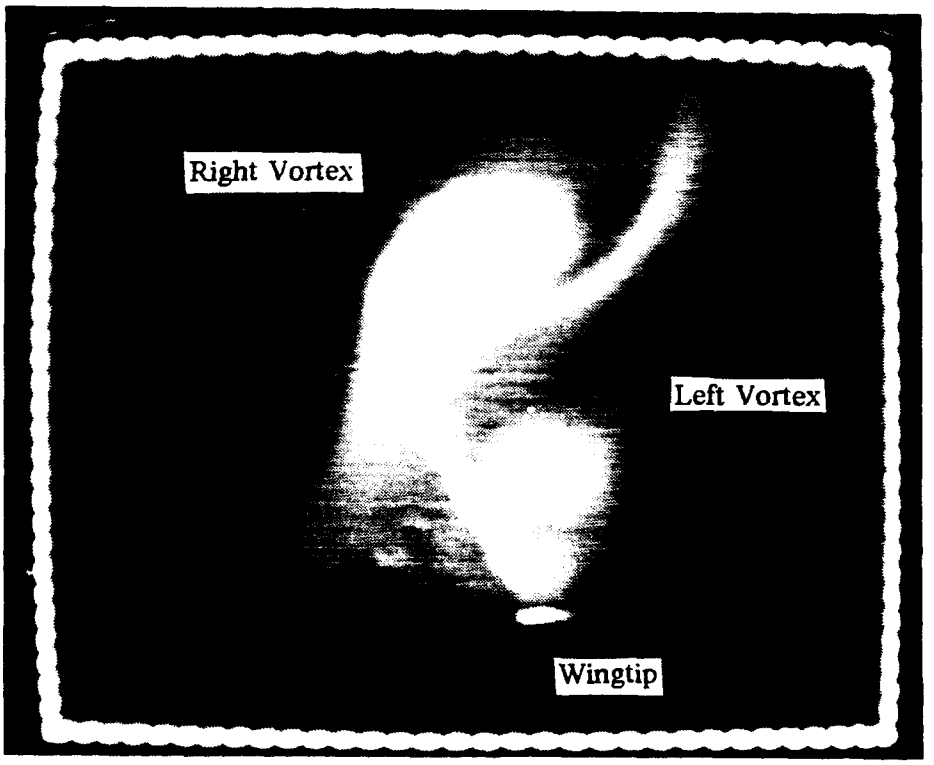

Fig. 29 (continued).

Test Matrix

Several tests were completed in both the water tunnel and the wind tunnel over a period of months. More data were reduced than can be included in this thesis and data are still being reduced at the time of this writing. Other data sets may be requested from Dr. Donald T. Ward, Aerospace Engineering Dept., Texas A&M University, College Station, TX 77843, (409) 845-1732. The following test matrices contain all inclusive tests that were completed.

Water Tunnel Test Matrix

All tests were conducted with the sting angle of attack and sideslip angle fixed at 35° and 0°, respectively.

Table 1 Wing rock experiments.

Model Configuration	Motion	Tunnel Speed (ips)	Number of Runs
Baseline	Steady	6, 10, 12, 15	3
	Buildup	6, 10, 12, 15	3
	Decay	6, 10, 12, 15	3
Model w/spinner	Steady	6, 10, 12, 15	3
	Buildup	6, 10, 12, 15	3
	Decay	6, 10, 12, 15	3

Table 2 Flow visualization tests.

Model Configuration	Tunnel Speed (ips)	Chord Position x/c	Roll Angle $\pm\phi$ (deg)	Number of Runs
Baseline Model	6, 10, 12, 15	0.25, 0.50, 0.65, 0.75, 0.85, 0.95	---	5
	6, 10, 12, 15	---	5, 15, 25, 30	5
Model w/spinner	6, 10, 12, 15	0.25, 0.50, 0.65, 0.75, 0.85, 0.95	---	5
	6, 10, 12, 15	---	5, 15, 25, 30	5

Wind Tunnel Test Matrix

All tests were conducted with the sting angle of attack and sideslip angle fixed at 35° and 0°, respectively. The tunnel was operated at a dynamic pressure of $\bar{q}$ = 1 psf or V_∞ = 29.0 fps. The model configuration depends on whether or not the added mass attachment was connected. If so, the disk number signifies the actual number of disks that were collared to the added mass fixture. For example, Disk 3 means that the added mass fixture contained three disks.

Table 3 Wing rock tests with added mass attachment.

Model Configuration	Support Rod Length (in)	Motion	Number of Runs
Baseline Model, Model w/spinner, Disks 1-10	14.75	Steady	3
		Buildup	2
		Decay	2
Baseline Model, Model w/spinner, Disks 1-10	13.00	Steady	2
		Buildup	2
		Decay	2

Table 4 Flow visualization tests.

Model Configuration	Chord Station x/c	Support Rod Length (in)	# of Runs
Baseline Model	0.25, 0.50, 0.65, 0.75, 0.85, 0.95	14.75	3
		13.00	3
Model w/spinner	0.25, 0.50, 0.65, 0.75, 0.85, 0.95	14.75	3
		13.00	3
Disk 3	0.25, 0.50, 0.65, 0.75, 0.85, 0.95	14.75	3
		13.00	3
Disk 6	0.25, 0.50, 0.65, 0.75, 0.85, 0.95	14.75	3
		13.00	3
Disk 10	0.25, 0.50, 0.65, 0.75, 0.85, 0.95	14.75	3
		13.00	3

CHAPTER III

DISCUSSION OF WING ROCK RESULTS

This chapter discusses the wing rock results of an 80° delta wing tested in both a wind tunnel and water tunnel. Both an investigation of the motion as well as of the vortical flow field was completed. Tests were also conducted to quantify the differences in magnitude of the rolling moments between water and wind tunnel results.

Wind Tunnel Test Results

The wind tunnel tests were conducted in two separate phases; an analysis of the wing rock motion and flow visualization experiments. The first phase of the investigation consisted of tracking the model's wingtip with the EV motion analysis system. The second phase, utilizing a laser and smoke system, consisted of tracking the leading edge vortices at specified chord locations.

Tests were conducted using two different model support rod lengths. The results presented here are for the spinner placed 2.5 spinner diameters aft of the delta wing model.

Summary of Test Methods

All tests were conducted at a dynamic pressure of 1 psf or freestream velocity of 29.0 fps. At this low $\bar{q}$, there was a ±5% error in tunnel speed. The cameras were located on the top and side of the test section and were adjusted to provide a

good view of the model. The viewing windows on top of the tunnel test section were arranged such that an orthogonal camera setup was impossible while still providing an adequate view of the model and vortices. Calibration tests were completed to determine the residual error of the camera setup. The cameras were readjusted a number of times to achieve the lowest residual calibration error. The wing rock tests included observations of steady limit cycle motion, buildup to the limit cycle, and decay to the limit cycle. Added mass effects were also examined, as previously described. Data were collected as the inertia disks were added incrementally.

The flow visualization phase involved installing a laser above the tunnel and creating a light sheet with a glass rod. A smoke wand was placed approximately three feet in front of the model. The smoke was then entrained into the leading edge vortices. The light sheet bisected the model at a chordwise location and illuminated the cross sections of the right and left vortices. The data were recorded on 200 Hz video tape and reduced at a later time with a frame by frame editing process.

General Observations

The initial model configuration was such that the spinner could be attached to the support rod 4.0 diameters aft of the wing. During the first tests, vibration of the model was observed and the wing rock motion had large changes in roll amplitudes during a run. The wing had large roll amplitudes for a few oscillations which damped to small amplitudes for a few oscillations and then again to the larger ones. Apparently, the structural vibrations affected the roll oscillations by creating a low frequency beating signal on top of the limit cycle. To reduce this vibration, the model support rod was sequentially shortened until the delta wing appeared to have a steady limit cycle.

The flow visualization tests were originally attempted with a 300 Watt slide projector and a slide with a fine slit. Although it projected a thin light sheet, the intensity of the light was too low to adequately illuminate the vortices and allow tracking with EV. A 5 watt laser was substituted and provided more than adequate intensity. Markings were made on the top surface of the model at the $0.25\bar{c}$, $0.50\bar{c}$, $0.65\bar{c}$, $0.75\bar{c}$, $0.85\bar{c}$, and $0.95\bar{c}$ chordwise locations. The light sheet was then placed at each location by moving the glass rod forward or aft. The following sections present the quantified results and analysis for the wind tunnel tests.

Model Motion

Two different model configurations are presented; the baseline model which was configured without added mass components and the model with spinner which had only the added mass attachment without any disks. These configurations are referred to as the baseline model and model w/spinner, respectively, throughout the text and figures.

Baseline Model

The following figures are time series of the roll angle, rate, and acceleration for an established wing rock cycle. The roll angle envelope (Fig. 30) varied with time. This variation was evidently due to the structural vibration discussed earlier and caused by the flexibility of the support rod. Positive roll angles varied between 38.5° and 43.0°, with an average magnitude of ϕ = 41.4°. The negative roll angles varied between -33.6° and -37.2°, with an average magnitude of ϕ = -35.7°. The total average magnitude between both positive and negative roll angles was ϕ = 38.5°. The period of motion varied between 0.350 sec and 0.374 sec, and the average period was T = 0.362 sec. This average period corresponded to an average frequency of ω

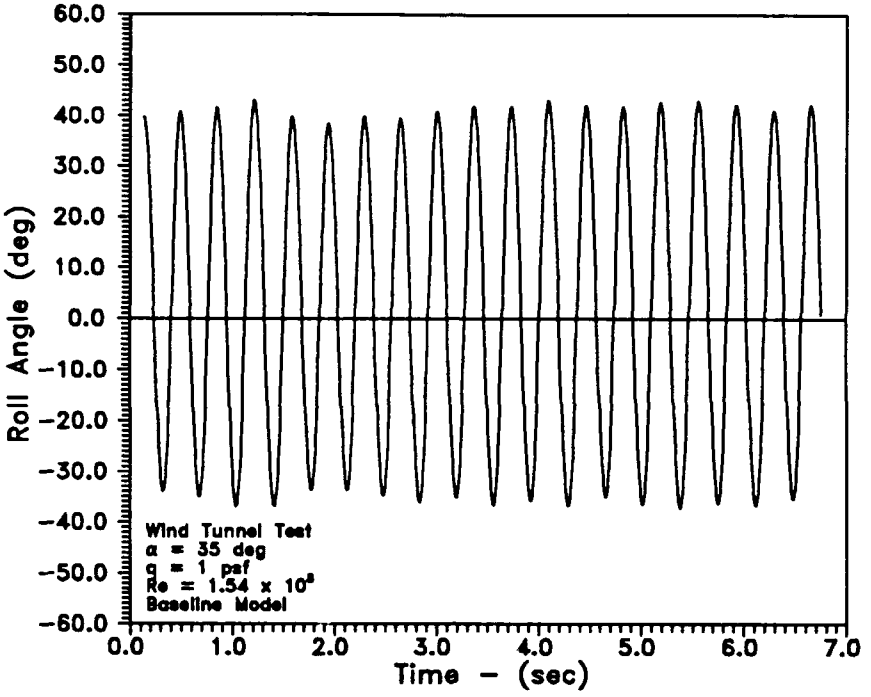

Fig. 30 Roll angle time history.

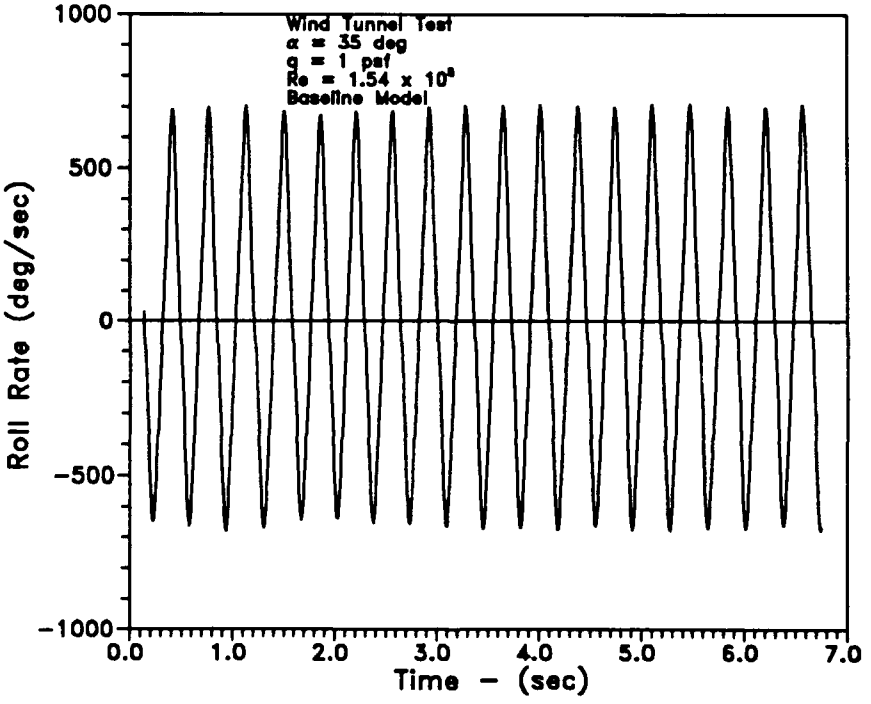

Fig. 31 Roll rate time history.

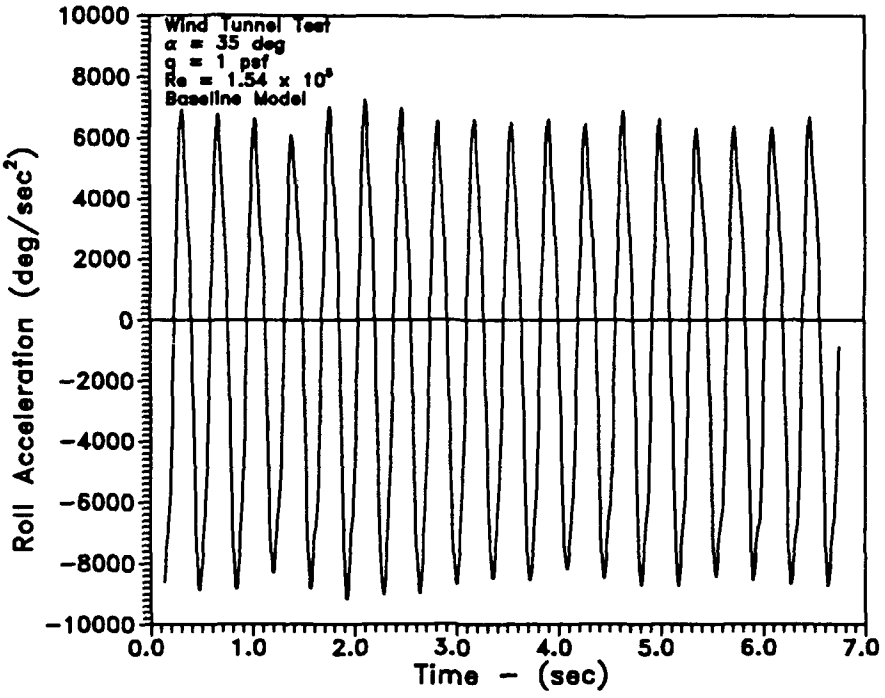

Fig. 32 Roll acceleration time history.

= 17.34 rad/sec. The reduced frequency defined as

$$k=\frac{\omega b}{2V_{\infty}} \tag{9}$$

was 0.088.

A slight model mass and/or position asymmetry was hypothesized as the reason for the variation in average positive and negative roll angles. The flexible support rod, when under loading, was one plausible explanation of this asymmetry. The reference axis system was defined for a static model at ϕ = 0° with no load applied; roll angles were calculated from this reference frame. During wing rock, the model had a lifting force at ϕ = 0°, which caused a measurement asymmetry. The DYNAMIC code was modified to adjust for a dynamic load on the model by incorporating an offset parameter in the reference z axis direction. These parameters

had magnitudes in the hundredths of an inch. The second explanation was a mass inertia imbalance and was continually addressed during testing. Prior to each run the model was evaluated for any mass imbalance. If a mass imbalance was detected it was corrected by readjusting the set screws in the free-to-roll or added mass components.

Morris'[3] data were more consistent at the same test conditions. His model was also fitted with a shorter support rod and had slightly less mass inertia. He reported that the average limit cycle amplitude was 34.8° with maximum cycle to cycle deviation of less than ±1°. The period varied from 0.332 sec to 0.344 sec, with an average value of 0.335 sec. The average frequency was 18.8 rad/sec and the reduced frequency was 0.095. When the results were compared, the current study's average

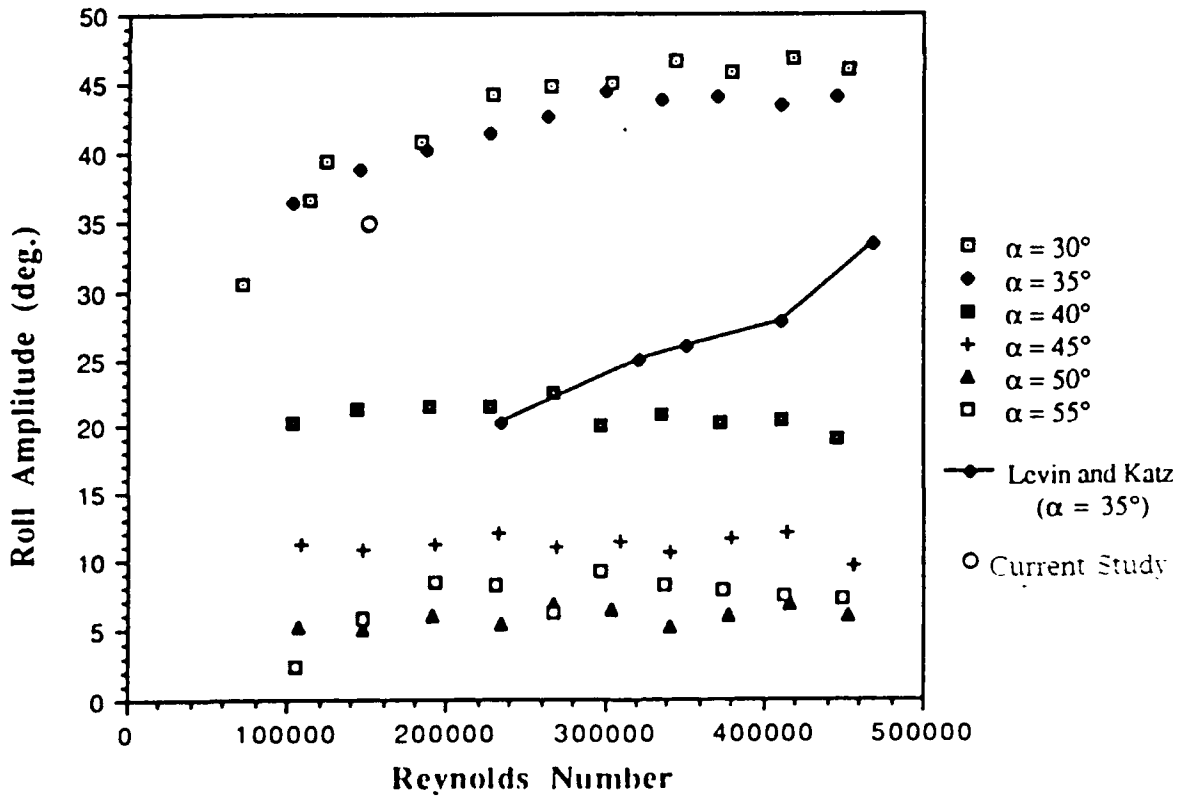

Fig. 33 Roll amplitude versus Reynolds number.[4]

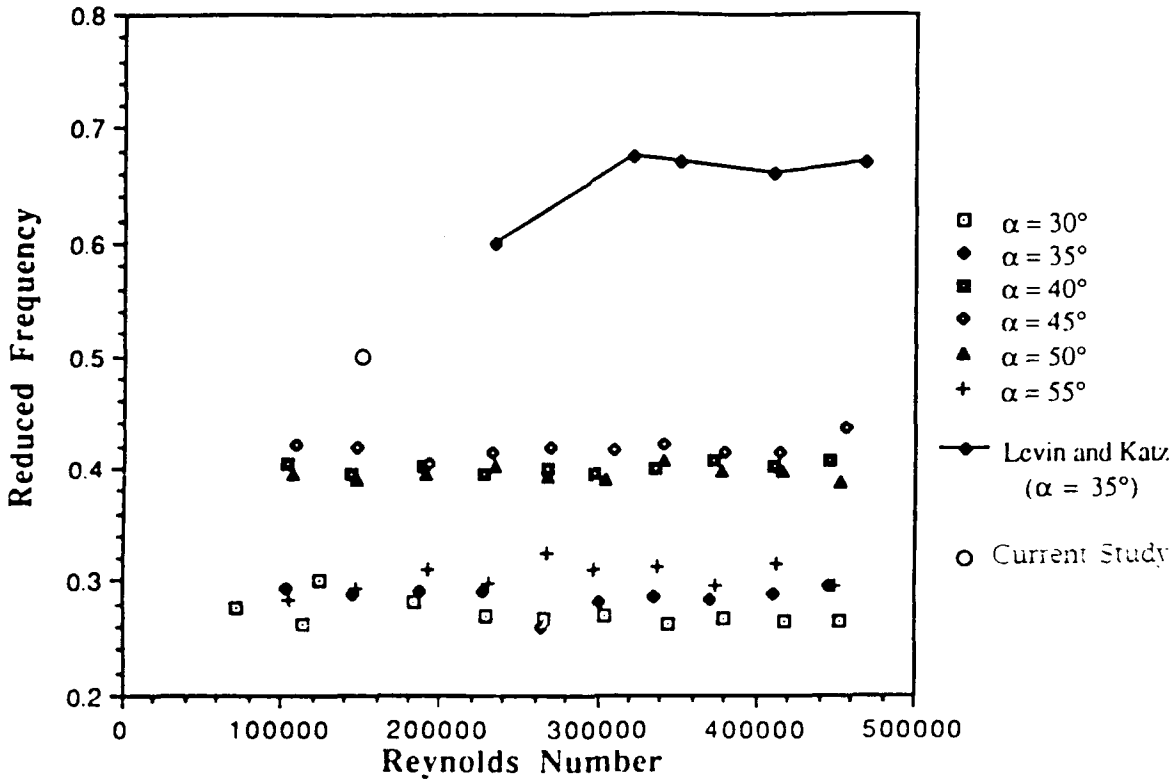

Fig. 34 Wing rock reduced frequency versus Reynolds number.[4]

roll magnitudes were larger than Morris' data as were the average periods. From Arena's[4] data (Fig. 33), the average roll amplitude was roughly 39° for an 80° delta wing at α = 35° and a Reynolds number of Re = 1.5 x 10^5. Arena calculated the reduced frequency by multiplying the wing oscillation frequency by $2\pi c_r$, and then divided by V_∞. At the same conditions and from Fig. 34, the reduced frequency was 0.39. Recalculating the reduced frequency based on his method, a reduced frequency of 0.50 was computed for the current study. While this value was higher than Arena's result, the Levin and Katz[8] data from the same figure gave a reduced frequency of 0.60 for a Reynolds number of 2.25 x 10^5.

A phase portrait for a typical limit cycle is shown in Fig. 35. The unsteadiness was more noticeable at the maximum roll amplitudes. The delta wing had a maximum positive roll rate of 700 deg/sec and a maximum negative roll rate

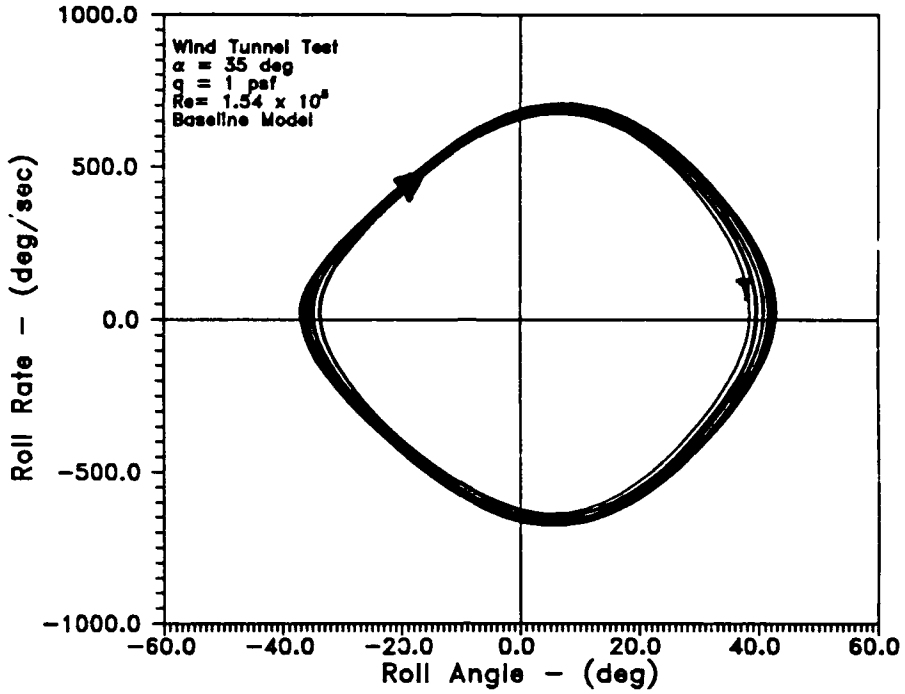

Fig. 35 Phase portrait for the baseline model.

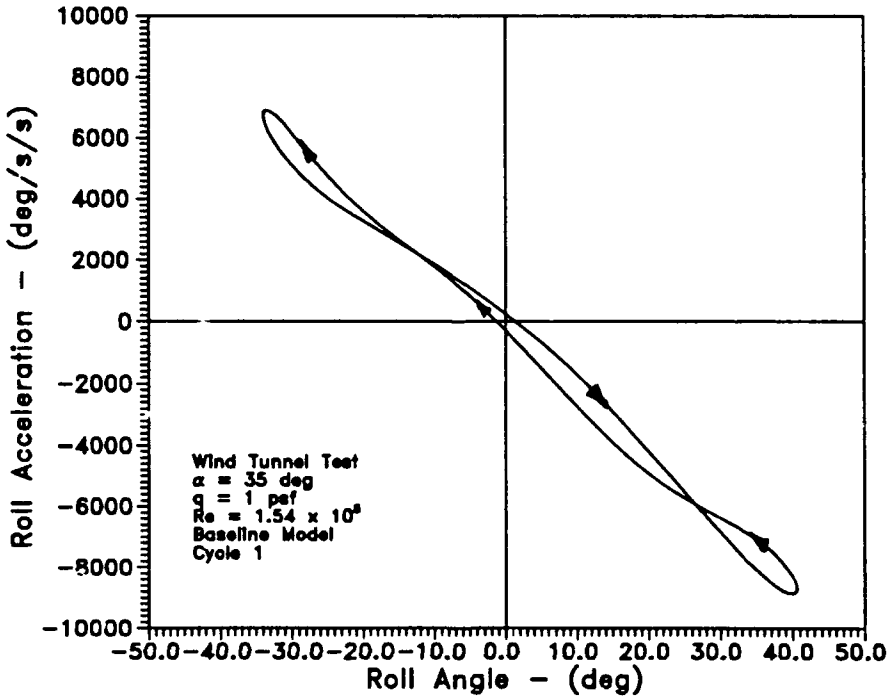

Fig. 36 Wind tunnel roll acceleration versus roll angle.

of -660 deg/sec. A one cycle history of the roll acceleration curve is shown in Fig. 36. For this cycle, the maximum positive roll acceleration was 6900 deg/sec^2 while the maximum negative magnitude was -8800 deg/sec^2. An interesting feature of this curve was that at the larger roll amplitudes, the curve sloped away from the coordinate axis instead of drooping down towards this axis, as presented in other studies. Having analytically solved for the mass moment of inertia, the rolling moment was computed by

$$L(t)=I_{xx}\ddot{\phi}(t) \tag{10}$$

where

$$L(t)=C_l(t)\bar{q}Sb \tag{11}$$

The rolling moment coefficient was solved as

$$C_l(t)=\frac{I_{xx}}{\bar{q}Sb}\ddot{\phi}(t) \tag{12}$$

Fig. 37 and Fig. 38 compare rolling moment coefficients at the same test conditions. The delta wing model was the same with a slight increase in mass inertia due to the longer support rod. The magnitude in the rolling moment coefficients for both studies was very similar, each about 0.15. The hysteresis in these curves is characteristic of a nonlinear system. The direction of the curve's path is also consistent with other wind tunnel test data.[4-8]

In addition to the steady limit cycle, the wing rock motion was observed during buildup to the limit cycle (Fig. 39) and decay to the limit cycle. The buildup occurred in two seconds and with maximum roll amplitude of 43°. The magnitude

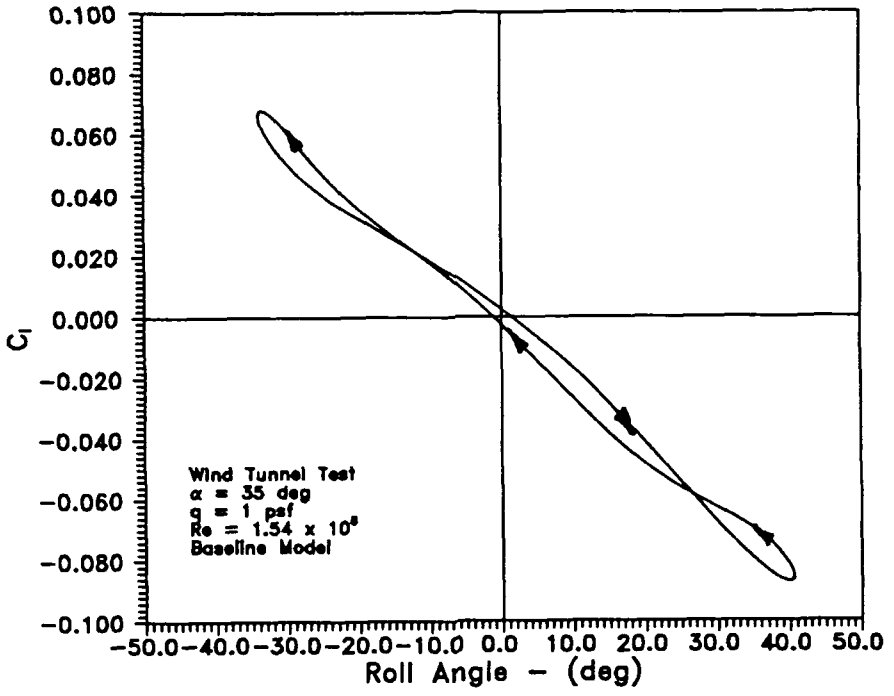

Fig. 37 Wind tunnel rolling moment coefficient versus roll angle.

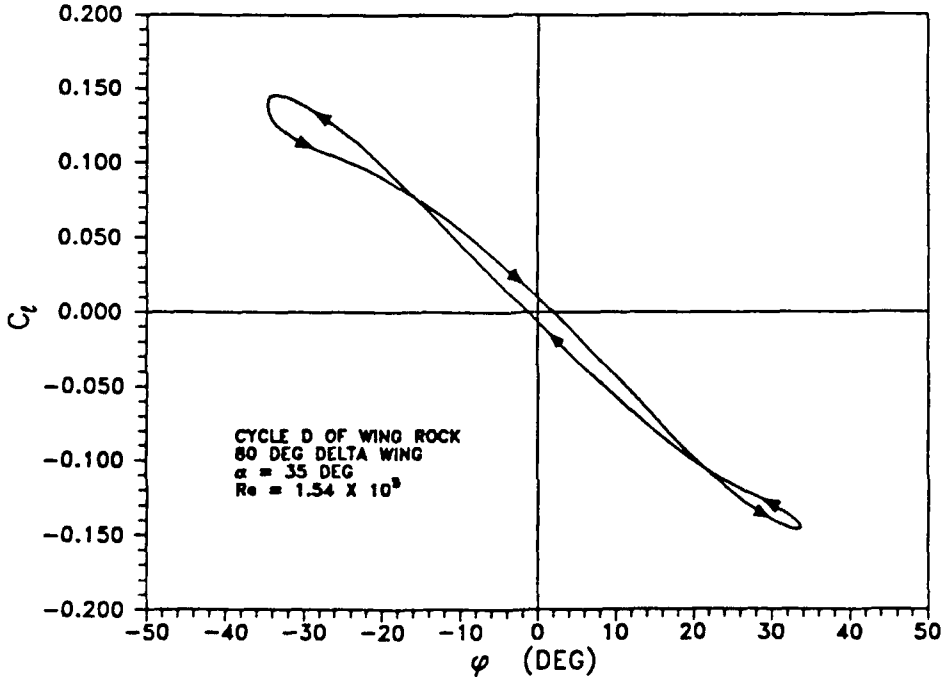

Fig. 38 Rolling moment coefficient versus roll angle.[3]

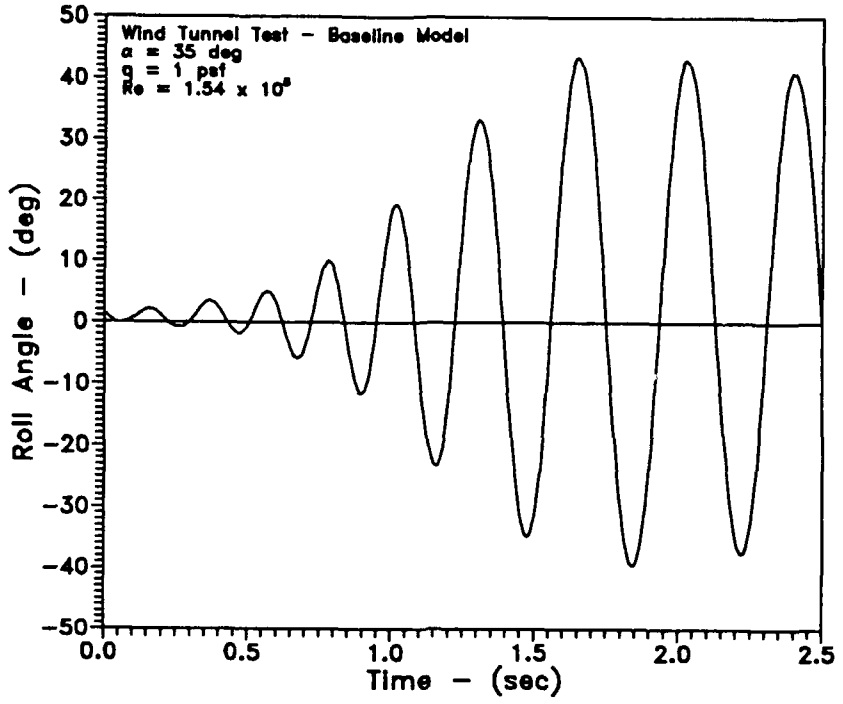

Fig. 39 Wind tunnel roll angle during wing rock buildup.

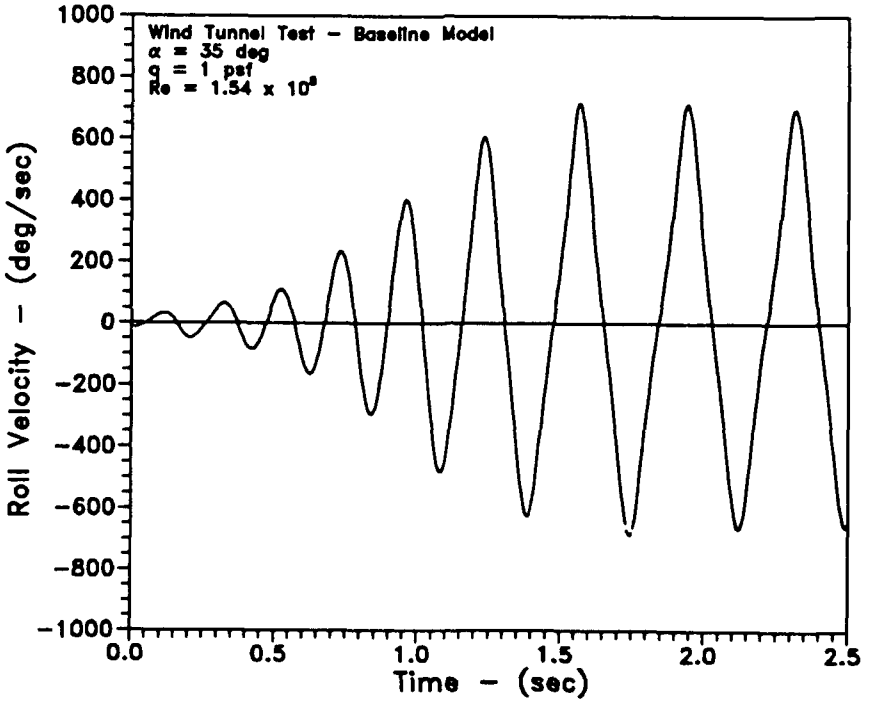

Fig. 40 Wind tunnel roll rate during wing rock buildup.

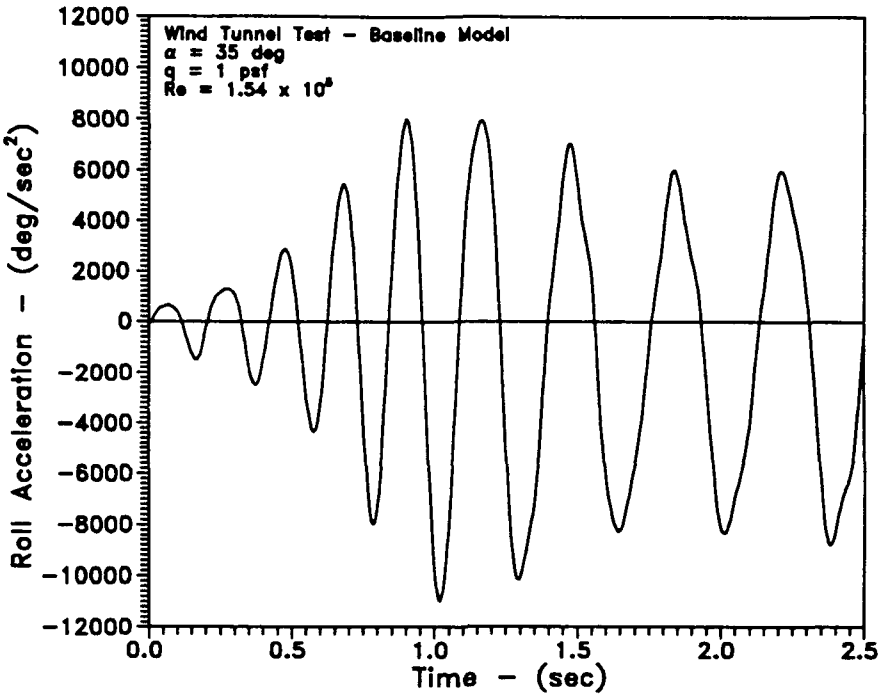

Fig. 41 Wind tunnel roll acceleration during wing rock buildup.

decreased slightly over the next cycle. Again, a quasi-steady limit cycle was present for the entire run. Fig. 40 and Fig. 41 show the roll rates and roll accelerations during the buildup cycles. The maximum roll rates were around 700 deg/sec and the maximum roll accelerations reached were 11000 deg/sec^2. The roll accelerations (Fig. 41) had an overshoot of approximately 2000 deg/sec^2 before settling to a quasi-steady limit cycle.

Further examination of the wing rock roll acceleration buildup can be seen in Fig. 42. The flexibility in the support rod was evident in these initial figures. The roll acceleration curves were not aligned with the zero roll angle, apparently because

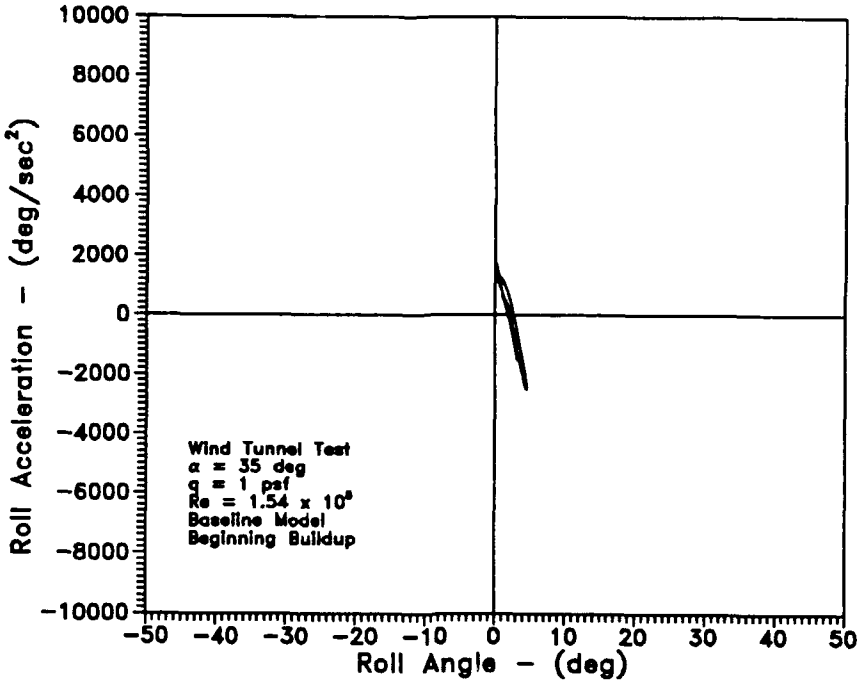

a)

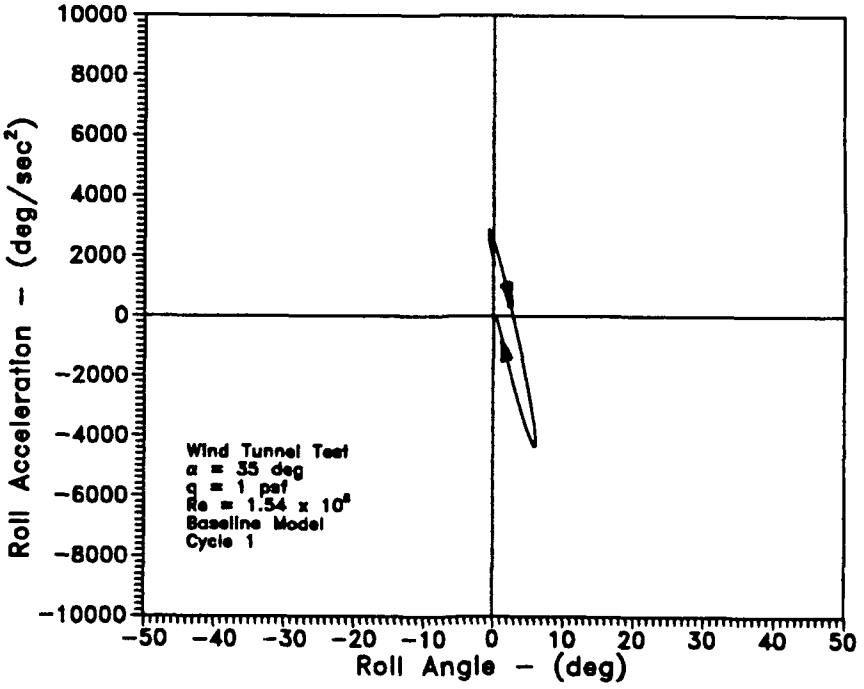

b)

Fig. 42 Wind tunnel roll acceleration buildup.

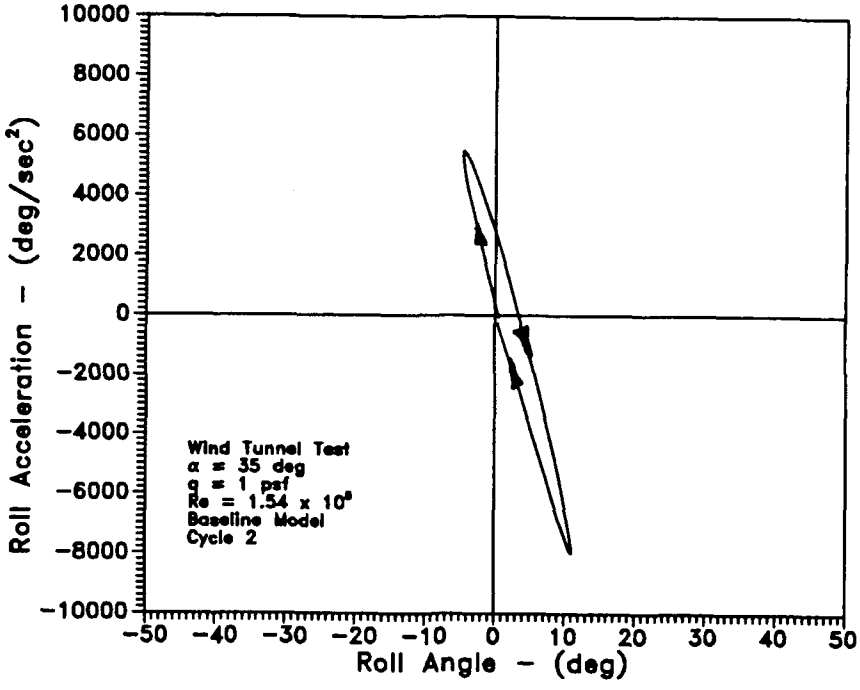

c)

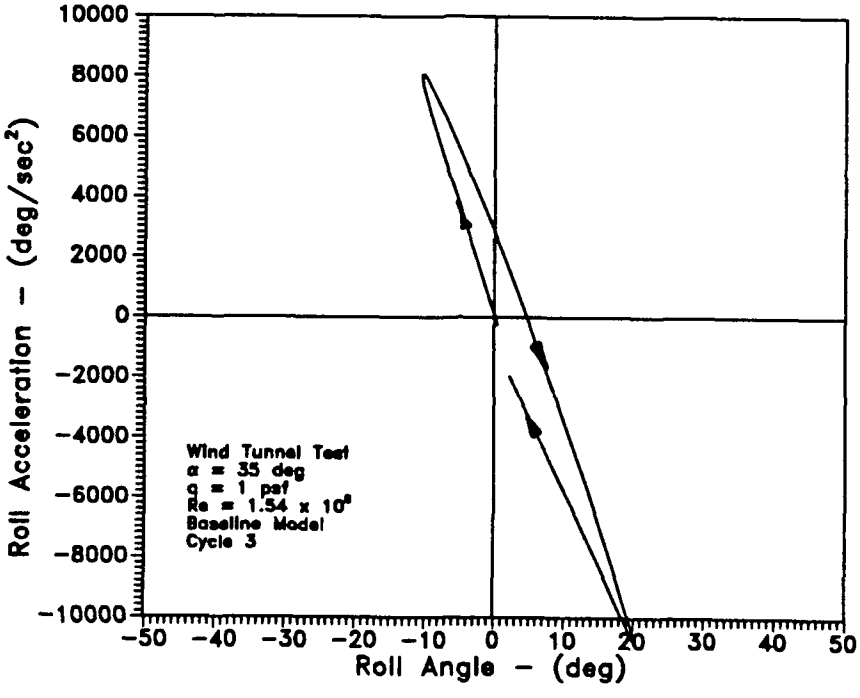

d)

Fig. 42 (continued)

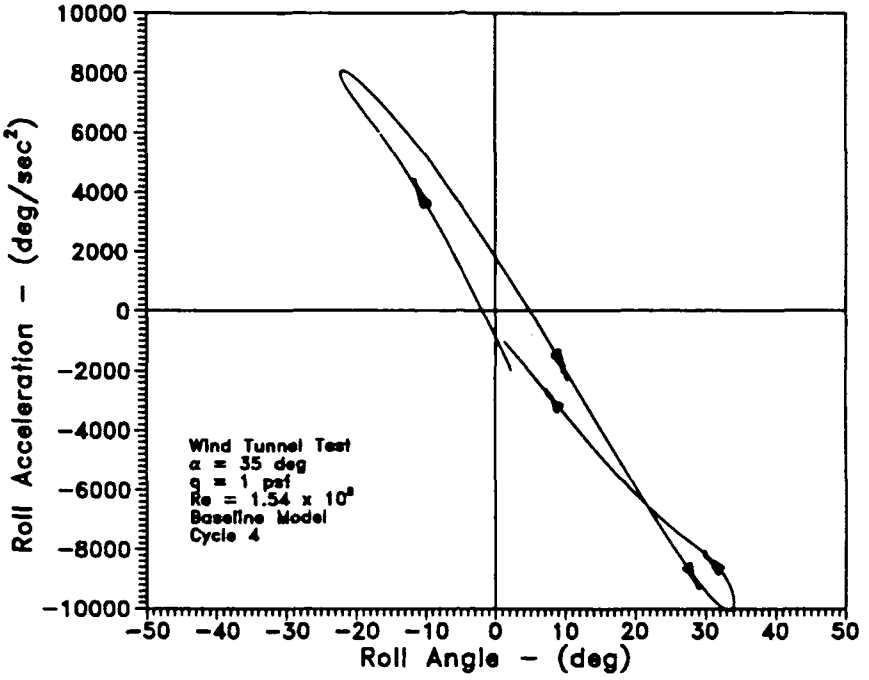

e)

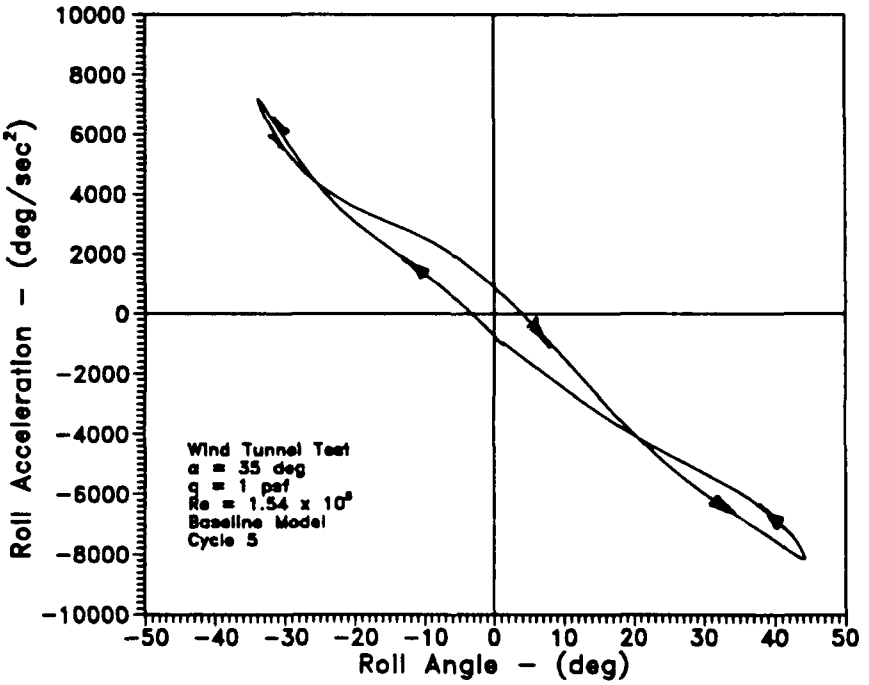

f)

Fig. 42 (continued)

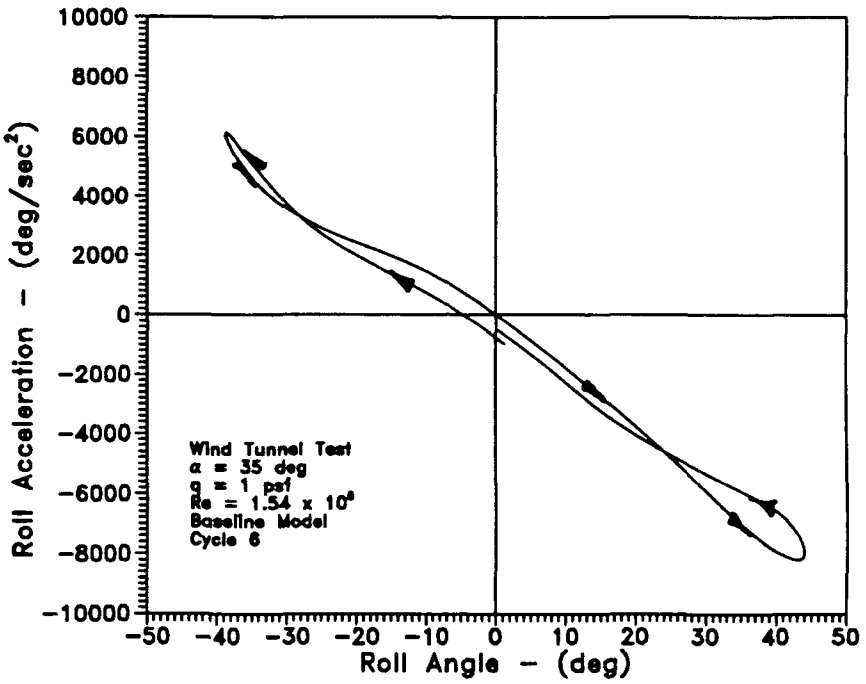

g)

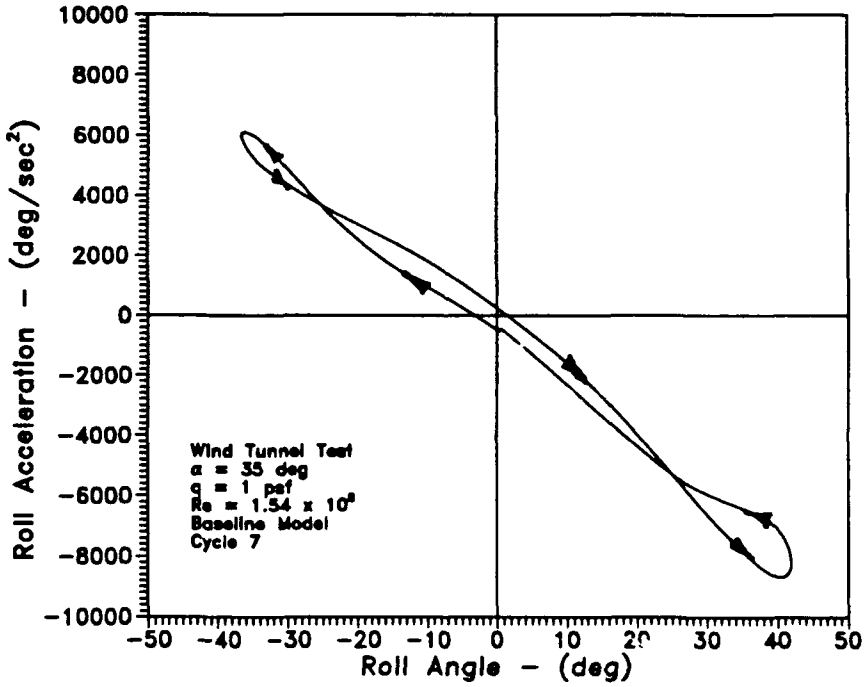

h)

Fig. 42 (continued)

the magnitude of the time averaged lift reduced as roll amplitudes increased. Therefore, the relative positions between the static reference frame and the dynamic body fixed reference frame changed. The offset parameter discussed earlier was a constant, fixed for the steady motion. The buildup began with a relatively steep roll acceleration versus roll angle curve (Fig. 42a). The slope of this curve began to flatten out by the fourth cycle (Fig. 42e). Also in this cycle the lower branch of the curve began to show the characteristic lower lobe of the developed limit cycle. In the next cycle, Fig. 42f, the upper branch crossed back over itself, taking on the upper lobe character of an established wing rock limit cycle. Through the next two cycles the slopes of these curves decreased and increased respectively. The quasi-steady limit cycle had been reached.

Nguyen, Yip, and Chambers[7] derived a work-energy relationship in a limit cycle oscillation;

$$\Delta E=\bar{q}Sb\int_{t_1}^{t_2} C_\ell(t)\dot{\phi}(t)dt$$

which can be rewritten as the line integral of C_ℓ along the path C with respect to ϕ;

$$\Delta E=\bar{q}Sb\oint_{C} C_\ell(\phi)d\phi$$

where C is the C_ℓ versus ϕ curve from t_1 to t_2.

A small program was written to solve for the kinetic energy exchange during wing rock buildup and decay in both the wind tunnel and the water tunnel. Fig. 43 contains the energy plots for the motion corresponding to Fig. 42. During initial buildup, the net kinetic energy was definitely more positive and showed that energy

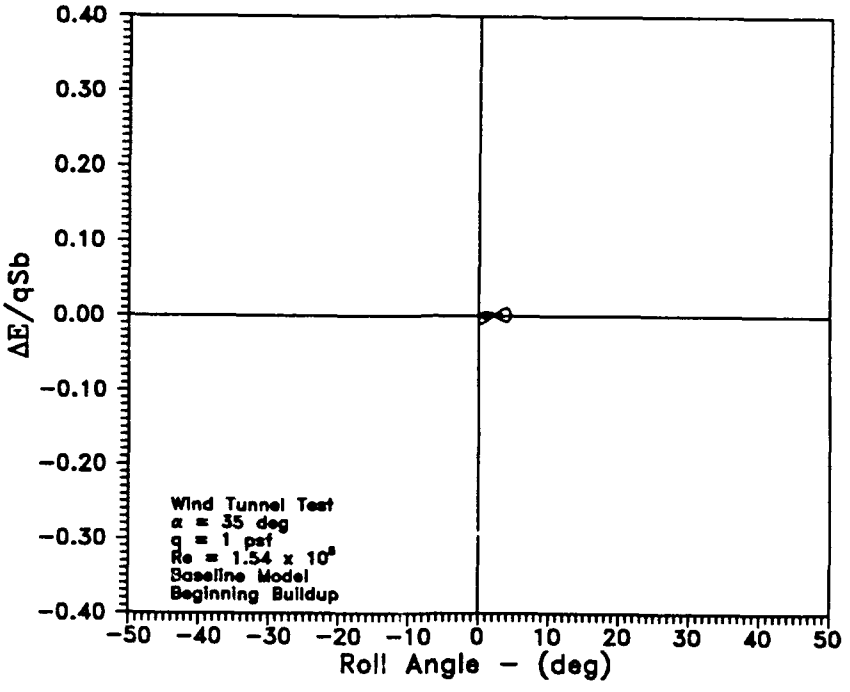

a)

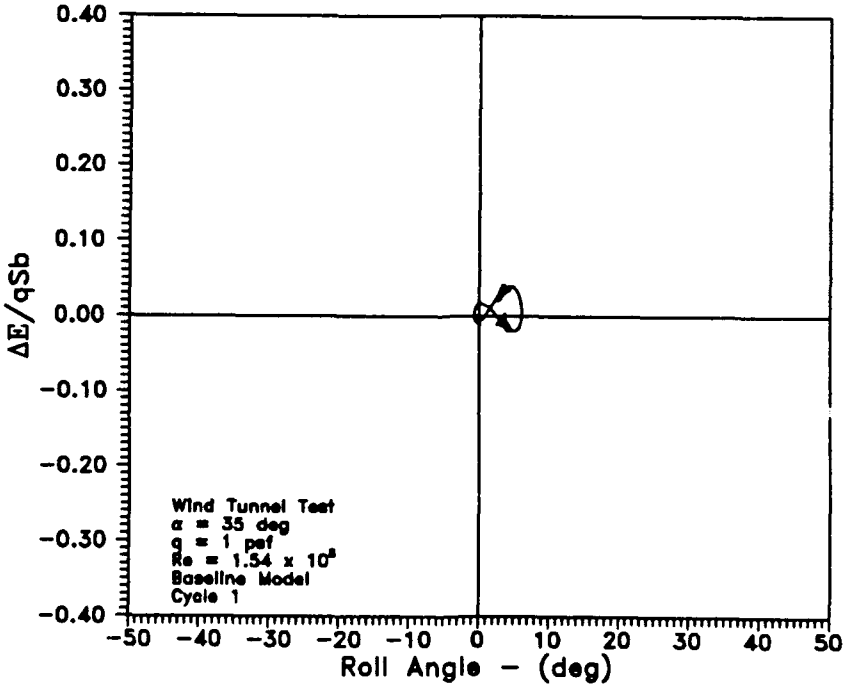

b)

Fig. 43 Wind tunnel energy exchange during wing rock buildup.

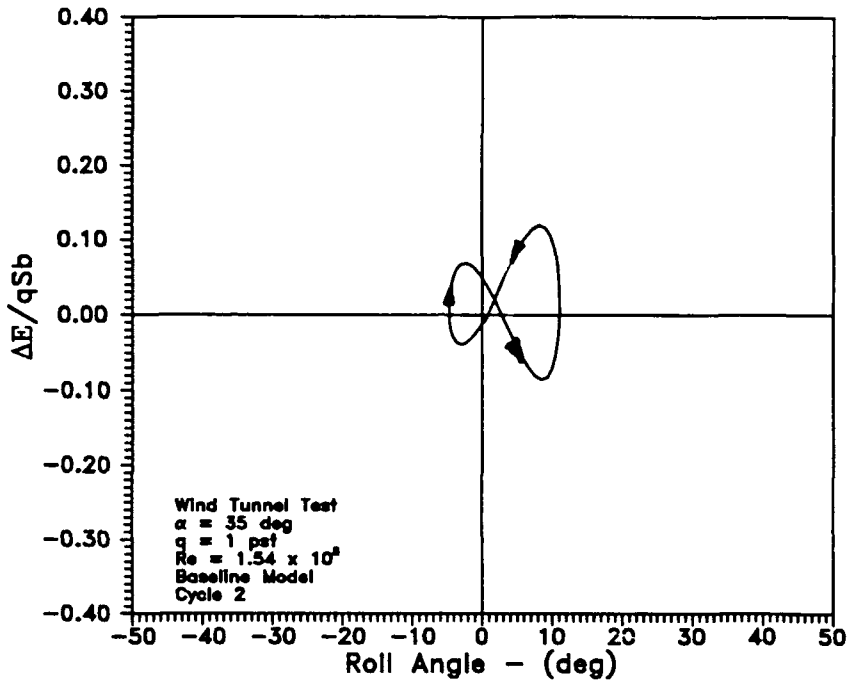

c)

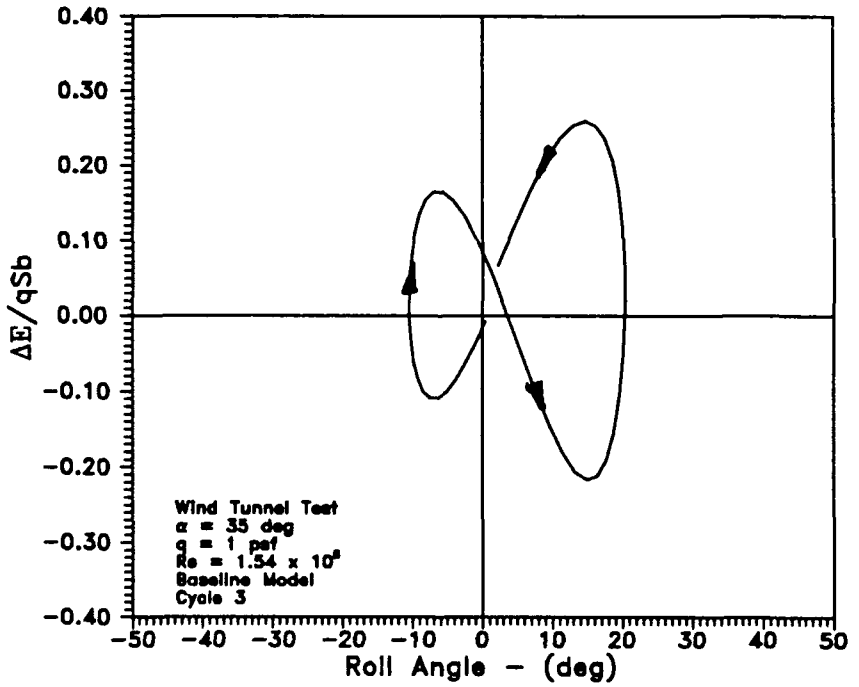

d)

Fig. 43 (continued)

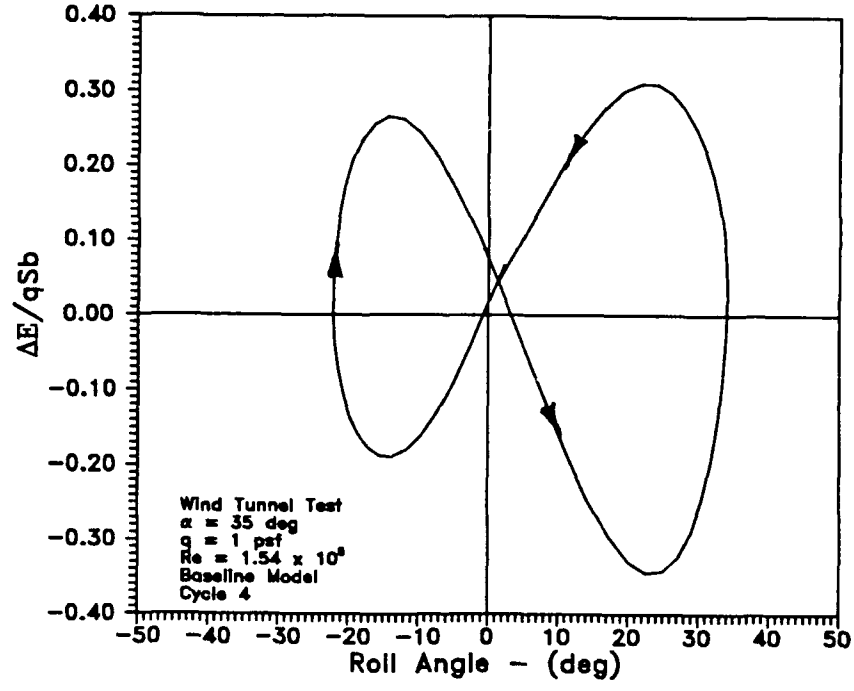

e)

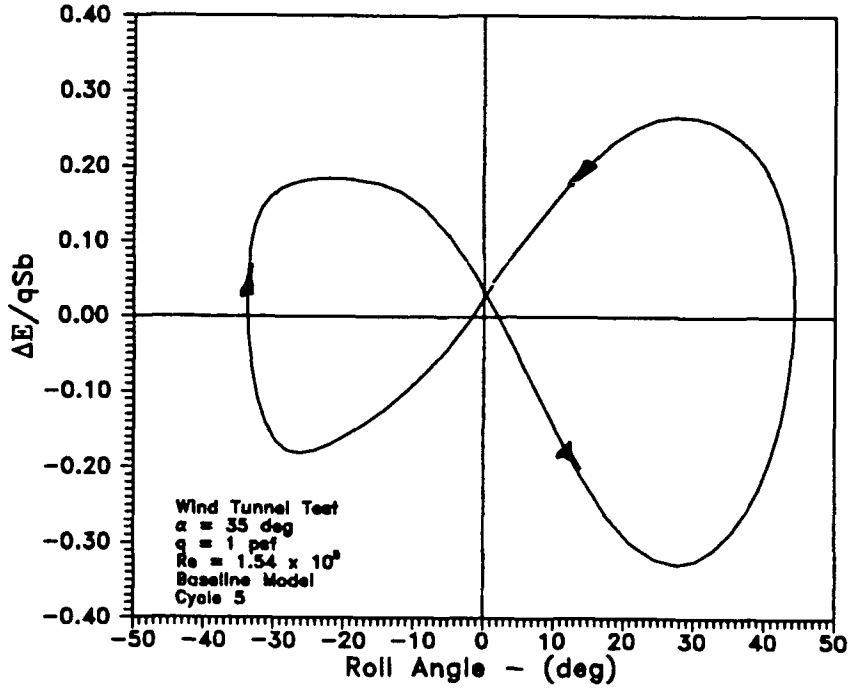

f)

Fig. 43 (continued)

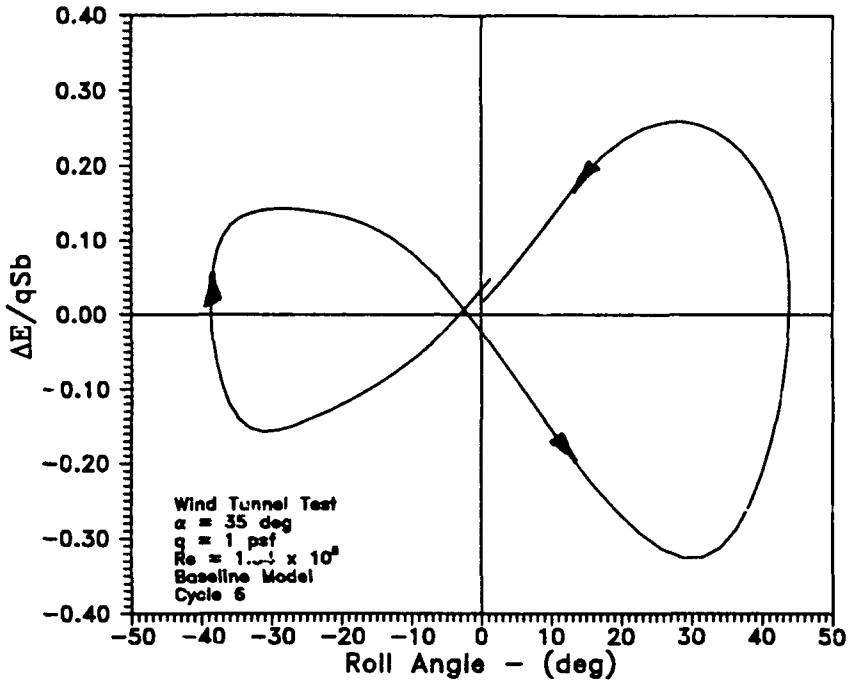

g)

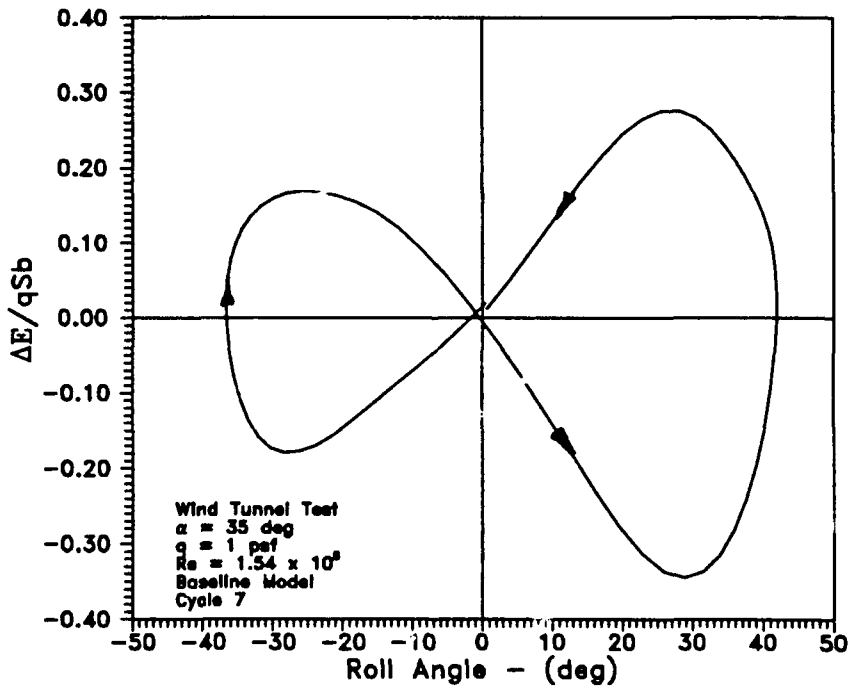

h)

Fig. 43 (continued)

was being added to the system. From Fig. 43a, the energy curve was a small figure eight turned on its side. Again, like the roll acceleration curves, energy curves were not centered about the origin. As the buildup continued, the energy curve enlarged and became more centered around the origin. Careful observation of these energy curves revealed that the energy at the small roll angles remained positive, signifying that energy was being added to the system. At the maximum roll angle magnitudes the energy change was zero, which meant that ΔE represented a kinetic energy change. The potential energy of the system, similar to a spring, depended upon the relative position of the wing to the oncoming flow. The potential energy was therefore dependent upon the roll angles and the right and left vortex locations above the wing. This energy does not show up in the ΔE term. It has been well documented that vortex asymmetries in the flow field cause wing rock. These asymmetries will be discussed further in the flow visualization section.

Added Mass Experiments

Experiments were conducted to determine the added inertia of the water during water tunnel tests. Steel disks were added incrementally to an added mass attachment and the model's motion was tracked. The designation for the model with the added mass attachment and no disks is model w/spinner. If three disks were added, the configuration is called model w/disk 3. The following results summarize the addition of the added mass attachment without any disks first and then with disks.

The model w/spinner configuration exhibited more unsteadiness than did the baseline model. The following time series figures show the quasi-steady wing rock motion for the model w/spinner. The inertia of the model was increased by over 6½ times, going from the baseline model inertia of 2.0282×10^{-5} slug-ft^2 to the model w/spinner inertia of 1.3561×10^{-4} slug-ft^2. The added mass attachment, again,

consisted of the plastic spinner and the aluminum fixture with a collar to hold the disks. Fig. 44 shows the roll amplitude time series. The positive roll amplitude fluctuated between 16.1° and 29.7° with an average positive amplitude of 24.8°. The negative roll amplitude fluctuated between -15.4° and -26.6° with an average negative amplitude of -21.2°. The overall average amplitude was 23.0°. The period of the motion varied from a low of 0.453 sec to 0.569 sec, a difference of 0.116 sec. The average frequency was 11.99 rad/sec which corresponded to a reduced frequency of 0.061. The time fluctuations of the roll angle magnitudes had a period of approximately 4.0 sec or a frequency of 1.57 rad/sec. This motion was somewhat unsteady as well. The roll rate time series is shown in Fig. 45 from which the maximum roll rate was 330 deg/sec. Again, the beating can be seen. Lastly, from

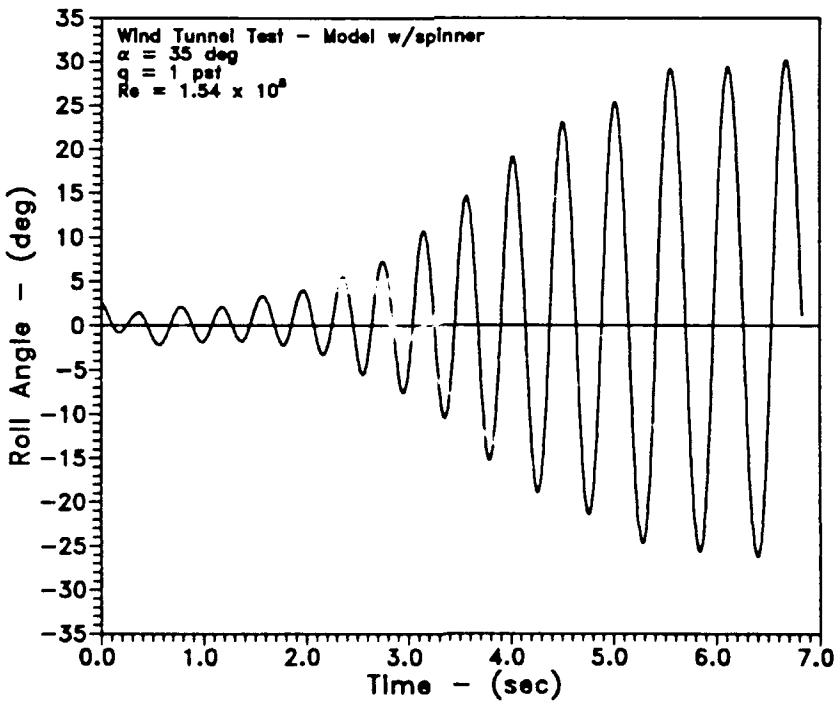

Fig. 44 Wind tunnel model w/spinner during roll angle buildup.

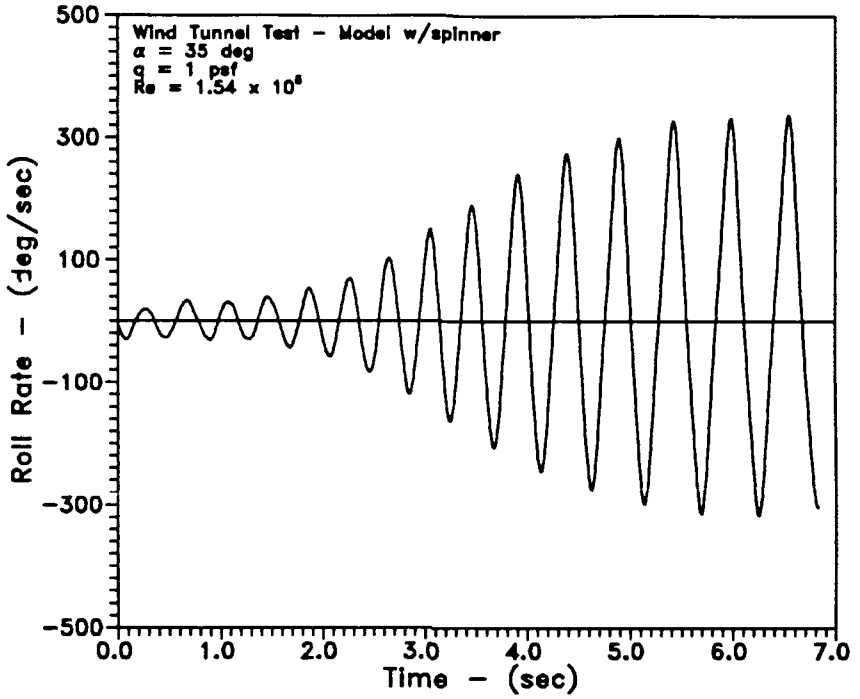

Fig. 45 Wind tunnel model w/spinner during roll rate buildup.

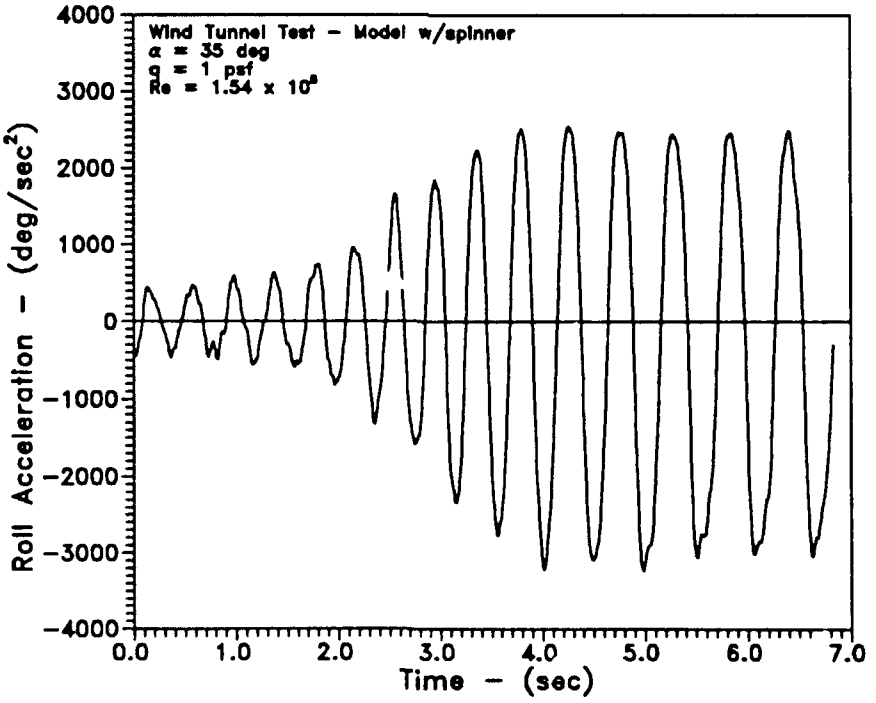

Fig. 46 Wind tunnel model w/spinner during roll acceleration buildup.

Fig. 46, the maximum roll acceleration was 3200 deg/sec^2. The added inertia of the spinner reduced the roll amplitudes, rates and accelerations as expected. However, the unsteady motion was not anticipated.

Another view of the unsteady nature of the system can be seen in Fig. 47. The C_ℓ versus ϕ curve varied about the origin much more than did the baseline model (Fig. 48). In addition, the rolling moment coefficient of the model w/spinner was over twice that of the baseline model. The spinner significantly affected the motion of the model. Ericsson[22] summarized various aerodynamic problems encountered when conducting dynamic tests on forebodies, describing the effect of asymmetric forebody vortices on a rolling model in wing rock. The Magnus effect, which involves a rotating cylinder in a flow field, causes a favorable pressure gradient,

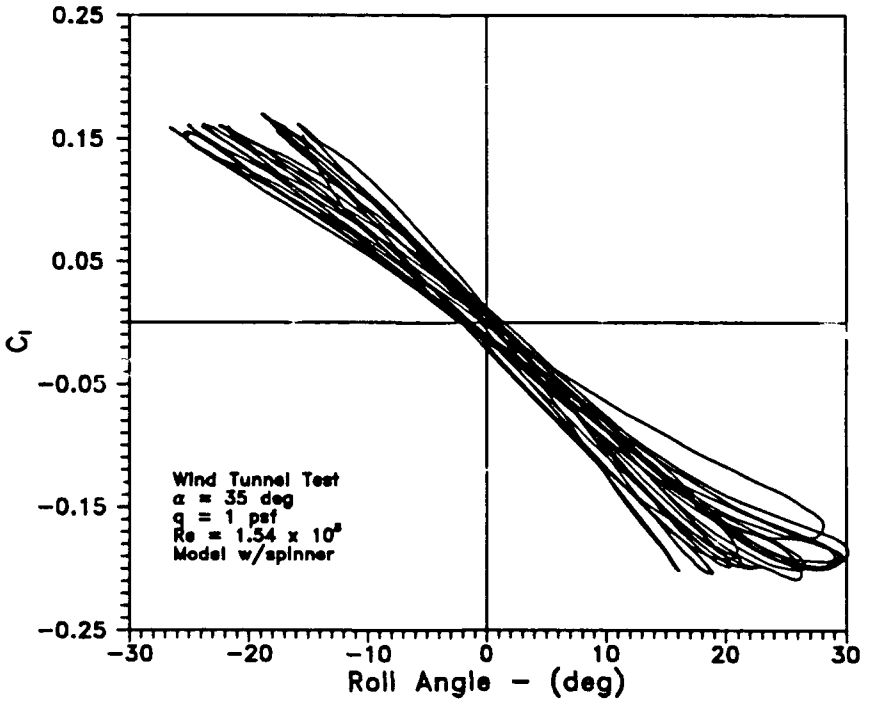

Fig. 47 Rolling moment coefficient of model w/spinner in the wind tunnel.

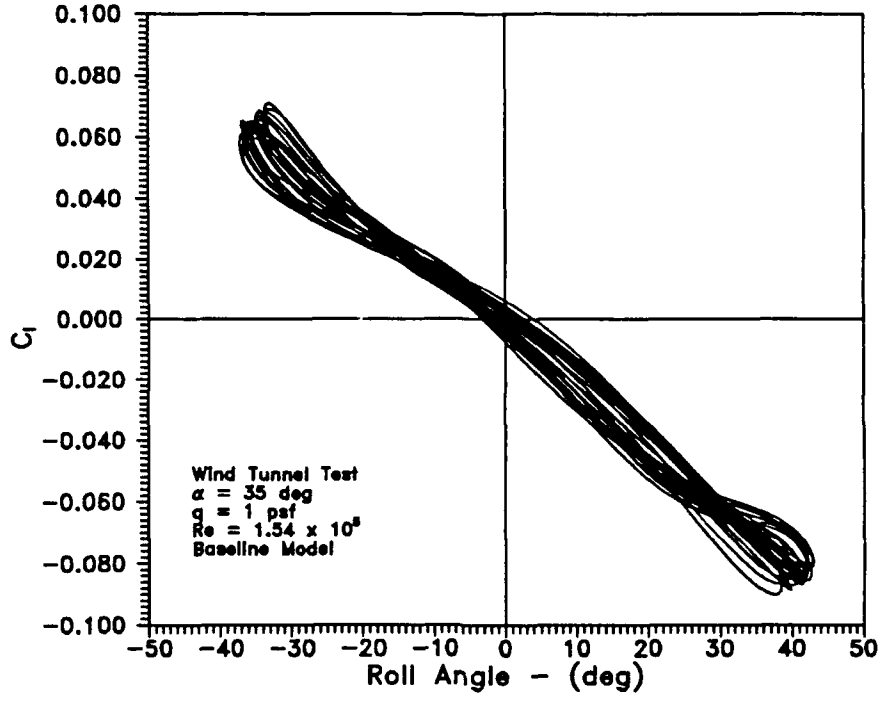

Fig. 48 Rolling moment coefficient of baseline model in the wind tunnel.

resulting in delay of flow separation on one side of the cylinder and an adverse pressure gradient, leading to flow separation on the other. The spinner was evidently behaving like a rotating cylinder during wing rock with vortex asymmetries on the spinner. Additionally, the effect of the spinner on the delta wing's leading edge vortices may have increased the rolling moment coefficient. The spinner was also used in water tunnel testing and again showed an increase in rolling moment coefficient.

As steel disks were added to the model, the motion decreased as expected. Fig. 49 shows the decrease in acceleration as the inertia was added to the model. The slopes of the curves decreased with each disk added. This figure shows the decrease in roll amplitudes as well. The rolling moment coefficients (Fig. 50) also decreased in magnitude. However, as the rolling moment coefficients decreased along with the

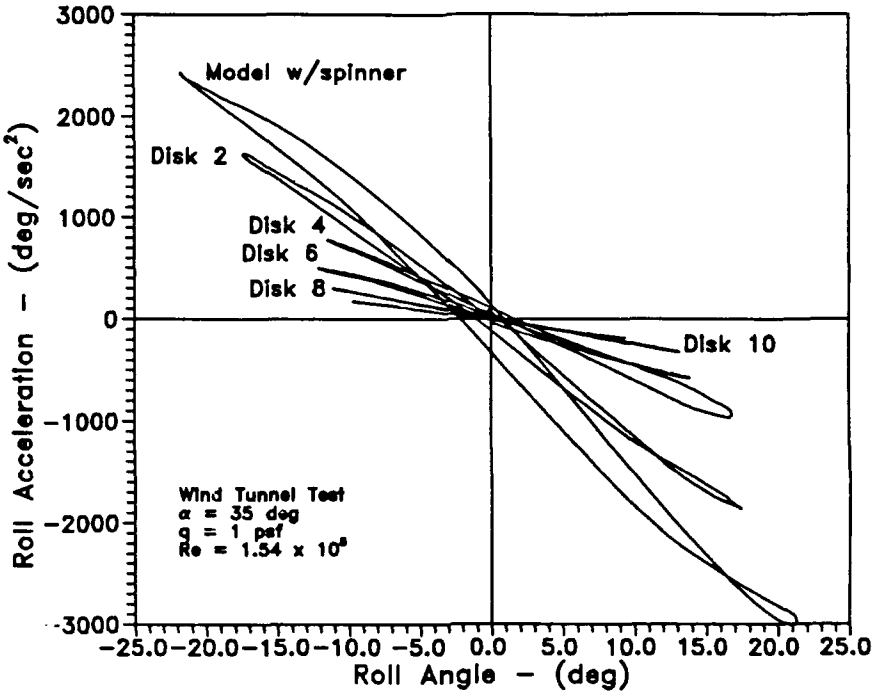

Fig. 49 Roll acceleration versus roll angle with several mass configurations.

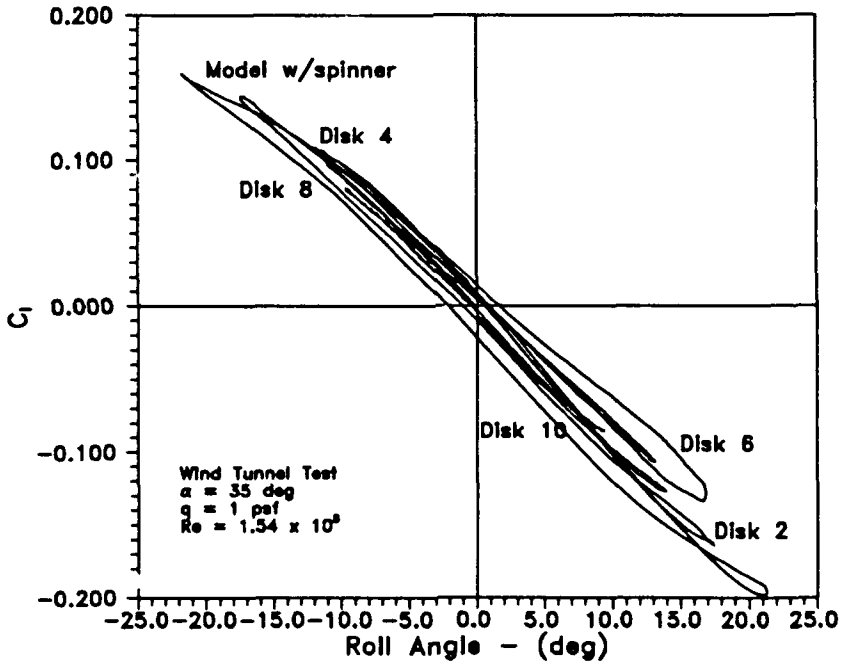

Fig. 50 Rolling moment coefficients versus roll angle for several mass configurations.

roll amplitudes, the slope of these curves remained the same, as expected since flow conditions were not changing. The primary goal of these results was to simulate the added mass of the water being displaced by the wing in the water tunnel.[23] Further comparisons will be made during the water tunnel discussion.

Vortex Trajectory

Reduction of flow visualization data was a tedious and time consuming chore. Frame by frame editing had to be conducted for these data. Video data were collected at the $0.25\bar{c}$, $0.50\bar{c}$, $0.65\bar{c}$, $0.75\bar{c}$, $0.85\bar{c}$, $0.95\bar{c}$ chord stations using a laser light sheet. These data were then reduced using the EV system after testing was completed. The $0.25\bar{c}$ and $0.50\bar{c}$ data were not reducible, because of too much smoke and the closeness of the vortices to the wing. The data presented here are for the latter four chord stations of the baseline model. The figures are in the order of spanwise vortex location versus roll angle, normal vortex location versus roll angle, and spanwise versus normal locations for each chord location. Data have been normalized to the model's semi-span. Roll angles during flow visualization tests had larger magnitudes than the wing rock results presented above. The smoke wand was hand held from above the tunnel test section and placed approximately three feet in front of the model. The wand was constructed with a ½" probe three feet long to port the smoke to the test section. The wand disturbed the airflow enough to affect the flow field over the model.

The spanwise vortex locations for $0.65\bar{c}$ can be seen in Fig. 51. There is a very small hysteresis loop as compared with the normal vortex hysteresis loop (Fig. 52). At a roll angle of -40°, the left vortex was near the centerline of the model and nearly 0.4 semi-span above the wing, while the right vortex was outside the wingtip and over one semispan above it. Considering the position of the vortices

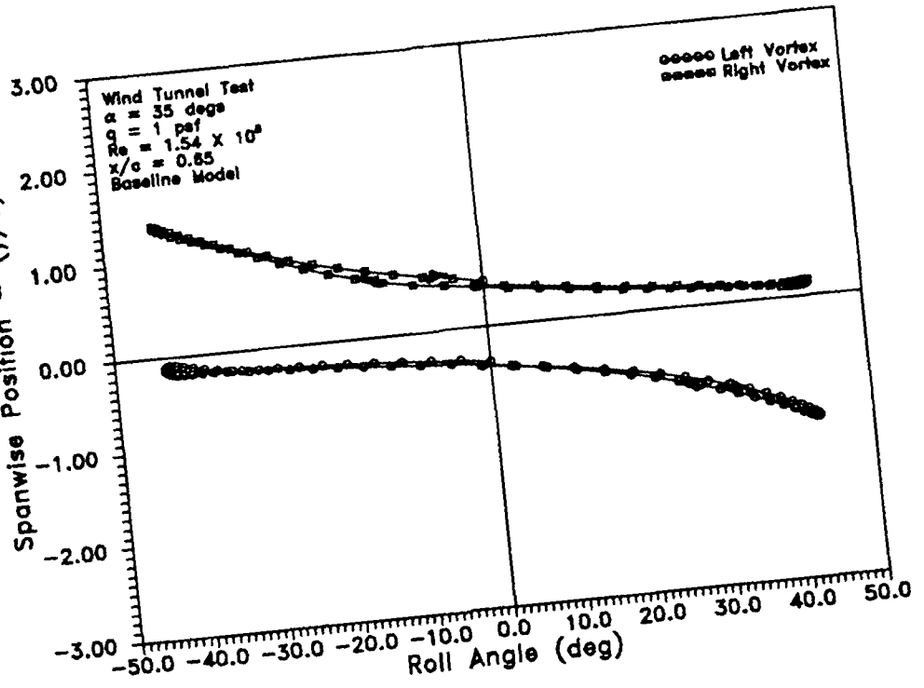

Fig. 51 Wind tunnel spanwise vortex core movement at x/c = 0.65.

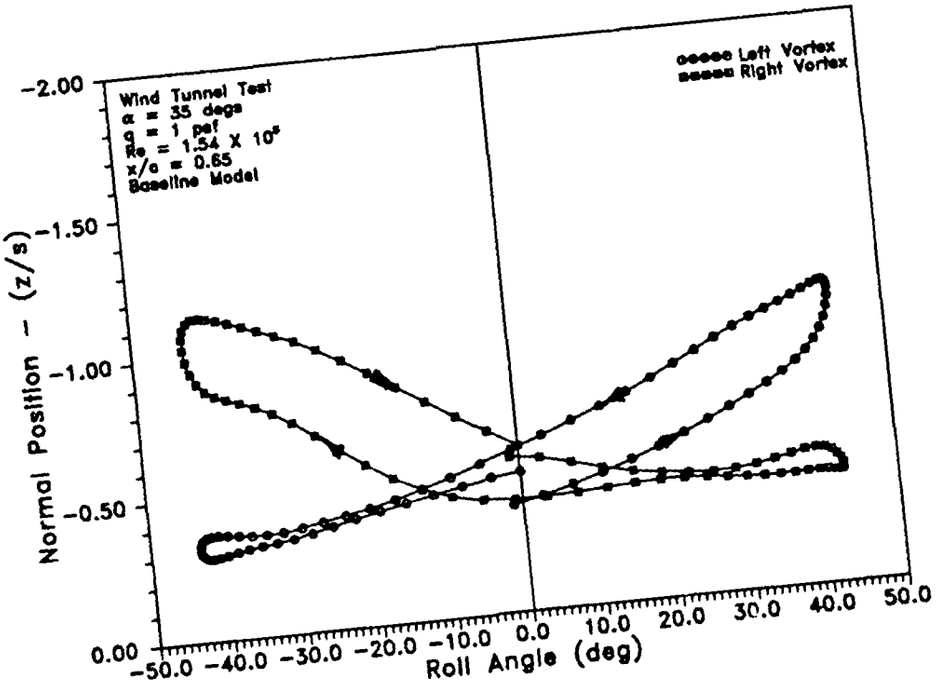

Fig. 52 Normal wind tunnel vortex core movement at x/c = 0.65.

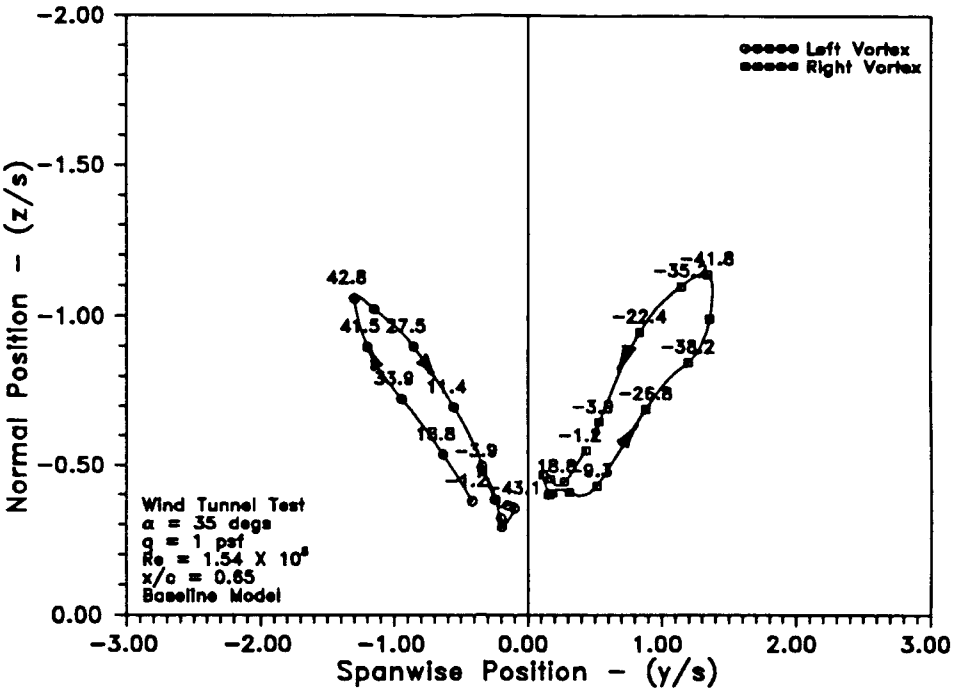

Fig. 53 Wind tunnel normal versus spanwise vortex positions at x/c = 0.65.

only, the left vortex contributed to a restoring (positive) rolling moment to reverse the delta wing's motion and roll it back to the other extreme. As the wing oscillated, the vortices alternately moved in close to the surface and centerline of the wing or slid out and lifted off the wing. The asymmetric liftoff and reattachment of the leading edge vortices have in many papers been considered the driving mechanism of the wing rock motion. Fig. 53 has the frame of reference of looking from the trailing edge of the model towards the apex. The figure shows positions of the vortex core relative to the wing surface. Included in this and the rest of the normal versus spanwise figures are the associated roll angles for each core path.

The further aft that the vortex cores were surveyed, the more evident was the hysteresis in both vortices' spanwise and normal directions. Fig. 54 and Fig. 55

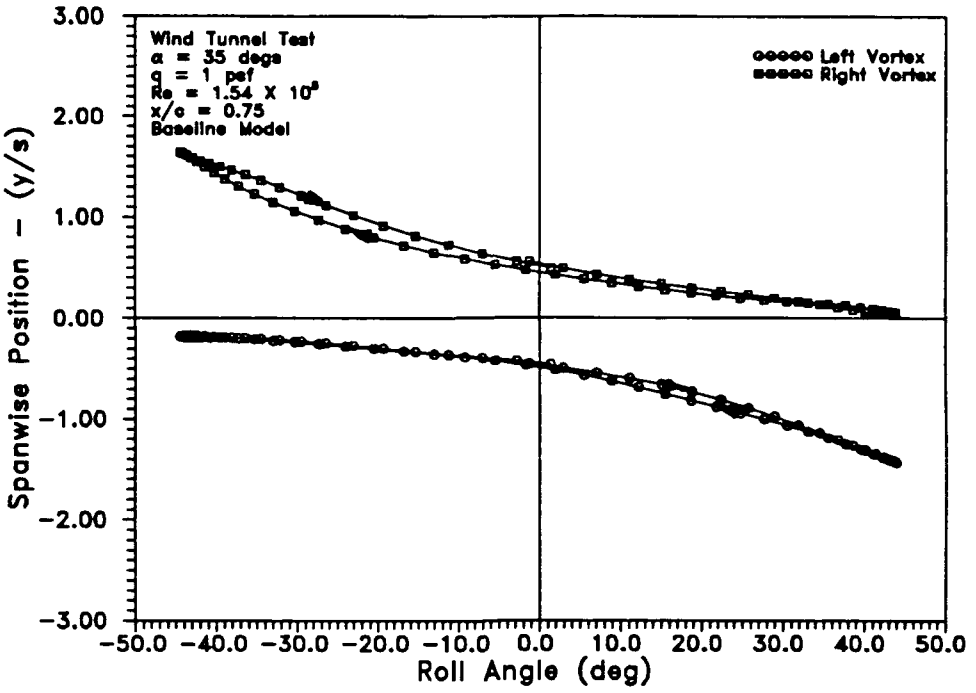

Fig. 54 Wind tunnel spanwise vortex core movement at x/c = 0.75.

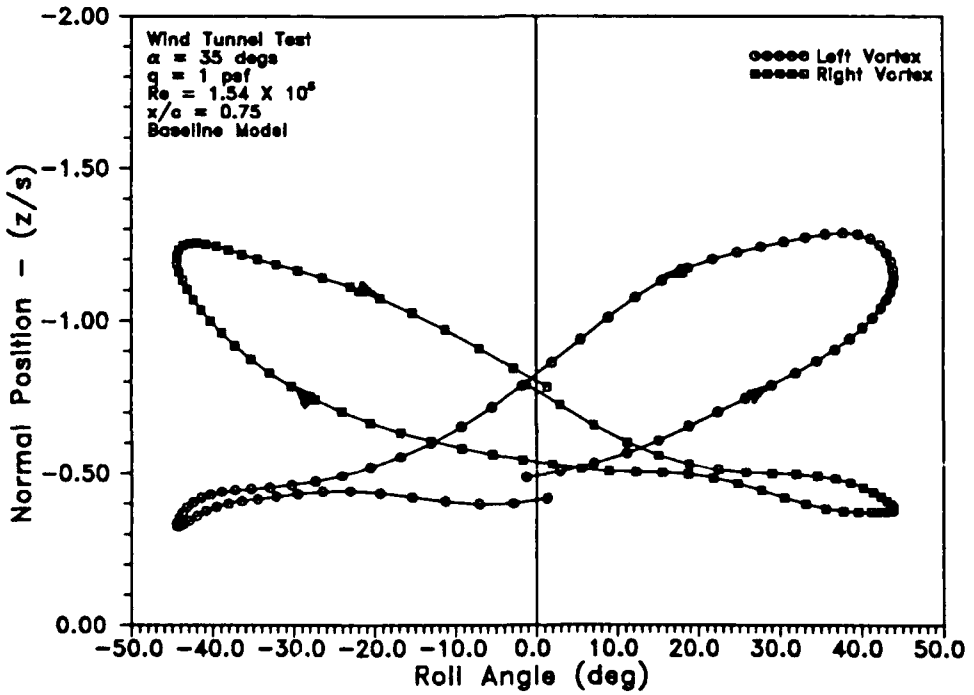

Fig. 55 Normal wind tunnel vortex core movement at x/c = 0.75.

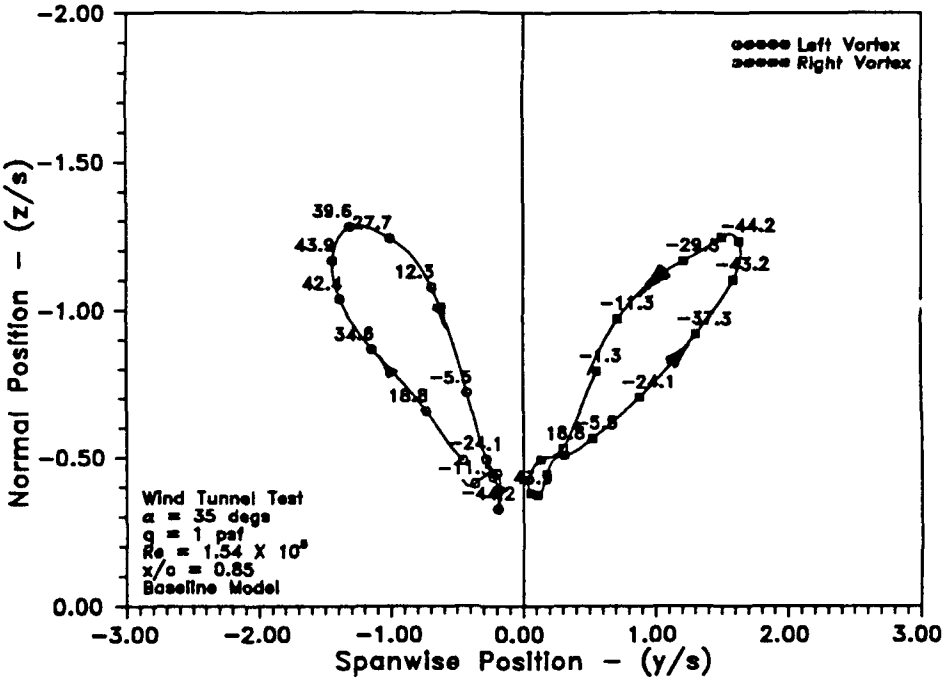

Fig. 56 Wind tunnel normal versus spanwise vortex positions at x/c = 0.75.

show the spanwise and normal vortex paths at $0.75\bar{c}$. The hysteresis was obvious even in the spanwise locations and was more prevalent for the leeward vortex that lifted off the wing. Fig. 56 shows that the paths of the right and left vortex were slightly larger than at the $0.65\bar{c}$ chord location. The loops were also elevated more than at the previous chord station. This difference was expected for the wind tunnel results since the cores appeared as nearly linear paths above the surface of the delta wing. This shape is distinctly different than was observed in the water tunnel.

Vortex burst did occur on the 80° delta wing at α = 35° during wing rock. As the wing rolled, the windward vortex moved closer to the wing and towards the centerline. The windward edge of the delta wing also had a decrease in effective sweep angle, which caused the vortex to burst closer to the apex. The opposite holds

for the leeward vortex and leading edge: leading edge sweep angle was effectively increased, reducing the strength of the vortex. The burst point was further aft. Vortex bursting has a time lag related to the wing motion.[4] During flow visualization runs, vortex burst location was not quantified, but core breakdown resulted in the small black area in the video disappearing momentarily. However, for the most part, the smoke engulfed the model and vortex breakdown was not observed. So, while vortex breakdown occurred, the more turbulent core could still be tracked and quantified for position.

Hysteresis in the spanwise path for $0.85\bar{c}$ became still larger (Fig. 57). The left vortex moved just across the centerline to the right side of the model at the maximum negative roll amplitude. The normal path also displayed larger loops and

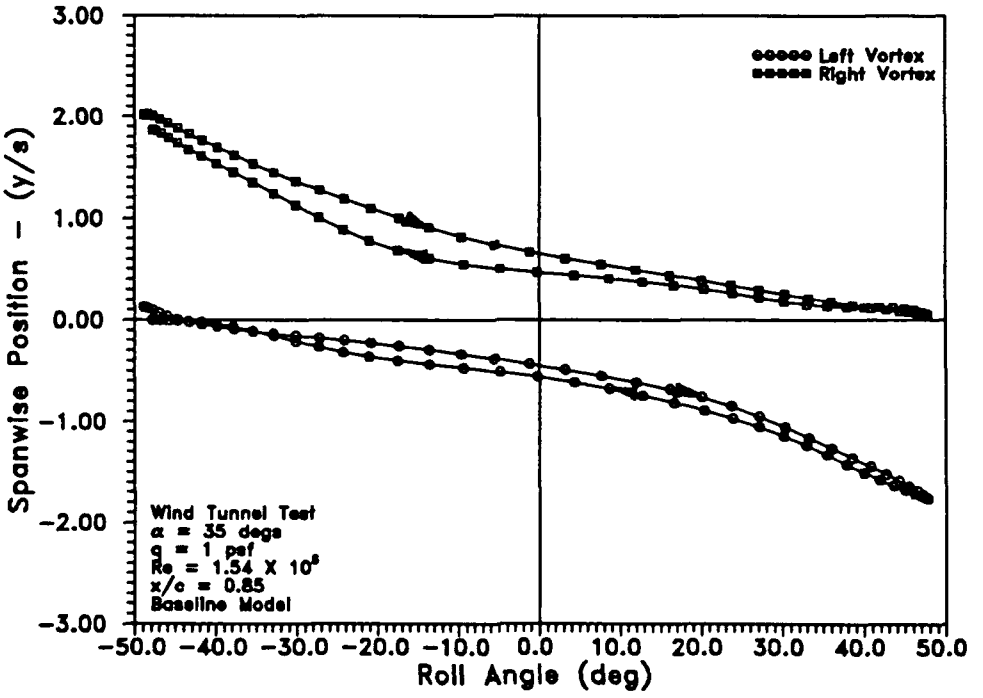

Fig. 57 Wind tunnel spanwise vortex core movement at x/c = 0.85.

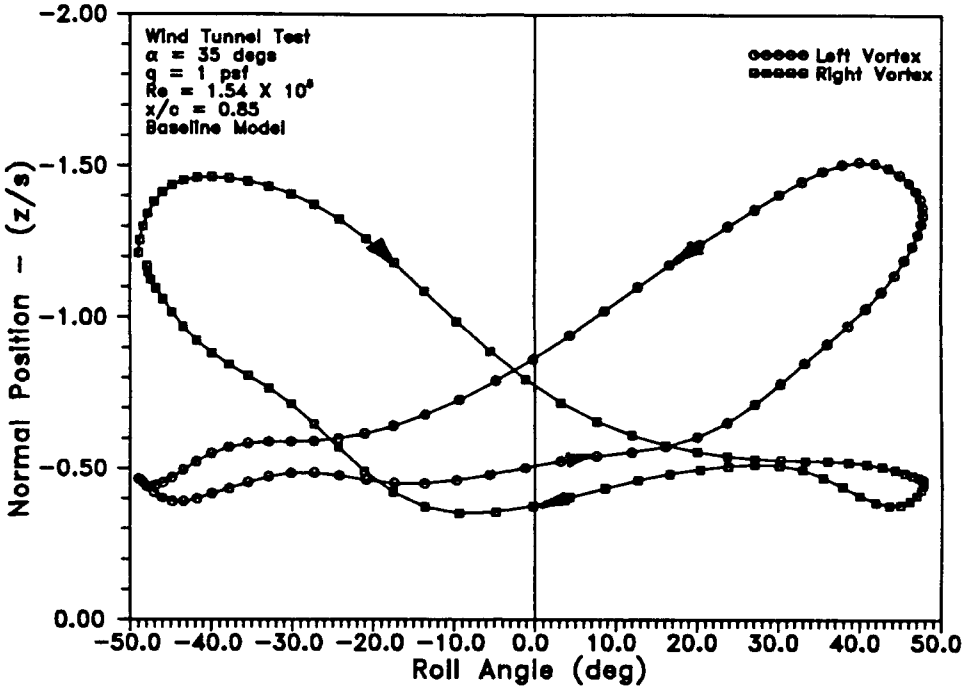

Fig. 58 Normal wind tunnel vortex core movement at x/c = 0.85.

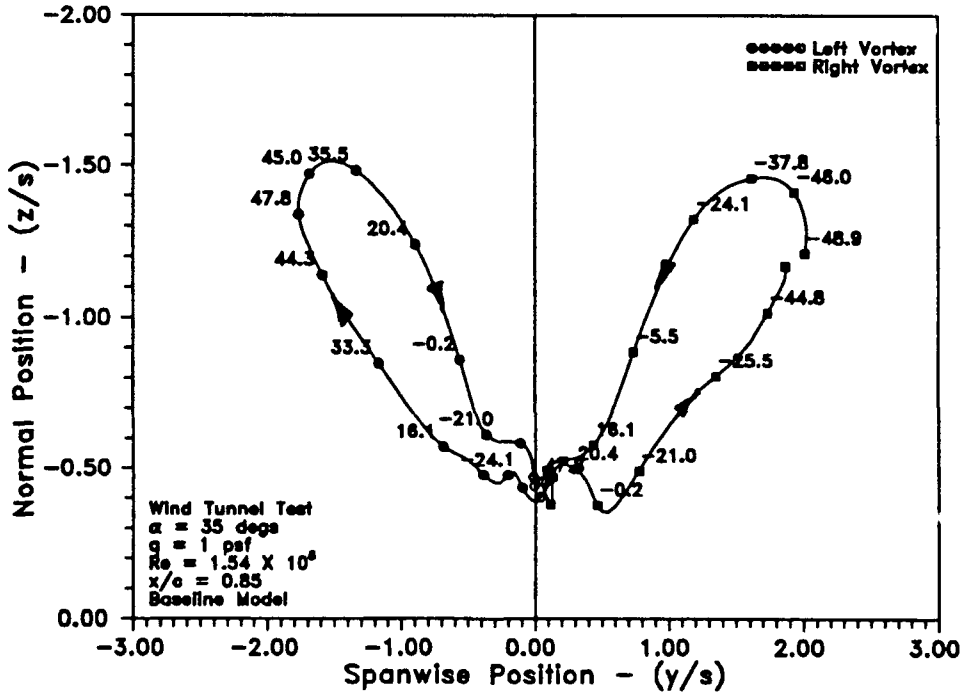

Fig. 59 Wind tunnel normal versus spanwise vortex positions at x/c = 0.85.

higher liftoff at the larger roll angles (Fig. 58). Compared with the two previous spanwise versus normal loops, Fig. 59 shows the crossing of the centerline by the windward vortex at the maximum roll amplitudes. Also from this figure, the windward vortex at the maximum roll amplitude had not reached its maximum normal position. The spanwise vortex position was a maximum at these maximum roll amplitudes.

Arena[4] conducted flow visualization tests on an 80° delta wing at an angle of attack of 30°. The tests were completed at a tunnel Reynolds number of 3.48×10^5 based on the root chord. These experiments were carried out in a similar manner utilizing a laser light sheet and a smoke wand placed in front of the model. The $0.95\bar{c}$ location was investigated during wing rock; Fig. 60 and Fig. 61 compare spanwise results. The hysteresis in Arena's spanwise vortex positions was very slight compared to the current study, perhaps because of the higher Reynolds number (twice that of the current experiment). Fig. 62 and Fig. 63 show vortex normal positions for both experiments. Note that Arena's z coordinate orientation is positive above the wing. Here the hysteresis was much larger than for spanwise positions. While model roll angles were larger than the current investigation, the normalized distance from the upper wing surface was less. Fig. 62 shows that the maximum normal vortex liftoff distance was z/s = -1.9 for the left vortex. The maximum normal vortex position for Arena's experiment was about z/s = 1.2 for the left vortex. Physical differences between each model configuration may explain these differences. Arena's model had a 45° bevel on the lower surface of the leading edge. The current model had a 20° bevel on the upper surface of the leading edge. The 5° difference in angles of attack is also a significant factor. The last pair of figures, Fig. 64 and Fig. 65, compare the cross-section of the flowfield at x/c = 0.95. The spanwise positions are similar in magnitude, about y/s = 2.0. From Arena's data, the normal vortex positions closest

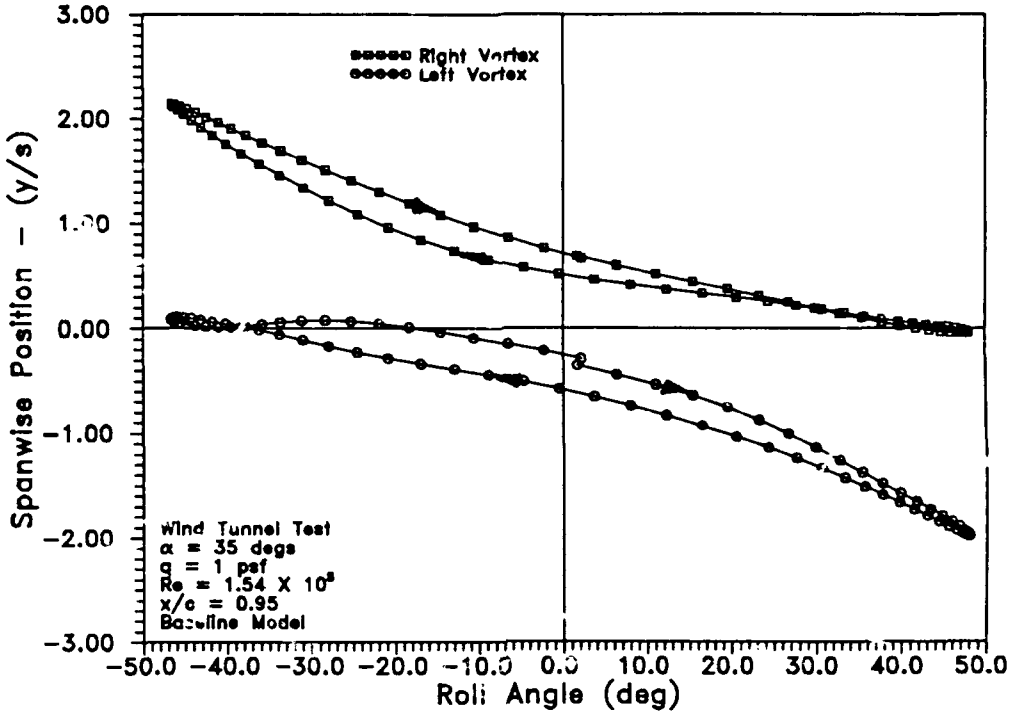

Fig. 60 Current study of spanwise vortex positions at x/c = 0.95.

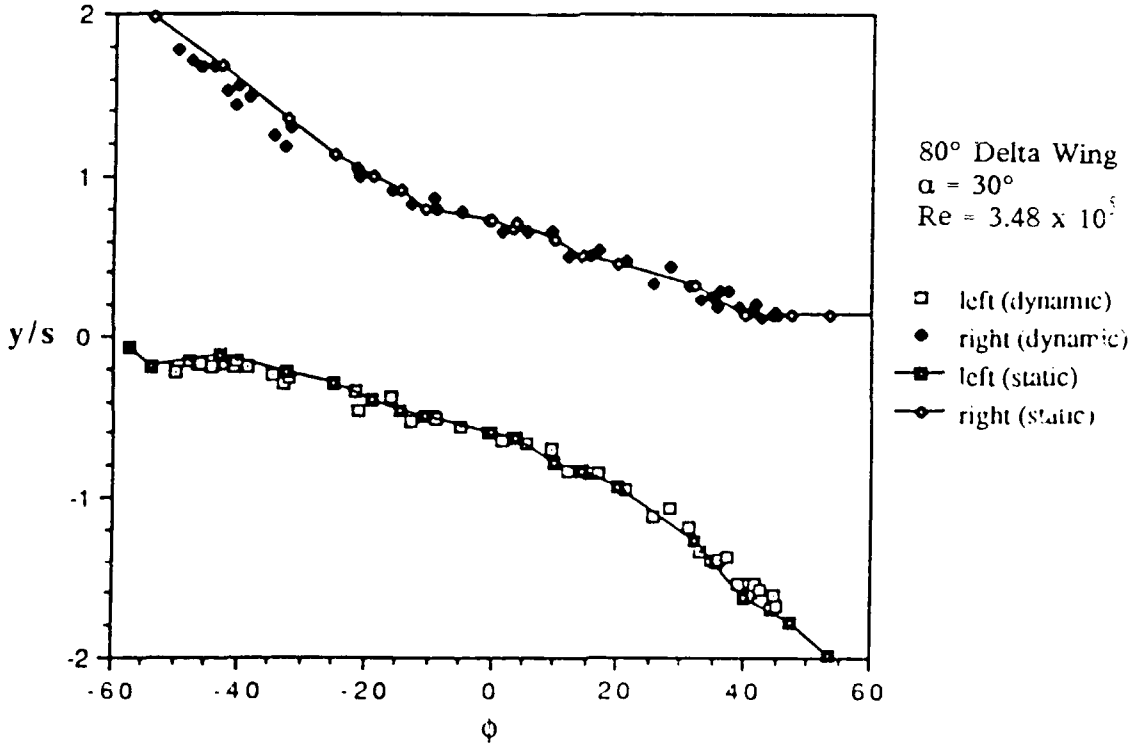

Fig. 61 Previous study of spanwise vortex position at x/c = 0.95.[4]

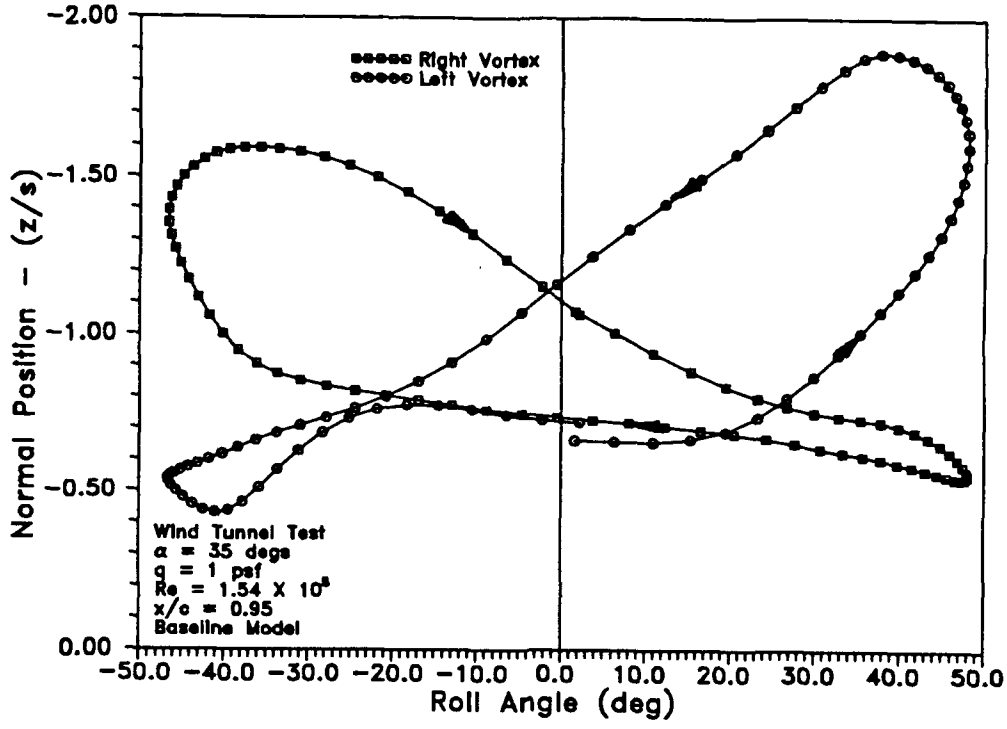

Fig. 62 Current study of normal vortex positions at x/c = 0.95.

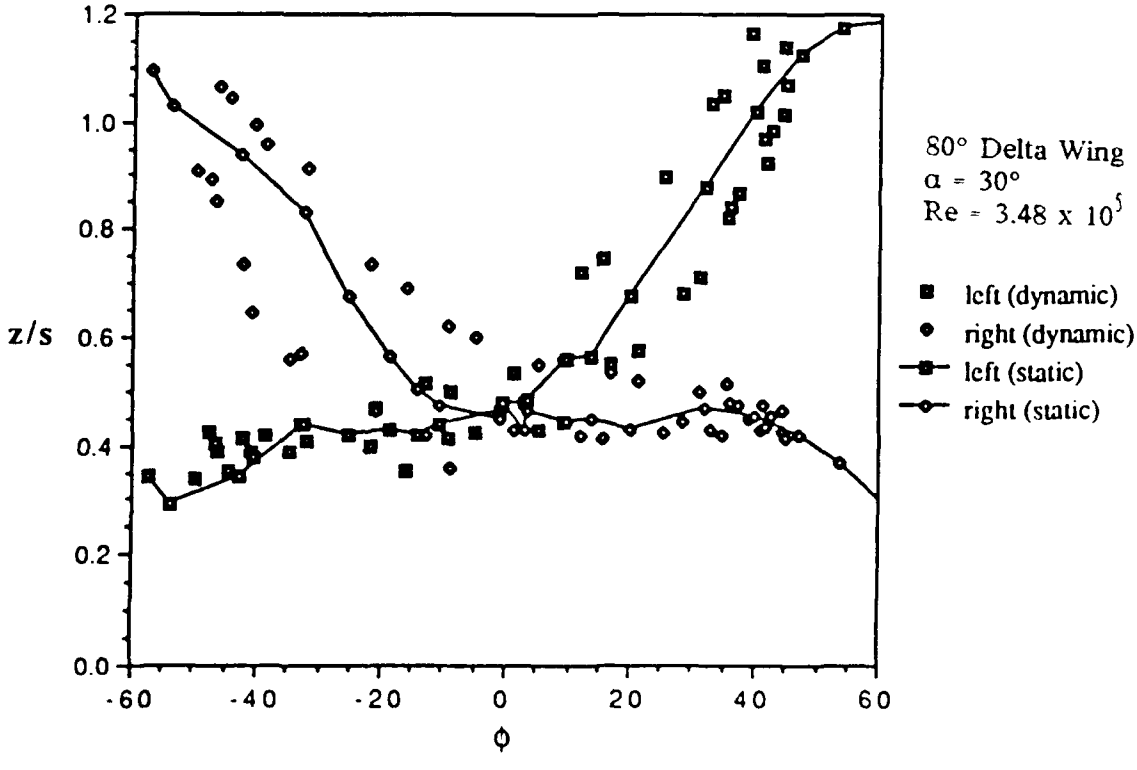

Fig. 63 Previous study of normal vortex positions at x/c = 0.95.[4]

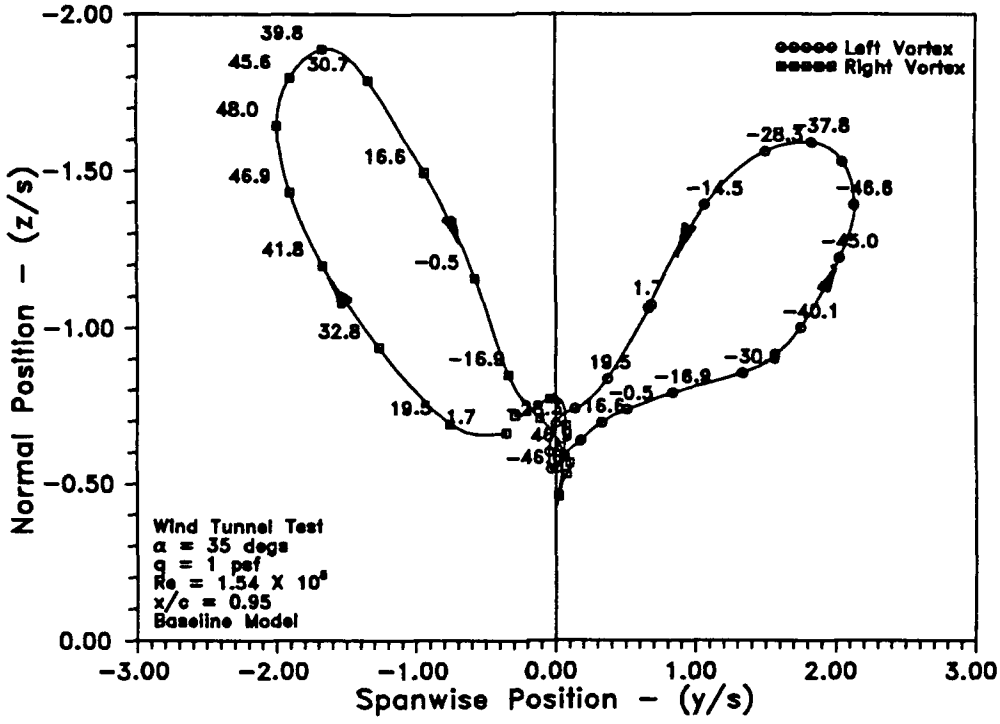

Fig. 64 Wind tunnel vortex core movement at x/c = 0.95.

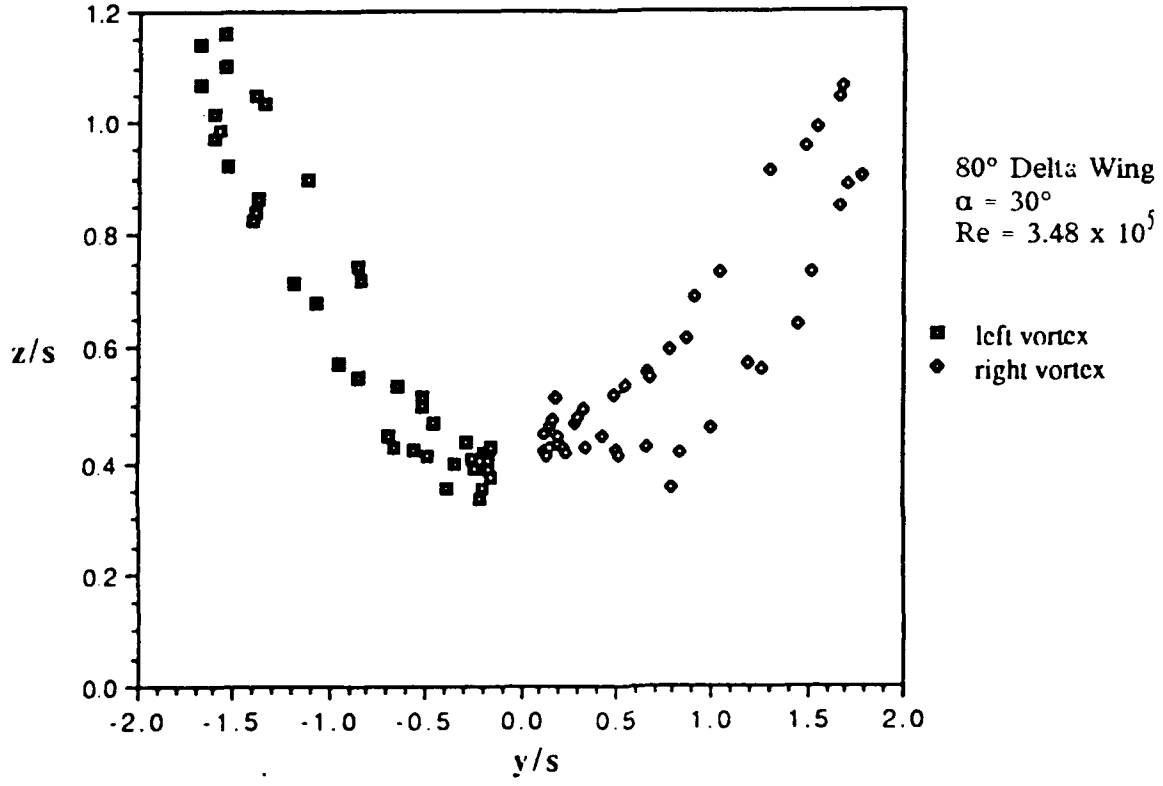

Fig. 65 Previous study of vortex core movements at x/c = 0.95.[4]

to the wing had magnitudes of z/s = 0.35. The current study's smallest normal vortex positions were z/s = -0.45.

Summary of Wind Tunnel Data

Both motion and flow visualization data have been presented for an 80° delta wing undergoing wing rock. The results were similar to past investigations. The model w/spinner results revealed aerodynamic interference which actually increased the rolling moment as compared to baseline data. The flow visualization experiments included flow field surveys at four different chord locations. These results characterized the leeward vortex lift-off and reattachment causing the wing rock motion. In addition, curvature of the vortices was not visible in the current data.

Water Tunnel Test Results

Water tunnel tests were conducted tc compare with Morris' results[3] presented and further study the phenomena. Morris' model was tested in a smaller test section. In addition, the current model's support rod was different and the apex had been modified slightly. Primary goals were to quantify the dynamic motion of the model and the flow field during wing rock. Specifically, the hysteresis direction of the rolling moment versus roll angle curve was to be addressed in conjunction with the positions of the leading edge vortices. In addition, the model was tested with the added mass attachment connected to examine the aerodynamic effects of the spinner on the rolling moment of the model. A summary of the tests conducted is presented below.

Summary of Test Methods

The delta wing model was tested at tunnel speeds of 6, 10, 12, and 15 ips. The upper tunnel speed limit was established because of model vibrations at higher velocities. Wing rock motion and flow visualization investigations were completed for both the baseline model and the model w/spinner. The data were collected using three cameras at 60 frames per second.

General Observations

The water tunnel, an excellent flow visualization tool, provided a suitable environment to track the vortical flow field over the entire wing. The wing rock frequency at the 6 ips tunnel speed was almost an order of magnitude smaller than that obtained in the wind tunnel. Curvature of the vortices was easily observed and confirmed that convective time lags were present during the motion. Another interesting observation was the vortex breakdown over the wing. From previous wind tunnel results[4], the burst point of a vortex moved continuously both forward and aft during a limit cycle. During water tunnel tests, the vortex breakdown acted differently.

First, motion of the right vortex during a wing rock cycle will be discussed; left vortex motion was the same, merely opposite in roll angle. The initial condition placed the wing in a positive (right) bank with it rolling to the right also. The right or leeward vortex retained its tight structure until slightly before the maximum roll amplitude was reached. This vortex appeared to instantaneously burst at about the $0.30\bar{c}$ location, and left the downstream structure intact. As the wing rolled to the maximum roll angle and then in the opposite direction or to the left, the burst point moved aft toward the trailing edge. As the wing continued to roll through the zero roll angle and towards the maximum negative roll angle, the movement of the right

vortex burst point slowed. The burst area, though, continued to become larger downstream. As the wing began to roll through the maximum negative roll angle, the left vortex burst and both burst points moved aft. The wing then rolled to the right in the original direction and the right burst point moved past the trailing edge. Again, the total right vortex structure was intact prior to vortex breakdown. This phenomena was studied during the flow visualization tests.

Model Motion

The fully developed wing rock will be discussed for the baseline model at four different tunnel speeds. The buildup and decay of these motions will be presented for the baseline model at only one tunnel speed. And finally, the wing rock motion of the model w/spinner configuration will be examined.

A time history of wing rock for a flow rate of 6 ips is shown in Fig. 66. The roll angle data have been smoothed using the Tukey window smoothing algorithm within EV. This algorithm was used to remove the high frequency noise before differencing these data. The positive roll acceleration increased after the wing rolled through the maximum negative roll amplitude. This result was similar to Morris'[3] data during water tunnel tests. Table 5 is a comparison of the motion parameters between the two studies. The same initial flow conditions were used for both tests, however, Morris' runs were completed in a smaller test section (12" x 15" x 72"). The frequency of the motion was very similar, but there was a 9° difference in the average roll magnitudes.

Difference in inertia, because of the lengthened support rod, may have contributed to the roll angle disparity. The setup could have been a factor as well. Angle of attack and sideslip measurements were made with a rule relative to the tunnel walls. A difference in angle of attack would affect the maximum roll

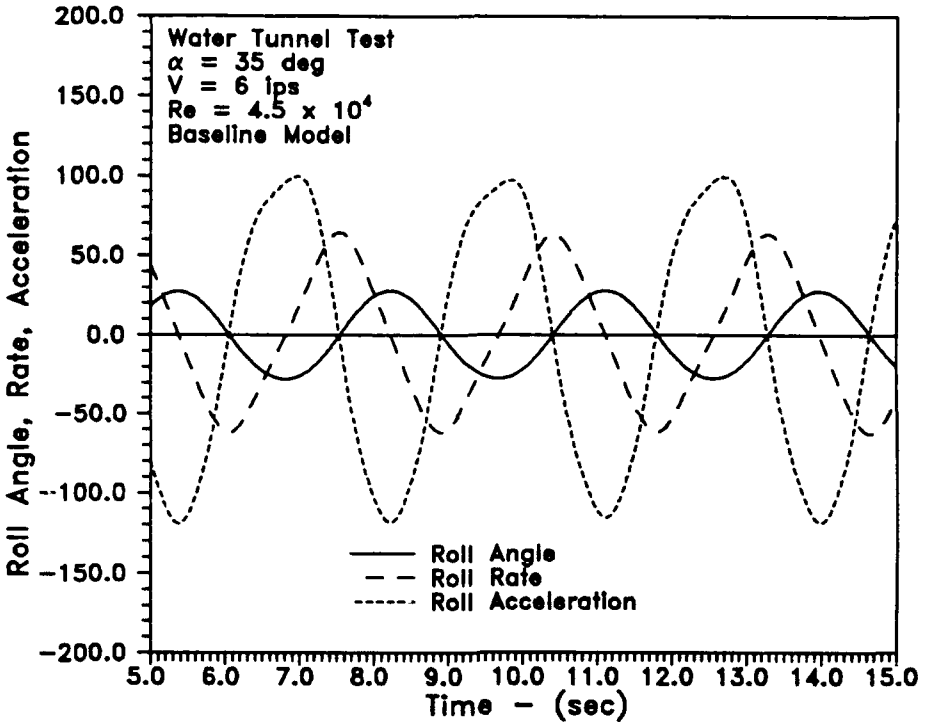

Fig. 66 Wing rock time series at V_∞ = 6 ips.

Table 5 Comparison of Motion Parameters at V_∞ = 6 ips.

Studies	Average Maximum Roll Amplitude (deg)	Average Period (sec)	Average Frequency (rad/sec)	Reduced Frequency
Current	27.7	2.85	2.21	0.648
Morris	36.6	2.86	2.20	0.645

amplitudes, while a difference in sideslip angle would reflect as an offset for roll angles. In addition, differences in the model's apex, as mentioned earlier, would also affect the leading edge vortices over the wing.

Fig. 67 shows the phase plot for the system. Table 6 compares the roll results from the two investigations. Fig. 68 is the roll acceleration versus roll angle for one cycle. The hysteresis at the positive roll angles was smaller than at negative ones, a characteristic of roll angles during other runs as well. The direction of the hysteresis loop was again contrary to that seen in wind tunnel experiments. Both outside loops moved in a clockwise sense, while the interior loop moved in a counter clockwise sense. The rolling moment coefficient is shown in Fig. 69. The differences in the moments may be due to the added inertia, the apex modification, and the size of the tunnel test sections. Both experiments computed the inertia based on model geometry and material.

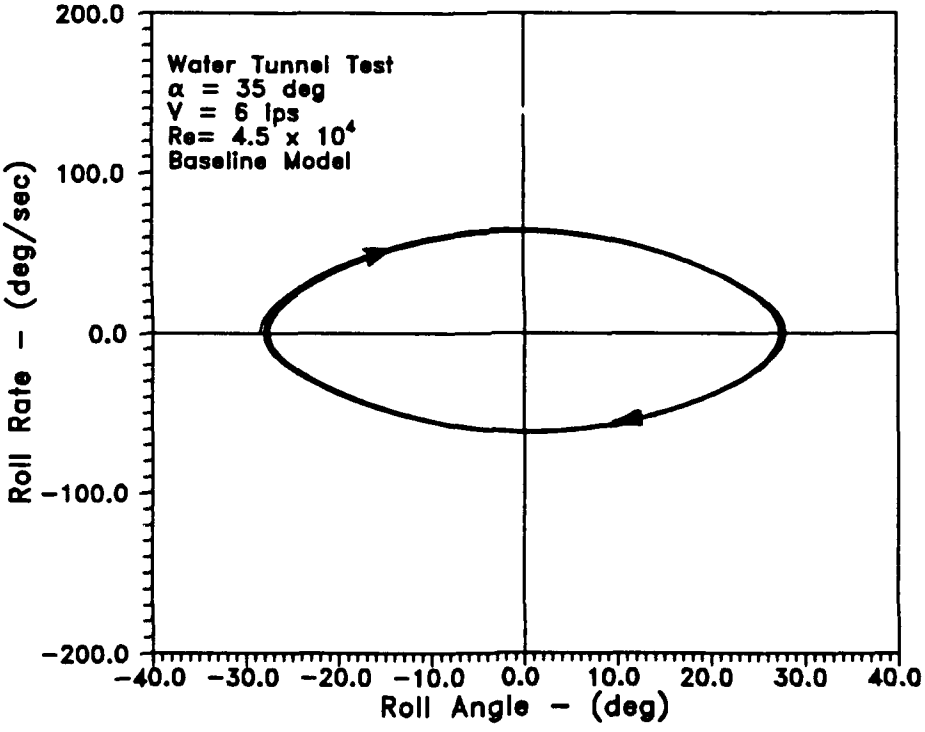

Fig. 67 Wing rock phase portrait at V_∞ = 6 ips.

Table 6 Comparison of Roll Parameters at V_∞ = 6 ips.

Studies	Roll Rate (deg/sec)	Roll Acceleration (deg/sec^2)	Rolling Moment Coefficient
Current	65	120	0.0047
Morris	81	161	0.0085

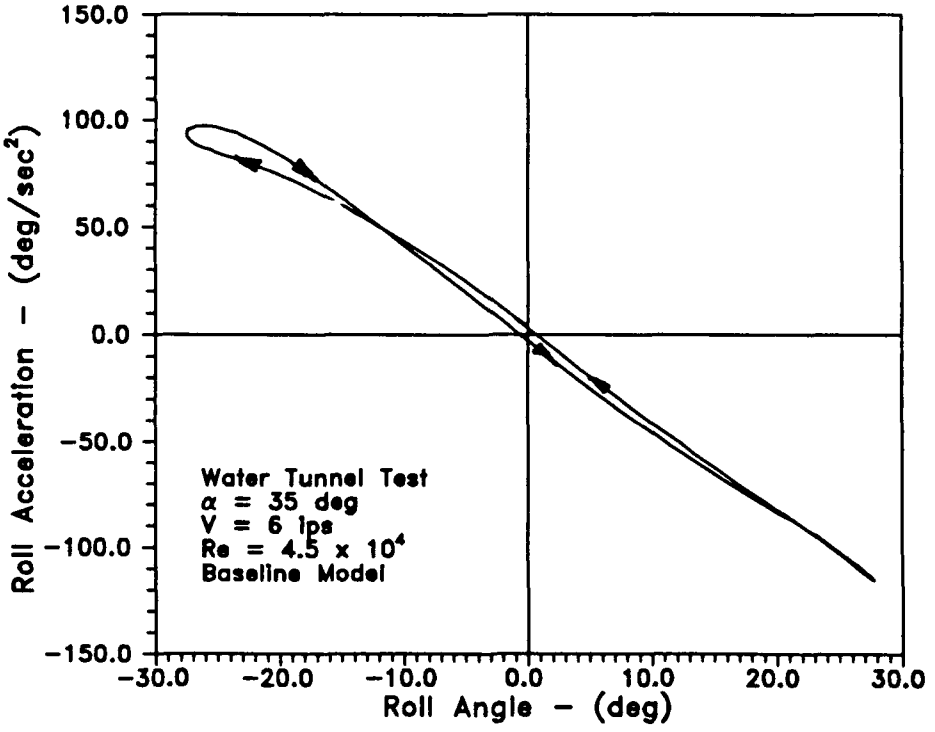

Fig. 68 Roll acceleration versus roll angle at V_∞ = 6 ips.

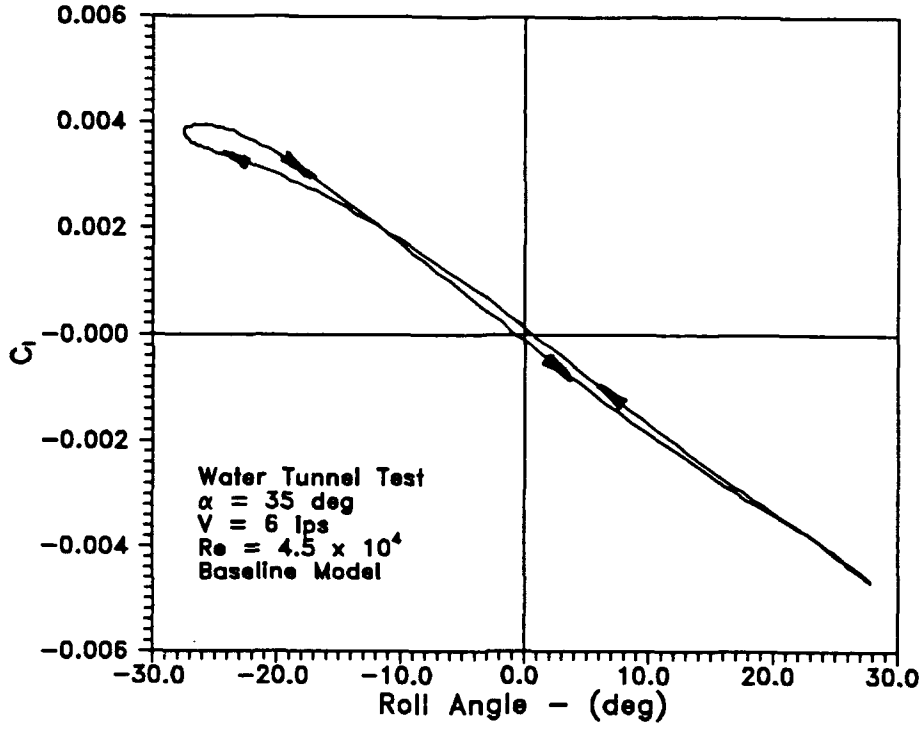

Fig. 69 Rolling moment coefficient versus roll angle at V_∞ = 6 ips.

The next set of runs were made at a tunnel speed of V_∞ = 10 ips, Re = 7.5 x 10^4. Fig. 70 shows the time history of the motion. Table 7 is a comparison between the motion parameters. There is a little over 1% difference in frequency between these two data sets.

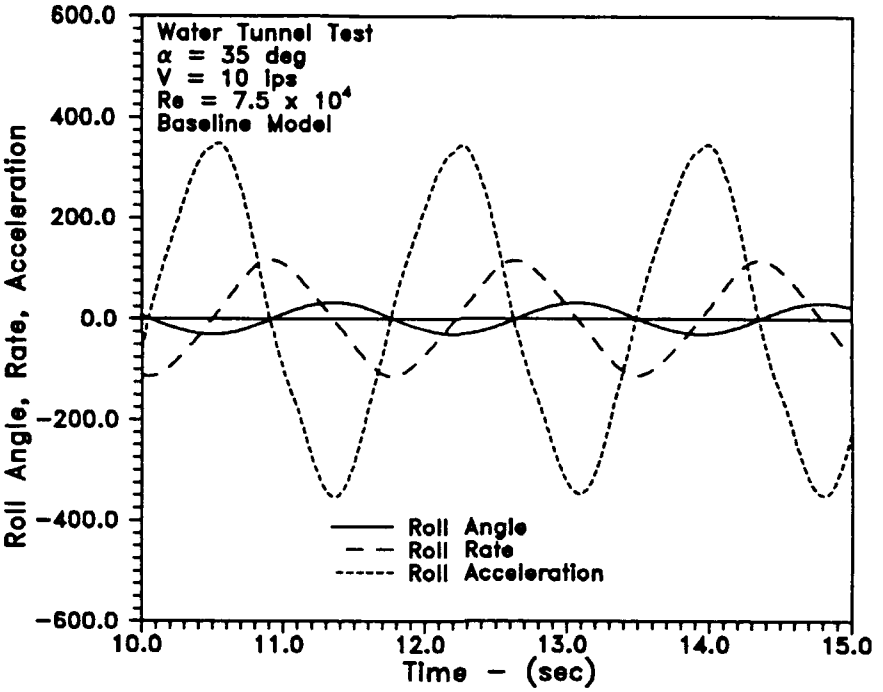

Fig. 70 Wing rock time series at V_∞ = 10 ips.

Table 7 Comparison of Motion Parameters at V_∞ = 10 ips.

Studies	Average Maximum Roll Amplitude (deg)	Average Period (sec)	Average Frequency (rad/sec)	Reduced Frequency
Current	31.0	1.71	3.68	0.650
Morris	36.7	1.73	3.64	0.642

Fig. 71 is the phase portrait for the system. Table 8 contains the roll parameters extracted from the two studies. Fig. 72 is the roll acceleration versus roll angle curve. The lower loop is slightly large than the 6 ips data. The

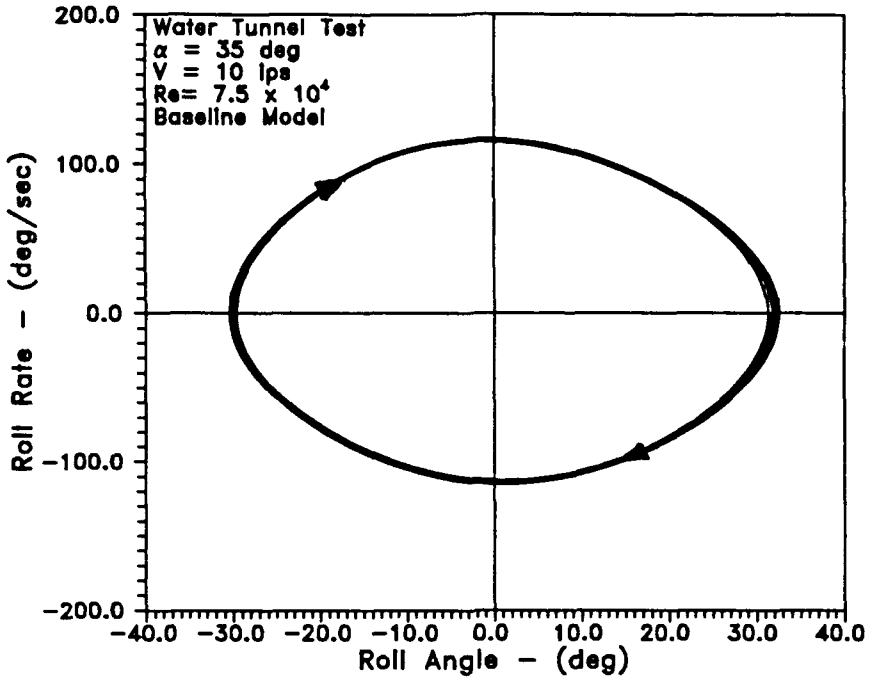

Fig. 71 Wing rock phase portrait at V_∞ = 10 ips.

hysteresis is in the same direction as the previous test. The rolling moment coefficient curve is shown in Fig. 73.

Table 8 Comparison of Roll Parameters at V_∞ = 10 ips.

Studies	Roll Rate (deg/sec)	Roll Acceleration (deg/sec^2)	Rolling Moment Coefficient
Current	117	350	0.0052
Morris	138	451	0.0085

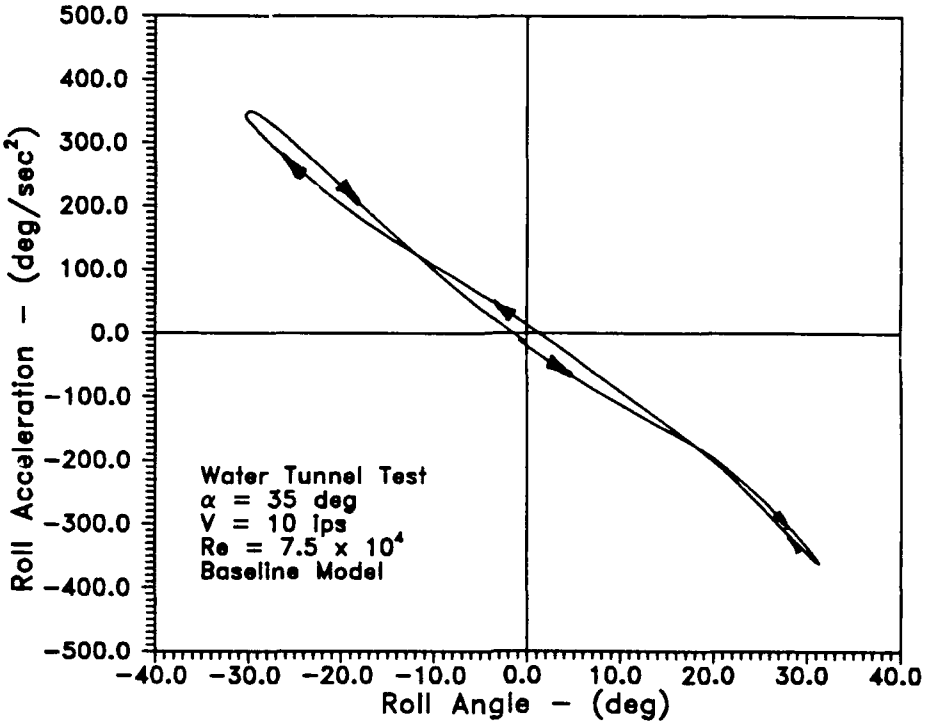

Fig. 72 Roll acceleration histogram at V_∞ = 10 ips.

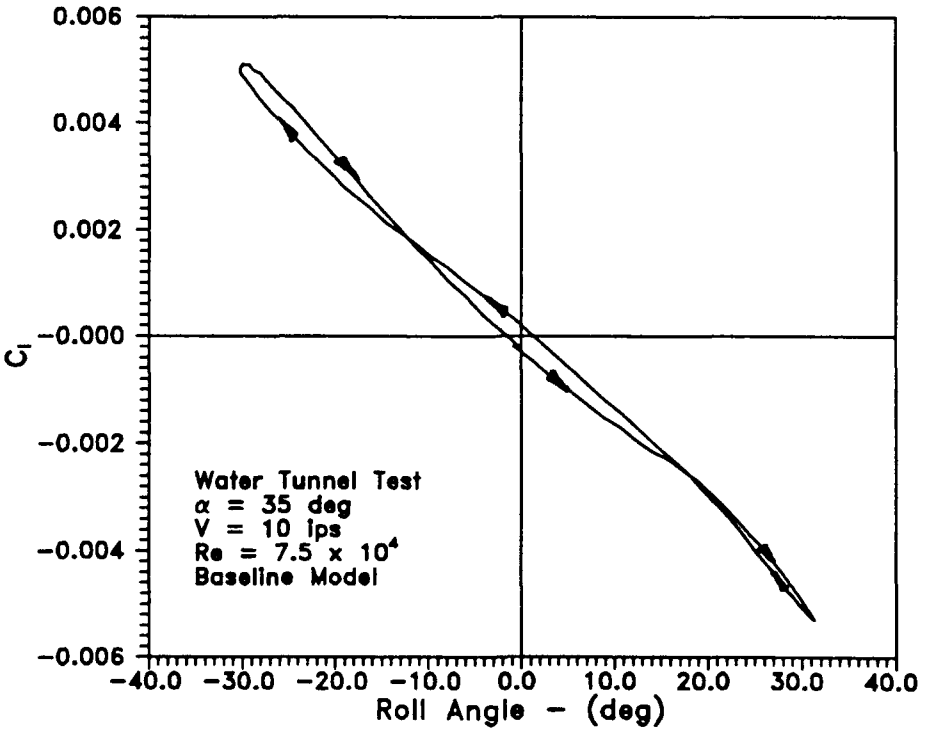

Fig. 73 Rolling moment coefficient histogram at V_∞ = 10 ips.

Table 9 Summary of Motion Parameters for Baseline Model

Speed (ips)	ϕ (deg)	$\dot{\phi}$ (deg/sec)	$\ddot{\phi}$ (deg/sec^2)	C_t	Period (sec)	ω (rad/sec)	k
6	27.7	65	110	0.0047	2.849	2.205	0.648
10	31.0	117	350	0.0052	1.706	3.683	0.650
12	31.3	142	525	0.0055	1.418	4.431	0.651
15	30.1	166	780	0.0049	1.168	5.379	0.632

Note: **All data presented are averaged values.**

Table 9 is a tabulated summary of the above results and includes 12 and 15 ips data. While the roll acceleration increased in magnitude, the rolling moment coefficient was relatively insensitive to the freestream velocities investigated.

Wing rock buildup data will now be presented. Data sets were at V_∞ = 15 ips corresponding to a Reynolds number of 1.125 x 10^5. Fig. 74 shows the phase portrait buildup to an established limit cycle, achieved in less than three oscillations. This same trajectory segment is shown in Fig. 75 with roll acceleration plotted versus roll rate.

A series of cycles during buildup were included in Fig. 76. The first cycle during buildup had a loop that traveled in the clockwise sense, indicating that energy was being pumped into the system. There was also a very slight crossover on the lower branch of this curve. In Fig. 76b, the curve continued to buildup in the

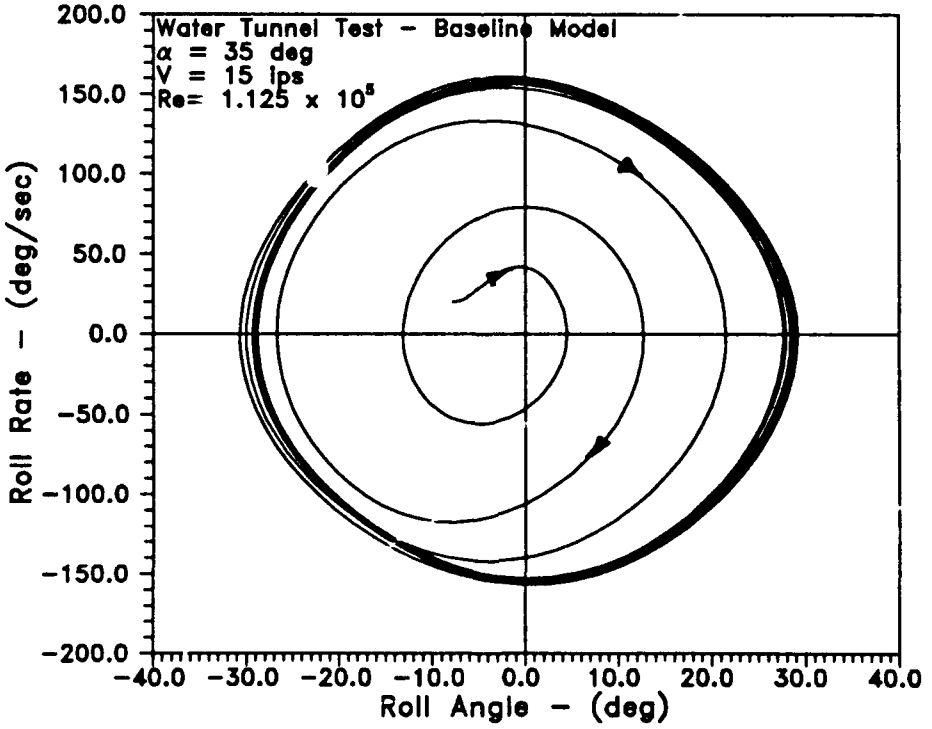

Fig. 74 Wing rock buildup phase portrait at V_∞ = 15 ips.

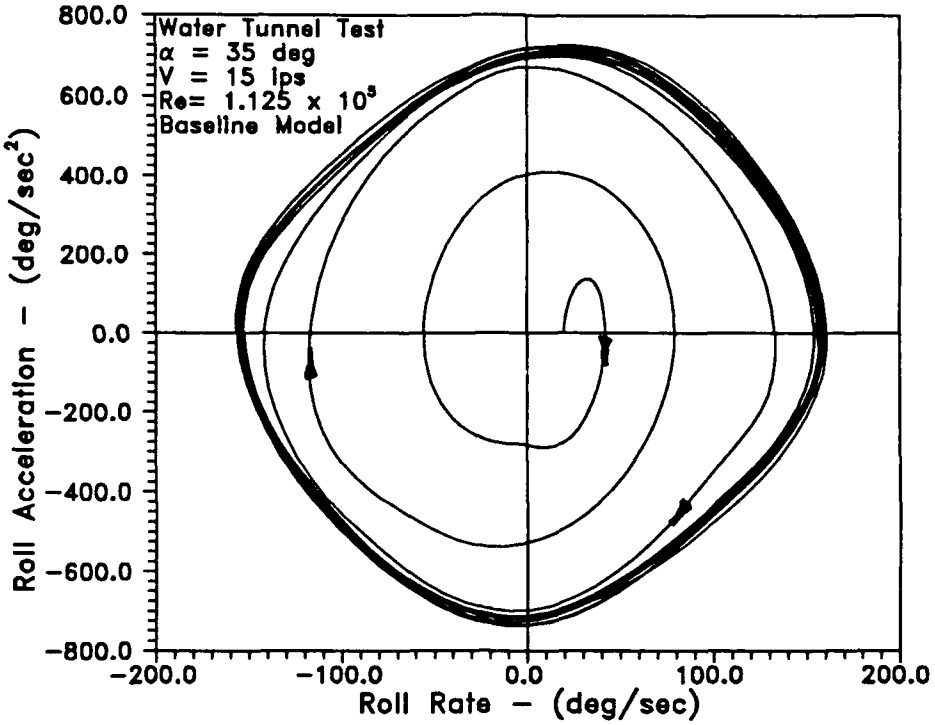

Fig. 75 Buildup of roll acceleration versus roll rate at V_∞ = 15 ips.

clockwise sense. No crossover was observed in this cycle. However, the loci after the local maximum negative roll angle, shifted downward and passed the origin on the right side. The next figure shows that a crossover occurred in the lower branch forming a large clockwise loop. The upper branch had no crossover and still traveled in the clockwise direction. In Fig. 76d, the curve began to look more like the typical curves seen before. The hysteresis loop traveled in the opposite direction of the wind tunnel data with the outer loops going clockwise and the inner loop counter-clockwise. Fig. 76e is a roll acceleration versus roll angle curve of the established limit cycle.

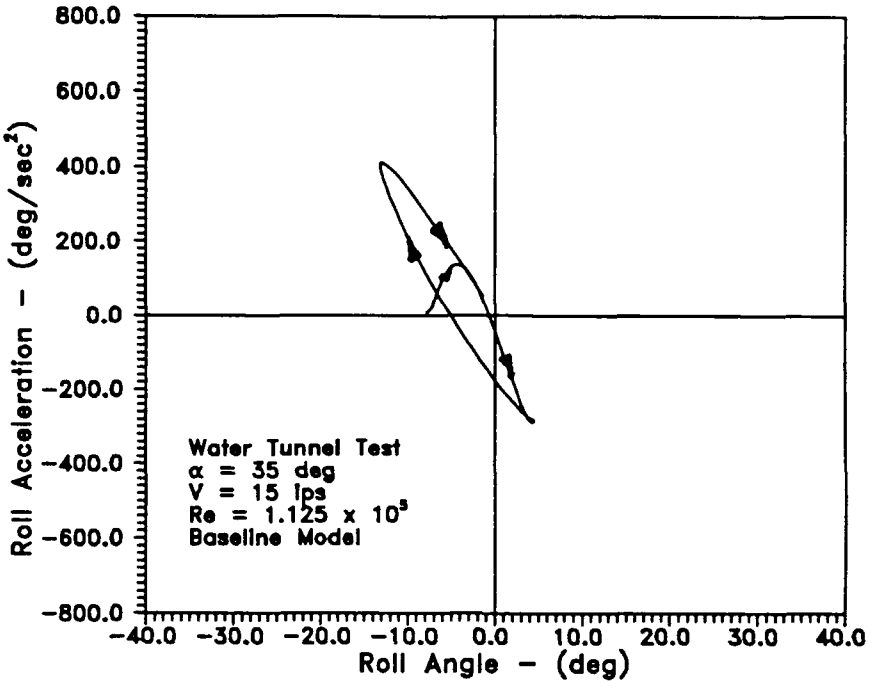

a)

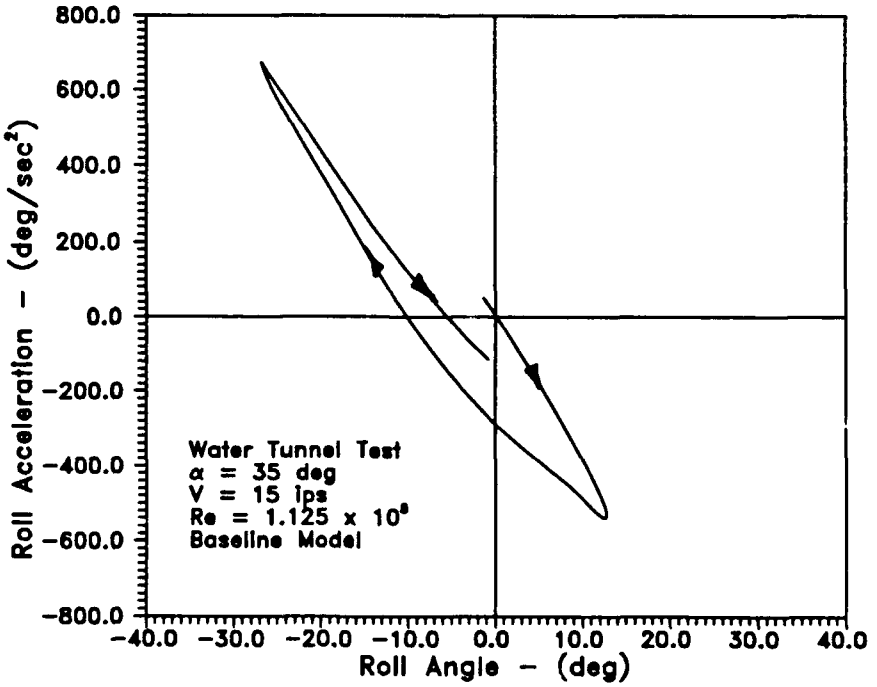

b)

Fig. 76 History of roll acceleration buildup at V_∞ = 15 ips.

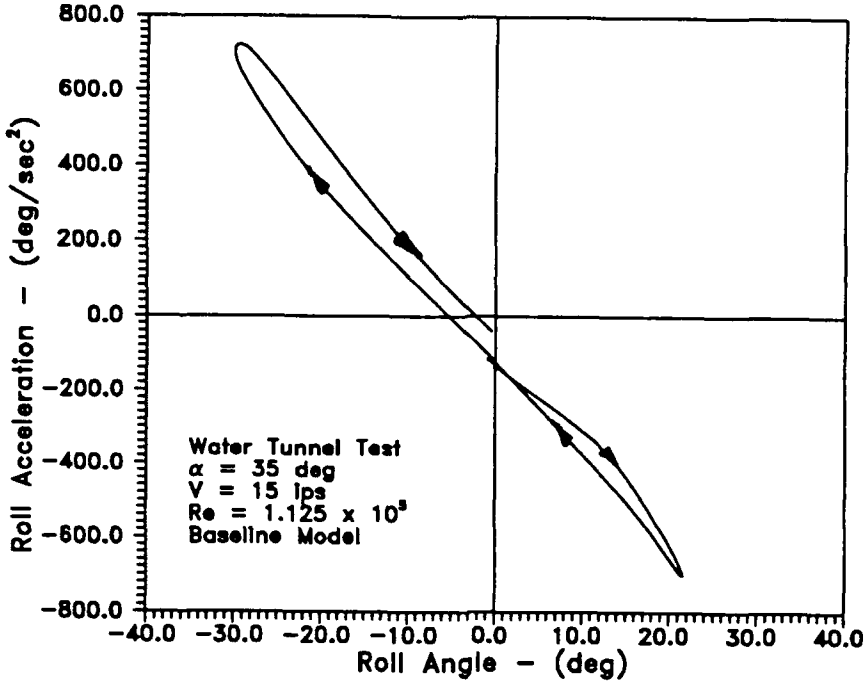

c)

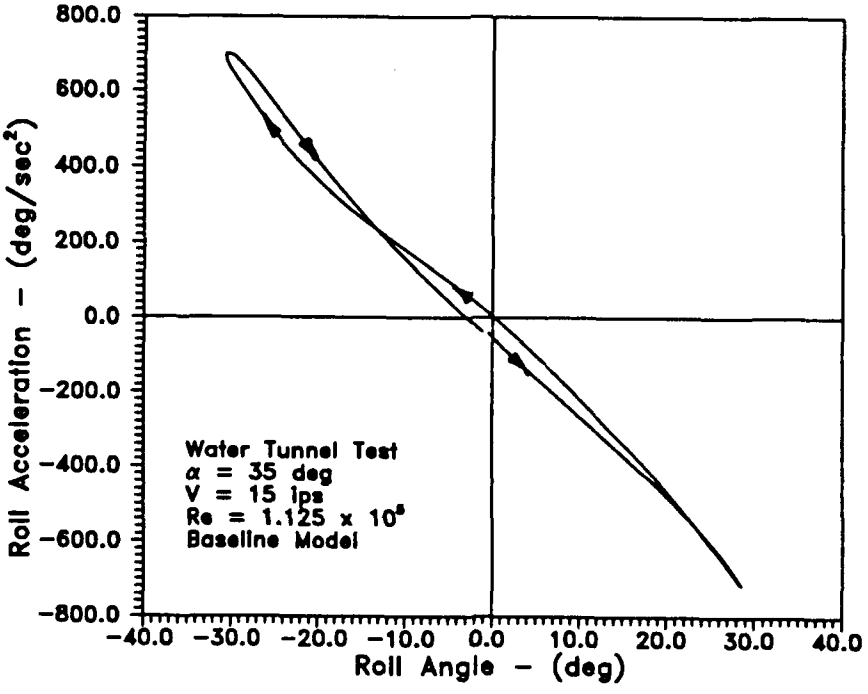

d)

Fig. 76 (continued).

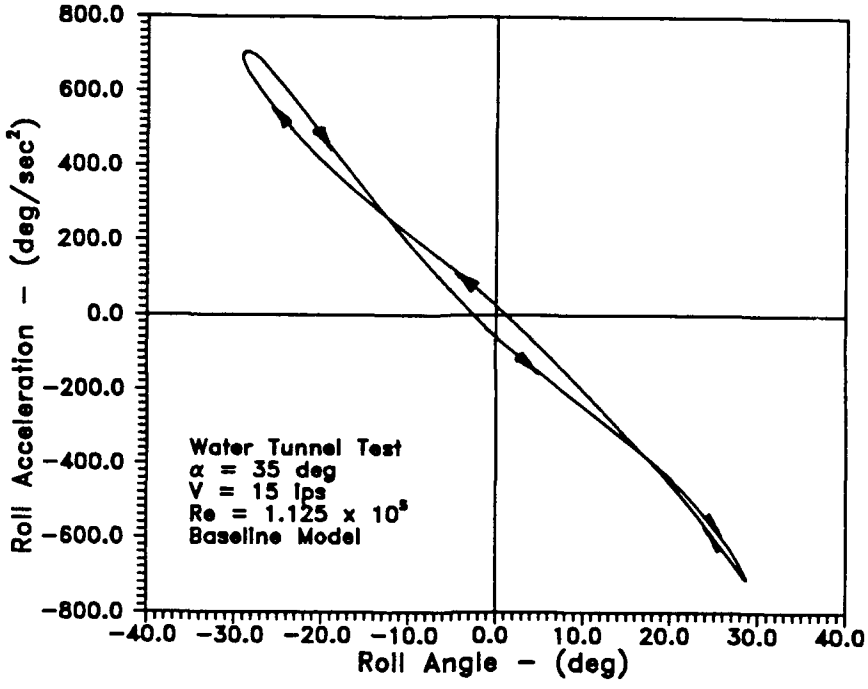

e)

Fig. 76 (continued).

Much of the research that has been conducted recently has related the work energy method developed by Nguyen, Yip, and Chambers[7] to describe the wing rock limit cycle. The energy method was discussed earlier in the wind tunnel discussion. A major point was that the direction of the rolling moment hysteresis loop determined whether energy was increasing without bound (unstable) or negative (damping or stable). Clockwise hysteresis loops added energy to the system while counter-clockwise ones dissipated energy. The following energy plots correspond to the roll acceleration wing rock buildup figures above. They were constructed using the previously discussed energy equation (14).

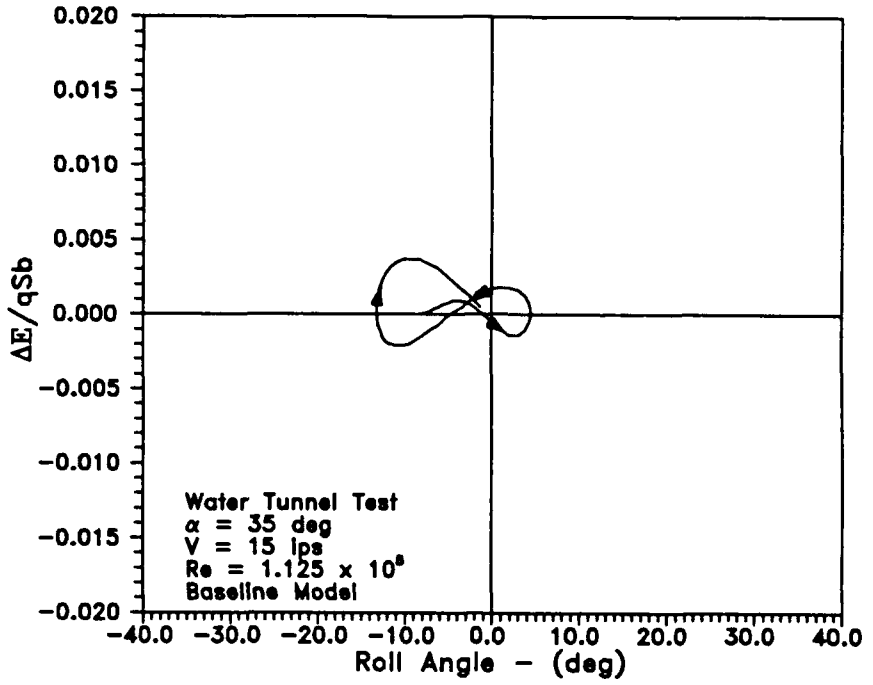

a)

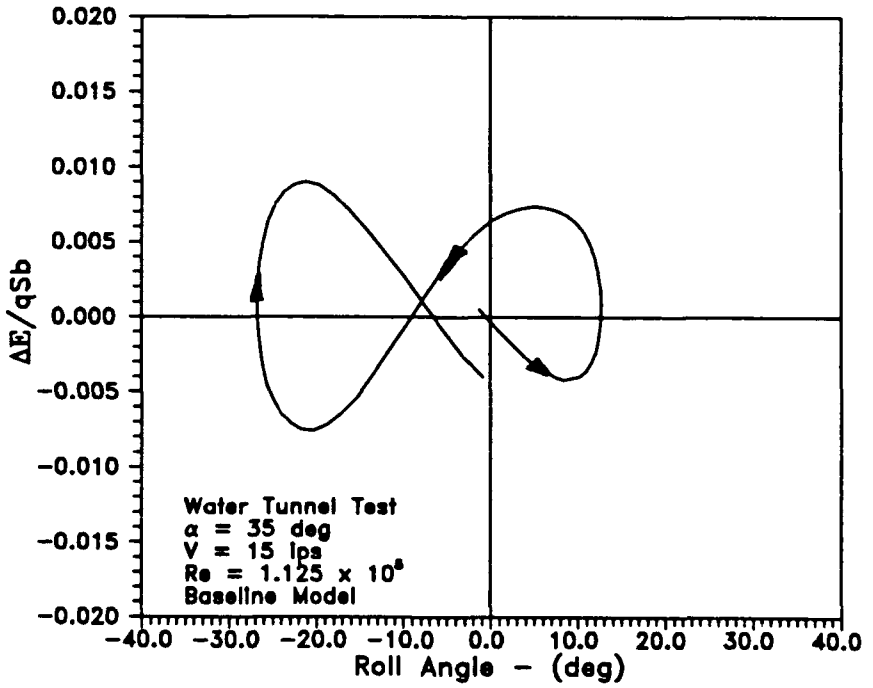

b)

Fig. 77 Energy buildup at V_{∞} = 15 ips.

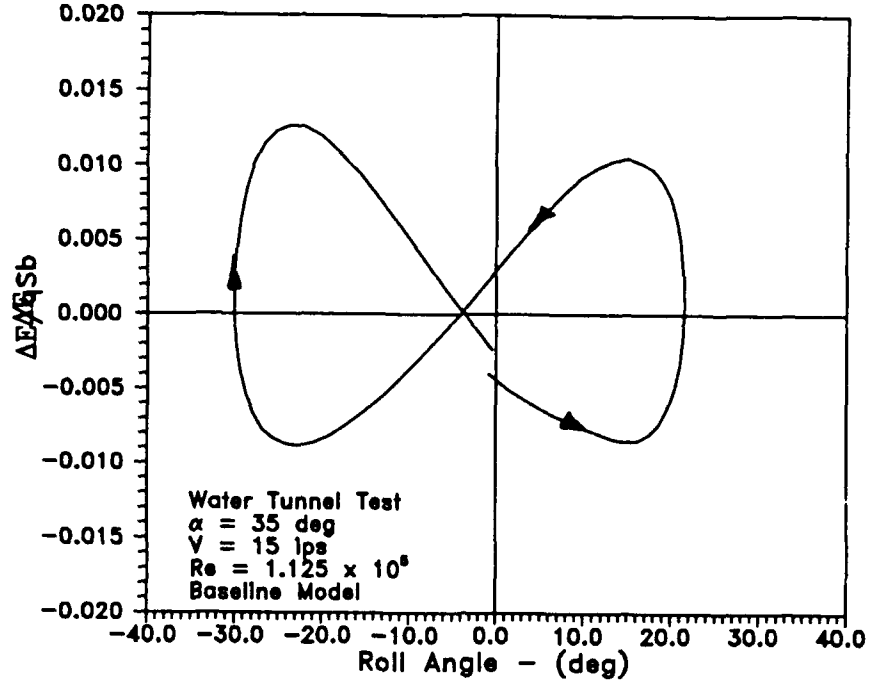

c)

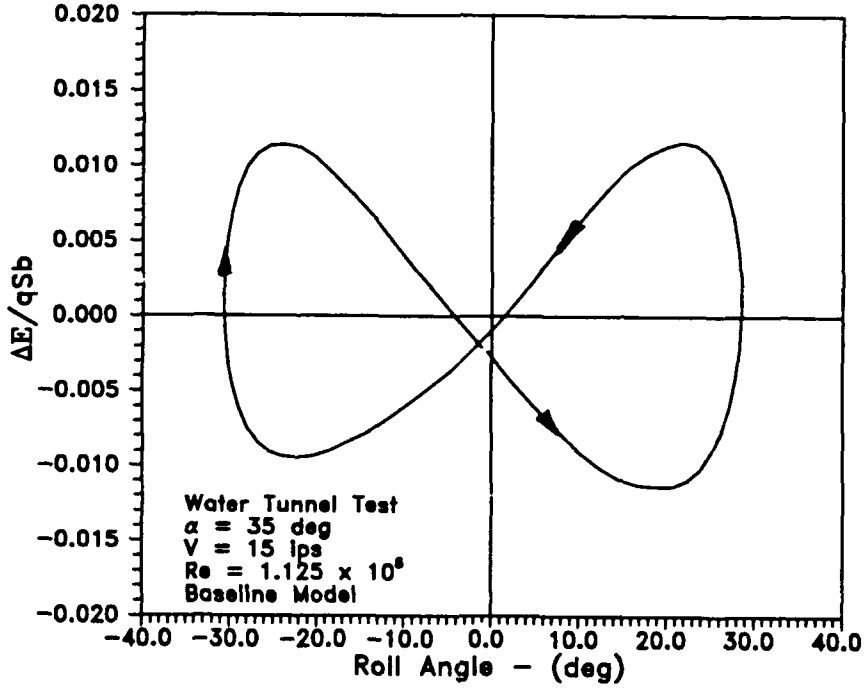

d)

Fig. 77 (continued).

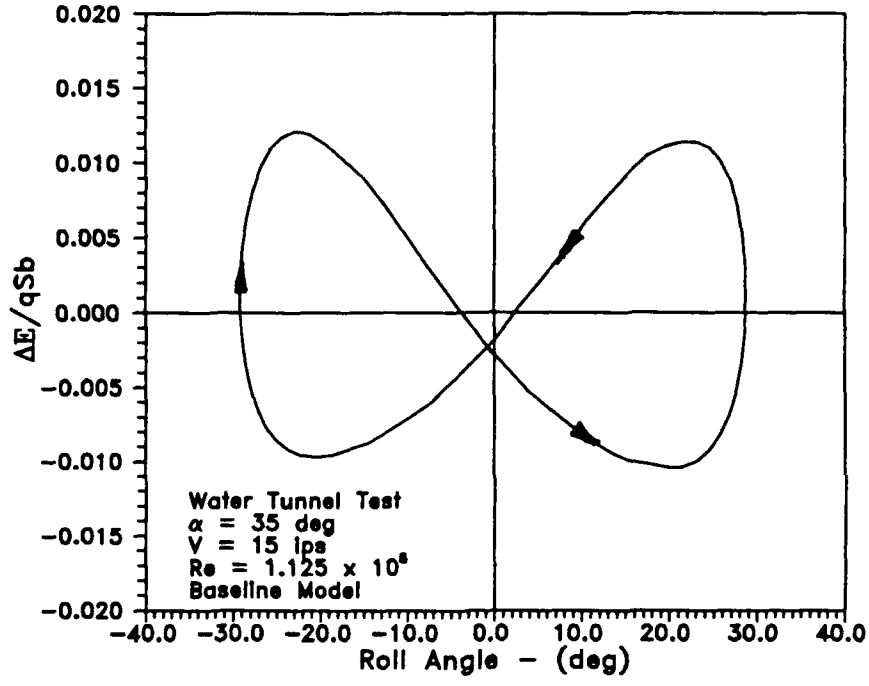

e)

Fig. 77 (continued).

The first cycle of the energy buildup is shown in Fig. 77a. The curve is a horizontal figure eight. Initially, the point at which the curve crossed itself, was at a positive energy state (Fig. 77a). The energy cycle continued to build (Fig. 77b) and the crossing point was still with ΔE positive but shifted further to negative bank angles. The distance between the two endpoints suggested that the motion was still building up. In Fig. 77c, the crossing point dropped to a zero energy level and shifted to the right. The distance between endpoints has decreased. Finally, (Fig. 77d and e) a stable energy cycle is attained with the crossing point well below the roll angle axis at a negative energy state. Energy was being removed from the system before the model passes through the zero roll angle. Energy must be conserved for each cycle or set of cycles for a limit cycle to occur. Therefore, if energy was being extracted at small roll angles (Fig. 77e), a net addition must occur elsewhere in order

to sustain the limit cycle. After examining the roll amplitudes near their maximum state, net positive energy was required if a limit cycle was to exist. The energy had a larger magnitude after the model passed through its maximum roll angle.

Model w/spinner

The model was also fitted with the added mass attachment with no disks during testing. The model w/spinner configuration was tested to observe if an increase in rolling moment occurred as it did during wind tunnel testing. Table 10 summarizes the motion parameters at different tunnel speeds. The rolling moment coefficient was approximately five times larger than the baseline model result.

Another peculiar result occurred at the lowest tunnel speed of V_∞ = 6 ips. The hysteresis went in both directions for the same tunnel velocities. In some cases, the hysteresis traveled in the same direction as the other water tunnel results (Fig. 78). Yet in other cases (Fig. 79), the hysteresis traveled in the same direction as wind tunnel results. The hysteresis was very slight in both cases as compared with the other results. Fig. 78 shows the rolling moment versus roll angle curve and Fig. 80 is the energy cycle for the same limit cycle. The energy was fairly evenly balanced between increasing and decreasing roll angles. Hysteresis direction randomness was not evident at the three higher tunnel speeds. Apparently a bifurcation point in the wing rock dynamics was discovered at V_∞ = 6 ips. The tunnel speed was the only variable changed during testing of the model w/spinner configuration and it is believed that this phenomena was Reynolds number dependent. Tunnel speeds less than 6 ips were not examined. In summary, the spinner not only had an effect on the rolling moment magnitudes, but also on the direction of the hysteresis.

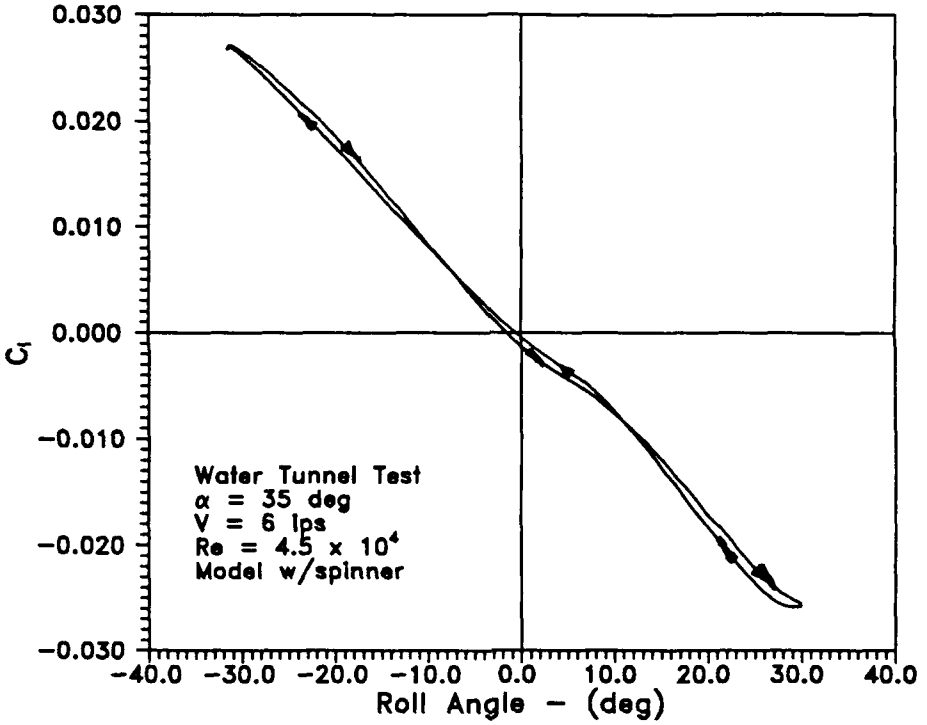

Fig. 78 Rolling moment coefficient of model w/spinner at V_∞ = 6 ips.

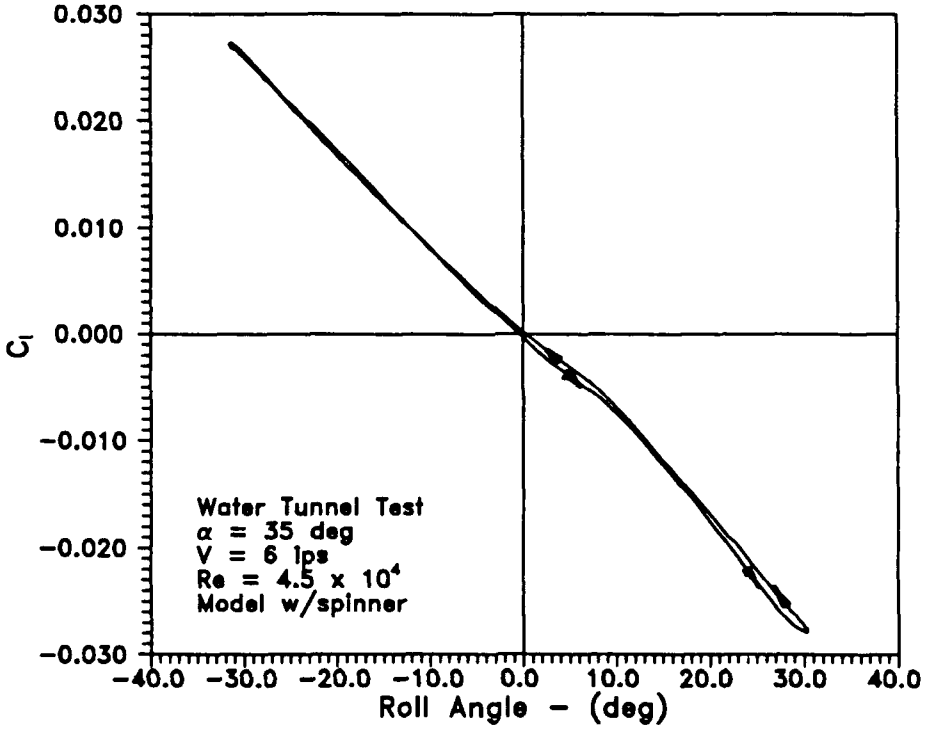

Fig. 79 Opposite rolling moment hysteresis, V_∞ = 6 ips.

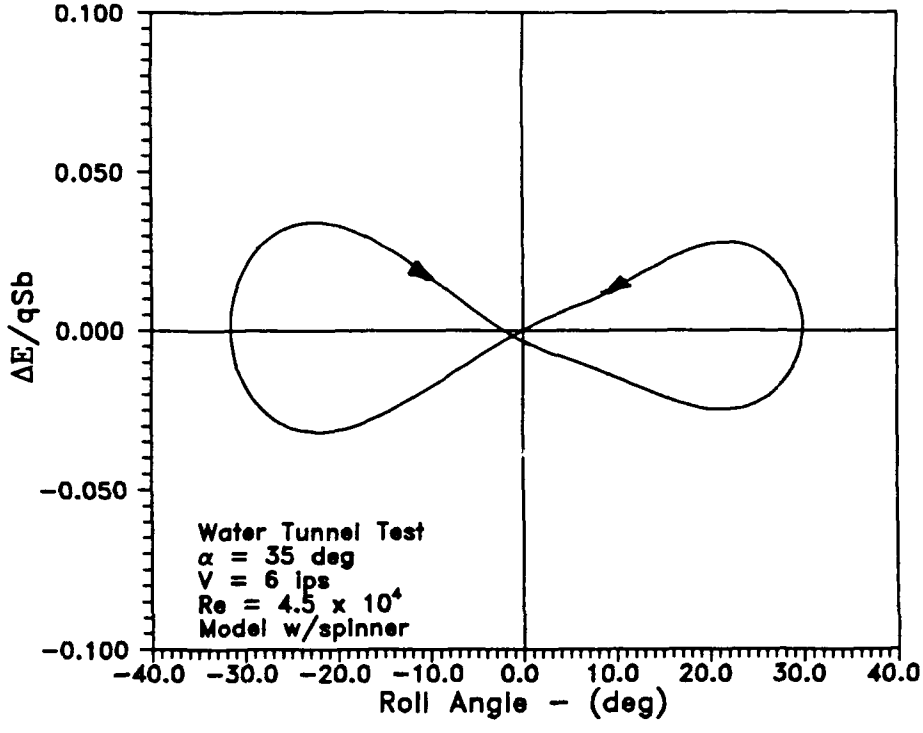

Fig. 80 Energy cycle of model w/spinner at V_∞ = 6 ips.

Table 10 Summary of Motion Parameters for Model w/spinner.

Speed (ips)	ϕ (deg)	$\dot{\phi}$ (deg/sec)	$\ddot{\phi}$ (deg/sec^2)	C_t	Period (sec)	ω (rad/sec)	k
6	30.8	68	95	0.05400	3.098	2.028	0.596
10	34.2	105	248	0.05000	1.992	3.155	0.556
12	34.7	124	375	0.05000	1.683	3.734	0.549
15	34.9	151	550	0.05000	1.392	4.514	0.531

Note: **All data presented are averaged values.**

Vortex Trajectory

Data were gathered at four water tunnel speeds and with both the baseline model and the model w/spinner. The data presented here consist of results collected only at V_∞ = 6 ips. The milk worked well as a flow visualization seed and provided good contrast against the black model. Water tunnel data collection was not limited by tunnel velocities as it was during the wind tunnel tests. Data could be collected over the entire delta wing. The data was structured with the DYNAMIC program into the same format used during wind tunnel data reduction. Data at the $0.25\bar{c}$, $0.50\bar{c}$, $0.65\bar{c}$, $0.75\bar{c}$, $0.85\bar{c}$, and $0.95\bar{c}$ stations will be presented. In addition, plots of the vortex structures at the ±5°, ±15°, ±25°, and ±30° roll angles were constructed. Together with the dynamics of the system, these data provide more information on the phenomenon of wing rock.

The right and left vortex positions affected the entire wing rock motion. The asymmetries in their positions caused the wing to oscillate back and forth. To further define the vortex positions, they were separated into spanwise and normal movements above the wing at a specific wing chord location. The spanwise position determined the moment arm about the roll axis while the normal position set the effective strength or force on the wing. For example, as a vortex moved closer to a wing, the core velocity creates a low pressure in this region, increasing lift there. Further away from the wing, lift decreases. For the same normal vortex position, the vortex that was further from the wing centerline had a larger moment arm and gave a larger torque. Another important factor was the actual strength of the vortex core. The strengths of the vortices varied during the roll oscillations. Vortex breakdown reduced the strength of the core at that point. This study did not quantify information on the actual

strength of the vortices. Therefore, only a partial assessment could be made in terms of how the right and left vortex positions affect wing rock.

The spanwise and normal vortex core movements are shown in Fig. 81 and Fig. 82 at x/c = 0.25. To help clarify terminology, at positive roll angles the windward vortex is the right one and the leeward vortex is the left one. The opposite is true at negative roll angles. As the wing rolled to the right, the windward vortex moved inboard while the leeward vortex moved outboard. The spanwise figure shows slight hysteresis in the vortex core path near the right and left vortex liftoff locations. Fig. 82 shows that liftoff of the leeward vortex occurred slightly before reaching the maximum roll amplitude. From this figure, the hysteresis was larger for the normal vortex movement than for the spanwise component. Fig. 83 is a cross-section of the wing at the x/c = 0.25 location. Both the right and left vortex core locations are

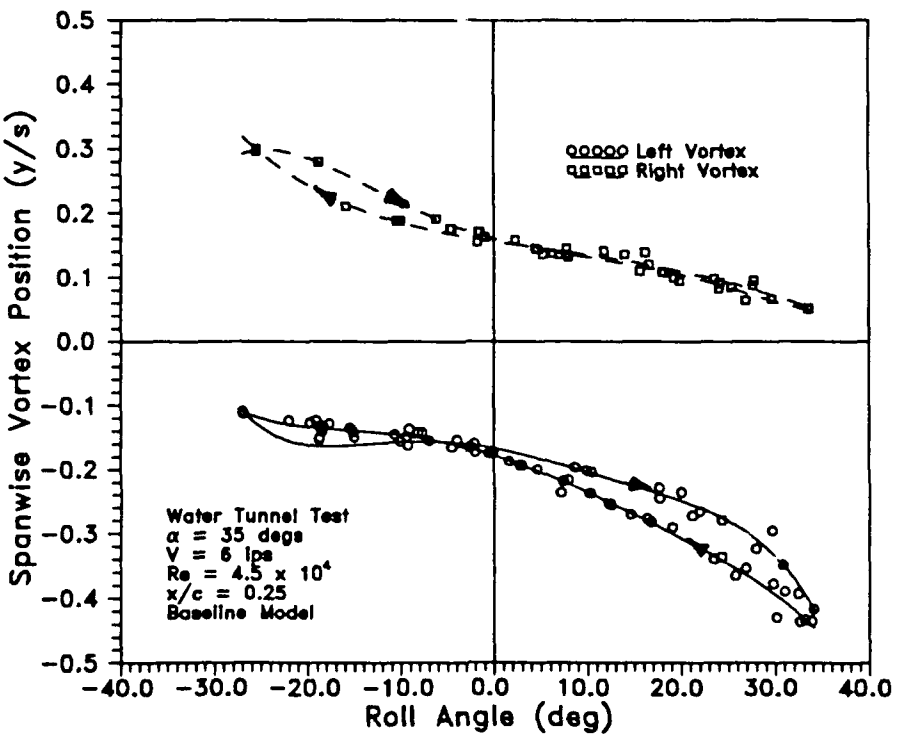

Fig. 81 Spanwise vortex core movement at x/c = 0.25.

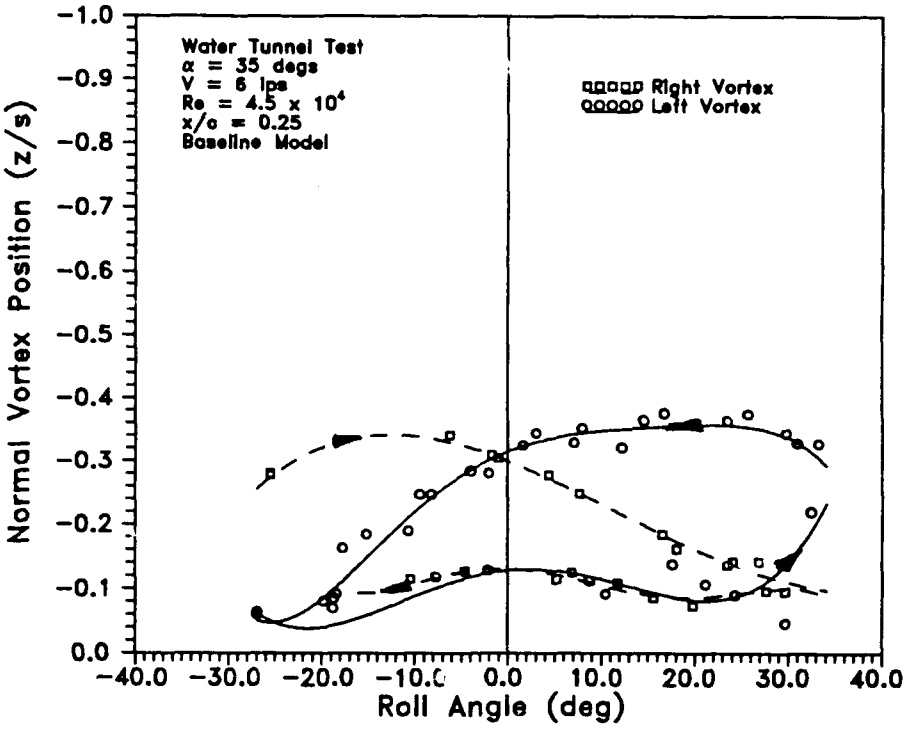

Fig. 82 Normal vortex core movement at x/c = 0.25.

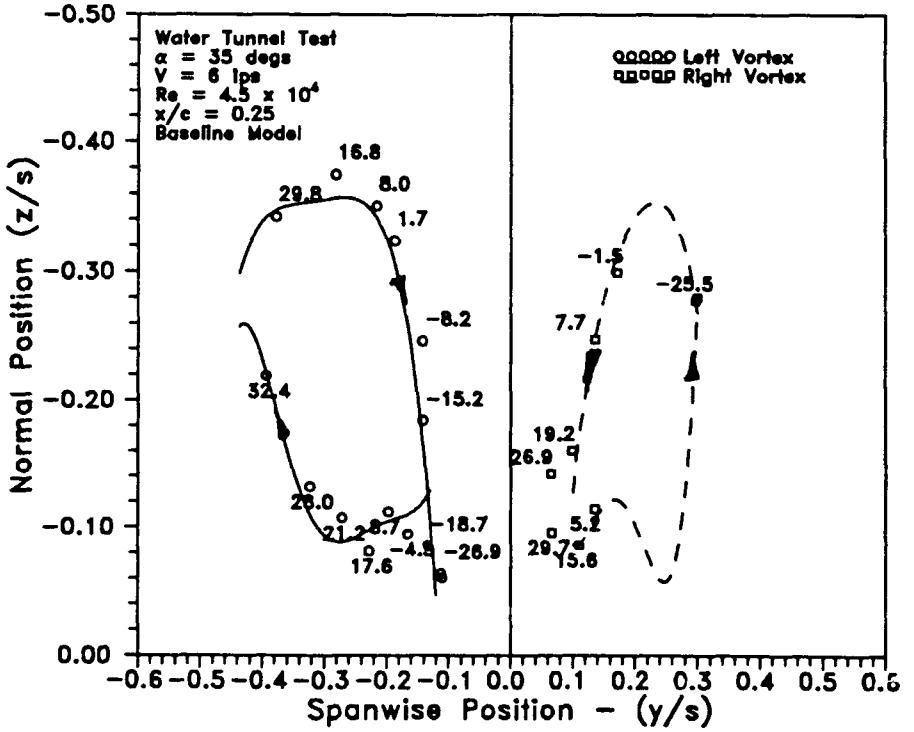

Fig. 83 Vortex core movement at x/c = 0.25.

labeled with the roll angles for every fifth point. There are also two branches of points for each vort' :; as the wing rolled from a negative to positive maximum roll amplitude and from a positive to negative amplitude.

At the 50% chord station, the hysteresis of the core spanwise movement became larger for the leeward vortex (Fig. 84). The windward vortex also moved closer to the centerline than the $0.25\bar{c}$ data. The hysteresis loop in the normal vortex positions (Fig. 85) enlarged as compared with the results at x/c = 0.25. In addition, the maximum magnitude of the normal vortex position shifted in towards the zero roll angle. While the data were sparse in certain areas, Fig. 86 showed that the spanwise versus normal vortex position paths became larger as expected.

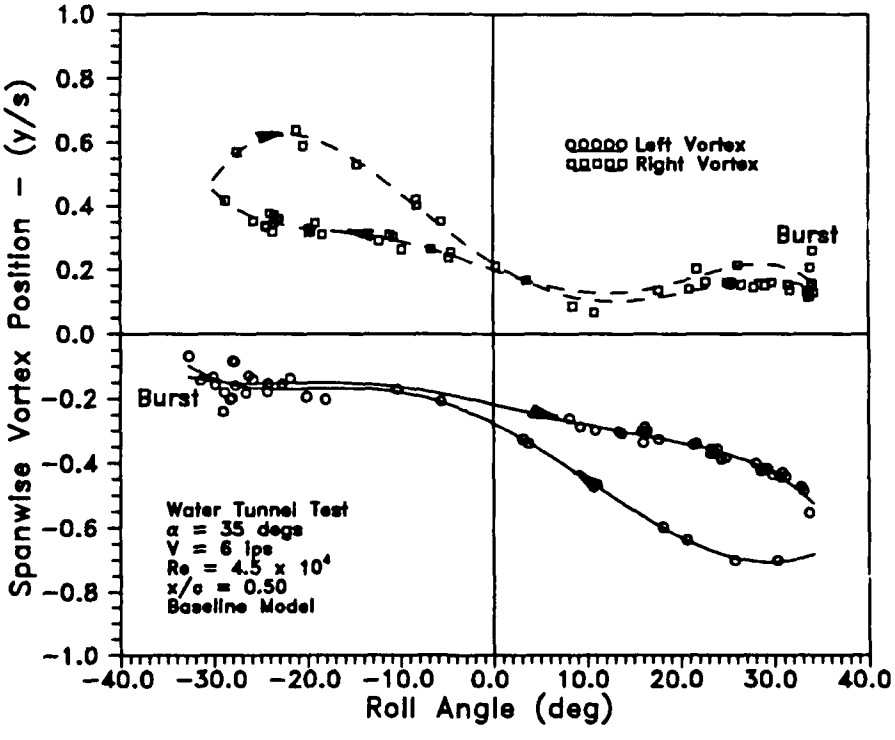

Fig. 84 Spanwise vortex core movement at x/c = 0.50.

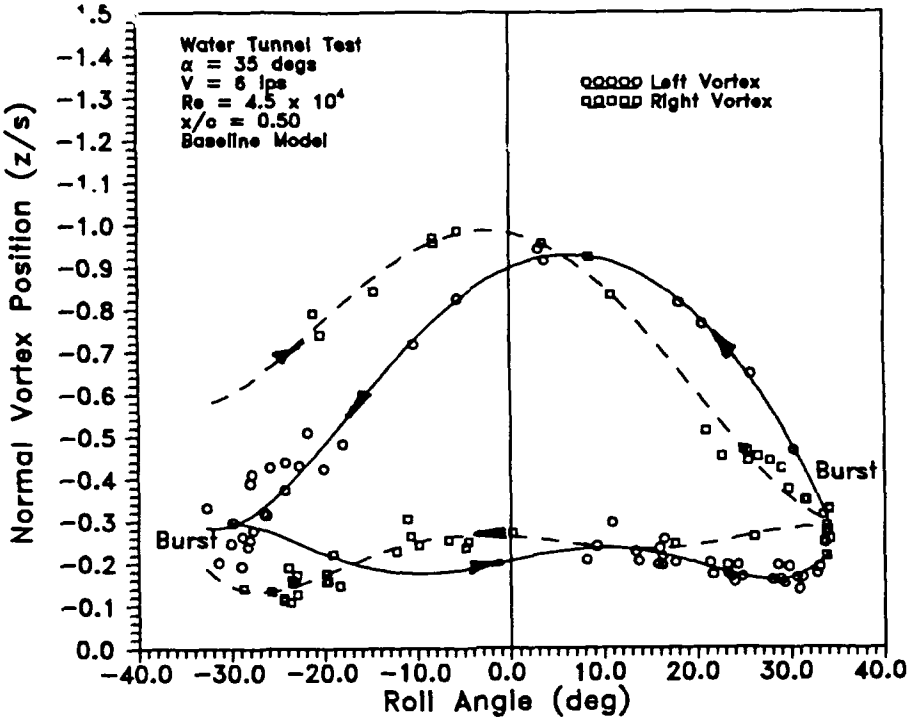

Fig. 85 Normal vortex core movement at x/c = 0.50.

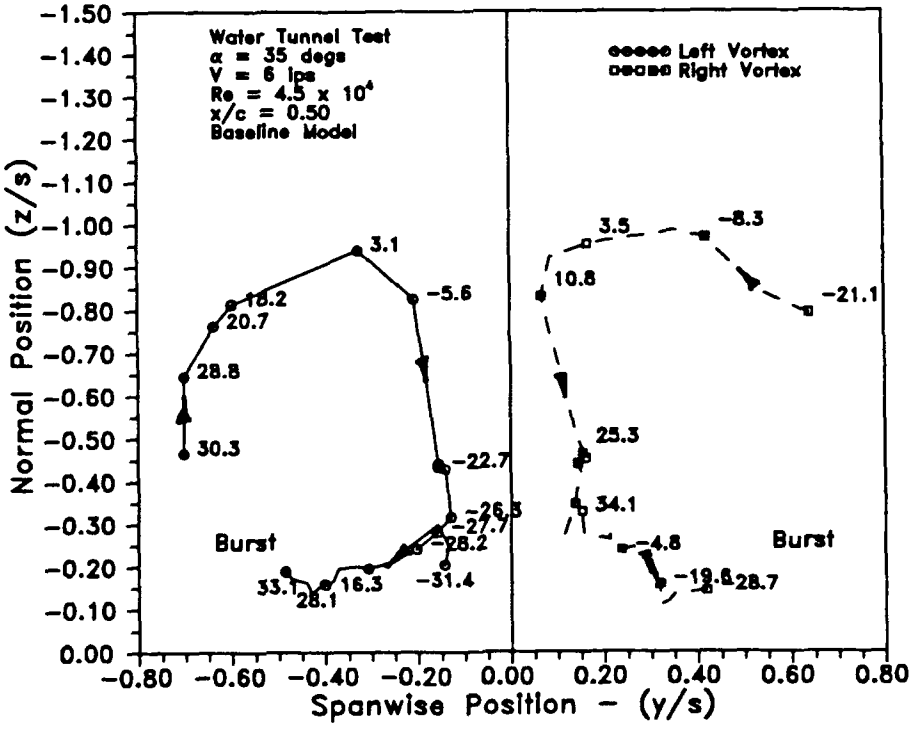

Fig. 86 Vortex core movement at x/c = 0.50.

As the survey locations moved further back on the wing, data became more sparse in certain areas due to vortex breakdown over the wing. Hysteresis in the spanwise positions continued to grow in size as seen in Fig. 87. The windward vortex moved closer to the centerline of the model. The normal vortex positions (Fig. 88) reached maximum values of z/s = 1.28. The maximum magnitude of the normal vortex position shifted through the zero roll angle. Fig. 89 shows the core locations for the spanwise versus normal positions at x/c = 0.65. Using this figure, a qualitative analysis relating core positions at this station only and the rolling moment will be made. The reader is cautioned that vortex strength changes are not considered in this analysis.

As the wing rolled to a positive maximum roll amplitude (34.3°), the left vortex had a spanwise position of y/s = -0.57 and a normal position of z/s = -0.24.

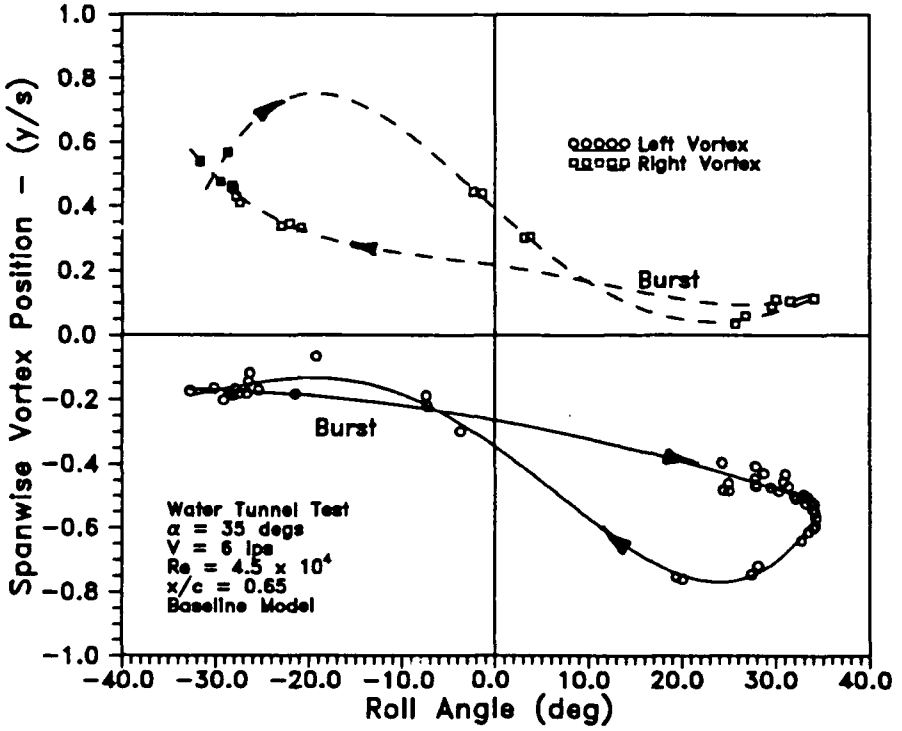

Fig. 87 Spanwise vortex core movement at x/c = 0.65.

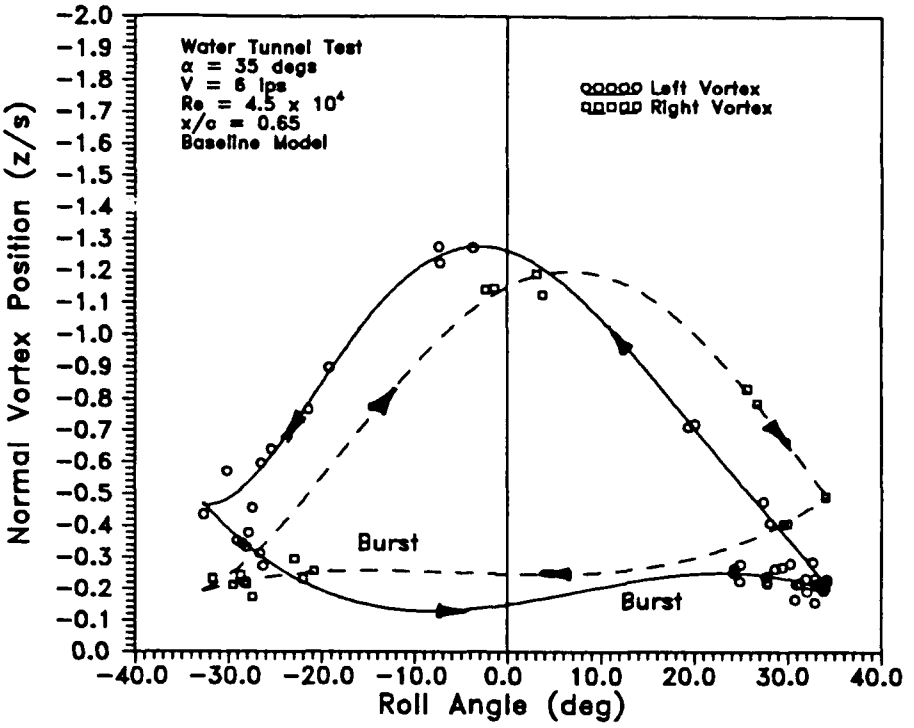

Fig. 88 Normal vortex core movement at x/c = 0.65.

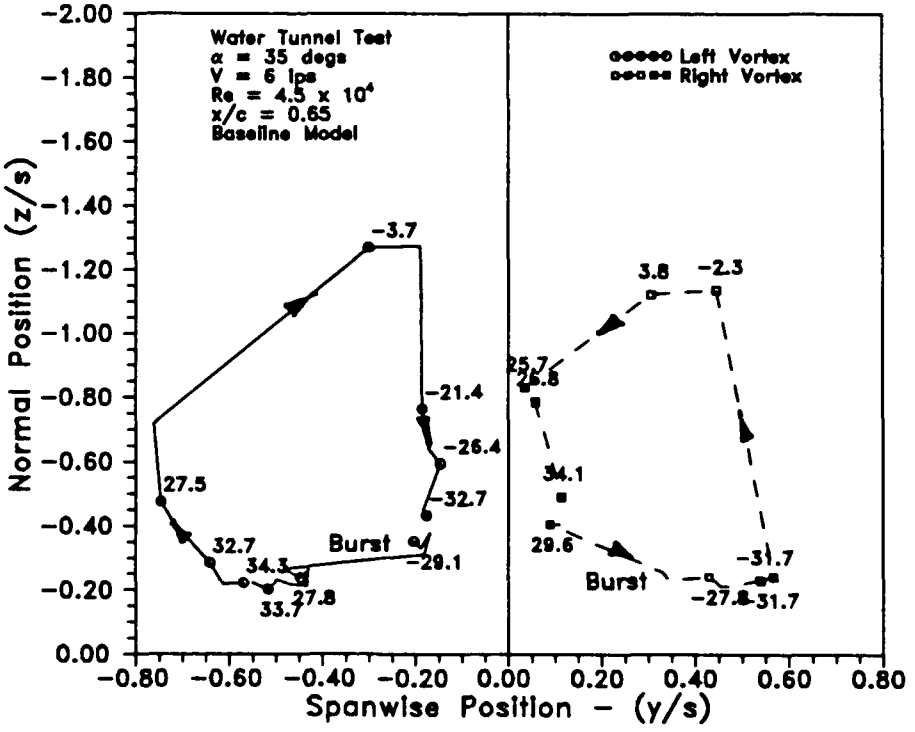

Fig. 89 Vortex core movement at x/c = 0.65.

The corresponding right vortex had a spanwise position of y/s = 0.12 and a normal position of z/s = -0.48. For this roll angle the left vortex had a larger moment arm and was closer to the upper wing than the right vortex. Based on vortex position only and no breakdown at this position, this arrangement would cause a positive delta moment on the wing. Recalling that at the maximum positive roll amplitude the total aerodynamic moment was negative (Fig. 73), the effect of the vortex positions would reduce the magnitude of the moment. As the wing began to roll in the opposite direction towards the zero roll angle, the left vortex (Fig. 89) moved outboard and away from the wing and the right vortex moved slightly outboard and down towards the wing. At a roll angle of 27.5°, the left vortex had a spanwise position of y/s = -0.75 and a normal position of z/s = -0.47. The right vortex was approximately at y/s = 0.11 and z/s = -0.38. Notice also that the left vortex moved beyond the edge of the wing (y/s = 0.65), which meant that the contribution to a moment by the left vortex was minor. The greater contribution to a moment was from the right vortex, resulting in a negative moment increment. Going back to the total aerodynamic rolling moment at a returning roll angle slightly smaller than the maximum roll angle, the addition of the negative moment and the negative moment increment from the right vortex resulted in an increased rolling moment magnitude. In addition, the windward vortex (in this case, the right one) nearly burst almost instantaneously at about the 30% chord location and the maximum roll angle. (This characteristic was observed only in the water tunnel; the burst point in the wind tunnel moved forward at an observable rate.) Significantly, the downstream vortex remained intact in the water tunnel. As the wing began to return through the zero roll angle, the burst point moved aft. At the positive roll amplitude, the right vortex at x/c = 0.65 still had its tight structure and, therefore, presumably its strength. If so, it provided a strong negative restoring moment to the wing. This analysis was for one specific chord

location on the wing. A continuation of this analysis will be made later over the entire model. It is also stressed here that vortex lift contribution is based on the core location relative to the wing and the vortex strength. During this study only a qualitative assessment could be made for vortex strength.

At the x/c = 0.75 chord station, Fig. 90 shows that the right vortex crossed the centerline of the model shortly before the model reached the maximum roll amplitude. The normal vortex positions are shown in Fig. 91. Compared with the x/c = 0.25 data (Fig. 82), the core path maximum magnitudes were at opposite roll angles. The cross-section of the flow field, Fig. 92, was similar to the previous chord station (Fig. 89).

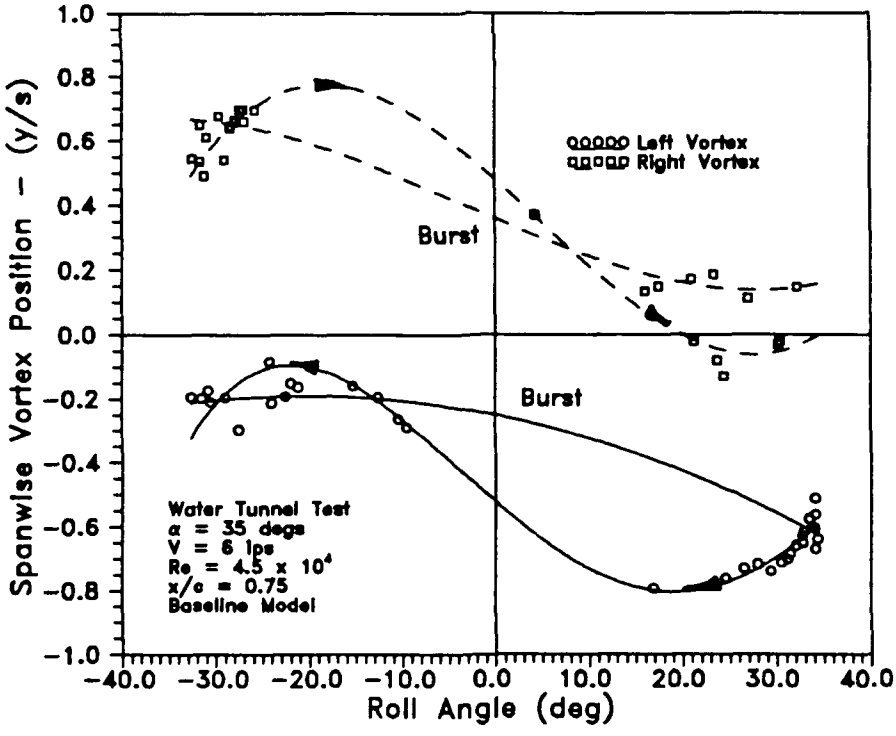

Fig. 90 Spanwise vortex core movement at x/c = 0.75.

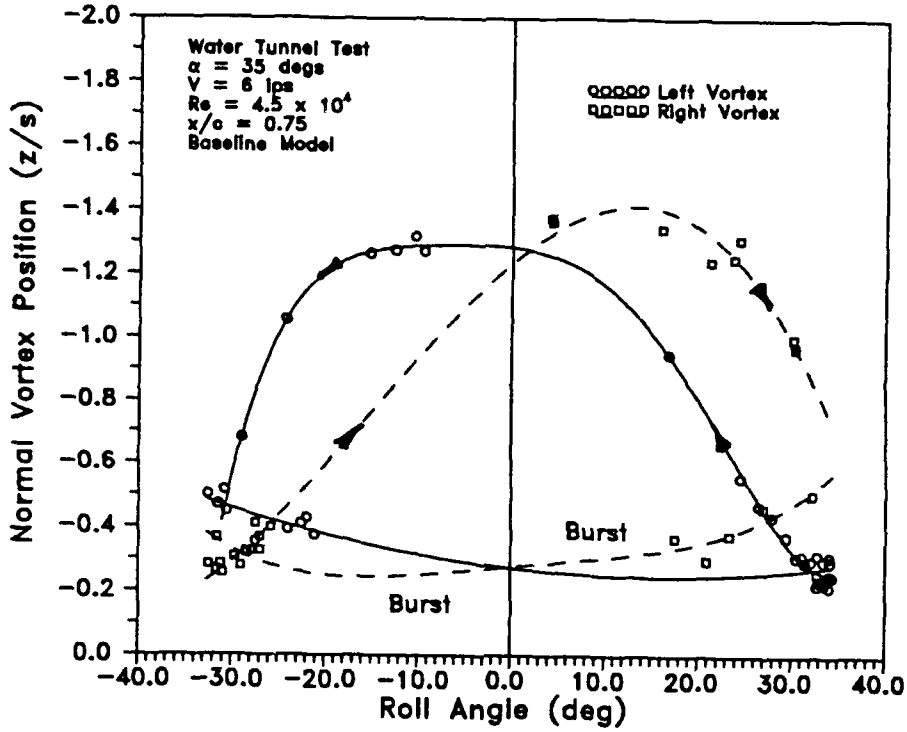

Fig. 91 Normal vortex core movement at x/c = 0.75.

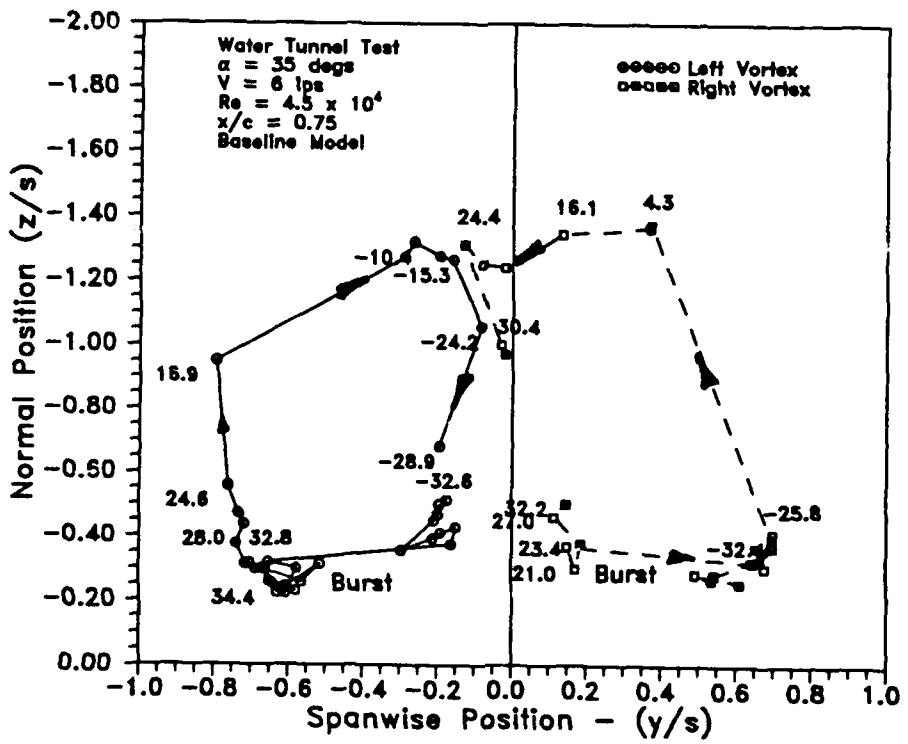

Fig. 92 Vortex core movement at x/c = 0.75.

At the 85% chord station (Fig. 93), the leeward vortex path was incomplete due to vortex breakdown. The windward vortex moved across the centerline as the maximum roll angle was approached and the back across as the wing returned toward the zero roll angle. The hysteresis was larger (Fig. 94) and the normal vortex core paths have swapped positions as compared to the data at x/c = 0.25. The spanwise versus normal vortex positions showed partial paths of the movement of the cores during wing rock (Fig. 95).

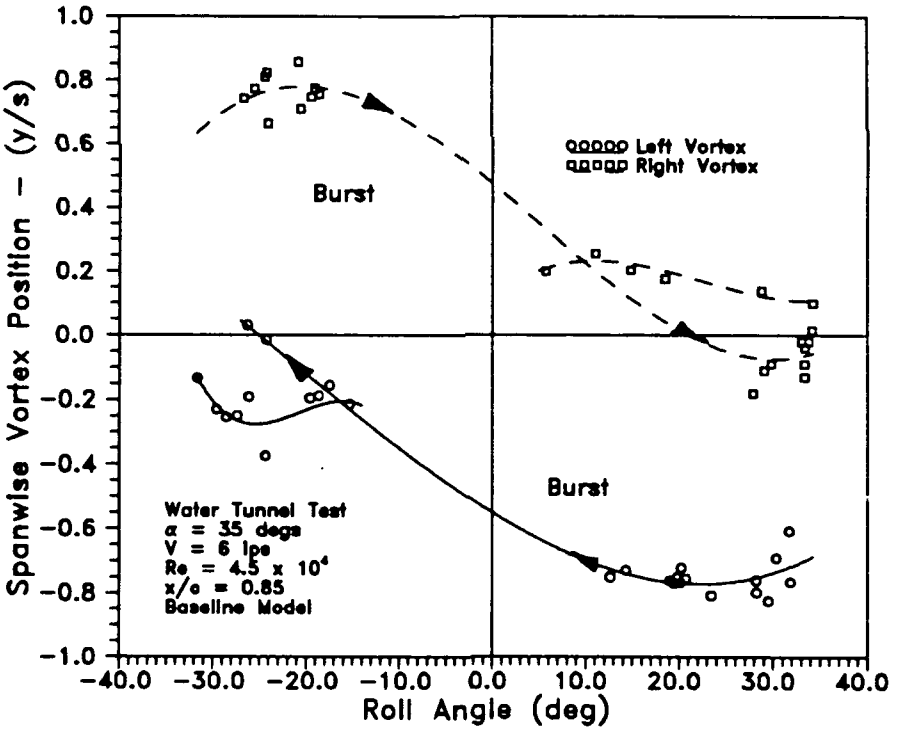

Fig. 93 Spanwise vortex core movement at x/c = 0.85.

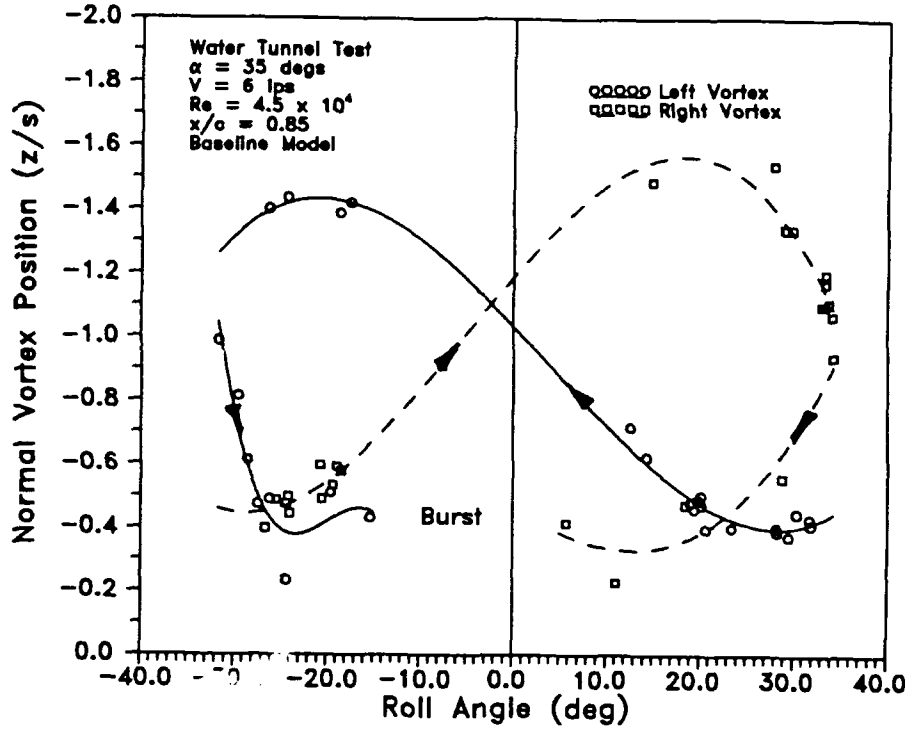

Fig. 94 Normal vortex core movement at x/c = 0.85.

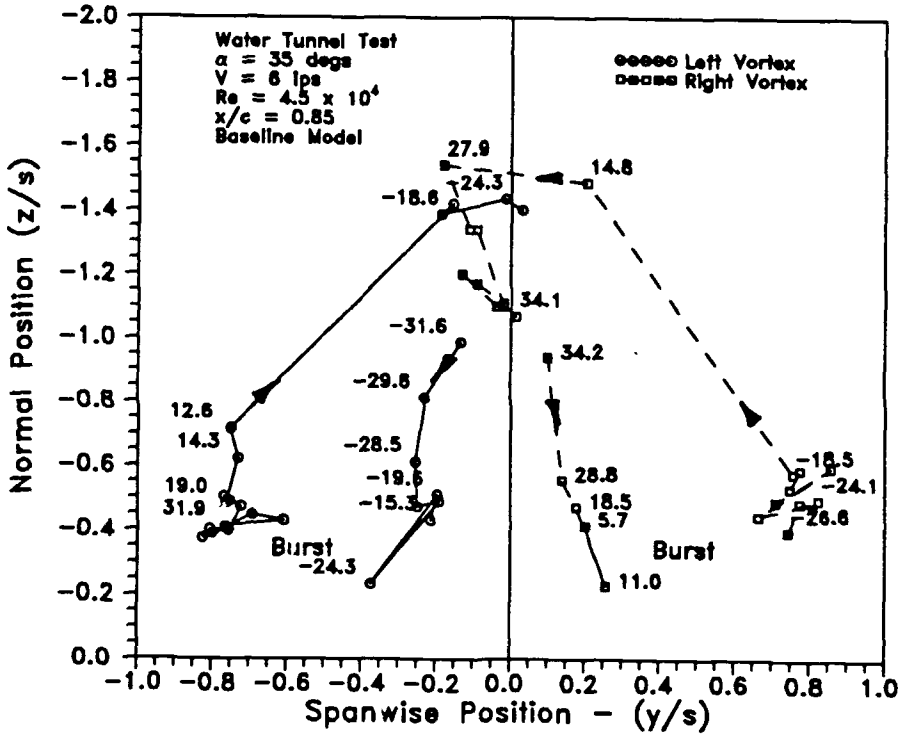

Fig. 95 Vortex core movement at x/c = 0.85.

The final chordwise station, x/c = 0.95, contained only a small number of data points. The spanwise core positions (Fig. 96) contained more data on the windward vortex than on the leeward vortex due to the asymmetries in vortex breakdown and the nearly instant breakdown of the windward vortex. The pattern of the trajectories was recognizable from the earlier data sets. The normal vortex core paths (Fig. 97), again, provided more information for the windward vortex than the leeward vortex. The cross-section plot, Fig. 98, was basically a grouping of points at different locales along the vortex core trajectories. A more complete data set could be obtained by using a light sheet at the latter chord stations.

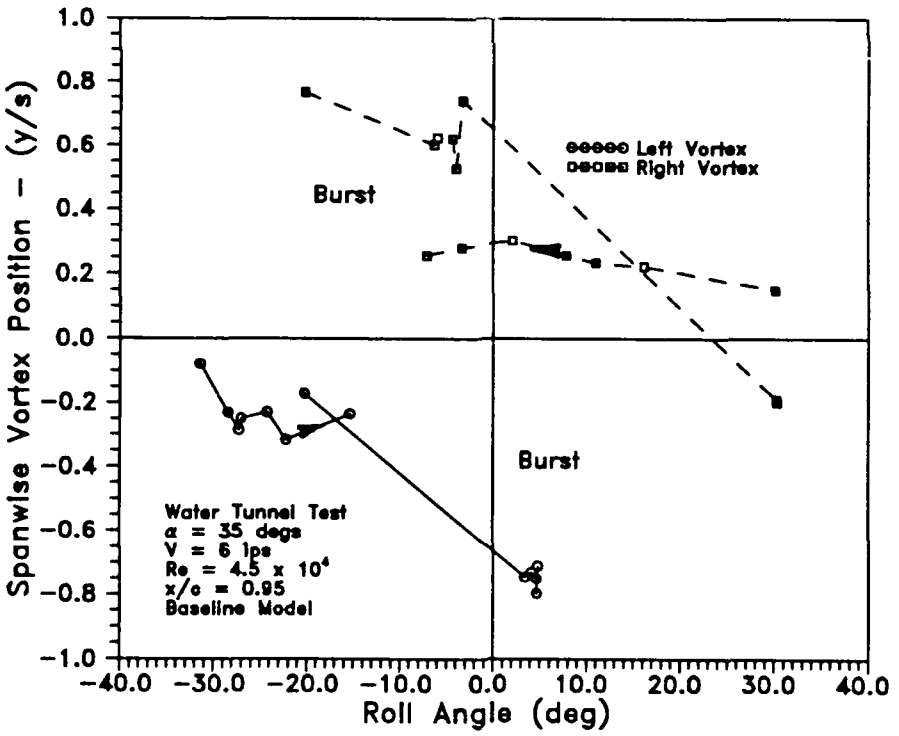

Fig. 96 Spanwise vortex core movement at x/c = 0.95.

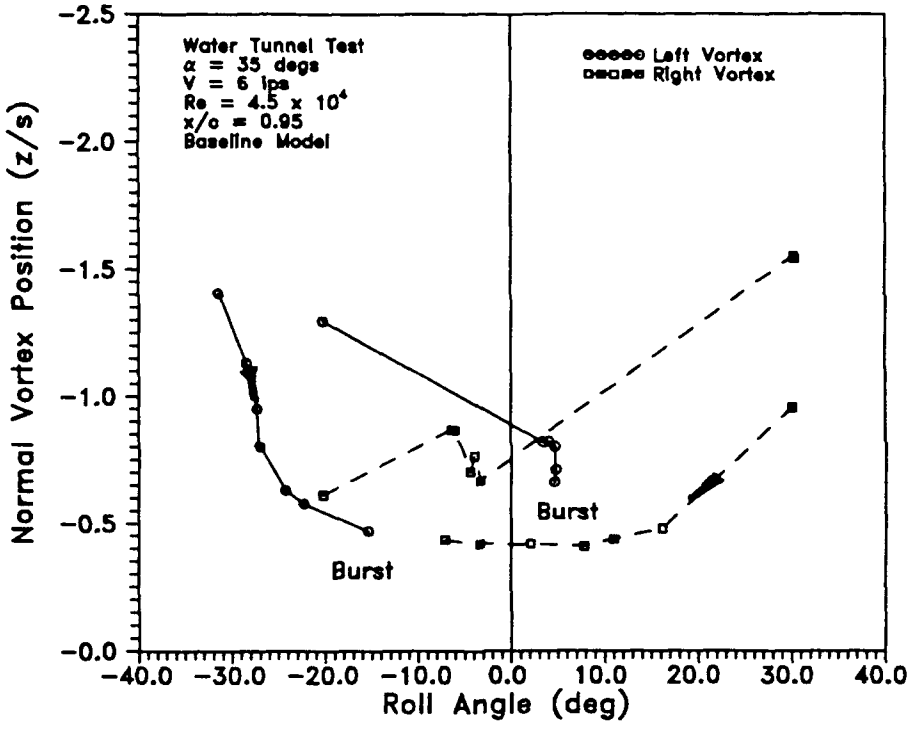

Fig. 97 Normal vortex core movement at x/c = 0.95.

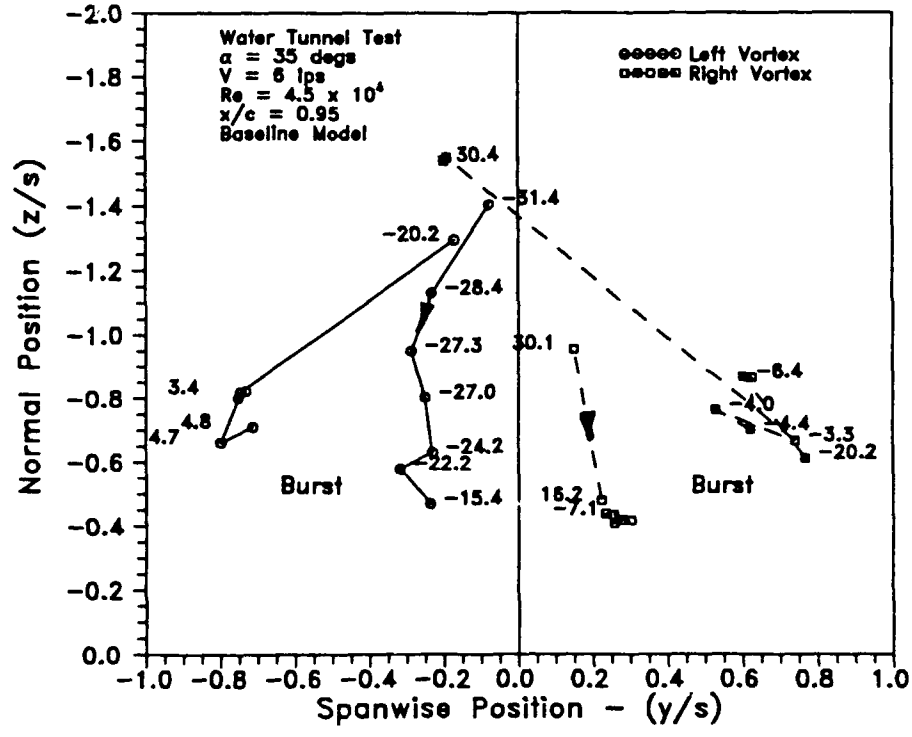

Fig. 98 Vortex core movement at x/c = 0.95.

Additionally, vortex core information was extracted for both spanwise and normal positions at specific roll angles. These data will be presented for the positive roll angles only. The plots include a spanwise figure in which the reader is looking down at the planform of the wing and a normal figure which positions the reader on the left side of the wing with the apex to the absolute left. These figures include vortex trajectories as the model rolls from both directions through the specified roll angle. From these plots, the hysteresis in the spanwise and normal vortex locations was evident. Again, only vortex core position information was collected; vortex strength was unknown.

The spanwise positions of the right and left vortices are shown in Fig. 99. The spanwise vortex positions determined the moment arm for each vortex's contribution to the rolling moment. Both left vortices were further outboard than the right ones were. Vortex lift on a wing depended on the core strength and the normal location above the wing. A qualitatively assessment can be made of vortex lift since only the normal core locations were known. Fig. 100 contains three plots of the normal vortex trajectory positions. Fig. 100a indicates both increasing and decreasing roll angle, showing the relative distances between them. The second and third figures are separate pairs of vortices for increasing and then decreasing roll angle. From these figures, a large shift in core normal location was evident. In Fig. 100b, the left vortex was closer to the wing than the right which meant that its circulation provided a more favorable pressure gradient, assuming similar vortex strengths. This gradient resulted in a larger force applied to the wing. Reviewing Fig. 99, it was determined, based on the vortex locations, that the wing was rolling right. From the normal trajectory (Fig. 100c), the left vortex was lifted off the wing and the right was closer. The right vortex would provide more lift, given similar vortex strengths. Since the

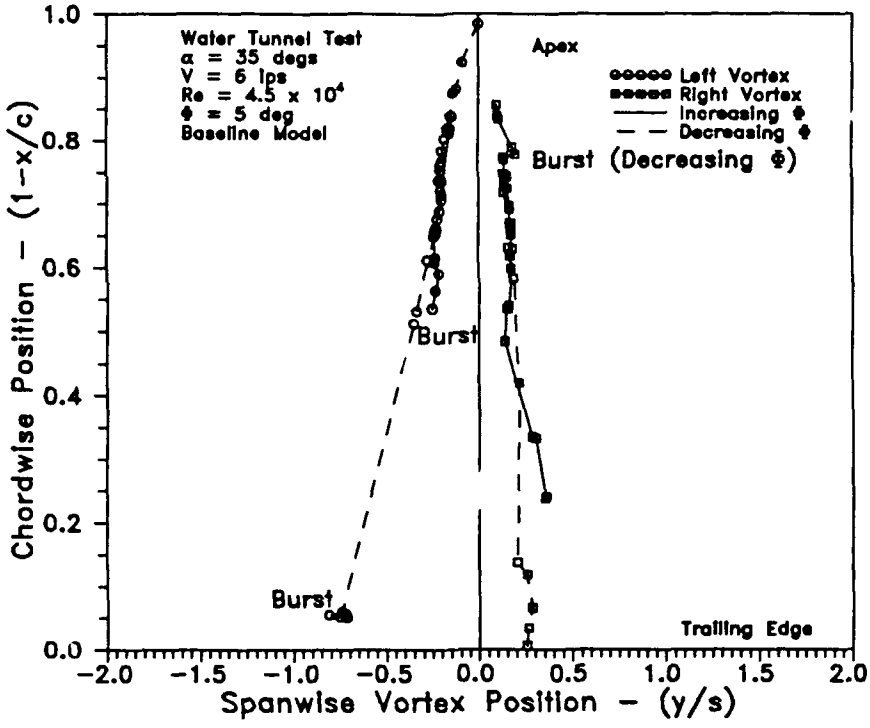

Fig. 99 Spanwise position of the leading edge vortices at $\phi = 5°$.

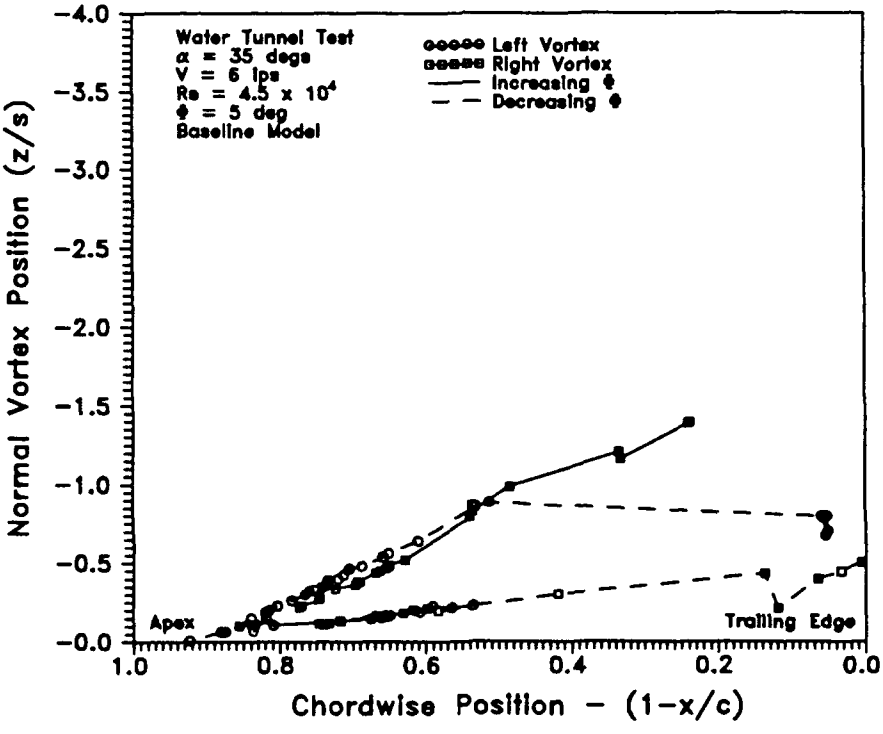

a)

Fig. 100 Normal position of leading edge vortices at $\phi = 5°$.

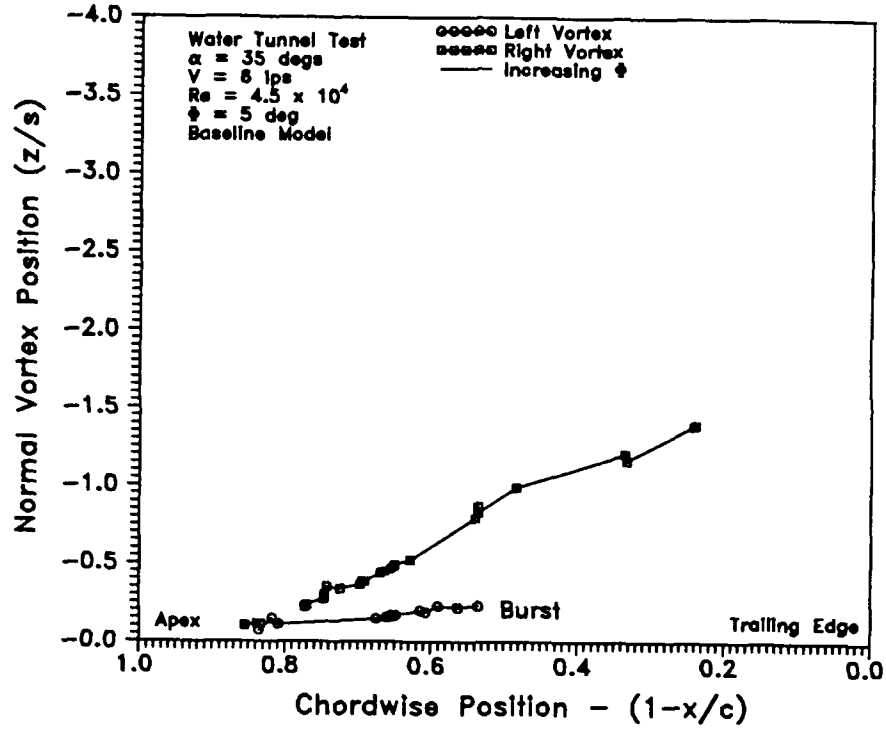

b)

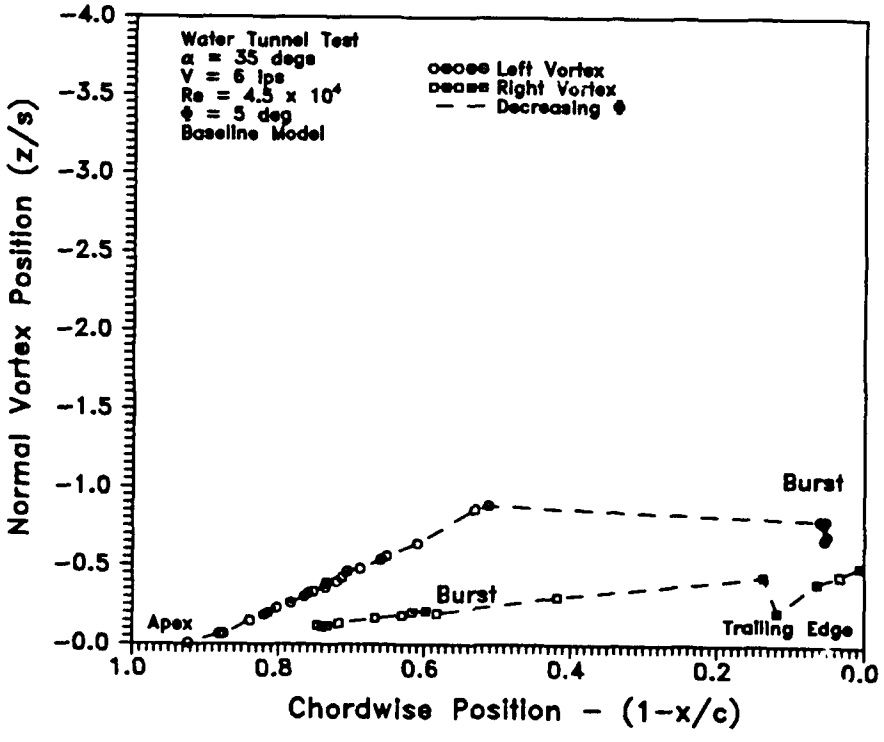

c)

Fig. 100 (continued).

wing is rolling left and although the left vortex was further outboard than the right one, the right vortex affected the wing more. While these results did not quantify the moment contributions due to vortex positions, and similar vortex strengths were assumed, an assessment of the vortex positions on the wing rock motion was made.

At ϕ = 15°, Fig. 101 shows the increasing shift in the spanwise direction of the vortex trajectories. The right vortex moved more inboard while the left one moved outboard for both roll directions. The right vortex crossed the centerline of the model at the 60% chord station as the wing was rolling toward the maximum roll amplitude. On the return, this vortex had no points that were on the left side of the wing. From Fig. 102, the vortex normal positions were similar to those at ϕ = 5°. The positions observed were consistent with the model motion. The right vortex (Fig. 100a and Fig. 102a) moved closer to the wing as the model rolled from 5° to 15°.

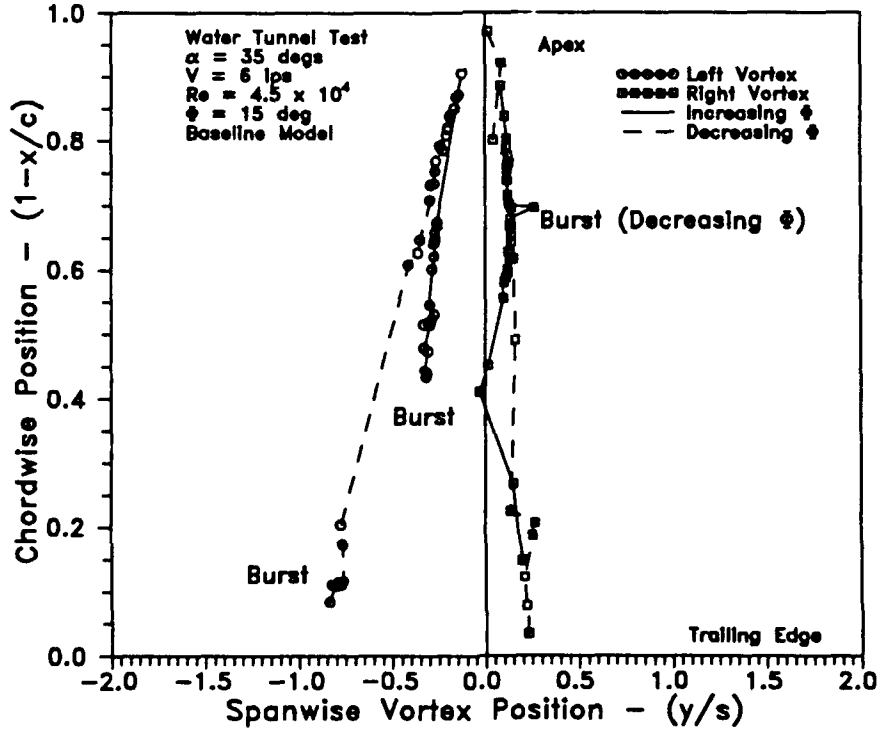

Fig. 101 Spanwise position of the leading edge vortices at ϕ = 15°.

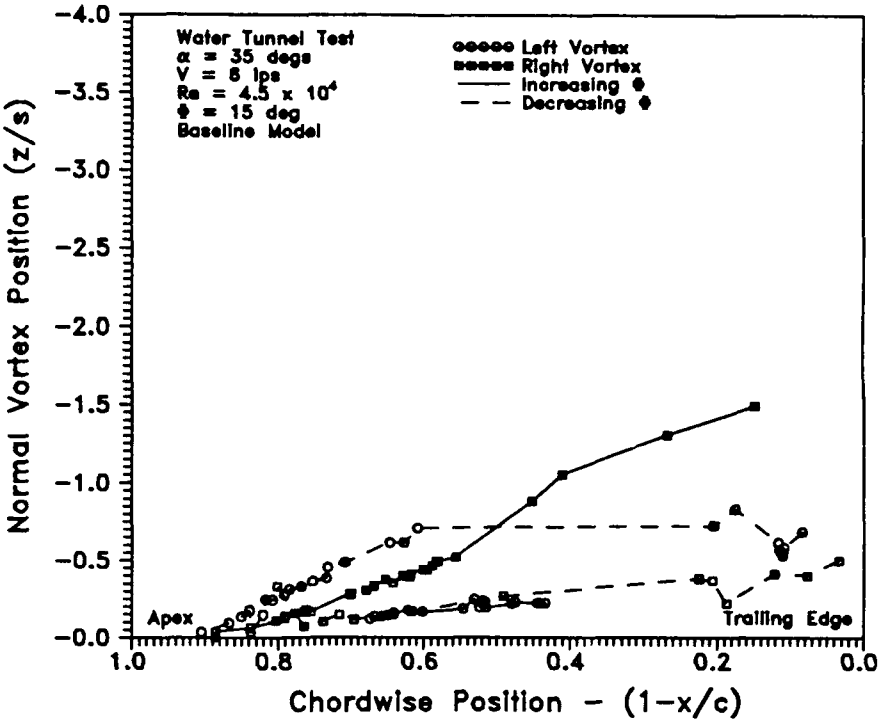

a)

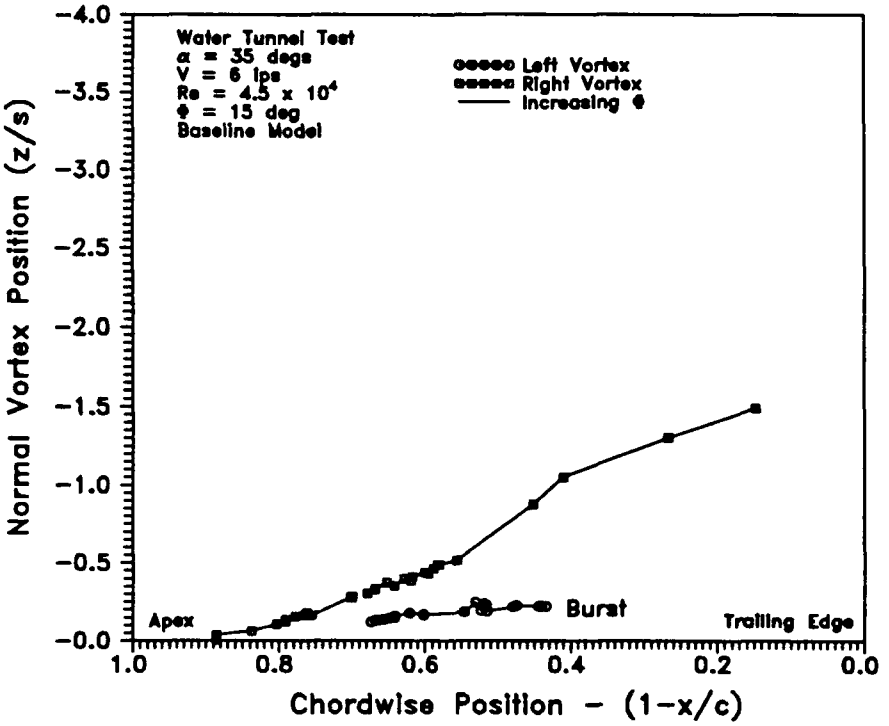

b)

Fig. 102 Normal position of leading edge vortices at ϕ = 15°.

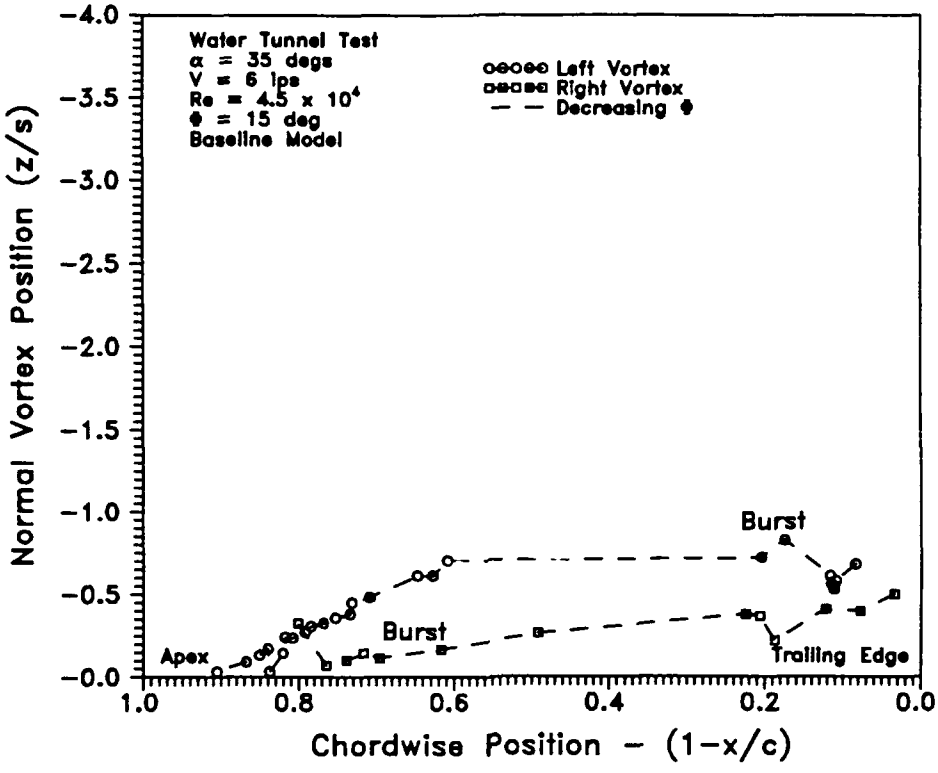

c)

Fig. 102 (continued).

In Fig. 103, the right vortices were still close to the centerline, while the left vortices were further outboard and in some parts, off the wing. As the wing was rolling right, the right vortex moved across the centerline at around the 75% chord station with ϕ passing through 25°. These points were transported further downstream at this bank angle than at 15° (Fig. 101 and Fig. 103) The vortex breakdown was also evident in Fig. 103 for the left vortex. The grouping of points and their wavy form at the end of the vortex was where the burst occurred. Breakdown of the right vortex was not as clear because of the nearly instantaneous bursting. The breakdown occurred ahead of the left burst point because of the effective leading edge sweep

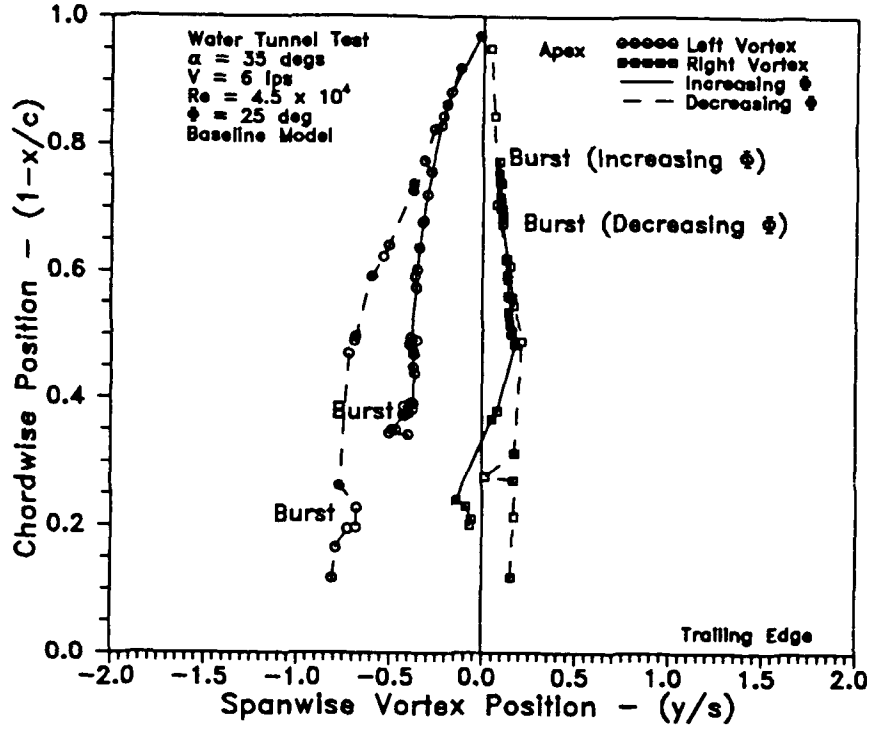

Fig. 103 Spanwise position of the leading edge vortices at $\phi = 25°$.

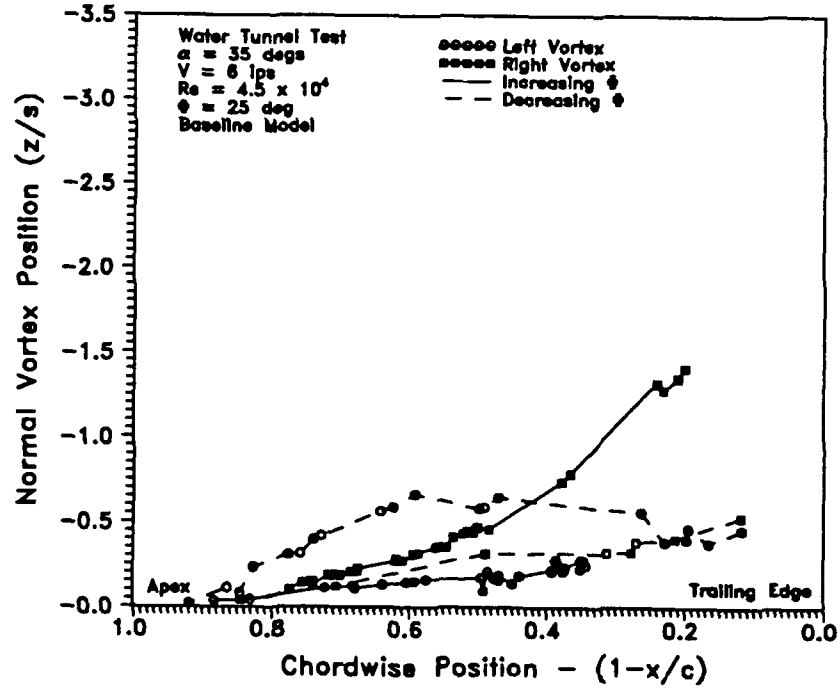

a)

Fig. 104 Normal position of leading edge vortices at $\phi = 25°$.

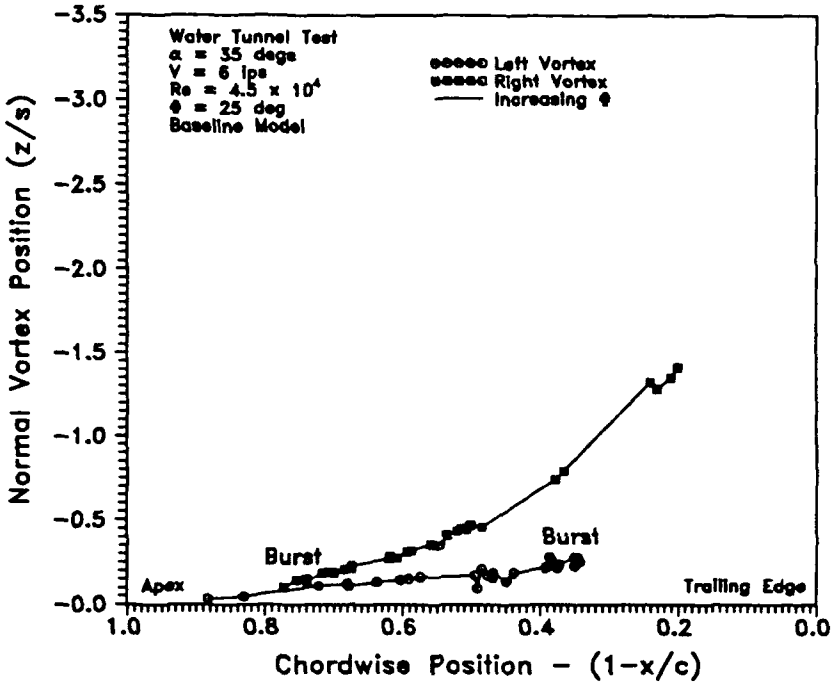

b)

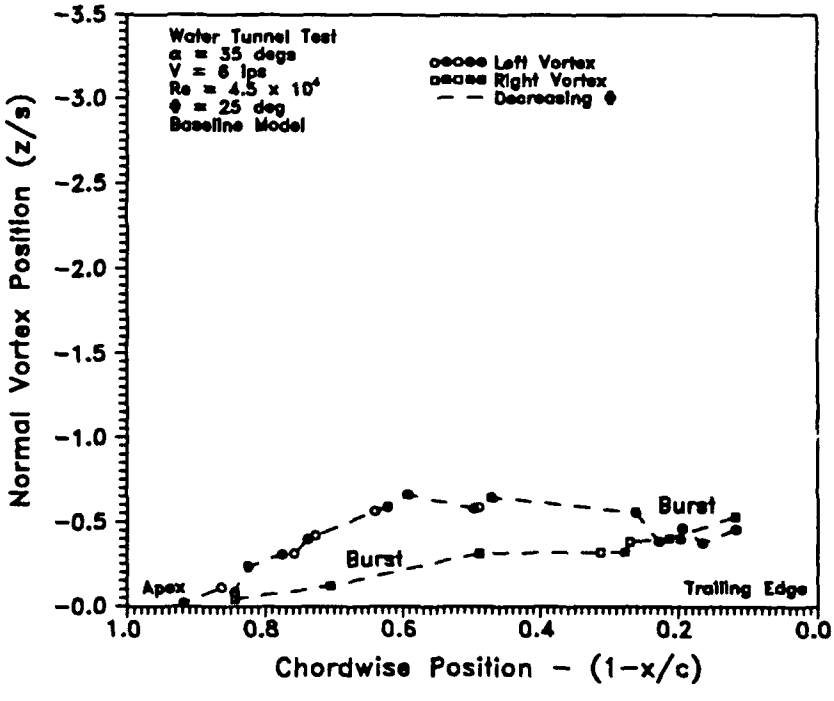

c)

Fig. 104 (continued).

angle. The burst locations were near the grouping of points in Fig. 103. The intact right vortex structure can be seen aft of the burst location. Curvature in the vortices is also noted from Fig. 104. The exchange of vortex positions was evident as the wing rolled in different directions (Fig. 104b and Fig. 104c), as required for the wing rock to continue.

Returning to the rolling moment discussion, the water tunnel wing rock data revealed an increase in rolling moment immediately after passing through the maximum roll amplitude, even though ϕ was decreasing. This hysteresis was opposite of the wind tunnel results. Looking again at the vortex positions as ϕ increased (Fig. 103), the left vortex was outboard on the wing while the right vortex was inboard. It actually crossed over the centerline at approximately x/c = 0.7. The left vortex was positioned nearer the wing than the right one (Fig. 104b). At these positions, assuming similar strengths, the vortices would contribute a positive moment increment. However, the aerodynamic moment was negative at this roll angle. Therefore, summing both the moment increment from the vortex contributions postulated and a sinusoidal aerodynamic moment as a baseline, led to a resultant decrease in magnitude. Remember, this occurred before the wing reached its maximum roll amplitude. After the model had rolled through the maximum roll angle (Fig. 103), the left vortex moved outboard past the wing while the right one stayed closest the wing, generating the lowest pressures. Although vortex burst had occurred, the downstream right vortex structure remained intact. The vortex positions immediately after the wing had passed through the maximum roll angle apparently contributed a negative moment increment. Summing this increment with a baseline sinusoidal aerodynamic moment resulted in an increase in the negative rolling moment. This condition occurred after the passing through the maximum roll angle. Summarizing the above qualitative analysis, a sinusoidal rolling moment was reduced

before rolling through the maximum roll angle and was increased after rolling through the maximum roll amplitude based solely on the positions of the leading edge vortices.

The last set of figures shows the vortex structures at ϕ = 30°. As ϕ increased (Figure 105), the left vortex moved left off the forward part of the wing. The right vortex stayed for the most part over the right half of the wing except aft of about 70% chord. As ϕ decreased, the left vortex continued to move out and up, away from the wing, and the right one stayed close to the centerline. The normal positions of the vortices again reversed depending on the direction of roll. These figures provide additional insight into the complexity of the vortical flow field during wing rock.

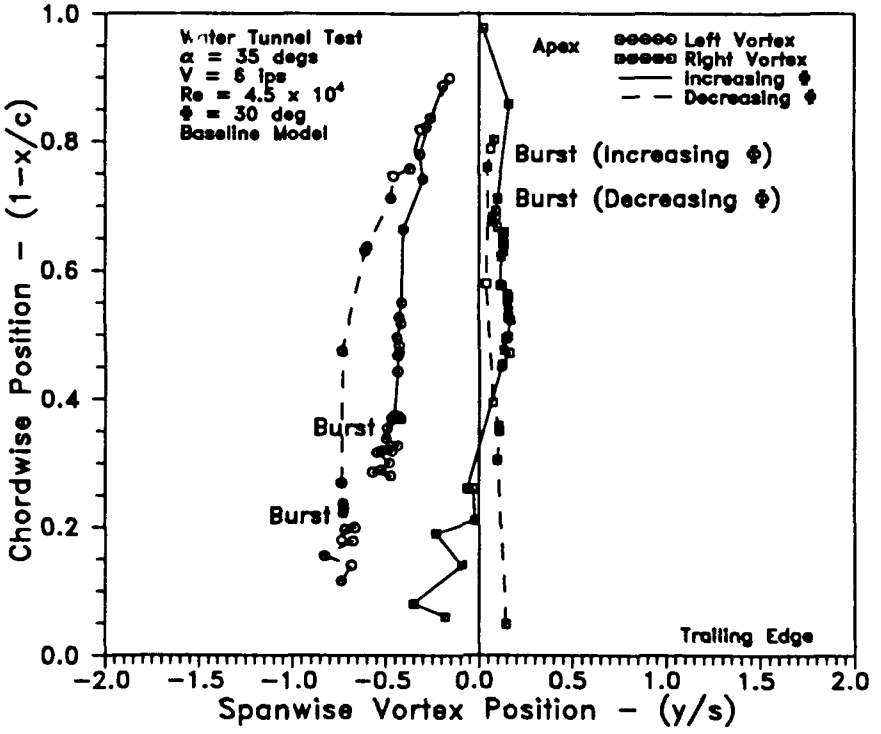

Fig. 105 Spanwise position of the leading edge vortices at ϕ = 30°.

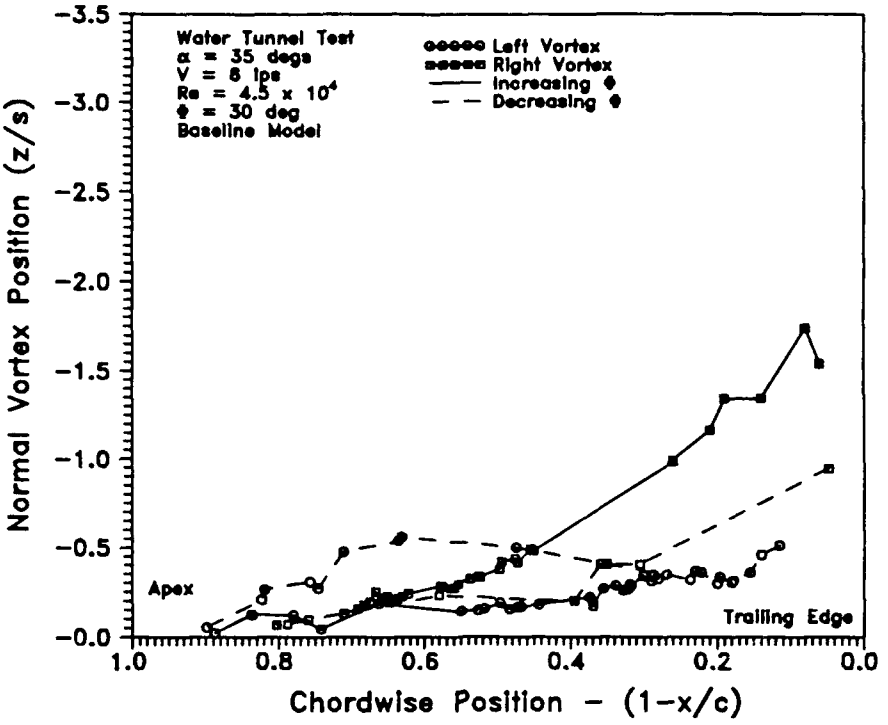

a)

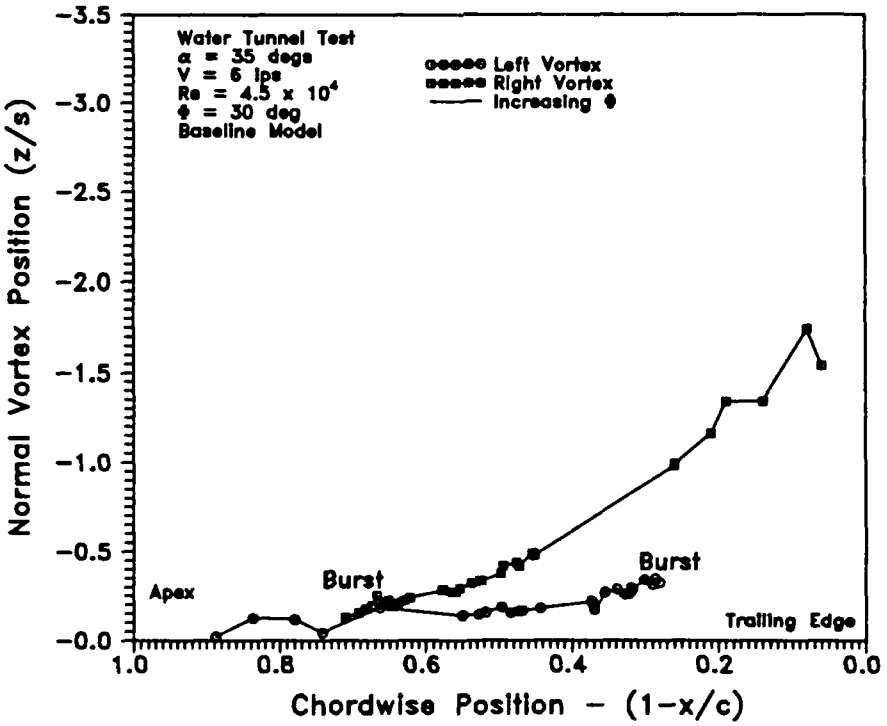

b)

Fig. 106 Normal position of leading edge vortices at $\phi = 30°$.

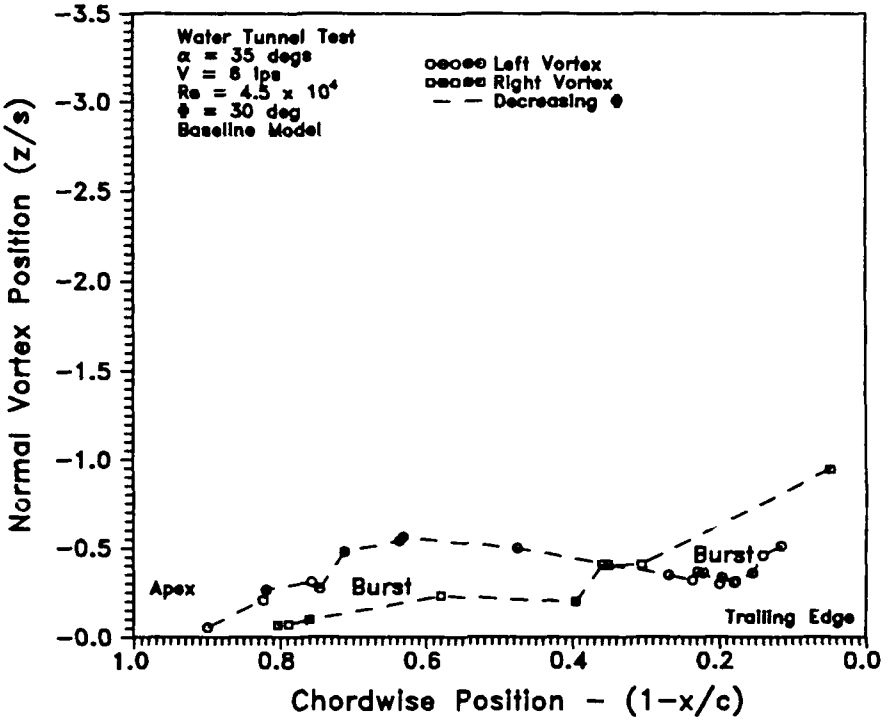

c)

Fig. 106 (continued).

Summary of Water Tunnel Results

The measurements in the water tunnel again showed that there usually was an opposite hysteresis loop compared with wind tunnel measurements. However, a hysteresis direction reversal was recorded at 6 ips for the model w/spinner configuration. Since this phenomenon was not present at the higher tunnel speeds, the direction of hysteresis and its consistency was evidently dependent on the model's Reynolds number. It is postulated that the vortex asymmetries over the spinner were strongly affecting the rolling moment at these conditions. While tunnel turbulence may have contributed to this reversal, the baseline model did not experience this phenomenon at 6 ips. The model w/spinner configuration also had a larger measured

rolling moment than the baseline model alone. Flow visualization results provided a qualitative assessment of the effect of vortex positions on the model motion. A partial explanation for the opposite hysteresis direction was presented based solely on the relative position of the leading edge vortices. Additional vortex core and surface pressure measurements are required to complete this analysis. The flow field in the water tunnel was complex. The three dimensional vortex trajectories showed significant curvature across the model. Also, large hysteresis loops in both the vortex normal and spanwise positions were observed.

Comparative Summary of the Wind and Water Tunnel Results

The results of both a wind tunnel and water tunnel investigation have been presented and discussed above. This section summarizes and compares the wind and water tunnel wing rock and flow visualization studies.

Comparison of Wing Rock Results

A self sustaining wing rock motion occurred in both the wind and water tunnel. Wind tunnel tests conducted on the baseline model at a Reynolds number of 1.54 x 10^5, had an average roll amplitude of 38.5° and a reduced frequency of 0.088. The hysteresis in the rolling moment versus roll angle curve was in a direction such that the outer two loops were counter clockwise and the inner loop was clockwise. The average magnitude of the rolling moment was 0.15, which was very similar to Morris'[3] results. The highest Reynolds number attempted in the water tunnel was 1.125 x 10^5 which corresponded to V_∞ = 15 ips. The average roll amplitude was 30.1° with a reduced frequency of 0.632. The average rolling moment magnitude was 0.0099. The hysteresis in the rolling moment versus roll angle was opposite in direction of the wind tunnel results, except for one particular case. At 6 ips for the

model w/spinner configuration, the hysteresis traveled in both directions for different runs. Hysteresis was very slight at V_∞ = 6 ips as compared with the higher water tunnel speeds. An energy analysis was conducted investigating the buildup of the wing rock motion in both the water and wind tunnels. The results confirm that the change in energy over one cycle must be constant. Water tunnel results did show that energy was being removed from the system at small roll angles and added to the system at large ones.

Added Mass Results

Added mass experiments were also conducted in the wind tunnel. The motion of the wing decreased as mass was added to the model. With all disks on the model, motion diminished. At times, the limit cycle could not be sustained and the model had to be externally disturbed to restart the wing rock. The roll acceleration versus roll angle figures showed how the slope and magnitude of the acceleration curve decreased with increasing inertia. The rolling moment curve was dependent on the inertia of the model and decreased only in magnitude and not slope. Therefore, to solve for the added mass term in the water tunnel, a dynamic similitude between the water tunnel and wind tunnel had to be achieved. In other words, the Reynolds numbers in the water tunnel had to match the Reynolds number in the wind tunnel. To match these Reynolds numbers, the water tunnel had to be run at 18.75 ips. During water tunnel tests, tunnel speeds above 15 ips caused the model to vibrate excessively. Tests could not be conducted above 15 ips simply because the model support rod was not stiff enough.

Comparison of the Flow Visualization Results

The wind tunnel flow visualization surveyed five chordwise stations on the wing. Hysteresis in the vortex normal position was evident and to a lesser degree in the spanwise direction. Data at the x/c = 0.95 station were compared with Arena's[4] results of a delta wing at an angle of attack at 30° and a Reynolds number of 3.48 x 10^5. The spanwise vortex core positions were both similar; y/s = 2.0 to 2.2 for the current study compared with Arena's y/s = 1.7 to 1.85. The current study's vortex normal core positions were higher, z/s = -1.9, as compared with Arena's z/s = 1.2. Variations in angle of attack, Reynolds number, and model configuration (e.g. leading edge bevel) are all plausible explanations for these magnitude differences. The five chordwise stations together showed that the leading edge vortices were basically straight with no noticeable curvature, definitely different from the water tunnel vortex structure.

Water tunnel data revealed three dimensional vortex structures of highly asymmetric character during wing rock. The hysteresis in the vortex core positions was in the normal as well as spanwise directions. Because of tunnel speed and density in the water tunnel, the normal core positions at the $0.25\bar{c}$ and $0.85\bar{c}$ were reversed in position. In addition an analysis based solely on the vortex core positions was presented to partially explain the rolling moment hysteresis loops in the water tunnel.

CHAPTER IV
CONCLUSIONS AND RECOMMENDATIONS

These conclusions are made based on the results presented in Chapter III. They spring from the observed dynamics of the wing rock motion and from the flow visualization of the vortical flow field. Recommendations for continued added mass and flow visualization experiments will also be presented.

Conclusions

Wing Rock Motion

Wing rock in a wind tunnel and in a water tunnel have similarities as well as differences in the motion. In either medium, the model established a self-sustaining limit cycle which developed from a buildup or decay initial condition. Other wind tunnel experiments had similar results compared with the wind tunnel data presented. The water tunnel information also compared well with Morris'[3] data. The fluid densities, over 800 times different, resulted in dissimilar magnitudes in the motion. The rolling moments of the baseline model tested in air was 15 times larger than the water tunnel result. With the spinner the difference decreased to 7 times. These differences were at least partly attributed to the added mass of the water being displaced by the delta wing during oscillation. Reynolds numbers differed as well between water tunnel and wind tunnel tests, and they also led to dynamic variations. The wind tunnel results revealed a slight unsteadiness in the roll oscillations. The support rod connected to the model was lengthened to reduce interference effects of the added mass attachment, but its flexibility then contributed to excessive model vibrations. As the rod was shortened, the variation in maximum roll angles between

cycles gradually decreased, though slight variations were still present in the reduced data.

The direction of the rolling moment hysteresis loop was also different between the two testing media. This difference was present in the water tunnel data except that for the model w/spinner configuration at 6 ips. For this special case, hysteresis was observed traveling in both ways between the different runs. At higher tunnel speeds, the data were consistent with the baseline results. It was concluded that for this one model configuration, hysteresis was Reynolds number dependent. The hysteresis observed in this particular case was much smaller than for higher tunnel speeds. The data were consistent with the hysteresis direction that Morris[3] had discovered, except for this one set of runs.

Kinetic energy changes were calculated continuously for both water and wind tunnel cases to provide further insight into the dynamics of the motion. The net kinetic energy exchange during both experiments was balanced for the steady motion, as expected for a limit cycle to exist. In the water tunnel data, at the outer lobes of the rolling moment coefficient curve, the net energy exchange was positive. To balance this gain, the system lost energy before reaching the zero roll angle. If such were not the case, the system would have diverged and no limit cycle would have been possible. The buildup case in the water tunnel revealed a positive net energy change over each cycle until the amplitudes for the steady limit cycle were reached.

Kinetic energy plots for the wind tunnel data showed opposite characteristics. The energy increment was higher before the maximum roll angle and less afterward. The energy was positive as the model crossed the zero roll angle giving a net energy of zero during the steady cycle. During buildup it was observed as well that the net energy per cycle was positive until the limit cycle had been reached. While the

kinetic energy analyses were consistent for both cases, visualization of the vortical flow was required for more insight into the driving mechanisms.

Flow Visualization Studies

Previous studies have concluded that the motion exists due to asymmetries between the leading edge or forebody vortices. Flow visualization experiments were conducted and analyzed carefully to quantify right and left vortex locations. The results of the wind tunnel investigation show relatively straight vortices alternately lifting off and reattaching to the delta wing during wing rock. There is no apparent change in the vortices from chord station to chord station other than an increase in size of the cross-section path. There was a 14° difference in maximum roll angle magnitudes between wing rock and flow visualization measurements, perhaps due to interference effects of the upstream smoke wand. Variation in the smoke stream and lighting changes resulted in no video data at the 25% and 50% chord stations. While these problems existed, the EV system was able to track and quantify vortex locations over the wing at other chord stations.

The water tunnel flow visualization revealed a much more complex vortical flow field. The vortices were three-dimensional in form as compared to the essentially two-dimensional wind tunnel counterparts. The data obtained were collected into cross sectional chordwise plots and trajectory plots that spanned the length of the model. Analysis of the right and left vortex locations at various roll angles constructed a partial explanation for the opposite hysteresis loop in the rolling moment data. The vortex asymmetries in spanwise and normal positions before and after the model reached maximum roll amplitudes provide a possible explanation. While specific burst locations were not quantitatively tracked, qualitative information showed that the windward vortex burst instantaneously about the 30% chord station and that the

downstream structure remained intact. This phenomenon led to an actual increase in the moment after the wing passed through the maximum roll amplitude. Wind tunnel investigations have shown the burst locations moving forward and aft during roll oscillations. This movement of the windward vortex burst point was very different in the water tunnel. Once again, flow visualization, especially when quantified using video imaging, added to the understanding of wing rock dynamics.

Added Mass Experiment

The investigation of the added mass associated with water tunnel testing provided an experimental foundation for future analyses. Wind tunnel tests were successful in quantifying the wing rock motion as mass inertia was incremented. However, an unexpected increase in the rolling moment was discovered when the added mass attachment was connected to the model. Possible causes for this increase, were asymmetric vortices shedding from the spinner and interference effects of the spinner on the leading edge vortices over the wing. Although no visual data were obtained over the spinner, testing of this configuration both in the wind tunnel and water tunnel provided similar results. Rolling moments increased for both tests.

Dynamic similitude with wind tunnel data was not achieved during water tunnel testing because of structural vibrational problems with the model support. Above 15 ips, the model began to vibrate excessively. A water tunnel speed of 18.75 ips was required to match the Reynolds number of the wind tunnel. The wind tunnel was operated at a dynamic pressure of 1 psf. At this low speed the tunnel control was imprecise, holding $\bar{q}$ at ±5%. Additional testing will be required to accurately achieve dynamic similitude and quantify apparent mass observed in the water tunnel.

Recommendations

The recommendations fall into three main areas; quantifying vortical flow, added mass experiments, and flow visualization improvements. Improving these areas should provide more substantial information in evaluating differences between wind and water tunnel tests.

Quantifying Vortical Flow

The water tunnel vortex position data were presented and analyzed to explain the observed rolling moment hysteresis. The strength of the vortices was not quantified, making the analysis incomplete. It is recommended that a system, such as a laser doppler velocimeter system, be used to determine the axial core velocities of the leading edge vortices during wing rock. From this information the strength of each vortex will be known along the wing and more conclusive information concerning the rolling moment hysteresis can be presented.

Added Mass Experiments

Further analysis between wind and water tunnel results can made if the added mass component can be found. The support system of the current model must be redesigned to provide a stiffer support rod for the model. In addition to this support redesign, consideration must be made for the flow over the added mass attachment and effects of the upstream flow on the model. It clearly affected the model's limit cycle. The most obvious fix would be to remove it from the flow entirely. This would require a longer support rod to keep the model in the smooth flow stream. Other possibilities include shielding the oscillating spinner from the oncoming flow. The support rod would have to be lengthened accordingly to reduce flow interference effects about the model. In addition, to reduce the Reynolds number gap, using a

wind tunnel with better flow characteristics at low speeds would be helpful or increasing the water tunnel flow rate. Solving for the added mass term does not require incrementing mass if the Reynolds numbers are equivalent, but doing so would provide experimental redundancy.

Flow Visualization

Flow visualization was an integral part of this work and will continue to grow in importance with video-based analysis systems. Future wind tunnel flow visualization should include a more repeatable seeding technique for the video data. Excessive smoke engulfed the model and made tracking of the vortex cores a frame by frame editing chore. Disturbances were also introduced upstream by the smoke wand. Smoke may be entrained into the leading edge vortices by porting it through hypodermic tubing along the bottom of the model, like the water tunnel tests. Although a major task, pressure tests will have to be completed to quantify the exit pressure at the apex. The laser light sheet illuminated the vortex cores adequately at specific chordwise locations. Without this equipment, there would have been no wind tunnel quantified vortex positions from the flow visualization.

Water tunnel flow visualization was relatively successful. One recommendation would be to complete more runs to enlarge the data sets, especially at the aft chordwise positions. Another possibility is to use the laser light sheet in the same way as in the wind tunnel tests. Specific chordwise data could then be obtained and reduced.

REFERENCES

[1]Ross, A.J., "Investigation of Nonlinear Motion Experienced on a Slender-Wing Research Aircraft," *Journal of Aircraft*, Vol. 9, Sept. 1972, pp. 625-631.

[2]"High Alpha Technology Program Workshop," Ames-Dryden Flight Research Facility, Nov. 1-2, 1989.

[3]Morris, S.L., "A Video-Based Experimental Investigation of Wing Rock," Ph.D. Dissertation, Texas A&M University, August 1989.

[4]Arena, A.S., "An Experimental Study of the Nonlinear Wing Rock Phenomenon," M.S. Thesis, University of Notre Dame, April 1990.

[5]Arena, A.S., Nelson, R.C., and Schiff, L.B.,"An Experimental Study of the Nonlinear Dynamic Phenomenon Known as Wing Rock," AIAA Paper 90-2812-CP, June 1990.

[6]Arena Jr., A.S., and Nelson, R.C., "The Effect of Asymmetric Vortex Wake Characteristics on a Slender Delta Wing Undergoing Wing Rock Motion," AIAA Paper 89-3348, Aug. 1989.

[7]Nguyen, L.T., Yip, L., and Chambers, J.R.,"Self-Induced Wing Rock of Slender Delta Wings," AIAA Paper 81-1883, August 1981.

[8]Levin, D., and Katz, J., "Dynamic Load Measurements with Delta Wings Undergoing Self-Induced Roll Oscillations," *Journal of Aircraft*, Vol. 21, Jan. 1984, pp. 30-36.

[9]Jun, Y.W., and Nelson, R.C., "Leading Edge Vortex Dynamics on a Delta Wing Undergoing a Wing Rock Motion," AIAA Paper 87-0332, Jan. 1987.

[10]Ericsson, L.E., "The Fluid Mechanics of Slender Wing Rock," *Journal of Aircraft*, Vol. 21, May 1984, pp. 322-328.

[11]Polhamus, E.C., "Predictions of Vortex-Lift Characteristics by a Leading-Edge Suction Analogy," *Journal of Aircraft*, Vol. 8, April 1971, pp. 193-199.

[12]Hsu, C.H., and Lan, C.E., "Theory of Wing Rock," *Journal of Aircraft*, Vol. 22, Oct 1985, pp. 920-924.

[13]Beecham, L.J., and Titchener, I.M., "Some Notes on Approximate Solution for the Free Oscillation Characteristics of Non-Linear Systems Typified by $\ddot{x}+F(x,\dot{x})=0$," British ARC R&M 3651, Aug. 1969.

[14]Konstadinopoulos, P., Mook, D.T., and Nayfeh, A.H., "Subsonic Wing Rock of Slender Delta Wings," *Journal of Aircraft*, Vol. 22, Mar. 1985, pp. 223-228.

[15]Ericsson, L.E., and Reding, J.P., "Review of Support Interference in Dynamic Tests," *AIAA Journal*, Vol. 21, Dec. 1983, pp. 1652-1666.

[16]Kubler, T.J., "Design of a High Angle of Attack Robotic Sting Mount for Tests in a Low Speed Wind Tunnel," M.S. Thesis, Texas A&M University, August 1989.

[17]ExpertVision Reference Manual, Motion Analysis Corporation, Santa Rosa, California, 1991.

[18]ExpertVision User Manual, Motion Analysis Corporation, Santa Rosa, California, 1991.

[19]"Video Analog Collection System", Motion Analysis Corporation, Santa Rosa California, Jan. 1991.

[20]"ExpertVision Programmers Reference Manual," Motion Analysis Corporation, Santa Rosa, California, 1989.

[21]Ward, D.T.,"Nonlinear Analysis Tools for Dynamics and Control of Aircraft and Spacecraft", Notes, pp. 35-43.

[22]Ericsson, L.E., Beyers, M.E., "Rotary-Balance Testing for Aircraft Dynamics," AGARD-AR-265, pp. 77-97, 1990.

[23]Fox, R.W., and McDonald, A.T., "Introduction to Fluid Mechanics,", 2nd Ed., Wiley & Sons, New York, 1978, pp. 318-321.

APPENDIX A

DYNAMIC CODE LISTING

```
/*  DYNAMIC.C:  This program was designed to transform and reduce track data of
a delta wing during wing rock.  The program is centered around two subroutines.  The
first subroutine opens an EV binary track file that is used only for computing the
reference frame of the delta wing.  The second subroutine opens the track file which
contains the dynamic data.  This routine transforms the data to a body reference frame
and outputs a data file for each target tracked.  Specific setup procedures are discussed
in each subroutine.                                                    */

/*  Written:  3 Dec 1990  Revised:  1 May 1991  Number:  3
    By:  Michael D. Nelson  PTL                                        */

#include <stdio.h>
#include <math.h>
#include <string.h>

#define PI (4*atan(1.0))
#define R2D (180.0/(4*atan(1.0)))
#define D2R (4*atan(1.0)/180.0)

main()
{
   int i;
   float **ref, *dang, *posref, *angref;
   float dz, dphi, dtheta, dpsi, airspeed, airdensity, waterspeed, waterdensity;
   float qbar, ixx, dumnum, ch;
   char *stfile, *dyfile, *dumstring;
   char choice;
   int choice1;
   FILE *fp;

/*  Reference position of body coordinate axes  */

   ref = (float **) malloc( 3 * sizeof(float *));
   for(i=0; i<3; i++)
      ref[i] = (float *) malloc( 3 * sizeof(float));

   dang = (float *) malloc( 3 * sizeof(float));
   posref = (float *) malloc( 3 * sizeof(float));
   angref = (float *) malloc( 3 * sizeof(float));
   stfile = (char *) malloc( 10 * sizeof(char));
   dyfile = (char *) malloc( 10 * sizeof(char));
   dumstring = (char *) malloc( 10 * sizeof(char));

start:

/*  Measurement adjustments to correct for offset of static points in
```

```
    the model reference frame  */

   dz     =  0.135;
   dphi   = -0.100;
   dtheta =  0.020;
   dpsi   =  0.0;

/*  Binary data file that contains initial information  */

   if((fp=fopen( "dynamic.dat", "r+b" )) == NULL)
   {
     printf( "Error opening file\n" );
     exit(1);
   }

   fread(&stfile[0], sizeof(char), 10, fp);
   fread(&dyfile[0], sizeof(char), 10, fp);
   fread(&ixx, sizeof(float), 1, fp);
   fread(&qbar, sizeof(float), 1, fp);
   fread(&waterspeed, sizeof(float), 1, fp);
   fread(&waterdensity, sizeof(float), 1, fp);
   fread(&airspeed, sizeof(float), 1, fp);
   fread(&airdensity, sizeof(float), 1, fp);

/*  Assignment of delta angle pointer  */

   *(dang+0) = dphi;
   *(dang+1) = dtheta;
   *(dang+2) = dpsi;

/*  Main menu for inputs  */

menu:
   printf("\f");
   printf("\t\t EV DATA REDUCTION PROGRAM\n\n\n");
   printf("Change a default value and/or reduce data\n\n");
   printf("\ta. Static Data File \t\t%s\n", stfile );
   printf("\tb. Dynamic Data File\t\t%s\n", dyfile );
   printf("\tc. Model Inertia     \t\t%6.4e slugs-ft^2\n", ixx );
   printf("\td. Dynamic Pressure \t\t%6.4f psf\n", qbar );
   printf("\te. Reduce Data\n\n" );
   scanf("%1sc", &choice );

   switch (choice)
   {
     case 'a':
          printf("\tEnter Static Data File < %s >: ", stfile );
          scanf("%s", stfile );
          goto menu;

     case 'b':
          printf("\tEnter Dynamic Data File < %s >: ", dyfile );
```

```
        scanf("%s", dyfile );
        goto menu;

      case 'c':
        printf("\tEnter Model Inertia, Ixx < %6.4e >: ", ixx );
        scanf("%f", &dumnum);
        if( dumnum != 0 )
          ixx = dumnum;
        goto menu;

      case 'd':
        printf("\t\t1. Watertunnel\n");
        printf("\t\t2. Windtunnel\n\n");
        scanf( "%d", &choice1 );

        if(choice1 == 1)
        {
          printf("\tTunnel speed < %6.4f > ips ", waterspeed );
          scanf("%f", &dumnum );
          if( dumnum != 0 )
            waterspeed = dumnum;

          printf("\n\n\tDensity < %6.4e > slugs/ft^3 ", waterdensity );
          scanf("%f", &dumnum );
          if( dumnum != 0 )
            waterdensity = dumnum;

          qbar = 0.5 * waterdensity * waterspeed * waterspeed / 144.0;
        }
        else
        {
          printf("\tTunnel speed < %6.4f > fps ", airspeed );
          scanf("%f", &dumnum );
          if( dumnum != 0 )
            airspeed = dumnum;

          printf("\n\n\tDensity < %6.4e > slugs/ft^3 ", airdensity );
          scanf("%f", &dumnum );
          if( dumnum != 0 )
            airdensity = dumnum;

          qbar = 0.5 * airdensity * airspeed * airspeed;
        }
        goto menu;

      case 'e':

        rewind(fp);
        fflush(fp);

/*  Rewriting information to binary file  */
```

```
            fwrite(&stfile[0], sizeof(char), 10, fp);
            fwrite(&dyfile[0], sizeof(char), 10, fp);
            fwrite(&ixx, sizeof(float), 1, fp);
            fwrite(&qbar, sizeof(float), 1, fp);
            fwrite(&waterspeed, sizeof(float), 1, fp);
            fwrite(&waterdensity, sizeof(float), 1, fp);
            fwrite(&airspeed, sizeof(float), 1, fp);
            fwrite(&airdensity, sizeof(float), 1, fp);

            fclose(fp);

            goto execute;

        default:
            exit(1);
            break;
    }

execute:

/*  Compute body reference angles and positions relative to inertial axes  */

    reference( ref, dang, dz, posref, angref, stfile );

/*  Transform data into a moving body reference frame  */

    trans( ref, dang, dz, posref, angref, ixx, qbar, dyfile );

    goto start;
}


/*************************************************************************/
        reference( refp, dangp, dz, posref, angref, stfile )
        float **refp, *dangp, dz, *posref, *angref;
        char *stfile;
/*************************************************************************/

/*  This subroutine opens a binary file containing static data for the
    three points on the delta wing, where point 1 is the body origin at the
    trailing edge and centerline of the delta wing; point 2 is the 0.5c,
    and point 3 is on the wing tip of the delta wing.  This information is
    used to compute the translation coordinates and euler angle rotations to
    transform the dynamic data into the appropriate body frame.  When taking
    this video data, the delta wing should be at zero bank angle.          */

{
    FILE *fp;
    short int nmpts;
    int i, j, mark;
    float **x, **y, **z;
    float dumx, dumy, dumz, dummy, *xcross, *ycross, *zcross;
```

```
    float *xavg, *yavg, *zavg, *xt, *yt, *zt, *xdum, *ydum, *zdum;
    float *xtrans, *ytrans, *ztrans, *pos, *ang;
    float *rang, *rdang, rdz;

/*  Reference unit vectors to compute orthogonal body axes  */

    static float xref[] = { 0, 1, 0 };
    static float yref[] = { 0, 0, 1 };
    static float zref[] = { 0, 0, 0 };

/*  Coordinate locations read from static wing data  */

    x = (float **) malloc( 200 * sizeof(float *));
    y = (float **) malloc( 200 * sizeof(float *));
    z = (float **) malloc( 200 * sizeof(float *));

    for(i=0; i<200; i++)
    {
       x[i] = (float *) malloc( 3 * sizeof(float));
       y[i] = (float *) malloc( 3 * sizeof(float));
       z[i] = (float *) malloc( 3 * sizeof(float));
    }

    xavg = (float *) malloc( 3 * sizeof(float) );
    yavg = (float *) malloc( 3 * sizeof(float) );
    zavg = (float *) malloc( 3 * sizeof(float) );
    xdum = (float *) malloc( 3 * sizeof(float) );
    ydum = (float *) malloc( 3 * sizeof(float) );
    zdum = (float *) malloc( 3 * sizeof(float) );
    xt = (float *) malloc( 3 * sizeof(float) );
    yt = (float *) malloc( 3 * sizeof(float) );
    zt = (float *) malloc( 3 * sizeof(float) );
    xcross = (float *) malloc( 2 * sizeof(float) );
    ycross = (float *) malloc( 2 * sizeof(float) );
    zcross = (float *) malloc( 2 * sizeof(float) );
    pos = (float *) malloc( 3 * sizeof(float) );
    ang = (float *) malloc( 3 * sizeof(float) );
    rang = (float *) malloc( 3 * sizeof(float) );
    rdang = (float *) malloc( 3 * sizeof(float) );
    xtrans = (float *) malloc( 3 * sizeof(float) );
    ytrans = (float *) malloc( 3 * sizeof(float) );
    ztrans = (float *) malloc( 3 * sizeof(float) );

/*  Opening static data file  */

    if((fp = fopen(stfile,"rb"))==NULL)
    {
      printf("Error opening file\n");
      exit(1);
    }

/*  Number of points in the largest data record  */
```

```
   fseek(fp, 14, 0);
   fread(&nmpts, 2, 1, fp);

/* Actual data points minus record information, divided by three coordinate
   directions and two two-byte words */

   nmpts = (nmpts-14)/2/3;

   mark = 512;                  /* Byte marker for binary file */

   for( j=0; j<3; j++ )         /* Loop to read from binary file */
   {
     fseek(fp, mark+28, 0);     /* Location of first data point */

     dumx = 0;
     dumy = 0;
     dumz = 0;

     for( i=0; i<nmpts; i++ )       /* Incrementing points of target */
     {
       fread(*(x+j)+i, 4, 1, fp);
       fread(*(y+j)+i, 4, 1, fp);
       fread(*(z+j)+i, 4, 1, fp);

       dumx = dumx + *(*(x+j)+i);       /* Summing points */
       dumy = dumy + *(*(y+j)+i);
       dumz = dumz + *(*(z+j)+i);
     }

     mark = ftell(fp);        /* File position of stream */

     fseek(fp, mark+28, 0);

     *(xavg+j) = dumx/nmpts;          /* Taking average locations */
     *(yavg+j) = dumy/nmpts;
     *(zavg+j) = dumz/nmpts;
   }

   *(pos+0) = *(xavg+0);
   *(pos+1) = *(yavg+0);
   *(pos+2) = *(zavg+0);
   *(posref+0) = *(xavg+0);
   *(posref+1) = *(yavg+0);
   *(posref+2) = *(zavg+0);

/* Translation of data to delta wing origin */

   translation( xavg, yavg, zavg, xt, yt, zt );

/* Correction for non orthogonal points on wing */

   crossproduct( *(xt+1),*(yt+1),*(zt+1),*(xt+2),*(yt+2),*(zt+2),
```

```
                    xcross,ycross, zcross );

    crossproduct( *xcross,*ycross,*zcross,*(xt+1),*(yt+1),*(zt+1),
                  &xcross[1],&ycross[1],&zcross[1] );

    *(xt+2) = *(xcross+1);
    *(yt+2) = *(ycross+1);
    *(zt+2) = *(zcross+1);

/*  Calculation of the angles between inertial and initial body axes  */
/*                          3-2-1 Rotation  */

    rotation1( xt, yt, zt, ang );

/*  Reference angles used in trans subroutine to compute dynamic data  */

    for(i=0; i<3; i++)
      *(angref+i) = *(ang+i);

/*  Points on wing transformed to the delta wing body axes; a check  */

    rotate( xavg,yavg,zavg,pos,ang,dangp,xtrans,ytrans,ztrans,dz );

    for(i=0; i<3; i++)
    {
       *(rang+i) = - *(ang+i);
       *(rdang+i) = - *(dangp+i);
    }

    rdz = -dz;

/*  Transforming Body Reference Axes to Inertial Reference frame  */

    revrotate( pos,xref,yref,zref,rang,rdang,xtrans,ytrans,ztrans,rdz );

/*  Location of body coordinate axes relative to inertial frame  */

    for( i=0; i<3; i++)
    {
       *(*(refp+i)+0) = *(xtrans+i);
       *(*(refp+i)+1) = *(ytrans+i);
       *(*(refp+i)+2) = *(ztrans+i);
    }

    fclose(fp);

/* Freeing memory up  */

    free(x);
    free(y);
    free(z);
```

```
   return;
}


/*************************************************************************/
      translation( x, y, z, xtp, ytp, ztp )
      float x[3], y[3], z[3], *xtp, *ytp, *ztp;
/*************************************************************************/

{
   int i;

/*  Translation of inertial axes to centerline point at 1.0c station  */

   for( i=0; i<3; i++ )
   {
      *(xtp+i) = x[i] - x[0];
      *(ytp+i) = y[i] - y[0];
      *(ztp+i) = z[i] - z[0];
   }

   return;
}


/*************************************************************************/
      crossproduct( x1, y1, z1, x2, y2, z2, x3, y3, z3)
      float x1, y1, z1, x2, y2, z2, *x3, *y3, *z3;
/*************************************************************************/
{

/*  Taking cross products to form an orthogonal axis system  */

   *x3 = y1*z2 - y2*z1;
   *y3 = z1*x2 - x1*z2;
   *z3 = x1*y2 - x2*y1;

   return;
}


/*************************************************************************/
      rotation1( xp, yp, zp, ang )
      float *xp, *yp, *zp, *ang;
/*************************************************************************/

/*  This subroutine calculates the angles between the body fixed axes
    and the inertial axes. The transform is a 3-2-1 transformation from
    the body to the inertial axis system.  */

{
   int i;
```

```
    float x1[3], y1[3], z1[3], x2[3], y2[3], z2[3];

/*  Psi calculation and rotation  */

    *(ang+2) = acos(*(xp+1)/sqrt(*(xp+1) * *(xp+1) + *(yp+1) * *(yp+1)));

    if( *(yp+1) < 0 )
      *(ang+2) = -fabs( *(ang+2) );
    else
      *(ang+2) = fabs( *(ang+2) );

    for(i=0; i<3; i++)
    {
       x1[i] = *(xp+i)*cos(*(ang+2)) + *(yp+i)*sin(*(ang+2));
       y1[i] = -*(xp+i)*sin(*(ang+2)) + *(yp+i)*cos(*(ang+2));
       z1[i] = *(zp+i);
    }

/*  Theta calculation and rotation  */

    *(ang+1) = acos(x1[1]/sqrt(x1[1]*x1[1] + z1[1]*z1[1]));

    if( z1[1] < 0 )
      *(ang+1) =  fabs( *(ang+1) );
    else
      *(ang+1) = -fabs( *(ang+1) );

    for(i=0; i<3; i++)
    {
       x2[i] = x1[i]*cos(*(ang+1)) - z1[i]*sin(*(ang+1));
       y2[i] = y1[i];
       z2[i] = x1[i]*sin(*(ang+1)) + z1[i]*cos(*(ang+1));
    }

/*  Phi calculation and rotation  */

    *(ang+0) = acos(y2[2]/sqrt(y2[2]*y2[2] + z2[2]*z2[2]));

    if( z2[2] < 0 )
      *(ang+0) = - fabs( *(ang+0) );
    else
      *(ang+0) = fabs( *(ang+0) );

    for(i=0; i<3; i++)
    {
       *(xp+i) = x2[i];
       *(yp+i) = y2[i]*cos(*(ang+0))+ z2[i]*sin(*(ang+0));
       *(zp+i) = -y2[i]*sin(*(ang+0))+ z2[i]*cos(*(ang+0));
    }

    return;
}
```

```
/*************************************************************************/
      rotation( xp, yp, zp, ang )
      float *xp, *yp, *zp, *ang;
/*************************************************************************/

/*  This subroutine computes angles between two body axes systems  */

{
   int i;
   float x1[3], y1[3], z1[3], x2[3], y2[3], z2[3];

/*  Psi calculation and rotation  */

   *(ang+2) = acos(*(xp+1)/sqrt(*(xp+1) * *(xp+1) + *(yp+1) * *(yp+1)));

   if( *(yp+1) < 0 )
     *(ang+2) = fabs( *(ang+2) );
   else
     *(ang+2) = - fabs( *(ang+2) );

   for(i=0; i<3; i++)
   {
      x1[i] = *(xp+i)*cos(*(ang+2)) + *(yp+i)*sin(*(ang+2));
      y1[i] = -*(xp+i)*sin(*(ang+2)) + *(yp+i)*cos(*(ang+2));
      z1[i] = *(zp+i);
   }

/*  Theta calculation and rotation  */

   *(ang+1) = acos(x1[1]/sqrt(x1[1]*x1[1] + z1[1]*z1[1]));

   if( z1[1] < 0 )
     *(ang+1) = - fabs( *(ang+1) );
   else
     *(ang+1) = fabs( *(ang+1) );

   for(i=0; i<3; i++)
   {
      x2[i] = x1[i]*cos(*(ang+1)) - z1[i]*sin(*(ang+1));
      y2[i] = y1[i];
      z2[i] = x1[i]*sin(*(ang+1)) + z1[i]*cos(*(ang+1));
   }

/*  Phi calculation and rotation  */

   *(ang+0) = acos(y2[2]/sqrt(y2[2]*y2[2] + z2[2]*z2[2]));

   if( z2[2] < 0 )
     *(ang+0) =  fabs( *(ang+0) );
   else
     *(ang+0) = - fabs( *(ang+0) );
```

```
   for(i=0; i<3; i++)
   {
      *(xp+i) = x2[i];
      *(yp+i) = y2[i]*cos(*(ang+0))+ z2[i]*sin(*(ang+0));
      *(zp+i) = -y2[i]*sin(*(ang+0))+ z2[i]*cos(*(ang+0));
   }

   return;
}


/*********************************************************************/
      rotate( xp, yp, zp, pos, ang, dang, xnew, ynew, znew, dz )
      float *xp,*yp,*zp,*pos,*ang,*dang,*xnew,*ynew,*znew,dz;
/*********************************************************************/

/*  This subroutine is used to transform the data in the inertial frame
    to a body frame   */

{
   int i;
   float xt[3], yt[3], zt[3], x1[3], y1[3], z1[3];
   float x2[3], y2[3], z2[3], x3[3], y3[3], z3[3], x4[3], y4[3], z4[3];
   float xa[3], ya[3], za[3], xb[3], yb[3], zb[3];
   float phi, theta, psi, dphi, dtheta, dpsi;

   phi = *(ang+0);
   theta = *(ang+1);
   psi = *(ang+2);

   dphi = *(dang+0);
   dtheta = *(dang+1);
   dpsi = *(dang+2);

/*  Rotation from inertial to offset body axes  */

   for( i=0; i<3; i++ )
   {

/*  Translation  */

      *(xt+i) = *(xp+i) - *(pos+0);
      *(yt+i) = *(yp+i) - *(pos+1);
      *(zt+i) = *(zp+i) - *(pos+2);

/*  Psi rotation  */

      xa[i] = *(xt+i)*cos(psi) +*(yt+i)*sin(psi);
      ya[i] = -*(xt+i)*sin(psi) +*(yt+i)*cos(psi);
      za[i] = *(zt+i);

/*  Theta rotation  */
```

```
    float phi, theta, psi, dphi, dtheta, dpsi;

    phi = *(ang+0);
    theta = *(ang+1);
    psi = *(ang+2);

    dphi = *(dang+0);
    dtheta = *(dang+1);
    dpsi = *(dang+2);

    for(i=0; i<3; i++ )
      *(zr+i) = *(zr+i) - dz;

    for(i=0; i<3; i++ )
    {
      x1[i] = *(xr+i)*cos(dpsi) + *(yr+i)*sin(dpsi);
      y1[i] = -*(xr+i)*sin(dpsi) + *(yr+i)*cos(dpsi);
      z1[i] = *(zr+i);

      x2[i] = x1[i]*cos(dtheta) - z1[i]*sin(dtheta);
      y2[i] = y1[i];
      z2[i] = x1[i]*sin(dtheta) + z1[i]*cos(dtheta);

      x3[i] = x2[i];
      y3[i] = y2[i]*cos(dphi) + z2[i]*sin(dphi);
      z3[i] = -y2[i]*sin(dphi) + z2[i]*cos(dphi);
    }

/*  Phi rotation  */

   for(i=0; i<3; i++)
   {
      xb[i] = x3[i];
      yb[i] = y3[i]*cos(phi)+ z3[i]*sin(phi);
      zb[i] = -y3[i]*sin(phi)+ z3[i]*cos(phi);

/*  Theta rotation  */

      xa[i] = xb[i]*cos(theta) - zb[i]*sin(theta);
      ya[i] = yb[i];
      za[i] = xb[i]*sin(theta) + zb[i]*cos(theta);

/*  Psi rotation  */

      xt[i] = xa[i]*cos(psi) +ya[i]*sin(psi);
      yt[i] = -xa[i]*sin(psi) +ya[i]*cos(psi);
      zt[i] = za[i];
   }

/*  Translation  */

   for( i=0; i<3; i++ )
```

```
    {
        *(xnew+i) = xt[i] + *(ppos+0);
        *(ynew+i) = yt[i] + *(ppos+1);
        *(znew+i) = zt[i] + *(ppos+2);
    }

    return 0;
}


/*********************************************************************/
        rotate_target( xp, yp, zp, pos, ang, dang, dz )
        float *xp,*yp,*zp,pos[3],ang[3],dang[3],dz;
/*********************************************************************/

/*  This routine is used to compute target locations, velocities and
    accelerations  */

{
    int i;
    float xt, yt, zt, x1, y1, z1;
    float x2, y2, z2, x3, y3, z3, x4, y4, z4;
    float xa, ya, za, xb, yb, zb;
    float phi, theta, psi, dphi, dtheta, dpsi;

    phi = ang[0];
    theta = ang[1];
    psi = ang[2];

    dphi = dang[0];
    dtheta = dang[1];
    dpsi = dang[2];


/*  Translation  */

    xt = *xp - pos[0];
    yt = *yp - pos[1];
    zt = *zp - pos[2];

/*  Psi rotation  */

    xa = xt*cos(psi) +yt*sin(psi);
    ya = -xt*sin(psi) +yt*cos(psi);
    za = zt;

/*  Theta rotation  */

    xb = xa*cos(theta) - za*sin(theta);
    yb = ya;
    zb = xa*sin(theta) + za*cos(theta);
```

```
/*  Phi rotation  */

   x1 = xb;
   y1 = yb*cos(phi)+ zb*sin(phi);
   z1 = -yb*sin(phi)+ zb*cos(phi);

/*  Rotation and translation from offset body axes to body fixed axes  */

   x2 = x1;
   y2 = y1*cos(dphi) + z1*sin(dphi);
   z2 = -y1*sin(dphi) + z1*cos(dphi);


   x3 = x2*cos(dtheta) - z2*sin(dtheta);
   y3 = y2;
   z3 = x2*sin(dtheta) + z2*cos(dtheta);

   x4 = x3*cos(dpsi) + y3*sin(dpsi);
   y4 = -x3*sin(dpsi) + y3*cos(dpsi);
   z4 = z3;

   *xp = x4;
   *yp = y4;
   *zp = z4 - dz;

   return 0;
}


/*************************************************************************
*****/
      trans( refp, dangp, dz, posref, angref, ixx, qbar, dyfile )
      float **refp, *dangp, dz, *posref, *angref, ixx, qbar;
      char *dyfile;
/*************************************************************************
*****/

/*  This subroutine takes the dynamic data and transforms it into the model
    reference frame. The first point tracked must always be the origin.
    The second and third points must be the 0.5c chord and the wingtip,
    respectively. Position, velocity and acceleration data will be reduced
    using EV smoothed and central differenced data files. These data files
    must have the extensions p.trx, p.try, p.trz, v.trx, v.try, v.trz, a.trx,
    a.try, a.trz. Output from this subroutine includes two data files. The
    first contains model movement of the origin and changes in stability axis
    angles. The second file contains the roll angles, rates, and accelerations
    of the delta model. The next series of files are tagged with the .trg
    extension denoting the targets tracked relative the the wing. The next
    group of files contains data at the quarter, half, three-quarter, and
    95% chord loctions. The last series contains points at different
    bank angles. This information will be used to form vortex locations
    relative to a bank angle.                                          */
```

```
{
   FILE *fp1,*fp2,*fp3,*fp4,*fp5,*fp6,*fp7,*fp8,*fp9,*fp10,*fp11,*fp12;
   FILE *fp13, *fp14, *fp15, ***fptr;
   int i, j, jj, k, l, m, mark, limit, frame_rate, npts, numtargs, incdec;
   int switch25, switch50, switch65, switch75, switch85, switch95;
   int switchi, switchd, switchmi, switchmd, count, rollname, roll1, roll2;
   short int largest_record, number_of_records, frame, ii, lp, n;
   char *dfile, *dfile1, *dfile2, *data_file, *root_file, *dum_file;
   char *fxp, *fyp, *fzp, *fxv, *fyv, *fzv, *fxa, *fya, *fza, *data_filem;
   char *numb, *numb1, ch, *ubar, *bankangle, croll1, croll2;
   float **x, **y, **z, *xref, *yref, *zref, *xtref, *ytref, *ztref;
   float dumx, dumy, dumz, dummy, r, *xcross, *ycross, *zcross;
   float *xavg, *yavg, *zavg, *xt, *yt, *zt, **delx, **dely, **delz;
   float *px, *py, *pz, *xvel, *yvel, *zvel, *xacc, *yacc, *zacc;
   float **xdot, **ydot, **zdot, **xdotdot, **ydotdot, **zdotdot;
   float **dtx, **dty, **dtz;
   float *dotx, *doty, *dotz, *dotdotx, *dotdoty, *dotdotz;
   float *xtrans, *ytrans, *ztrans, **pos, **ang, **delang, *zero;
   float *phi, *phidot, *phidotdot, **xtarg, **ytarg, **ztarg;
   float **xvtarg, **yvtarg, **zvtarg, **xatarg, **yatarg, **zatarg;
   float *targ25,*targ50,*targ65,*targ75,*targ85,*targ95,*bank,*roll,*rollmom;
   float wingarea, wingspan, b, c, zdel;
   short int **frame_ptr;

   x       = (float **) malloc( 1500 * sizeof( float * ));
   y       = (float **) malloc( 1500 * sizeof( float * ));
   z       = (float **) malloc( 1500 * sizeof( float * ));
   dtx     = (float **) malloc( 1500 * sizeof( float * ));
   dty     = (float **) malloc( 1500 * sizeof( float * ));
   dtz     = (float **) malloc( 1500 * sizeof( float * ));
   xdot    = (float **) malloc( 1500 * sizeof( float * ));
   ydot    = (float **) malloc( 1500 * sizeof( float * ));
   zdot    = (float **) malloc( 1500 * sizeof( float * ));
   xdotdot= (float **) malloc( 1500 * sizeof( float * ));
   ydotdot= (float **) malloc( 1500 * sizeof( float * ));
   zdotdot= (float **) malloc( 1500 * sizeof( float * ));
   delx    = (float **) malloc( 1500 * sizeof( float * ));
   dely    = (float **) malloc( 1500 * sizeof( float * ));
   delz    = (float **) malloc( 1500 * sizeof( float * ));
   delang = (float **) malloc( 1500 * sizeof( float * ));
   pos     = (float **) malloc( 1500 * sizeof( float * ));
   ang     = (float **) malloc( 1500 * sizeof( float * ));
   phi     = (float *) malloc( 1500 * sizeof( float ));
   phidot = (float *) malloc( 1500 * sizeof( float ));
   phidotdot = (float *) malloc( 1500 * sizeof( float ));
   rollmom = (float *) malloc( 1500 * sizeof( float ));
   xtarg  = (float **) malloc( 1500 * sizeof( float * ));
   ytarg  = (float **) malloc( 1500 * sizeof( float * ));
   ztarg  = (float **) malloc( 1500 * sizeof( float * ));
   xvtarg  = (float **) malloc( 1500 * sizeof( float * ));
   yvtarg  = (float **) malloc( 1500 * sizeof( float * ));
```

```
    zvtarg  = (float **) malloc( 1500 * sizeof( float * ));
    xatarg  = (float **) malloc( 1500 * sizeof( float * ));
    yatarg  = (float **) malloc( 1500 * sizeof( float * ));
    zatarg  = (float **) malloc( 1500 * sizeof( float * ));
    frame_ptr = (short **) malloc( 1500 * sizeof( short * ));
    fptr    = (FILE ***) malloc( 20 * sizeof( FILE ** ));

/*  Initializing pointers  */

    for(i=0; i<1500; i++)
    {
       x[i]       = (float *) malloc( 3 * sizeof( float ));
       y[i]       = (float *) malloc( 3 * sizeof( float ));
       z[i]       = (float *) malloc( 3 * sizeof( float ));
       dtx[i]     = (float *) malloc( 3 * sizeof( float ));
       dty[i]     = (float *) malloc( 3 * sizeof( float ));
       dtz[i]     = (float *) malloc( 3 * sizeof( float ));
       xdot[i]    = (float *) malloc( 3 * sizeof( float ));
       ydot[i]    = (float *) malloc( 3 * sizeof( float ));
       zdot[i]    = (float *) malloc( 3 * sizeof( float ));
       xdotdot[i]= (float *) malloc( 3 * sizeof( float ));
       ydotdot[i]= (float *) malloc( 3 * sizeof( float ));
       zdotdot[i]= (float *) malloc( 3 * sizeof( float ));
       delx[i]    = (float *) malloc( 3 * sizeof( float ));
       dely[i]    = (float *) malloc( 3 * sizeof( float ));
       delz[i]    = (float *) malloc( 3 * sizeof( float ));
       delang[i] = (float *) malloc( 3 * sizeof( float ));
       pos[i]     = (float *) malloc( 3 * sizeof( float ));
       ang[i]     = (float *) malloc( 3 * sizeof( float ));
    }

/*  Initializing file pointers for bank angle data  */

    for(i=0; i<20; i++)
    {
      fptr[i]     = (FILE **) malloc( 8 * sizeof( FILE *));

      for(j=0; j<8; j++)
        fptr[i][j] = (FILE *) malloc( sizeof( FILE ));
    }

    xavg = (float *) malloc( 3 * sizeof(float) );
    yavg = (float *) malloc( 3 * sizeof(float) );
    zavg = (float *) malloc( 3 * sizeof(float) );
    px = (float *) malloc( 3 * sizeof(float) );
    py = (float *) malloc( 3 * sizeof(float) );
    pz = (float *) malloc( 3 * sizeof(float) );
    xvel = (float *) malloc( 3 * sizeof(float) );
    yvel = (float *) malloc( 3 * sizeof(float) );
    zvel = (float *) malloc( 3 * sizeof(float) );
    xacc = (float *) malloc( 3 * sizeof(float) );
    yacc = (float *) malloc( 3 * sizeof(float) );
```

```
zacc = (float *) malloc( 3 * sizeof(float) );
dotx = (float *) malloc( 3 * sizeof(float) );
doty = (float *) malloc( 3 * sizeof(float) );
dotz = (float *) malloc( 3 * sizeof(float) );
dotdotx = (float *) malloc( 3 * sizeof(float) );
dotdoty = (float *) malloc( 3 * sizeof(float) );
dotdotz = (float *) malloc( 3 * sizeof(float) );
xt = (float *) malloc( 3 * sizeof(float) );
yt = (float *) malloc( 3 * sizeof(float) );
zt = (float *) malloc( 3 * sizeof(float) );
xcross = (float *) malloc( 2 * sizeof(float) );
ycross = (float *) malloc( 2 * sizeof(float) );
zcross = (float *) malloc( 2 * sizeof(float) );
xtrans = (float *) malloc( 3 * sizeof(float) );
ytrans = (float *) malloc( 3 * sizeof(float) );
ztrans = (float *) malloc( 3 * sizeof(float) );
xref = (float *) malloc( 3 * sizeof(float) );
yref = (float *) malloc( 3 * sizeof(float) );
zref = (float *) malloc( 3 * sizeof(float) );
xtref = (float *) malloc( 3 * sizeof(float) );
ytref = (float *) malloc( 3 * sizeof(float) );
ztref = (float *) malloc( 3 * sizeof(float) );
zero = (float *) malloc( 3 * sizeof(float) );
targ25 = (float *) malloc( 9 * sizeof(float) );
targ50 = (float *) malloc( 9 * sizeof(float) );
targ65 = (float *) malloc( 9 * sizeof(float) );
targ75 = (float *) malloc( 9 * sizeof(float) );
targ85 = (float *) malloc( 9 * sizeof(float) );
targ95 = (float *) malloc( 9 * sizeof(float) );
bank = (float *) malloc( 9 * sizeof(float) );
roll = (float *) malloc( 20 * sizeof(float) );
bankangle = (char *) malloc( 2 * sizeof( char ));

dfile = (char *) malloc( 12 );        /*  Initializtion of memory for */
data_file = (char *) malloc( 12 );    /*  for string pointers         */
data_filem = (char *) malloc( 12 );
dfile1 = (char *) malloc( 12 );
dfile2 = (char *) malloc( 12 );
root_file = (char *) malloc( 12 );
dum_file = (char *) malloc( 12 );
fxp = (char *) malloc( 12 );
fyp = (char *) malloc( 12 );
fzp = (char *) malloc( 12 );
fxv = (char *) malloc( 12 );
fyv = (char *) malloc( 12 );
fzv = (char *) malloc( 12 );
fxa = (char *) malloc( 12 );
fya = (char *) malloc( 12 );
fza = (char *) malloc( 12 );
numb = (char *) malloc( 2 );
numb1 = (char *) malloc( 2 );
ubar = (char *) malloc( 2 );
```

```
    for(j=0; j<3; j++)
    {
      *(xref+j) = *(*(refp+j)+0);
      *(yref+j) = *(*(refp+j)+1);
      *(zref+j) = *(*(refp+j)+2);
      *(zero+j) = 0.0;
    }

/*  Constant data  */

    frame_rate = 60;   /*  Frame rate of the data recorded  */
    r          = 1.81; /*  Radius of wingtip  */

    count      = 4;    /*  Number of bank angles tracked  */
    *(roll+0)  = 30.0; /*  Bank angles in degrees observed  */
    *(roll+1)  = 25.0; /*  Note that both positive and negative angles  */
    *(roll+2)  = 15.0; /*      are recorded  */
    *(roll+3)  = 5.0;

    wingarea  = 17.6327/144.0;
    wingspan  = 3.5265/12.0;
    b         = wingspan * 12.0/2.0;
    c         = 9.8;

    j=0;
    while( *(dyfile+j) != 0 )
    {
      *(root_file+j) = *(dyfile+j);
      j++;
    }

    mark = 512;

    strcpy(dfile1, root_file);  /* Assign root filename  */
    strcpy(dfile2, root_file);
    strcpy(fxp, root_file);
    strcpy(fyp, root_file);
    strcpy(fzp, root_file);
    strcpy(fxv, root_file);
    strcpy(fyv, root_file);
    strcpy(fzv, root_file);
    strcpy(fxa, root_file);
    strcpy(fya, root_file);
    strcpy(fza, root_file);

    strcat( dfile1, "d.dat" );
    strcat( dfile2, "r.dat" );

    strcat( fxp, "p.trx" );
    strcat( fyp, "p.try" );
    strcat( fzp, "p.trz" );
    strcat( fxv, "v.trx" );
```

```
    strcat( fyv, "v.try" );
    strcat( fzv, "v.trz" );
    strcat( fxa, "a.trx" );
    strcat( fya, "a.try" );
    strcat( fza, "a.trz" );

/*  Opening all EV dynamic data files for reading  */

    if((fp1 = fopen(fxp,"rb"))==NULL)
    {
      printf("Error opening file\n");
      exit(1);
    }

    if((fp2 = fopen(fyp,"rb"))==NULL)
    {
      printf("Error opening file\n");
      exit(1);
    }

    if((fp3 = fopen(fzp,"rb"))==NULL)
    {
      printf("Error opening file\n");
      exit(1);
    }
    if((fp4 = fopen(fxv,"rb"))==NULL)
    {
      printf("Error opening file\n");
      exit(1);
    }

    if((fp5 = fopen(fyv,"rb"))==NULL)
    {
      printf("Error opening file\n");
      exit(1);
    }

    if((fp6 = fopen(fzv,"rb"))==NULL)
    {
      printf("Error opening file\n");
      exit(1);
    }
    if((fp7 = fopen(fxa,"rb"))==NULL)
    {
      printf("Error opening file\n");
      exit(1);
    }

    if((fp8 = fopen(fya,"rb"))==NULL)
    {
      printf("Error opening file\n");
      exit(1);
```

```
    }

    if((fp9 = fopen(fza,"rb"))==NULL)
    {
      printf("Error opening file\n");
      exit(1);
    }

/*  Reading from the table of contents of the track file  */

    fseek(fp1, 14, 0);                    /* Largest record in file */
    fread(&largest_record, 2, 1, fp1);

    npts = (largest_record - 14)/2;

    fseek(fp1, 18, 0);                    /* Number of records in file */
    fread(&number_of_records, 2, 1, fp1);

    numtargs = number_of_records - 3;  /* Subtracting 3 points on wing  */

    for( i=0; i<1500; i++)
    {
      frame_ptr[i] = (short *) malloc( (short) numtargs * sizeof( short ));
      xtarg[i] = (float *) malloc( numtargs * sizeof( float ));
      ytarg[i] = (float *) malloc( numtargs * sizeof( float ));
      ztarg[i] = (float *) malloc( numtargs * sizeof( float ));
      xvtarg[i] = (float *) malloc( numtargs * sizeof( float ));
      yvtarg[i] = (float *) malloc( numtargs * sizeof( float ));
      zvtarg[i] = (float *) malloc( numtargs * sizeof( float ));
      xatarg[i] = (float *) malloc( numtargs * sizeof( float ));
      yatarg[i] = (float *) malloc( numtargs * sizeof( float ));
      zatarg[i] = (float *) malloc( numtargs * sizeof( float ));
    }

    fseek(fp1, 518, 0);      /* Beginning frame number of record */
    fread(&frame, 2, 1, fp1);

    fseek(fp1, mark+28, 0);   /*  Location of first data point  */
    fseek(fp2, mark+28, 0);   /*  Location of first data point  */
    fseek(fp3, mark+28, 0);   /*  Location of first data point  */
    fseek(fp4, mark+28, 0);   /*  Location of first data point  */
    fseek(fp5, mark+28, 0);   /*  Location of first data point  */
    fseek(fp6, mark+28, 0);   /*  Location of first data point  */
    fseek(fp7, mark+28, 0);   /*  Location of first data point  */
    fseek(fp8, mark+28, 0);   /*  Location of first data point  */
    fseek(fp9, mark+28, 0);   /*  Location of first data point  */

    for( j=0; j<3; j++ )        /*  Loop to read from binary file  */
    {
      for( i=0; i<npts; i++ )       /*  Incrementing points of target */
      {
        fread(*(x+i)+j, 4, 1, fp1);
```

```
            fread(*(y+i)+j, 4, 1, fp2);
            fread(*(z+i)+j, 4, 1, fp3);
            fread(*(xdot+i)+j, 4, 1, fp4);
            fread(*(ydot+i)+j, 4, 1, fp5);
            fread(*(zdot+i)+j, 4, 1, fp6);
            fread(*(xdotdot+i)+j, 4, 1, fp7);
            fread(*(ydotdot+i)+j, 4, 1, fp8);
            fread(*(zdotdot+i)+j, 4, 1, fp9);
          }

          mark = ftell(fp1);  /*  Marking current place in file stream  */

          fseek(fp1, mark+28, 0);
          fseek(fp2, mark+28, 0);
          fseek(fp3, mark+28, 0);
          fseek(fp4, mark+28, 0);
          fseek(fp5, mark+28, 0);
          fseek(fp6, mark+28, 0);
          fseek(fp7, mark+28, 0);
          fseek(fp8, mark+28, 0);
          fseek(fp9, mark+28, 0);
        }

    /*  Using points at each time step  */

        for(l=0; l<npts; l++)
        {
          for(j=0; j<3; j++)
          {
            *(xavg+j) = *(*(x+l)+j);
            *(yavg+j) = *(*(y+l)+j);
            *(zavg+j) = *(*(z+l)+j);
            *(xvel+j) = *(*(xdot+l)+j);
            *(yvel+j) = *(*(ydot+l)+j);
            *(zvel+j) = *(*(zdot+l)+j);
            *(xacc+j) = *(*(xdotdot+l)+j);
            *(yacc+j) = *(*(ydotdot+l)+j);
            *(zacc+j) = *(*(zdotdot+l)+j);
          }

          *(*(pos+l)+0) = *(xavg+0);
          *(*(pos+l)+1) = *(yavg+0);
          *(*(pos+l)+2) = *(zavg+0);

    /*  Translation to the body fixed origin  */

          translation( xavg, yavg, zavg, xt, yt, zt );

    /*  Correction for non orthogonal points on wing  */

          crossproduct( *(xt+1),*(yt+1),*(zt+1),*(xt+2),*(yt+2),*(zt+2),
                        xcross,ycross, zcross );
```

```
        crossproduct( *xcross,*ycross,*zcross,*(xt+1),*(yt+1),*(zt+1),
                      &xcross[1],&ycross[1],&zcross[1] );

    /*  Corrected y axis.  Now orthogonal axis system  */

        *(xt+2) = *(xcross+1);
        *(yt+2) = *(ycross+1);
        *(zt+2) = *(zcross+1);

    /*  Calculation of the angles between inertial and initial body axes  */
    /*                          3-2-1 Rotation  */

        rotation1( xt, yt, zt, &ang[l][0] );

    /*  Reference Axis System transformed to rolling axes              */

        rotate( xref,yref,zref,&pos[l][0],&ang[l][0],dangp,&delx[l][0],
                &dely[l][0],&delz[l][0],dz);

    /*  Velocity and Acceleration files transformed to the fixed reference axes  */
    /*
                                        r     o     t     a     t     e     (
    xavg,yavg,zavg,&pos[l][0],&ang[l][0],dangp,&dtx[l][0],&dty[l][0],&dtz[l][0],dz );
    */
        rotate( xvel,yvel,zvel,zero,&ang[l][0],dangp,dotx,doty,dotz, 0.0 );

        rotate( xacc,yacc,zacc,zero,&ang[l][0],dangp,dotdotx,dotdoty,dotdotz,0.0 );

    /*  Computing translational and rotational displacement between fixed
        and rolling axes systems  */

        translation( &delx[l][0], &dely[l][0], &delz[l][0], xtref, ytref, ztref );

        zdel = .00;
        for(i=0;i<3;i++)
          *(ztref+i) = *(ztref+i) + zdel;

        rotation( xtref, ytref, ztref, &delang[l][0] );

    /*  Computing roll rate and roll acceleration of the delta wing  */

        *(phidot+l) = (*(dotz+2)*cos(*(*(delang+l)+0)) -
                       *(doty+2)*sin(*(*(delang+l)+0)))/r;

        *(phidotdot+l) = (*(dotdotz+2)*cos(*(*(delang+l)+0)) -
                          *(dotdoty+2)*sin(*(*(delang+l)+0)))/r;

        *(rollmom+l) = *(phidotdot+l) * ixx /qbar /wingarea / wingspan;
      }

        if((fp10 = fopen(dfile1,"w"))==NULL)
        {
```

```
      printf("Error opening file\n");
      exit(1);
    }

    if((fp11 = fopen(dfile2,"w"))==NULL)
    {
      printf("Error opening file\n");
      exit(1);
    }

/*  Output of data_file_1.dat  */

      fprintf(fp10,"Frame Time(secs) dX(in)  dY(in)  dZ(in)  Phi(deg)  Theta(deg)
Psi(deg)\n\n");

      for(i=0; i<npts; i++)
        fprintf(fp10,"%4d  %7.4f  %7.4f  %7.4f  %7.4f  %8.4f  %8.4f  %8.4f\n",
          i+frame, (float) (i+frame-1)/frame_rate,
          *(*(delx+i)+0), *(*(dely+i)+0), *(*(delz+i)+0),
          *(*(delang+i)+0)*R2D, *(*(delang+i)+1)*R2D, *(*(delang+i)+2)*R2D);

      fclose(fp10);

      fprintf(fp11,"Frame Time(secs) Phi(deg) Phi.(d/s) Phi..(deg/s/s) Cl\n\n");

      for(i=0; i<npts; i++)
        fprintf(fp11,"%4d  %7.4f  %8.4f %9.4f %10.4f %8.4f\n",
          i+frame, (float) (i+frame-1)/frame_rate,
          *(*(delang+i)+0)*R2D, *(phidot+i)*R2D, *(phidotdot+i)*R2D,
          *(rollmom+i));

      fclose(fp11);

/* * * * * * * * * * * * * * * * * * * * * * * * * * * * * * * * * * * * * * */
/*  This part of the program reduces vortex data relative to a rolling
    reference frame                                                          */
/* * * * * * * * * * * * * * * * * * * * * * * * * * * * * * * * * * * * * * */

   if(numtargs<=0)
     return;

/*  Creating and opening data files for quarter, half, three-quarters, and
    95% chord locations  */

   strcpy(data_file, root_file);  /* Assign root filename  */
   strcat( data_file, "25c.dat" );

   if((fp10 = fopen(data_file,"w"))==NULL)
   {
     printf("Error opening file\n");
     exit(1);
   }
```

```
   fprintf(fp10,"Frame I/D  Phi(deg)  X/c      Y/b      Z/b     X.(in/sec) Y.(in/sec)
Z.(in/sec) X..(in/s/s) Y..(in/s/s) Z..(in/s/s)\n\n");

   strcpy(data_file, root_file); /* Assign root filename */
   strcat( data_file, "50c.dat" );

   if((fp11 = fopen(data_file,"w"))==NULL)
   {
     printf("Error opening file\n");
     exit(1);
   }

   fprintf(fp11,"Frame I/D  Phi(deg)  X/c      Y/b      Z/b     X.(in/sec) Y.(in/sec)
Z.(in/sec) X..(in/s/s) Y..(in/s/s) Z..(in/s/s)\n\n");

   strcpy(data_file, root_file); /* Assign root filename */
   strcat( data_file, "65c.dat" );

   if((fp12 = fopen(data_file,"w"))==NULL)
   {
     printf("Error opening file\n");
     exit(1);
   }

   fprintf(fp12,"Frame I/D  Phi(deg)  X/c      Y/b      Z/b     X.(in/sec) Y.(in/sec)
Z.(in/sec) X..(in/s/s) Y..(in/s/s) Z..(in/s/s)\n\n");

   strcpy(data_file, root_file); /* Assign root filename */
   strcat( data_file, "75c.dat" );

   if((fp13 = fopen(data_file,"w"))==NULL)
   {
     printf("Error opening file\n");
     exit(1);
   }

   fprintf(fp13,"Frame I/D  Phi(deg)  X/c      Y/b      Z/b     X.(in/sec) Y.(in/sec)
Z.(in/sec) X..(in/s/s) Y..(in/s/s) Z..(in/s/s)\n\n");

   strcpy(data_file, root_file); /* Assign root filename */
   strcat( data_file, "85c.dat" );

   if((fp14 = fopen(data_file,"w"))==NULL)
   {
     printf("Error opening file\n");
     exit(1);
   }

   fprintf(fp14,"Frame I/D  Phi(deg)  X/c      Y/b      Z/b     X.(in/sec) Y.(in/sec)
Z.(in/sec) X..(in/s/s) Y..(in/s/s) Z..(in/s/s)\n\n");

   strcpy(data_file, root_file); /* Assign root filename */
```

```
   strcat( data_file, "95c.dat" );

   if((fp15 = fopen(data_file,"w"))==NULL)
   {
     printf("Error opening file\n");
     exit(1);
   }

   fprintf(fp15,"Frame I/D  Phi(deg)  X/c      Y/b      Z/b      X.(in/sec) Y.(in/sec)
Z.(in/sec) X..(in/s/s) Y..(in/s/s) Z..(in/s/s)\n\n");

/*  Character for underscore  */

   *(ubar) = 95;
   *(ubar+1) = 0;

/*  Creating and opening data files for specific bank angle data  */

   for(k=0; k<count; k++)
   {
     strcpy(data_file, root_file);  /* Constructing filename  */
     strcpy(data_filem, root_file);
     strcat( data_filem, "m" );
     rollname = (int) *(roll+k);
     roll1 = (int) (rollname/10);
     roll2 = rollname % 10;
     croll1 = 48 + roll1;
     croll2 = 48 + roll2;
     *(bankangle+0) = croll1;
     *(bankangle+1) = croll2;
     strcat( data_file, bankangle );
     strcat( data_filem, bankangle );
     *bankangle = '\0';
     strcpy( dfile, data_file );
     strcat( dfile, "ir.dat" );

     if((fptr[k][0] = fopen(dfile,"w"))==NULL)
     {
       printf("Error opening file\n");
       exit(1);
     }

     fprintf(fptr[k][0],"Frame Phi(deg)  X/c      Y/b      Z/b      X.(in/sec) Y.(in/sec)
Z.(in/sec) X..(in/s/s) Y..(in/s/s) Z..(in/s/s)\n\n");

     strcpy(dfile, data_file);  /* Assign root filename  */
     strcat( dfile, "il.dat" );

     if((fptr[k][1] = fopen(dfile,"w"))==NULL)
     {
       printf("Error opening file\n");
       exit(1);
```

```
    }

    fprintf(fptr[k][1],"Frame Phi(deg)  X/c     Y/b     Z/b     X.(in/sec) Y.(in/sec)
Z.(in/sec) X..(in/s/s) Y..(in/s/s) Z..(in/s/s)\n\n");

    strcpy(dfile, data_file);  /* Assign root filename  */
    strcat( dfile, "dr.dat" );

    if((fptr[k][2] = fopen(dfile,"w"))==NULL)
    {
      printf("Error opening file\n");
      exit(1);
    }

    fprintf(fptr[k][2],"Frame Phi(deg)  X/c     Y/b     Z/b     X.(in/sec) Y.(in/sec)
Z.(in/sec) X..(in/s/s) Y..(in/s/s) Z..(in/s/s)\n\n");

    strcpy(dfile, data_file);  /* Assign root filename  */
    strcat( dfile, "dl.dat" );

    if((fptr[k][3] = fopen(dfile,"w"))==NULL)
    {
      printf("Error opening file\n");
      exit(1);
    }

    fprintf(fptr[k][3],"Frame Phi(deg)  X/c     Y/b     Z/b     X.(in/sec) Y.(in/sec)
Z.(in/sec) X..(in/s/s) Y..(in/s/s) Z..(in/s/s)\n\n");

    strcpy(dfile, data_filem);  /* Assign root filename  */
    strcat( dfile, "ir.dat" );

    if((fptr[k][4] = fopen(dfile,"w"))==NULL)
    {
      printf("Error opening file\n");
      exit(1);
    }

    fprintf(fptr[k][4],"Frame Phi(deg)  X/c     Y/b     Z/b     X.(in/sec) Y.(in/sec)
Z.(in/sec) X..(in/s/s) Y..(in/s/s) Z..(in/s/s)\n\n");

    strcpy(dfile, data_filem);  /* Assign root filename  */
    strcat( dfile, "il.dat" );

    if((fptr[k][5] = fopen(dfile,"w"))==NULL)
    {
      printf("Error opening file\n");
      exit(1);
    }

    fprintf(fptr[k][5],"Frame Phi(deg)  X/c     Y/b     Z/b     X.(in/sec) Y.(in/sec)
Z.(in/sec) X..(in/s/s) Y..(in/s/s) Z..(in/s/s)\n\n");
```

```
      strcpy(dfile, data_filem);  /* Assign root filename  */
      strcat( dfile, "dr.dat" );

      if((fptr[k][6] = fopen(dfile,"w"))==NULL)
      {
        printf("Error opening file\n");
        exit(1);
      }

      fprintf(fptr[k][6],"Frame Phi(deg)  X/c     Y/b     Z/b     X.(in/sec) Y.(in/sec)
Z.(in/sec) X..(in/s/s) Y..(in/s/s) Z..(in/s/s)\n\n");

      strcpy(dfile, data_filem);  /* Assign root filename  */
      strcat( dfile, "dl.dat" );

      if((fptr[k][7] = fopen(dfile,"w"))==NULL)
      {
        printf("Error opening file\n");
        exit(1);
      }

      fprintf(fptr[k][7],"Frame Phi(deg)  X/c     Y/b     Z/b     X.(in/sec) Y.(in/sec)
Z.(in/sec) X..(in/s/s) Y..(in/s/s) Z..(in/s/s)\n\n");
    }

/*  Main loop for reading from data files and transforming data  */

   for( l=0; l<numtargs; l++)
   {
      strcpy(data_file, root_file);  /* Assign root filename for target data  */
      strcat( data_file, ".dat.trg." );

      if(l<=8)   /*  Assigning tag to target files */
      {
        *(numb) = l+49;
        *(numb+1) = 0;
      }
      else
        if(l>8 && l<=18)
      {
        *(numb1) = 49;
        *(numb1+1) = 0;
        *(numb)  = l+39;
        *(numb+1) = 0;
        strcat( data_file, numb1);
      }
      else
        if(l>18 && l<=28)
      {
        *(numb1) = 50;
        *(numb1+1) = 0;
        *(numb)  = l+29;
```

```
    *(numb+1) = 0;
    strcat( data_file, numb1);
  }
  else
    if(l>28 && l<=38)
  {
    *(numb1) = 51;
    *(numb1+1) = 0;
    *(numb)  = l+19;
    *(numb+1) = 0;
    strcat( data_file, numb1);
  }
  else
    if(l>38 && l<=48)
  {
    *(numb1) = 52;
    *(numb1+1) = 0;
    *(numb)  = l+9;
    *(numb+1) = 0;
    strcat( data_file, numb1);
  }
  else
    if(l>48 && l<=58)
  {
    *(numb1) = 53;
    *(numb1+1) = 0;
    *(numb)  = l-1;
    *(numb+1) = 0;
    strcat( data_file, numb1);
  }
  else
    if(l>58 && l<=68)
  {
    *(numb1) = 54;
    *(numb1+1) = 0;
    *(numb)  = l-11;
    *(numb+1) = 0;
    strcat( data_file, numb1);
  }
  else
    if(l>68 && l<=78)
  {
    *(numb1) = 55;
    *(numb1+1) = 0;
    *(numb)  = l-21;
    *(numb+1) = 0;
    strcat( data_file, numb1);
  }
  else
    if(l>78 && l<=88)
  {
    *(numb1) = 56;
```

```
        *(numb1+1) = 0;
        *(numb)  = l-31;
        *(numb+1) = 0;
        strcat( data_file, numb1);
      }
      else
        if(l>88)
      {
        *(numb1) = 57;
        *(numb1+1) = 0;
        *(numb)  = l-41;
        *(numb+1) = 0;
        strcat( data_file, numb1);
      }

      strcat( data_file, numb );

      fseek(fp1, mark+6, 0);      /* Beginning frame number of record */
      fread(&frame_ptr[0][l], 2, 1, fp1);

      fseek(fp1, mark+28, 0);
      fseek(fp2, mark+28, 0);
      fseek(fp3, mark+28, 0);
      fseek(fp4, mark+28, 0);
      fseek(fp5, mark+28, 0);
      fseek(fp6, mark+28, 0);
      fseek(fp7, mark+28, 0);
      fseek(fp8, mark+28, 0);
      fseek(fp9, mark+28, 0);

      j = *(*(frame_ptr+0)+l);

/*  Reading target data from EV binary files  */

      do
      {
        if((j-1)==1500)
          break;
        fread((*(xtarg+(j-1))+l), 4, 1, fp1);
        fread((*(ytarg+(j-1))+l), 4, 1, fp2);
        fread((*(ztarg+(j-1))+l), 4, 1, fp3);
        fread((*(xvtarg+(j-1))+l), 4, 1, fp4);
        fread((*(yvtarg+(j-1))+l), 4, 1, fp5);
        fread((*(zvtarg+(j-1))+l), 4, 1, fp6);
        fread((*(xatarg+(j-1))+l), 4, 1, fp7);
        fread((*(yatarg+(j-1))+l), 4, 1, fp8);
        fread((*(zatarg+(j-1))+l), 4, 1, fp9);
        j = j + 1;
      } while( fabs(*(*(xtarg+(j-2))+l)) > 0.00001 );

      lp = j - 2 - *(*(frame_ptr+0)+l);
```

```
    mark = ftell(fp1) - 4;

    for(ii=1; ii<=lp; ii++)
      *(*(frame_ptr+ii)+l) = *(*(frame_ptr+0)+l) + ii;

    n = *(*(frame_ptr+lp)+l);

/*  Transforming position, velocity, and acceleration data to body axes  */

    for(ii=(*(*(frame_ptr+0)+l)); ii<= n; ii++)
    {
      rotate_target( &xtarg[ii-1][l],&ytarg[ii-1][l],&ztarg[ii-1][l],
                     &pos[ii-1][0],&ang[ii-1][0],dangp,dz);

      rotate_target( &xvtarg[ii-1][l],&yvtarg[ii-1][l],&zvtarg[ii-1][l],
                     zero,&ang[ii-1][0],dangp,0.0);

      rotate_target( &xatarg[ii-1][l],&yatarg[ii-1][l],&zatarg[ii-1][l],
                     zero,&ang[ii-1][0],dangp,0.0);
    }

/*  Switches for conditional statements in chord location routines  */

    switch25=0;
    switch50=0;
    switch65=0;
    switch75=0;
    switch85=0;
    switch95=0;

/*  Loop for computing target data at four chordwise locations  */

    for(ii=(*(*(frame_ptr+0)+l)); ii<= n; ii++)
    {
/*  Quarter chord condition and computation  */

      if((*(*(xtarg+(ii-1))+l) < 7.35) && (switch25 == 1) )
      {
        interpolate( xtarg[ii-2][l],xtarg[ii-1][l],7.35,ytarg[ii-2][l],
                     ytarg[ii-1][l],ztarg[ii-2][l],ztarg[ii-1][l],
                     delang[ii-2][0],delang[ii-1][0],xvtarg[ii-2][l],
                     xvtarg[ii-1][l],yvtarg[ii-2][l],yvtarg[ii-1][l],
                     zvtarg[ii-2][l],zvtarg[ii-1][l],xatarg[ii-2][l],
                     xatarg[ii-1][l],yatarg[ii-2][l],yatarg[ii-1][l],
                     zatarg[ii-2][l],zatarg[ii-1][l],targ25 );

        if(*(phidot+(ii-1)) < 0.0 )
          incdec = 0;
        else
          incdec = 1;
```

```
        fprintf(fp10,"%4d   %1d  %8.4f %7.4f %7.4f %7.4f  %8.4f   %8.4f   %8.4f
%8.4f   %8.4f   %8.4f\n",
         ii, incdec, *(targ25+2)*R2D, 7.35/c, *(targ25+0)/b, *(targ25+1)/b,
         *(targ25+3), *(targ25+4), *(targ25+5), *(targ25+6), *(targ25+7),
         *(targ25+8));
      }
/*  Half chord condition and computation  */

      else if((*(*(xtarg+(ii-1))+l) < 4.90) && (switch50 == 1) )
      {
        interpolate( xtarg[ii-2][l],xtarg[ii-1][l],4.9,ytarg[ii-2][l],
                     ytarg[ii-1][l],ztarg[ii-2][l],ztarg[ii-1][l],
                     delang[ii-2][0],delang[ii-1][0],xvtarg[ii-2][l],
                     xvtarg[ii-1][l],yvtarg[ii-2][l],yvtarg[ii-1][l],
                     zvtarg[ii-2][l],zvtarg[ii-1][l],xatarg[ii-2][l],
                     xatarg[ii-1][l],yatarg[ii-2][l],yatarg[ii-1][l],
                     zatarg[ii-2][l],zatarg[ii-1][l],targ50 );

        if(*(phidot+(ii-1)) < 0.0 )
          incdec = 0;
        else
          incdec = 1;

        fprintf(fp11,"%4d   %1d  %8.4f %7.4f %7.4f %7.4f  %8.4f   %8.4f   %8.4f
%8.4f   %8.4f   %8.4f\n",
         ii, incdec, *(targ50+2)*R2D, 4.9/c, *(targ50+0)/b, *(targ50+1)/b,
         *(targ50+3), *(targ50+4), *(targ50+5), *(targ50+6), *(targ50+7),
         *(targ50+8));
      }

/*  65% chord condition and computation  */

      else if((*(*(xtarg+(ii-1))+l) < 3.43) && (switch65 == 1) )
      {
        interpolate( xtarg[ii-2][l],xtarg[ii-1][l],3.43,ytarg[ii-2][l],
                     ytarg[ii-1][l],ztarg[ii-2][l],ztarg[ii-1][l],
                     delang[ii-2][0],delang[ii-1][0],xvtarg[ii-2][l],
                     xvtarg[ii-1][l],yvtarg[ii-2][l],yvtarg[ii-1][l],
                     zvtarg[ii-2][l],zvtarg[ii-1][l],xatarg[ii-2][l],
                     xatarg[ii-1][l],yatarg[ii-2][l],yatarg[ii-1][l],
                     zatarg[ii-2][l],zatarg[ii-1][l],targ65 );

        if(*(phidot+(ii-1)) < 0.0 )
          incdec = 0;
        else
          incdec = 1;

        fprintf(fp12,"%4d   %1d  %8.4f %7.4f %7.4f %7.4f  %8.4f   %8.4f   %8.4f
%8.4f   %8.4f   %8.4f\n",
         ii, incdec, *(targ65+2)*R2D, 3.43/c, *(targ65+0)/b, *(targ65+1)/b,
         *(targ65+3), *(targ65+4), *(targ65+5), *(targ65+6), *(targ65+7),
         *(targ65+8));
```

```
      }

/*  Three-quarters chord condition and computation  */

      else if((*(*(xtarg+(ii-1))+l) < 2.45) && (switch75 == 1) )
      {
        interpolate( xtarg[ii-2][l],xtarg[ii-1][l],2.45,ytarg[ii-2][l],
                     ytarg[ii-1][l],ztarg[ii-2][l],ztarg[ii-1][l],
                     delang[ii-2][0],delang[ii-1][0],xvtarg[ii-2][l],
                     xvtarg[ii-1][l],yvtarg[ii-2][l],yvtarg[ii-1][l],
                     zvtarg[ii-2][l],zvtarg[ii-1][l],xatarg[ii-2][l],
                     xatarg[ii-1][l],yatarg[ii-2][l],yatarg[ii-1][l],
                     zatarg[ii-2][l],zatarg[ii-1][l],targ75 );

        if(*(phidot+(ii-1)) < 0.0 )
          incdec = 0;
        else
          incdec = 1;

        fprintf(fp13,"%4d   %1d  %8.4f %7.4f %7.4f %7.4f  %8.4f   %8.4f   %8.4f
%8.4f   %8.4f   %8.4f\n",
         ii, incdec, *(targ75+2)*R2D, 2.45/c, *(targ75+0)/b, *(targ75+1)/b,
         *(targ75+3), *(targ75+4), *(targ75+5), *(targ75+6), *(targ75+7),
         *(targ75+8));
      }

/*  85% chord condition and computation  */

      else if((*(*(xtarg+(ii-1))+l) < 1.47) && (switch85 == 1) )
      {
        interpolate( xtarg[ii-2][l],xtarg[ii-1][l],1.47,ytarg[ii-2][l],
                     ytarg[ii-1][l],ztarg[ii-2][l],ztarg[ii-1][l],
                     delang[ii-2][0],delang[ii-1][0],xvtarg[ii-2][l],
                     xvtarg[ii-1][l],yvtarg[ii-2][l],yvtarg[ii-1][l],
                     zvtarg[ii-2][l],zvtarg[ii-1][l],xatarg[ii-2][l],
                     xatarg[ii-1][l],yatarg[ii-2][l],yatarg[ii-1][l],
                     zatarg[ii-2][l],zatarg[ii-1][l],targ85 );

        if(*(phidot+(ii-1)) < 0.0 )
          incdec = 0;
        else
          incdec = 1;

        fprintf(fp14,"%4d   %1d  %8.4f %7.4f %7.4f %7.4f  %8.4f   %8.4f   %8.4f
%8.4f   %8.4f   %8.4f\n",
         ii, incdec, *(targ85+2)*R2D, 1.47/c, *(targ85+0)/b, *(targ85+1)/b,
         *(targ85+3), *(targ85+4), *(targ85+5), *(targ85+6), *(targ85+7),
         *(targ85+8));
      }

/*  95% chord condition and computation  */
```

```
        else if((*(*(xtarg+(ii-1))+l) < 0.49) && (switch95 == 1) )
        {
          interpolate( xtarg[ii-2][l],xtarg[ii-1][l],0.49,ytarg[ii-2][l],
                       ytarg[ii-1][l],ztarg[ii-2][l],ztarg[ii-1][l],
                       delang[ii-2][0],delang[ii-1][0],xvtarg[ii-2][l],
                       xvtarg[ii-1][l],yvtarg[ii-2][l],yvtarg[ii-1][l],
                       zvtarg[ii-2][l],zvtarg[ii-1][l],xatarg[ii-2][l],
                       xatarg[ii-1][l],yatarg[ii-2][l],yatarg[ii-1][l],
                       zatarg[ii-2][l],zatarg[ii-1][l],targ95 );

          if(*(phidot+(ii-1)) < 0.0 )
            incdec = 0;
          else
            incdec = 1;

          fprintf(fp15,"%4d   %1d  %8.4f %7.4f %7.4f %7.4f  %8.4f   %8.4f   %8.4f
%8.4f   %8.4f   %8.4f\n",
           ii, incdec, *(targ95+2)*R2D, 0.49/c, *(targ95+0)/b, *(targ95+1)/b,
           *(targ95+3), *(targ95+4), *(targ95+5), *(targ95+6), *(targ95+7),
           *(targ95+8));
        }

/*  Conditions to switch on or off data gathering  */

        if(*(*(xtarg+(ii-1))+l) < 7.35 )
          switch25 = 0;
        else
          switch25 = 1;

        if(*(*(xtarg+(ii-1))+l) < 4.90 )
          switch50 = 0;
        else
          switch50 = 1;

        if(*(*(xtarg+(ii-1))+l) < 3.43 )
          switch65 = 0;
        else
          switch65 = 1;

        if(*(*(xtarg+(ii-1))+l) < 2.45 )
          switch75 = 0;
        else
          switch75 = 1;

        if(*(*(xtarg+(ii-1))+l) < 1.47 )
          switch85 = 0;
        else
          switch85 = 1;

        if(*(*(xtarg+(ii-1))+l) < 0.49 )
          switch95 = 0;
        else
```

```
        switch95 = 1;
    }

/*  Loop for computing bank angle data  */

    for( k=0; k<count; k++)
    {
/*  Conditional switches  */

      switchi=0;
      switchd=0;
      switchmi=0;
      switchmd=0;

      for(ii=(*(*(frame_ptr+0)+l)); ii<= n; ii++)
      {
/*  Bank angle condition for positive angle increasing */

        if((*(*(delang+(ii-1))+0) > (*(roll+k)*D2R)) && (switchi == 1))
        {

          interpolate( delang[ii-2][0],delang[ii-1][0],(*(roll+k)*D2R),
                       xtarg[ii-2][l],xtarg[ii-1][l],
                       ytarg[ii-2][l],ytarg[ii-1][l],
                       ztarg[ii-2][l],ztarg[ii-1][l],
                       xvtarg[ii-2][l],xvtarg[ii-2][l],
                       yvtarg[ii-2][l],yvtarg[ii-2][l],
                       zvtarg[ii-2][l],zvtarg[ii-2][l],
                       xatarg[ii-2][l],xatarg[ii-2][l],
                       yatarg[ii-2][l],yatarg[ii-2][l],
                       zatarg[ii-2][l],zatarg[ii-2][l],
                       bank );

/*  Condition for right or left vortex  */

          if(*(bank+1) > 0.0)
          {
            fprintf(fptr[k][0],"%4d    %5.2f %7.4f %7.4f %7.4f %8.4f    %8.4f    %8.4f
%8.4f    %8.4f    %8.4f\n",
              ii, *(roll+k), *(bank+0)/c, *(bank+1)/b, *(bank+2)/b,
              *(bank+3), *(bank+4), *(bank+5), *(bank+6),
              *(bank+7), *(bank+8));
          }
          else
          {
            fprintf(fptr[k][1],"%4d    %5.2f %7.4f %7.4f %7.4f %8.4f    %8.4f    %8.4f
%8.4f    %8.4f    %8.4f\n",
              ii, *(roll+k), *(bank+0)/c, *(bank+1)/b, *(bank+2)/b,
              *(bank+3), *(bank+4), *(bank+5), *(bank+6),
              *(bank+7), *(bank+8));
          }
        }
```

```
/*  Bank angle condition for positive angle decreasing */

        if((*(*(delang+(ii-1))+0) < (*(roll+k)*D2R)) && (switchd == 1))
        {

          interpolate( delang[ii-2][0],delang[ii-1][0],(*(roll+k)*D2R),
                       xtarg[ii-2][l],xtarg[ii-1][l],
                       ytarg[ii-2][l],ytarg[ii-1][l],
                       ztarg[ii-2][l],ztarg[ii-1][l],
                       xvtarg[ii-2][l],xvtarg[ii-2][l],
                       yvtarg[ii-2][l],yvtarg[ii-2][l],
                       zvtarg[ii-2][l],zvtarg[ii-2][l],
                       xatarg[ii-2][l],xatarg[ii-2][l],
                       yatarg[ii-2][l],yatarg[ii-2][l],
                       zatarg[ii-2][l],zatarg[ii-2][l],
                       bank );

/*  Condition for right or left vortex  */

           if(*(bank+1) > 0.0)
           {
            fprintf(fptr[k][2],"%4d    %5.2f %7.4f %7.4f %7.4f %8.4f    %8.4f    %8.4f
%8.4f    %8.4f    %8.4f\n",
               ii, *(roll+k), *(bank+0)/c, *(bank+1)/b, *(bank+2)/b,
               *(bank+3), *(bank+4), *(bank+5), *(bank+6),
               *(bank+7), *(bank+8));
           }
           else
           {
            fprintf(fptr[k][3],"%4d    %5.2f %7.4f %7.4f %7.4f %8.4f    %8.4f    %8.4f
%8.4f    %8.4f    %8.4f\n",
               ii, *(roll+k), *(bank+0)/c, *(bank+1)/b, *(bank+2)/b,
               *(bank+3), *(bank+4), *(bank+5), *(bank+6),
               *(bank+7), *(bank+8));
           }
        }
/*  Bank angle condition for negative angle decreasing */

        if((*(*(delang+(ii-1))+0) < (-*(roll+k)*D2R)) && (switchmi == 1))
        {
          interpolate( delang[ii-2][0],delang[ii-1][0],(-*(roll+k)*D2R),
                       xtarg[ii-2][l],xtarg[ii-1][l],
                       ytarg[ii-2][l],ytarg[ii-1][l],
                       ztarg[ii-2][l],ztarg[ii-1][l],
                       xvtarg[ii-2][l],xvtarg[ii-2][l],
                       yvtarg[ii-2][l],yvtarg[ii-2][l],
                       zvtarg[ii-2][l],zvtarg[ii-2][l],
                       xatarg[ii-2][l],xatarg[ii-2][l],
                       yatarg[ii-2][l],yatarg[ii-2][l],
                       zatarg[ii-2][l],zatarg[ii-2][l],
                       bank );
```

```
/*  Condition for right or left vortex  */

          if(*(bank+1) > 0.0)
          {
           fprintf(fptr[k][4],"%4d    %5.2f %7.4f %7.4f %7.4f %8.4f    %8.4f    %8.4f
 %8.4f    %8.4f    %8.4f\n",
              ii, *(roll+k), *(bank+0)/c, *(bank+1)/b, *(bank+2)/b,
              *(bank+3), *(bank+4), *(bank+5), *(bank+6),
              *(bank+7), *(bank+8));
          }
          else
          {
           fprintf(fptr[k][5],"%4d    %5.2f %7.4f %7.4f %7.4f %8.4f    %8.4f    %8.4f
 %8.4f    %8.4f    %8.4f\n",
              ii, *(roll+k), *(bank+0)/c, *(bank+1)/b, *(bank+2)/b,
              *(bank+3), *(bank+4), *(bank+5), *(bank+6),
              *(bank+7), *(bank+8));
          }
        }
/*  Bank angle condition for negative angle increasing */

        if((*(*(delang+(ii-1))+0) > (-*(roll+k)*D2R)) && (switchmd == 1))
        {
          interpolate( delang[ii-2][0],delang[ii-1][0],(-*(roll+k)*D2R),
                       xtarg[ii-2][l],xtarg[ii-1][l],
                       ytarg[ii-2][l],ytarg[ii-1][l],
                       ztarg[ii-2][l],ztarg[ii-1][l],
                       xvtarg[ii-2][l],xvtarg[ii-2][l],
                       yvtarg[ii-2][l],yvtarg[ii-2][l],
                       zvtarg[ii-2][l],zvtarg[ii-2][l],
                       xatarg[ii-2][l],xatarg[ii-2][l],
                       yatarg[ii-2][l],yatarg[ii-2][l],
                       zatarg[ii-2][l],zatarg[ii-2][l],
                       bank );

/*  Condition for right or left vortex  */

          if(*(bank+1) > 0.0)
          {
           fprintf(fptr[k][6],"%4d    %5.2f %7.4f %7.4f %7.4f %8.4f    %8.4f    %8.4f
 %8.4f    %8.4f    %8.4f\n",
              ii, *(roll+k), *(bank+0)/c, *(bank+1)/b, *(bank+2)/b,
              *(bank+3), *(bank+4), *(bank+5), *(bank+6),
              *(bank+7), *(bank+8));
          }
          else
          {
           fprintf(fptr[k][7],"%4d    %5.2f %7.4f %7.4f %7.4f %8.4f    %8.4f    %8.4f
 %8.4f    %8.4f    %8.4f\n",
              ii, *(roll+k), *(bank+0)/c, *(bank+1)/b, *(bank+2)/b,
              *(bank+3), *(bank+4), *(bank+5), *(bank+6),
              *(bank+7), *(bank+8));
```

```
        }
      }

/*  Conditions for switching data collecting on or off  */

      if(*(*(delang+(ii-1))+0) > (*(roll+k)*D2R))
        switchi = 0;
      else
        switchi = 1;

      if(*(*(delang+(ii-1))+0) < (*(roll+k)*D2R))
        switchd = 0;
      else
        switchd = 1;

      if(*(*(delang+(ii-1))+0) < (-*(roll+k)*D2R))
        switchmi = 0;
      else
        switchmi = 1;

      if(*(*(delang+(ii-1))+0) > (-*(roll+k)*D2R))
        switchmd = 0;
      else
        switchmd = 1;

    }
  }

/*  Opening XXXX.trg data files   */
/*
    if((fp14 = fopen(data_file,"w"))==NULL)
    {
      printf("Error opening file\n");
      exit(1);
    }

    fprintf(fp16,"Frame Time(secs) Phi(deg)   X/c      Y/b      Z/b      X.(in/sec)
Y.(in/sec) Z.(in/sec) X..(in/s/s) Y..(in/s/s) Z..(in/s/s) \n\n");

    for(ii=*(*(frame_ptr+0)+1); ii<= n; ii++)
      fprintf(fp14,"%4d  %7.4f  %8.4f %8.4f %8.4f %8.4f %8.4f   %8.4f   %8.4f
  %8.4f    %8.4f    %8.4f\n",
      ii, (float) (ii-1)/frame_rate, *(*(delang+(ii-1))+0)*R2D,
      *(*(xtarg+(ii-1))+1)/c,*(*(ytarg+(ii-1))+1)/b,*(*(ztarg+(ii-1))+1)/b,
      *(*(xvtarg+(ii-1))+1),*(*(yvtarg+(ii-1))+1),*(*(zvtarg+(ii-1))+1),
      *(*(xatarg+(ii-1))+1),*(*(yatarg+(ii-1))+1),*(*(zatarg+(ii-1))+1));

    fclose(fp16);
*/
  }
  fclose( fp1 );
  fclose( fp2 );
```

```
fclose( fp3 );
fclose( fp4 );
fclose( fp5 );
fclose( fp6 );
fclose( fp7 );
fclose( fp8 );
fclose( fp9 );
fclose( fp10 );
fclose( fp11 );
fclose( fp12 );
fclose( fp13 );
fclose( fp14 );
fclose( fp15 );

for(k=0; k<count; k++)
  for(i=0; i<8; i++)
    fclose(fptr[k][i]);

free(x);
free(y);
free(z);
free(dtx);
free(dty);
free(dtz);
free(xdot);
free(ydot);
free(zdot);
free(xdotdot);
free(ydotdot);
free(zdotdot);
free(delx);
free(dely);
free(delz);
free(delang);
free(pos);
free(ang);
free(phi);
free(phidot);
free(phidotdot);
free(rollmom);
free(xtarg);
free(ytarg);
free(ztarg);
free(xvtarg);
free(yvtarg);
free(zvtarg);
free(xatarg);
free(yatarg);
free(zatarg);
free(frame_ptr);

return;
```

```
}


/*************************************************************************/
      interpolate( x1,x2,xi,y1,y2,z1,z2,phi1,phi2,xv1,xv2,yv1,yv2,
                   zv1,zv2,xa1,xa2,ya1,ya2,za1,za2,out )

      float x1,x2,xi,y1,y2,z1,z2,phi1,phi2,xv1,xv2,yv1,yv2;
      float zv1,zv2,xa1,xa2,ya1,ya2,za1,za2,*out;
/*************************************************************************/

/*  Linear interpolation routine for position, velocity and acceleration data */
{

   *(out+0) = y1 + ((y1-y2)/(x1-x2))*(xi-x1);
   *(out+1) = z1 + ((z1-z2)/(x1-x2))*(xi-x1);
   *(out+2) = phi1 + ((phi1-phi2)/(x1-x2))*(xi-x1);
   *(out+3) = xv1 + ((xv1-xv2)/(x1-x2))*(xi-x1);
   *(out+4) = yv1 + ((yv1-yv2)/(x1-x2))*(xi-x1);
   *(out+5) = zv1 + ((zv1-zv2)/(x1-x2))*(xi-x1);
   *(out+6) = xa1 + ((xa1-xa2)/(x1-x2))*(xi-x1);
   *(out+7) = ya1 + ((ya1-ya2)/(x1-x2))*(xi-x1);
   *(out+8) = za1 + ((za1-za2)/(x1-x2))*(xi-x1);

   return;
}
```

VITA

Captain Michael Denis Nelson was born December 27, 1961, in Moorehead, Minnesota. He graduated from the University of Kansas in May 1985 with a Bachelor of Science in Aerospace Engineering and received a commission in the United States Air Force. He was assigned to Aeronautical Systems Division, Air Force Systems Command, at Wright-Patterson Air Force Base where his initial assignment was in the Airlift and Flight Trainers System Program Office. After two years, he was assigned to the Deputy for Developmental Planning. In June 1989, he entered graduate school at Texas A&M University to pursue a Master of Science in Aerospace Engineering.

Captain Nelson is married to the former Nivia Murphy, and they have one son, Benjamin.